NUMERICAL MODELING OF RC AND ECC ENCASED RC COLUMNS SUBJECTED TO CLOSE-IN EXPLOSION

PATRIA KUSUMANINGRUM

NATIONAL UNIVERSITY OF SINGAPORE

2010

NUMERICAL MODELING OF RC AND ECC ENCASED RC COLUMNS SUBJECTED TO CLOSE-IN EXPLOSION

PATRIA KUSUMANINGRUM

(*B. Eng.* (*Hons*), *ITB*)

A THESIS SUBMITTED

FOR THE DEGREE OF DOCTOR OF PHILOSOPHY

DEPARTMENT OF CIVIL ENGINEERING

NATIONAL UNIVERSITY OF SINGAPORE

2010

ACKNOWLEDGEMENTS

"*Fabi ayi 'ala irobbikuma tukadziban*" (QS. Ar-Rahman)

The author wishes to express her sincere gratitude to her supervisor, Assoc. Prof. Ong Khim Chye, Gary for his patience, invaluable guidance and constructive advices throughout the course of this study. The author would also like to thank Prof. Somsak Swaddiwudhipong, Assoc. Prof. Zhang Min Hong and Assoc. Prof. Mohammed Maalej for their helpful suggestions and comments.

The author heartfelt appreciation is dedicated to Dr. Lee Siew Chin, Dr. L.J. Malvar (Karagozian & Case, USA), Dr. Leonard Schwer (Schwer Engineering & Consulting Services, USA) and Stefano Mazzalai (LSTC, USA) for their contributions and continuous supports.

Sincere thanks are also extended to the Defence Science and Technology Agency (DSTA), Singapore, for assistance with the application of research grants (No. R-379-000-018-232 and R-379-000-018-646) through the Centre for Protective Technology NUS. The kind assistance from all the staff members of the NUS Concrete and Structural Engineering Laboratory is deeply appreciated.

Countless thanks and loves go to her beloved friends for their moral support and mutual understanding. And finally, special thanks to her husband, parents, sister and brother whose support and patient love enabled her to complete this work.

Thank you for making this study possible and may God bless all of you…

TABLE OF CONTENTS

CHAPTER 2 LITERATURE REVIEW

CHAPTER 3 BLAST LOADS ON STRUCTURE

CHAPTER 4 EXPERIMENT ON QUARTER SCALE STANDALONE RC AND ECC ENCASED RC CANTILEVER COLUMNS

SUMMARY

In a typical existing apartment block in Singapore, the ground floor, located close to car parks, is generally vacant comprising a void deck used to hold social functions for the residents. Another characteristic of such structures is that the ground floor RC columns as used in a typical apartment block generally have breadth to depth ratio (*B/H*) greater than two. Bearing in mind that Singapore is not within any earthquake zones, therefore the design and the detailing of the structural elements based on Singapore's building code CP65 only considered axial imposed loads together with a lateral load of either 1.0% of the factored dead loads or 0.5% of the combined factored dead loads and imposed loads, whichever is more significant. As a result, the ground floor columns in existing void deck may be vulnerable when subjected to close-in blast loads arising from vehicular bombs m typical of those used in the terrorist attack. The blast may propagate freely through the ground floor void deck with the columns, the ground and the 1st storey slabs present channeling the blast as it propagates from the source of explosion. Thus, with the prevalence of apartment blocks and the heavily built up environment, this study is carried out to evaluate the effects of close-in blasts on existing RC structures typical of such high rise apartments.

The methodology of the present study consists of numerical, theoretical and experimental analyses of blast waves propagation through the ground floor void deck and the dynamic response of structural elements, particularly critical ground floor columns, of typical existing RC apartment blocks in Singapore. The study starts with the dynamic response analysis of standalone RC cantilever columns when subjected to blast loads. The study is carried out further on the effects of the close-in blast loads acting on the edge columns nearest to the explosion charge.

The first phase of the present study involves the numerical modeling of standalone RC cantilever columns to resist external blast loads using LS DYNA FE code. For a standalone RC cantilever column subjected to blast, validation of the numerical results is carried out by incorporating an equivalent SDOF method as the analytical solution. Both elastic and inelastic conditions are examined for the standalone RC cantilever column cases. Analytical study of SDOF method is obtained by integrating Duhamel integral for elastic condition using the direct integration method and for inelastic condition by using a step by step piecewise linear integration method. Peak responses of the columns obtained from SDOF analyses are then compared to those obtained from the numerical analyses. Twenty columns of various dimensions are investigated. Some of columns chosen are typical of a high rise apartment blocks found in Singapore having a ratio of breadth, B to depth, H more than two.

Second part of the study is on blast wave propagations with respect to the structural lay-out and configurations. The study compares the blast overpressure and reflected pressure obtained from empirical predictions proposed by several researchers, with those obtained

using code and experimental results. The blast waves propagation through the ground floor void deck is investigated. Such ground floor void deck may create channeling of blast wave pulse. When blast waves are channeled, it may create higher reflected pressure and impulse acting on the ground floor columns. Critical ground floor columns may fail, leading to the progressive collapse of structure. Herein, the dynamic response of critical ground floor columns subjected to blast loads acting on its incident face is also studied.

Taking into account the reflected pressure and impulse obtained from the aforementioned blast wave propagation study, a parametric study of RC columns of different geometric dimensions with various boundary and loading conditions is presented. The study begins with standalone RC columns of 3m height subjected to uniformly distributed load obtained from the average P and I acting on the incident surface nodes of the column. Three types of column's BCs are modeled. The intention is to model the columns in such a way that their response mirrors that of an analysis of the full frame. Further parametric study is carried out on multi storey RC frames with column height of 3m subjected to non-uniform blast loads. As the blast is expected to affect only the ground floor of the RC frame, only the ground floor column is modeled. To account for imposed loads from the upper stories, an axial load was applied, acting on the top of the column before the dynamic response analysis of column when subjected to blast loads begins.

Furthermore, Engineered Cementitious Composite (ECC) material is used to study the effects of encasement of existing RC columns to assess improvements in resistance against blast loads. The idea is to improve blast resistance of the reinforced concrete by delaying such physical cracking. The critical RC column is encased with a layer of ECC with a certain thickness and the behavior of the composite columns is studied. Since no

literature on experimental results of ECC subjected to blast loads can be found, the characteristics of ECC as a protective material against blast is not well understood. For this purpose, experiments on RC and ECC encased RC columns were conducted with the assistance from Defence Science and Technology Agency (DSTA) Singapore.

It is expected that this research will contribute to the existing literature and hopefully lead to the recommendation of design guidelines for newly built apartment blocks in Singapore as well as guidelines for strengthening typical existing apartment blocks. In general term, this research is intentionally done to shed light on the performance of existing apartment blocks when subjected to blast loads arising from close-in explosions, particularly to understand the behavior of critical RC columns located at ground floor.

Keywords: close-in explosion, RC column, $B/H>2$, ECC encasement, numerical analysis, experiment, dynamic response, residual axial capacity.

LIST OF SYMBOLS

a_{ij}	Parameters defining the failure surfaces in MAT 72
A	Cross-sectional area
A_s	Area of bottom rebar
A_s'	Area of top rebar
A_r	Reflection coefficient
b	Breadth of concrete cross section
$b_{1,2}$	Damage scaling exponents in MAT 72
b_3	Damage multiplier in MAT 72
B	Column width
B/H	Loaded breadth to depth ratio of the column
c	Damping
c_{cr}	Critical damping
$\cos 3\theta$	Angle that represents the direction of the deviatoric stresses
C_m	Matrices of damping
C_c	Compression force of concrete
C_{RA}	Residual capacity of column
C_{UA}	Axial capacity of undamaged column
d_w	Distance from explosion charge to blast wall
d'	Concrete cover
DI	Damage Index
DIF	Effects of loading rate

e	Energy
e_{internal}	Internal energy
E	Young's modulus
E_C	Young's modulus of column
Em	Young's modulus of matrix
f_{cu}	Cube compressive strength of the concrete
f_c'	Unconfined uniaxial compressive strength of cylinder
f_{cd}	Dynamic compressive strength
f_{cs}	Static compressive strength
f_{td}	Dynamic tensile strength
f_{ts}	Static tensile strength
f_t	Unconfined uniaxial tensile strength
f_y	Yield stress
F	Force
F_D	Damping force
F_e	Equivalent term of force in SDOF analysis
F_{Ie}	Equivalent inertia
F_{Se}	Spring forces
G_f	Fracture energy
H	Column Depth
$H_{specific}$	Specific heat
HOB	Height of burst
i^-	Negative impulse
i^+	Positive impulse
I	Impulse
I_1	First invariant of hydrostatic stresses
I_{CR}	Moment of inertia of cracked section
I_G	Moment of inertia of uncracked section
I_R	Reflected impulse
I_{SO}	Incident impulse
J_2	Second invariant of deviatoric stress tensor
k	Stiffness

k_e	Equivalent stiffness in SDOF analysis
K_m	Matrices of stiffness
KE	Kinetic energy
K_L	Load transformation factor
K_M	Mass transformation factor
K_S	Stiffness transformation factor
L	Column length
LR	Longitudinal reinforcements
m	Mass
m_e	Equivalent mass in SDOF analysis
$\mathrm{M_m}$	Matrices of mass
M_u	Ultimate moment
P	Pressure
P_o	Atmospheric pressure
P_r	Reflected pressure
P_{so}	Incident overpressure
q	Bulk viscosity
R	Stand-off distance
R_u	Ultimate resistance force
S_f	Scaled factor
s_{ij}	Stress deviatoric tensor
t_A	Arrival time of blast wave
t_D	Loading duration
t_M	Peak response time
T	Natural period
$T_{s1,2}$	Rebar forces
TF	Transformation factor
TR	Transverse reinforcements
u	Displacement
u_c	Complimentary displacement
u_p	Particular displacement
$\dot{u}$	Velocity

$\ddot{u}$	Acceleration
v	Velocity
w	Localization width
W	Explosion specific charge
x	Distance from fixed support
X_p	Prototype parameter
Z	Logarithmic scaled distance
Δ	Axial displacement applied at the column
$\Delta\sigma$	Deviatoric stress
$\Delta\sigma_y$	Initial yield surface, initial yield deviatoric stress
$\Delta\sigma_r$	Residual failure surface, residual deviatoric stress
$\Delta\sigma_m$	Maximum failure surface, maximum deviatoric stress
$\Delta\lambda$	Incremental effective plastic strain
α_I	Angle of incidence
β	Parameter occupied to distinguish the type of plastic hardening in the material model
δ_{ij}	Kronecker delta ($\delta_{ij} = 1$ if $i = j$; otherwise, $\delta_{ij} = 0$)
ε	Strain
$\dot{\varepsilon}$	Dynamic Strain-rate
$\dot{\varepsilon}_c$	Compressive strain rate
$\dot{\varepsilon}_t$	Tensile strain rate
$\dot{\varepsilon}_s$	Quasi-static strain-rate
$\dot{\varepsilon}_{ij}$	Strain-rate tensor
Θ	Angle of similarity
ρ	Density
Σ	Stress
σ_a, σ_1	Applied axial stress
σ_c	Bridging stress
σ_{ij}	Cauchy stress
σ_r, σ_2, σ_3	Applied hydrostatic pressure in the radial direction
ψ	Ratio of tensile meridian point to compressive meridian point

ω	Natural frequency
ω_e	Undamped natural frequency
ω_{De}	Damped natural frequency
ε^p	Effective plastic strain
ε_v	Volumetric strain
$\varepsilon_{v,\ \text{yield}}$	Volumetric strain at yield
ϕ	Diameter
$\phi(x)$	Shape function
γ	Shear strain
	Adiabatic constant ratio
λ	Eigen value
τ	Shear stress
υ	Poisson's ratio
ξ	Damping ratio

LIST OF ABBREVIATIONS

ALE	Arbitrary Langrangian Eulerian
BATF	Bureau of Alcohol, Tobacco, Firearms and Explosives
BCs	Boundary Conditions
BEM	Boundary Element Method
BW	Blast Wall
CF	Conversion Factor
CFD	Computational Fluid Dynamics
CFRP	Carbon Fiber Reinforced Polymer
DAHS-CWE	Design and Analysis of Hardened Structure to Conventional Weapon Effects
DAQ	Data Acquisition System
DC	Displacement Control
DCC	Displacement Control Constrained (Column Tip)
DCU	Displacement Control Unconstrained (Column Tip)
DI	Damage index
DIA	Digital Image Analysis
DIF	Dynamic Increase Factor
DMF	Dynamic Magnification Factor
DSTA	Defence Science and Technology Agency
ECC	Engineered Cementitious Composite
EL	Eulerian-Lagrangian

EOS	Equations of State
FCT	Flux Corrected Transport
FDM	Finite Difference Method
FE	Finite Element
FEM	Finite Element Method
FEMA	Federal Emergency Management Agent
FVM	Finite volume method
HDB	Housing and Development Board
HFPB	High Fidelity Physic Based
HOB	Height of Burst
HSC	High Strength Concrete
ICP	Integrated Circuit Piezoelectric
JWL	John Wilkins Lee
LC	Load Control
LCU	Load Control Unconstrained (Column Tip)
MDOF	Multi Degree of Freedom
NSC	Normal Strength Concrete
PDEs	Partial Differential Equations
PGA	Peak Ground Acceleration
PI	Pressure-Impulse
RC	Reinforced Concrete
RCC	Reinforced Cement Concrete
RDX	Research Department Explosive / Royal Demolition Explosive
SCS	Steel-Concrete-Steel
SDOF	Single Degree of Freedom
SPH	Smooth Particle Hydrodynamics
ST Kinetics	Singapore Technology Kinetics
TFs	Transformation Factors
TNT	Trinitrotoluene
PFL	Plastic-baking Foil
PVC	Polyvinyl Chloride
UBC	Uniform Building Code
VBIED	Vehicle Borne Improvised Explosive Device

LIST OF FIGURES

LIST OF TABLES

1 Introduction

1.1 Background

In recent years, the severe impact of terrorism is getting much more attention from civil engineers around the world as many cases of such threats have happened recently. An often quoted example in 2001 of a devastating terrorist act was the WTC 9-11 attack in New York, leading to the structural collapse of two towers. It is caused by fuel gas explosions arising from the impact of airplanes, a rather rare type of occurrence. In view of the relatively more common terrorist threats, several categories of bombs generally used are suitcase bombs, package bombs and vehicular bombs. In terms of structural integrity, the most devastating may come from the last category. An example of a recent vehicular terrorist attack was in Islamabad, Pakistan in September 2008. A truck bomb of around 600kg of RDX and TNT explosives was detonated in front of the Marriott Hotel, creating a crater, 59 meters wide and 7 meters deep. Fifty three people were found dead within the remains of the hotel. The aforementioned examples illustrate the need to take blast loads into account in structural design.

New structures could have been designed to withstand blast loads. However, in the case of existing structures, ways to address this problem have to be found through studying the

response of such structures to blast loads. Besides, functionality of structure is one of the main concerns in designing blast resistant structure. With regards to its functionality, a structure can be classified as government or military structures, commercial buildings (offices, malls) and residential apartments. The first type generally has been purposely designed to sustain extreme loads such as blast loads. Structure of the latter type is the focus of this present research. For existing residential apartment blocks, further investigations in terms of structural integrity when exposed to blast loading as well as the economic feasibility of retrofit are needed. Such studies may end up with new design concepts for implementation in new structures or feasible retrofitting methods applied on existing structures.

In Singapore, approximately 80% to 90% of the populations are currently living in apartment blocks. For a typical apartment block in Singapore as shown in Figure 1.1, the ground floor is generally vacant comprising a void deck used to hold social functions for the residents. The ground floor void deck is also close to car parks located just next to the apartment block. Bearing in mind that Singapore is not within any earthquake zones, therefore the design and the detailing of the structural elements only consider axial imposed loads together with a lateral load of either 1.0% of the factored dead loads or 0.5% of the combined factored dead loads and imposed loads, whichever is more significant (based on Singapore's building code CP65). As a result, the ground floor columns in existing void deck may be vulnerable when subjected to close-in blast loads arising from terrorist threats. Thus, with the prevalence of apartment blocks and the heavily built up environment, it is important to study the effects of such blasts on existing RC structures typical of such high rise apartments.

Effects of blast loads on structures have been studied previously; numerically and experimentally. Crawford et al. (2001), Wu and Hao (2005) and Lan et al. (2005) studied the response of structure under blast loads using finite element codes. Although experimental studies on RC structure subjected to blast loads are common in the military, the results of such studies are usually of a confidential nature. Experimental results of reduced scale RC frames subjected to blast loads by Woodston (1999) are the only literature available locally. The aforementioned review shows that the effects of such extreme events on the structural integrity of RC structures have not been widely explored and that the RC structure is vulnerable when subjected to close-in blast loads due to the brittle behavior of concrete.

To enhance the blast resistance of an existing RC structure, several retrofit methods are available. The two most common methods used are steel jacketing and CFRP strips layering (Crawford et al., 1997). In general, the concept of RC strengthening is to mitigate against brittle failure of the concrete. Besides such conventional materials, engineered cementitious composite (ECC) was observed to have some potential. It is a cement based material containing a low volume of dispersed fibrous content (Zhang et al., 2005, 2007). The fibers are found to help the cement paste to exhibit multiple cracking and to generate higher fracture energy. Such materials have been tested under high velocity (Maalej et al., 2005) and low velocity impacts (Zhang et al., 2005). The tests show that ECC is proficient in reducing the damage due to spalling and scabbing and produce composites with higher energy absorbtion and higher amount of microcracks as compared to plain concrete. Under tension, ductile failure mode may be observed in ECC instead of the brittle mode as exhibited by conventional cementitious materials. Since no

literature on experimental results of ECC subjected to blast loads can be found, the characteristics of ECC material as protective material under blast is not well understood.

1.2 Objectives and Scope of Study

1.2.1 Objectives

In view of the observations arising from a review of available literature, there is a need for a comprehensive study on the response of critical structural elements of apartment blocks (e.g. ground floor column). There is a need to predict the responses of columns when subjected to such blast loads (e.g. failure mode), and study how to mitigate against the progressive collapse of the RC frame structure.

The main objective of this research is to study the structural response of a typical existing RC apartment block in Singapore subjected to close-in blast loads. A common feature of such structures is the ground floor void deck used for social functions, while the 1st storey onwards is an RC infilled frame. The blast may propagate freely through the ground floor void deck with the columns, the ground and the 1st storey slabs present channeling the blast as it propagates from the source of explosion. Another characteristic of such structure is that the RC columns as used in a typical apartment block generally have breadth to depth ratio (*B/H*) greater than two. For such columns, it is apparent that the column may fail when subjected to close-in blast loads parallel to its minor axis due to large incident surface area with a lower blast resistance.

The study begins with an investigation of standalone RC cantilever columns of various dimensions. The structural responses obtained from numerical method are then reviewed by the structural dynamics theory and code. Furthermore, blast wave propagation through

the ground floor void deck is studied, taking into account the effects of the geometric nature of the ground floor void deck. Experimental, numerical and some theoretical studies on the performance of critical RC columns typical of those found in Singapore's apartment blocks are carried out. To strengthen such critical column, Engineered Cementitious Composite (ECC) encasement is proposed. Other structural elements such as beams and slabs are beyond of the scope of study. From the blast loads point of view, the study is limited to an external hemispherical close-in explosion. The explosion of specific charge weight, W is placed just above the ground within a stand-off distance, R as illustrated in Figure 1.2. The range of charge weight, W studied follows the range given by BATF standard for vehicular bombs, while the stand-off distance, R studied represents the range of stand-off distance available in a typical apartment block due to the presence of adjacent carpark (Figure 1.1).

The specific objectives of the present study are as follows:

1. To develop numerical models of standalone RC cantilever columns to study the effects of column dimensions on the elastic and inelastic response of the column structural response when subjected to blast loading.
2. To provide theoretical validation of displacement time history for standalone RC cantilever column under blast loads using Equivalent SDOF method.
3. To review the transformation factors (TFs) proposed in TM5-1300 code by the US Army Corps of Engineers and TFs obtained from structural dynamics theory for standalone RC cantilever column under blast loads.
4. To give a clear understanding on the effects of upper reflecting surfaces and columns configuration on ground floor void deck as well as RC frame layout of a typical RC apartment blocks on blast loads received by the ground floor columns.

5. To conduct a parametric study evaluating the loading and geometric conditions of RC columns typically found in the ground floor void deck in Singapore and to review the resistance of the columns subjected to close-in blast.
6. To propose a strengthening method for existing RC columns typical of those Singapore's apartment blocks using ECC as encasement material
7. To provide experimental validation of the numerical results with regards to dynamic response of standalone RC and ECC encased RC columns subjected to blast loads parallel to the major and minor axis of the columns.

1.2.2 Scope of Study

The effects of blast load on typical reinforced concrete (RC) frames having typical RC structural elements are studied and presented herein. The methodology of the present study consists of numerical, theoretical and experimental analyses of blast waves propagation through the ground floor void deck and the dynamic response of structural elements, particularly ground floor columns, of typical existing RC apartment blocks in Singapore. The study starts with the dynamic response analysis of standalone RC cantilever columns when subjected to blast loads. The study is carried out further on the effects of the close-in blast loads acting on the edge columns nearest to the explosion charge.

With respect to the blast loads considered, the study is confined to a close-in explosion from chemical charge ignition of a vehicular bomb. For close-in explosion, the effect of peak ground acceleration (PGA) is very small as compared to the dynamic response obtained from blast overpressure. Thus, PGA effect is not considered herein the study.

Moreover, the blast occurs within milliseconds, so the effect of fire of explosion is negligible.

The first phase of the present study involves the numerical modeling of standalone RC cantilever columns to resist external blast loads using LS DYNA FE code. For a standalone RC cantilever column subjected to blast, validation of the numerical results is carried out by incorporating an equivalent SDOF method as the analytical solution. Both elastic and inelastic conditions are examined for the standalone RC cantilever column cases. Analytical study of SDOF method is obtained by integrating Duhamel integral for elastic condition using the direct integration method and for inelastic condition by using a step by step piecewise linear integration method. Peak responses of the columns obtained from SDOF analyses are then compared to those obtained from the numerical analyses. Twenty columns of various dimensions are investigated. Some of columns chosen are typical of a high rise apartment blocks found in Singapore having a ratio of breadth, B to depth, H more than two.

Second part of the study is on blast wave propagations with respect to the structural lay-out and configurations. The study compares the blast overpressure and reflected pressure obtained from empirical predictions proposed by several researchers, with those obtained using code and experimental results. The blast waves propagation through the ground floor void deck is investigated. Such ground floor void deck may create channeling of blast wave pulse. When blast waves are channeled, it may create higher reflected pressure and impulse acting on the ground floor columns. Ground floor columns may fail, leading to the progressive collapse of structure. Herein, the dynamic response of critical ground floor columns subjected to blast loads acting on its incident face is also studied.

Taking into account the reflected pressure and impulse obtained from the aforementioned blast wave propagation study, a parametric study of RC columns of different geometric dimensions with various boundary and loading conditions is presented. The study begins with standalone RC columns of 3m height subjected to uniformly distributed load obtained from the average *P* and *I* acting on the incident surface nodes of the column. Three types of column's BCs are modeled. The intention is to model the columns in such a way that their response mirrors that of an analysis of the full frame. Further parametric study is carried out on multi storey RC frames with column height of 3m subjected to non-uniform blast loads. As the blast is expected to affect only the ground floor of the RC frame, only the ground floor column is modeled. To account for imposed loads from the upper stories, an axial load was applied, acting on the top of the column before the dynamic response analysis of column when subjected to blast loads begins.

Furthermore, Engineered Cementitious Composite (ECC) material is used to study the effects of encasement of existing RC columns to assess improvements in resistance against blast loads. The critical RC column is encased with a layer of ECC with a certain thickness and the behavior of the composite columns is studied. Blast load tests were done with the assistance from Defence Science and Technology Agency (DSTA) Singapore in 2008. Two cantilever RC columns and two ECC encased RC cantilever of quarter scaled columns were tested against blast loads. The columns were aligned in such a way that the blast is parallel to either its minor or major axis.

It is expected that this research will contribute to the existing literature and hopefully lead to the recommendation of design guidelines for newly built apartment blocks in

Singapore as well as guidelines for strengthening typical existing apartment blocks. In general term, this research is intentionally done to shed light on the performance of existing apartment blocks when subjected to blast loads arising from close-in explosions, particularly to understand the behavior of critical RC columns located at ground floor.

1.3 Outline of Thesis

The present thesis on "The Effects of Blast Loads on RC and ECC Encased RC Columns" consists of 10 chapters, including introduction (Chapter 1) and conclusion (Chapter 10) parts. Each chapter comprises one particular topic of study as presented hereafter and the outline of this thesis is given as follows.

In Chapter 2, a literature review of blast loads and its propagation through the structures nearby the blast, Single Degree of Freedom (SDOF) approach and RC structure under blast loads are presented. In addition, background studies on ECC as protective materials and proposed research arising from the literature review are also summarized.

Blast loads and its effects on structures are reviewed in Chapter 3. The explosion, its definition, products and characteristics are briefly explained. The classification of blast loads with regards to location of explosive, confinement basis, and loading types are presented, leading to justification of scope of blast studied. Prediction of blast loading, the calculation of pressure obtained from empirical equations and code are examined.

Experimental study on quarter scale model includes obtaining similitude requirement for reduced scaled model, the methodology of experiment and its instrumentation, results and discussion are presented in Chapter 4.

The basic principles of numerical methods and element formulations generally used for modeling blast problems are reviewed in Chapter 5. Based on the reviews, elements formulation that are appropriate for modeling blast waves propagation and its effects on structure are identified. In this chapter, numerical concepts used in AUTODYN as well as the material models for air and TNT explosive are also discussed. The AUTODYN is occupied for modeling blast waves propagation with respect to structural layout and configurations. Herein, three types of structure are investigated; standalone column, columns configuration on the ground floor void deck, and infilled frame. The results obtained from numerical analysis are then verified with empirical equations and experimental results done by other researchers.

Chapter 6 presents a review of the concept of central difference method in the explicit integration scheme to obtain the equation of motion occupied in LS DYNA as well as the material models for reinforced steel, concrete and cementitious materials. Based on the review, suitable material models for each material are selected and discussed in this chapter.

Theoretical solutions obtained from a parametric study of various dimensions of standalone RC cantilever columns subjected to blast load ranging from low intensity to high intensity blasts are discussed in Chapter 7. For low intensity blast, the structure is still in its elastic condition, thus equivalent SDOF method using direct integration method of Duhamel integral was proposed. When the structure is subjected to high intensity blasts, the response is expected to be under inelastic conditions. Thus, for an inelastic structure, a piecewise linear-step by step integration method of Duhamel integral is

occupied. Numerical analysis of standalone RC cantilever columns is carried out for both elastic and inelastic conditions and the numerical results obtained are compared to the theoretical results for verifications.

A parametric study of standalone RC columns is carried out in Chapter 8. Ground floor RC columns of various boundary conditions (BCs) are modeled and the numerical results are presented herein. The effects of loading variables, type of loading, column dimensions and reinforcement details on the dynamic response of the column are also observed. To validate the numerical method, experimental study on quarter scale models of conventional RC cantilever columns was also carried out.

Chapter 9 presents the results of a numerical study to evaluate the performance of hybrid-fiber Engineered Cementitious Composite (ECC) as an encasement layer to strengthen conventional RC columns against blast loads. The aim is to evaluate the extent to which such encasement improves the resistance of RC columns under blast loads. Experimental study on quarter scale models of ECC encased RC cantilever columns was also carried out to provide validation of the numerical results.

Finally, the objectives and scope of this study are reviewed in Chapter 10 before the conclusions are drawn and the main findings are highlighted. Recommendations for future research are proposed.

Figure 1.1 Typical apartment blocks in Singapore

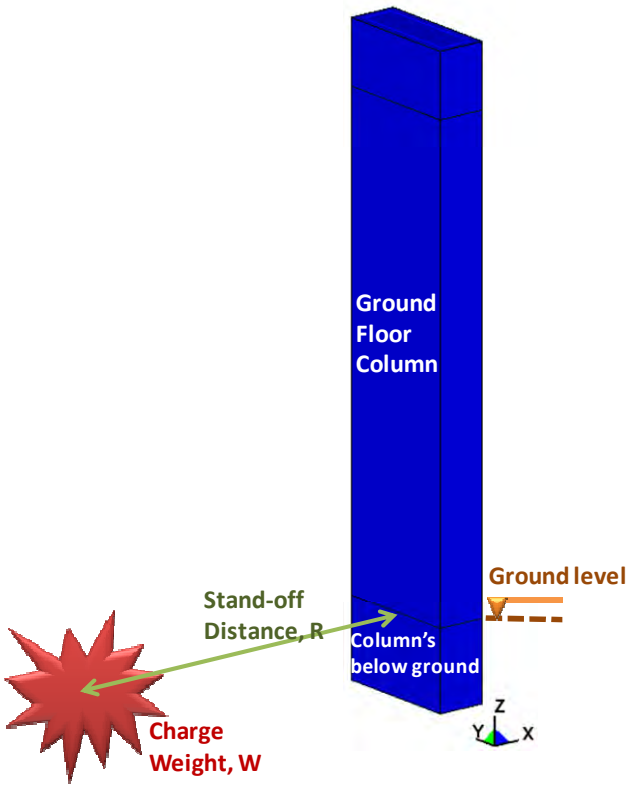

Figure 1.2 Illustration of hemispherical close-in explosion on minor axis direction

2 Literature Review

2.1 Introduction

New structures can be designed to resist extreme loads. However, existing structure may not have been designed to resist extreme loads such as blast. Since the response of such structures when subjected to blast loads is unknown, feasible ways to address the problems have to be found. In the following section, a brief literature review on the behavior of RC structures subjected to blast loads is presented. A review of blast propagation concepts is given and the response of RC structures subjected to such blast loading is discussed.

2.2 Blast Loads and Its Propagation

2.2.1 Empirical equation on blast wave parameters calculation

Numerous studies have been done by researchers on blast load parameters from conventional chemical explosion. Many empirical equations are available in the literature focusing on the calculation of blast wave parameters (e.g. incident overpressure P_{so}, reflected pressure P_r, incident impulse I_{so}, reflected impulse I_r, arrival time t_a and positive phase duration t_d). The empirical results generally correlate well with their respective experimental databases, even though the empirical equations may be based on available

numerical solutions. Such empirical equations can be divided into two groups based on the type of explosions, either spherical or hemispherical.

For spherical blast events, in which the explosive is placed at a height above the ground, a study on airblast pressure calculation was reported by Brode in 1958. The study, however, was only limited to the calculation of P_{so}. Newmark and Hansen (1961) extended the study of spherical blast. In addition to P_{so}, P_r was also examined for perpendicularly reflected waves when the shock front strikes a vertical wall. A comparative study of the calculations of blast wave parameters was done by Henrych (1977). By evaluating the empirical equations of P_{so} from Naumenko and Petrovskyi (1956), and Sadovskyi (1952), he proposed a set of empirical equations based on spherical blast conditions from the experimental data. The study was, again, limited to P_{so} calculations and did not consider other major parameters such as impulses and reflected pressure. A study by Baker et al. (1983) might be the most comprehensive study with regards to the range of spherical blast parameters used. The empirical measurements of P_{so}, I_{so}, P_r, I_r and t_a, parameters were investigated. Linking the spherical and hemispherical blast conditions, Mays and Smith (1995) proposed a conversion factor (*CF*) to adjust the empirical equations of spherical blasts for use in the case of hemispherical blasts. The *CF* given is within a range of 1.8 to 2.0, depending on the energy equivalent as a result of blast reflection.

A study on hemispherical blast in which the explosion is located just above the ground level was started by Kingery (1966). His comprehensive study resulted in empirical measurements of many parameters (e.g. P_{so}, t_a, t_d and I). Such parameters were obtained based on an experimental database of large explosions of 5, 20, 100 and 500 ton of TNT explosives. As shown in Figure 2.1, the impulse obtained from experiment was plotted

against scaled distance *Z*. For smaller scaled distance *Z*, the impulse tends to be larger. In 1984, Kingery in collaboration with Bulmash launched a computer program of ConWep by taking into account the empirical equations he proposed earlier. This program is able to evaluate most blast pressure parameters associated with both spherical and hemispherical explosions and also blast loads applied on single buildings which are rectangular in shape. In terms of reflected impulse I_r, Baker (1967) discovered that for close-in explosion, the effect of air mass is negligible on the scaled impulse. This agrees well with Hopkinson's scaling law. Meanwhile, for intermediate and far-field distance from the source of explosion, such effect is of greater significance. The scaled impulse for intermediate and far-field distances are found to be a function of scaled distance and sound velocity under ambient atmospheric conditions. Using experimental data from Pentolite charges, the predicted impulses obtained from Hopkinson's law are in a good agreement with the measured data for close-in explosion. However, it underestimates the impulse for an intermediate distance and overestimates that for far field explosions (Figure 2.2).

Most of the aforementioned approaches are, however, limited by the extent of the experimental database on which they are based. The parameters obtained from empirical equations proposed by a number of researchers are found to have significant differences. Therefore, rationalization of the generally accepted calculation of blast wave parameters is needed.

Another problem concerns the accuracy of empirical equations proposed that diminishes as the stand-off distance of the explosive reduces. Moreover, the aforementioned equations were generated from experimental studies with a limited range of test

conditions (i.e. blast on single obstacle environment in an open flat terrain). To deal with a wider range of blast with more specific structural layout and configurations, numerical analysis may be the solution.

2.2.2 Code and Experiments on Blast Wave Properties

To evaluate the available empirical equations and to set a standard for blast properties, a code is needed. To date, there is only one code available worldwide. The code was published by the US Army corps of engineer in 1990, namely TM5-1300 titled "Structure to resist effects of accidental explosion". This code not only provides information on blast properties calculation but also a design basis for protective Reinforced Concrete (RC) structures subjected to high explosive detonations. However, the blast properties obtained are applicable for a limited range of applications (e.g. pressures of hemispherical and spherical explosions at certain distances and pressures on finite and infinite walls located perpendicular to the source of explosion at certain distances). For complex structures with unusual geometries, experimental studies provide more reliable blast properties.

In terms of experimental validation of blast parameters with regards to its propagation on structural layout and configurations, a number of published literature is available for reference. Most of the experiments were conducted on small scaled models. The concept of scaled model was elaborated in detail by Baker (1973) in his book. Similitude requirement was proposed, stating that two systems are dynamically similar when their respective dimensionless parameters are equal. The scaled model is found to be more feasible, yet is time efficient and environmentally friendlier.

Experiments on explosions in tunnel and internal explosion were studied by Smith et al. (1992a). They presented their results on small scale models to investigate short duration blast propagation from general explosives in tunnels and from internal explosions. Eight types of straight, 90° bend, and T tunnels of $1/45_{th}$ scale were tested against hemispherical explosions of PE4 charge with mass less than or equal to 0.1 kg TNT equivalent. The charges were placed at various stand-off distances to the tunnel entrance. Since the ground conditions may affect blast wave signature, steel plates were placed in front of the tunnel entrances to provide similar fine reflecting surface. The results showed that only the peak pressure of 90° bend tunnel tests decreased by 6% as compared to the one obtained from smooth straight tunnel tests. This could be due to the low intensity blast tested. Meanwhile, for T tunnels, at the junction, half portion of peak overpressure arriving at that section was observed to be transmitted into the side branch. Such transmission results in the decay of the overpressure in the side branch with respect to time.

Several studies on blast propagation on protected structure by barrier configuration have been published. One was on an experiment done by Chapman et al. (1995a) on one-tenth scale target structures protected by blast walls against detonation of high explosive charges placed slightly above the ground level. The effects of several geometrical parameters on blast pressure obtained were investigated. The parameters observed were height of burst of the charge (HOB), height of target, height of blast wall, the stand-off distance between charge and blast wall and the distance between blast wall and structure. It was discovered that as the distances and height of the blast wall increase, the blast waves on a structure were attenuated by the presence of the blast wall resulting in smaller pressures being observed. However, the response to the variation in the structure's height

was unclear. Other small scale experiments on the blast barriers' functionality as a means of protection for structure were also carried out by Bogosian and Piepenburg (2002) and Rickman et al. (2006). Bogosian and Piepenburg (2002) focused merely on the type and width of the barrier as shown in Figure 2.3, while Rickman et al. (2006) reported on concrete barrier walls of several height placed at certain distances between the structure and the charge. The experiment showed that such blast barriers, even of modest height, could significantly reduce the reflected pressure on the structure and provide a significant amount of shielding for the structure.

Another experimental study on the interaction of shock waves with simple structures using shock tubes was established by Le (1999). Three types of small scale-structures were studied; wedge, cylinder and sphere structures. Several phenomena were observed i.e. unsteady flow fields, shocks, slip layers on contact surface, vortices and their interactions. However, the study was focused merely on low intensity blast loads as the range of pressures recorded in the experiments conducted was less than 6.5 times the atmospheric pressure.

Many researchers conducted experimental tests on blast propagation on city streets. Smith et al. in 2001 tested several configuration of junctions in city streets subjected to blast loads. One-fifth scale model was used and tested. The results showed that blast propagation on such city streets could enhance the reflected pressures and impulses obtained by up to five times the normally reflected waves. Such enhancement particularly occurs with small scaled distance. Another study on city street models was conducted by Rose et al. in 2002. The experiment was conducted on $1/40_{th}$ scale models of straight city streets, focusing more on the confinement effects on the positive and negative phase

impulse of blast waves provided by tall buildings bordering straight city streets. The results showed that the positive phase impulse increased significantly above the equivalent reflected level as a function of street width and building height (Figure 2.4). The negative phase impulse was also influenced by the presence of buildings. But up to a certain scaled distance, the effect is less than that on the positive phase impulse. However, beyond a certain scaled distance, the negative phase impulse was discovered to be much greater than the positive phase impulse for all cases tested. Thus, it showed that the negative phase impulse for such blast scenario should not be ignored.

The effect of structural facade on blast propagation was also studied experimentally by Smith et al. (2003) using scaled model of 10 storied RC structure. The investigation was focused on the effects of different façade configurations on the propagation of blast waves produced by an explosion in an urban setting. The study is, however, limited to certain conditions of "building porosity", a term used for the ratio between opening area on façade and frontal area.

A $1/10_{th}$ scale model of a Reinforced Cement Concrete (RCC) containment specimen was tested by Siddiqui and Ahmad in 2007. Experimental determination of relationships of airblast pressure time history as a function of charge weight, stand-off distance and height of structure on the hemispherical surface explosion with a range of impulsive loading conditions was studied. Charge weights within a range of 1 kg to 50 kg TNT were used in the experiment. The results as plotted in Figure 2.5 showed a linear correlation between logarithmic peak overpressure P_{so} and logarithmic scaled distance Z.

The aforementioned experimental studies involved field tests of a limited number. The constraints could be due to limitations in terms of time and budget available. Moreover, most of the studies presented in the literature did not provide full information regarding the dimensions of the structures. That might be related to the need for confidentiality of blast data common in studies conducted for military purposes.

2.2.3 Numerical simulation of blast propagation on building environment

To overcome the limitation of previous studies on empirical equations, code, and experiment, numerical simulation could be an option to simulate blast propagation when structural layout and configurations are varied. With numerical simulation, any type of structure can be modeled and reviewed. Moreover, such a simulation requires less effort, is time efficient yet more feasible to do. A number of finite element codes are available. Ngo et al. (2007) listed in their paper available FE softwares generally used to numerically predict blast pressure. Some of them are commercialized (e.g. AUTODYN, LS DYNA, DYNA 3D and ABAQUS). The first two softwares are utilized in the present study.

Numerical study on blast propagation on scaled model of rectangular box structure protected by blast wall was first started by Chapman et al. (1995b) using AUTODYN 2D FE code. The parametric study was focused mainly on 1D explosion model case studies. The numerical parameters investigated were the damping variables (linear and quadratic viscosity), cutoff variables (velocity, sound speed, radius and density), and the energy transport that are prescribed in AUTODYN and also and the effects of grid sizes on 1D explosion. The parametric study on grid size for a particular scaled distance of Z=1.19 $m/kg^{1/3}$ suggested that a 3 mm grid size provided the optimum result based on the desired

blast wave shape with minimum computational time. This grid size resulted in similar peak pressure and impulse as that obtained using a 1 mm grid size model. Several grid sizes were reviewed in terms of *P* and *I* obtained. The *P* and *I* obtained showed similar trends in magnitude, gradually decreasing for smaller mesh sizes. This indicated that a grid size factor can be specified to convert the *P* and *I* obtained using models with a larger mesh size. As the grid size reduces, the factor approaches unity. A numerical study of blast propagation through rectangular box structures protected by the blast walls was carried out by making use of a remap function from 1D spherical explosion to 2D model on AUTODYN. In this study, the explosive was placed at a small height of burst (*HOB*) at a specific stand-off distance (*R*) from the blast wall and structures. The *P* and *I* obtained from numerical analysis was then compared to experimental results. It showed good agreement particularly in the prediction of the first peak pressure, while the difference in impulse differed by around 5%.

Many studies (e.g. Smith et al., 2001; Luccioni et al., 2005; Remennikov and Rose, 2005) were focused on blast propagation from explosions in city streets, with rows of rectangular buildings of various dimensions. The study conducted by Smith et al. (2001) focused on the effects of junction configuration in blast propagation through city streets. The numerical study was carried out using AUTODYN3D and the results obtained were then compared with those obtained experimentally. Both peak reflected pressure and impulse were evaluated. It showed good agreement between numerical and experiment results with impulse differences of less than 10%. Meanwhile, Luccioni et al. (2005) focused on the analysis of iso-damage levels of the affected zones in a congested urban environment comprising rows of rectangular building. Numerical analysis was carried out to obtain pressure time history on several locations. The pressures acting at the building

facade were then related to the real damaged condition of structure assessed based on visual inspection of an actual explosion in a congested urban environment typical of Buenos Aires in Argentina. Such correlations resulted in damage contours and iso-damage curves obtained for such urban environment. Remennikov and Rose (2005) studied the shielding effects and reflection of pressure off adjacent structures present in a typical city street environment as shown in Figure 2.6. The pressures obtained were then compared to the ones obtained from a free field hemispherical explosion. The shielding effects of such nearby structure may enhance the peak reflected pressure obtained by up to ten times when compared to the case of a free field explosion (Figure 2.7).

A commercially available finite element code validated against proven prediction techniques and experiment data may provide a cost-effective means of examining such blast wave propagation models. To date, no numerical study on the blast propagation and the effects of channeling of the blast waves through ground floor void deck is found in available literature.

2.3 Single Degree of Freedom (SDOF) Approach

A simple approach using the single degree of freedom (SDOF) method to analyze structural elements subjected to blast loads has been performed by Mays and Smith (1995) in their book. A lumped mass equivalent SDOF system is proposed to predict the displacement of simplified structures subjected to blast by applying transformation factors of load, stiffness, and mass to the SDOF analysis. The blast pressure is transformed into an axial node force applied to the lumped mass of the structure. This method follows the TM5–1300 US Army Code (1990). Based on this code, the amplitude and the time of peak response can be obtained from the idealized charts based on the natural period of the

structure. As only the peak response is obtained, it is unable to provide additional information on displacement with respect to time.

Singhal et al. (1994) studied an equivalent of the SDOF analyses of steel panels using DUHAMEL integration technique to simulate blast pressure on flexible panels. MDOF analysis was also performed. The simply supported continuous panel system was idealized by the beam model that was discretized into 10 equal segments with each segment having its own stiffness and mass matrix. Each node's segments had 2DOF: translation in the vertical direction and bending rotation. The results showed that the peak responses obtained from the MDOF analysis were similar to those of the SDOF analyses. It was also discovered that the flexible thin panels were less responsive to blast loads than stiffer panels. However, it is noted that mesh sensitivity study may not have been carried out. It was not clear whether idealizing the beam with more than 10 segments would provide better results than the one modeled using 10 segments.

Crawford et al. (2001) also investigated the SDOF method applied on a the single column problem and used their own SDOF program to estimate the column's flexural capacity and to design its retrofitting. The SDOF method they proposed accounted for both tensile and tensile membrane actions in the calculation of resistance force of the RC structure. It follows the SDOF method given in the technical manual of Design and Analysis of Hardened Structure to Conventional Weapon Effects (DAHS-CWE) of UFC 3-340-01 (2002). As mentioned above, the displacement results calculated by numerical modeling with PRONTO 3D, the field test results (residual displacement) and the SDOF method were compared. It was shown in Figure 2.8 that the results obtained from PRONTO 3D and the SDOF analyses were rather different. The results reported showed big differences

between the displacement curves obtained from the numerical analysis and the SDOF analysis, even for the linear elastic portion of the curve.

SDOF analysis on two ways elements was first done by Krauthammer et al. in 2003 for slab elements. Modification of the simple SDOF method to achieve an advanced level of SDOF for deep and intermediate thicknesses of slabs was performed by reducing the compressive membrane region. It was observed that the main parameter governing strength is the span-to-depth ratio while the amount of tensile reinforcement becomes a secondary strength parameter. Another study on two-way elements was carried out by Morison (2006). He reviewed the transformation factors proposed by TM5-1300 for SDOF analyses of walls and slabs. A comprehensive theoretical study was conducted on two way slabs developed from the yield line theory of plates. Errors were found in some of the transformation factors of two way elements some reaching as much as 50%.

The aforementioned reviews show that none of the available papers compared the transformation factors obtained from theoretical study with those obtained from the numerical MDOF analyses or the field test results. This will be presented in this study in order to assess both theoretical and numerical results obtained.

2.4 RC Structure under Blast Loading

2.4.1 Numerical modeling of blast loads on RC structure

Many researchers have investigated the effects of blast loads on conventional RC structures by incorporating finite element code. Crawford et al. (1997) studied the behavior of RC frames and its retrofitting methods to resist blast effect through numerical analysis. Six storey RC frames were modeled using LS DYNA by incorporating hybrid

method. This method is a combination of structural (2D beam truss) and continuum (3D solid) elements. Slabs and beams were modeled using shell elements to reduce the problem's size. Meanwhile, RC columns were modeled using 3D solid elements for the concrete portions and 2D beam-truss elements to model steel reinforcement. The columns of square dimensions with two reinforcement designed based on requirements of seismic zone condition from UBC code (Zone 1 and 4) were subjected to similar blast loads.

Two retrofitting methods were presented; steel jacketed and CFRP wrapped RC columns. As predicted, frames in which the RC columns were retrofitted experienced less damage and smaller displacement as compared to frames in which RC columns were not retroftitted (Figure 2.9). The jacketing system resulted in confined conditions with the columns becoming more ductile. Such a system was also found to prevent the concrete materials from spalling and scabbing. However, the deformed shape of conventional RC columns as shown in Figure 2.10 indicates that the hourglass problem due to zero energy mode is very obvious. Such hourglass phenomenon and its control will be presented in detail in Chapter 6.

Dynamic response of masonry infilled RC frames and its collapse analysis under blast loads were studied by Wu and Hao (2005). Such frames were modeled three-dimensionally using homogenized continuum elements to represent an equivalent RC material. Such material was implemented into LS DYNA by user defined subroutines. In the paper, the safe stand-off distances against collapse of the structures were determined to ensure that the structural elements were still standing with minor damage. However, the infilled masonry wall was typically blown off by the blast. Wu et al. (2005) also investigated the effect air blast load on the structural response when the structure is

protected by surrounding protective walls by applying the homogenized continuum elements model. It was discovered that a well designed protective wall can reduce the collapse potential of the whole structure but the non-structural elements such as masonry walls may still collapse locally.

The ground shock effects and its combination with blast loads on the RC frame's structural response were investigated by Wu and Hao (2007). They discovered that starting from a certain critical scaled distance, ground shock should be invoked in the modeling and that the failures of some of the structural elements were governed by a combination of both air blast and ground shock. The value of this critical scaled distance is dependent on the configuration of the structural elements. Below the critical scaled distance, the explosion may be considered as close-in explosion and the effect of ground shock motion can be neglected as the structural response and damage are mainly governed by the airblast load. Since the scope of this study is within a range of close-in explosion, the ground shock effect is therefore neglected.

In terms of structural stability of an RC structure, RC columns play a dominant role. It transmits the load, through compressive forces, from the upper portion of the structure to the ground. For the purpose of extreme events such as blast, new structures could have such effects taken into account during the design and construction. Its critical structural elements such as RC columns may be designed to resist the resultant lateral loads. However, in the case of existing structures, ways to address this problem have to be found through studying the response of such as-built structures to blast loads. The resistance and redundancy of its critical columns against specific blast loads need to be analyzed to

ensure structural integrity. Herein, both the structural response and redundancy of critical RC columns are reviewed and studied.

A numerical study on the dynamic response of RC columns subjected to severe blast loads was carried out by Crawford et al. (2001). The numerical model was generated using PRONTO3D, a non-commercial code developed by Sandia National Laboratories. The study was focused on retrofitting of the normal strength RC column using CFRP materials, applied onto the columns in the form of vertical strips and horizontal wraps. A default rectangular RC column of typical dimension with its breadth, B similar to column's depth, H was studied. The RC column displacement obtained from numerical analysis was then compared with the residual displacement obtained experimentally. The results showed that numerical analysis provided a lower estimate of the residual displacement observed experimentally. As shown in Figure 2.11 the difference was rather significant, around 2 inches (50 mm) compared to the 10 inches (254 mm) residual displacement measured. Detailed information of the dimensions, reinforcements and material properties of the tested column and its retrofit system are however unavailable in the literature due to confidentiality issues.

A comparative study on the behavior of normal (NS) and high strength (HS) RC column under impulsive blast loads was reported by Ngo et.al. (2003). The RC columns compared have similar axial load capacity, but were of different breadth to depth (B/H) ratio. As in Figure 2.12, for the same axial capacity, the dimension of the HS RC column is smaller (350x750mm) than the NS RC column (500x900mm) with cross sectional area of $A_{HS\text{-}RC}$ around 60% of $A_{NS\text{-}RC}$. The cylinder compressive strength f_c' of HSC and NSC are 80 and 40 *MPa*, respectively. This study was carried out using LS DYNA FE code by

incorporating both geometric and material nonlinearity. A triangular blast pulse was applied on the facade of column's minor axis. The results showed that shear failure was the dominant mode of failure for close-in range of explosion. Dealing with such failure mode, HSC columns performed better than NS RC column and posses higher energy absorption (Figure 2.12).

Numerical study of RC columns subjected to suitcase bombs was performed by Lan et al. (2005). The study focused on the significance of tie spacing on structural redundancy. An in-house finite element code namely high-fidelity physic-based (HFPB) finite element models developed by Karagozian and Case (K&C) was incorporated in this paper. Such FE code is able to generate resistance functions as well as the pressure-impulse (*PI*) diagrams indicative of the ability of the column to sustain blast loads. LS DYNA was used to developed the finite element models employed (i.e. HFPB model). Fixed ended RC columns were modeled, taking into account the material erosion parameters to model the concrete spalling phenomenon which resulted in localized damage, a common occurrence in cases involving suitcase bombs. Damage curves for different tie spacing of RC columns were computed numerically. The results showed that the tie spacing significantly affects the post blast loading capacity of the columns. It also showed that the HFPB model developed is suitable for analyzing the response of structural elements when subjected to close-in suitcase bombs.

Another comprehensive numerical study on standalone RC columns subjected to blast loads was carried out by Shi et al. (2007). Interactions between blast waves and RC columns were simulated using a fully coupled Eulerian-Lagrangian (EL) formulation provided by AUTODYN. RC columns were modeled using the Lagrangian formulation

allowing the structure to deform. Meanwhile the explosive and air were modeled using the Eulerian formulation. Parametric study on column's dimension was carried out by modeling a coupled model of blast wave - column interaction. It is shown that column dimensions can significantly affect the pressure and impulse obtained on the incident face. A wide column amplifies the effects of blast waves acting as reflection surface. Such effect gradually diminishes, leading to convergence as the column width increases above a certain value. An increase in column dimension results in a longer gap between time of arrivals of the blast wave reaching the front and rear surfaces. A circular column results in less reflection but more refraction of the blast wave than a rectangular column. The *P* and *I* obtained from the fully coupled EL formulation model of blast wave-column interaction were then compared with the ones obtained from the Eulerian formulation by assuming that the structure is rigid. The results showed that the reflected pressure of fully coupled EL model is slightly smaller than those of a rigid structure model while the reflected impulse is higher. However, the differences were not significant as given in Table 2.1. Thus, in this present study, blast wave-column interaction is of least interest.

Table 2.1 Variation of Blast Loads w.r.t. Column's Stiffness (Shi et al, 2007)

Stiffness	Front Surface		Rear Surface		Deflection
K_C	P_R	I_R	P_R	I_R	d
N/m	*kPa*	*kPa.ms*	*kPa*	*kPa.ms*	*mm*
5.14E+05	3912	4395	215	910	38
5.14E+06	3938	4281	215	908	12
5.14E+07	3947	4272	214	903	3
Rigid	3964	4174	217	918	0

In terms of structural redundancy measured after the blast, Shi et al. (2007) was the first to conduct a numerical study on RC columns. The effects of cylinder compressive strength (f_c') and column's dimensions such as width (*B*), depth (*H*), and height (L), on

the response of rectangular RC columns with *B/H* less than two subjected to uniform blast pressure at the incident face of column were investigated in terms of damage index (*DI*). The damage index, ranged between 0 – 1, is calculated based on the percentage difference between the residual and the designed axial load carrying capacities of the RC columns. The damage index is presented in the form of pressure-impulse (*P-I*) curve in which the pressure and impulsive asymptotes are derived using the least squares curve fitting method. The procedure of obtaining the degree of damage was presented in the paper, consisting of 3 main stages: initial stressing, blast loading, residual analysis. However, the procedural description did not clearly mention the numerical method used, whether load control, displacement or combined load-displacement control.

Another numerical study on *DI* level of RC columns subjected to blast loads was also undertaken by Sun et al. (2009) on circular RC columns. Displacement control was used in all three stages of the analysis. Parametric study by varying the displacement control curve and the column's boundary conditions were carried out. The study presented in this paper, however, took into account the effects of loading rate (*DIF*) in all the three stages. In stages 1 and 3 where the initial stressing and residual analysis are conducted within 0.1s and 0.3s respectively, instead of dynamic loading analysis, a quasi-static loading analysis should be performed by neglecting the effects of loading rate (*DIF*=1).

Another study on *DI* level of RC frames subjected to blast loads was also carried out by Jayasooriya et al. (2009). Six blast loading cases of various charge weights of TNT explosives (*W* = 150, 350, 420, 500, 650 and 700 kg) located at a stand-off distance (*R*) of 10m on RC frames comprising 2 storey – 2 bays of square RC columns (400mm x 400mm) and rectangular beams (450mm x 300mm) were analyzed as 2D plane stress

frame. In this paper, the *DI* value refers to the percentage difference between the residual and the designed axial load carrying capacities of RC frames. Similar to that of Shi et al. (2007), this paper did not provide a clear description of the numerical method used in stage 2 (blast loading analysis), whether load or displacement control.

From the aforementioned review, the effects of uncommon column dimensions with B/H ratio >> 2, typical of Singapore's apartment block, on the structural response seemed not to have been studied previously. Moreover as seismic design is not a requirement in Singapore, only a lateral load of either: wind loads, 1.0% of the factored dead loads or 0.5% of the combined factored dead loads and imposed loads, whichever is more significant, is considered for most buildings. Lateral loads arising from extreme events are generally not considered in design. Therefore, such structures could sustain serious damage by close-in blast, depending on the blast intensity and structural resistance. Thus, there is a need to study the response of RC columns having B/H>>2 when subjected to blast loads. As the focus of this study is confined to close-in explosion cases (below the critical scaled distance), only the air blast effect will be considered in the numerical model.

2.4.2 Experimental Studies on Blast Loads on RC structures

An experimental study on the behavior of RC columns subjected to severe blast loads as shown in Figure 2.13 was conducted by Morril et al. (2001) and Crawford et al. (2001). The RC columns studied were rectangular in shape with breadth to depth ratios less than two. A default RC and strengthened RC columns were tested against similar blast loads. The experimental results showed that the default RC column tested was severely damaged

by the blast, heavily deformed and failed. The upper and lower parts of column experienced spalling and scabbing with exposed steel reinforcements.

Meanwhile, the RC column strengthened with CFRP layers, applied onto the columns in the form of 3 vertical strips and 6 horizontal wraps, showed no significant deformation. It demonstrates that encasement by CFRP is an efficient means to ensure survivability of such structures when subjected to extreme blast loads. However, the aforementioned study did not provide complete data of the blast loads, and geometrical and dimensional information in the literature reference, due to confidentiality issues.

The only literature found on experimental testing of RC columns subjected to blast was conducted by Woodson and Baylot (1999). The prototype was idealized to be one typical of RC structures in a low seismic risk region. Five models, quarter scaled with two bays, two storey RC frames were constructed based on the prototype design. The intention was to develop models that represent the exterior column region of a multi-bay, multi-storey RC structure. Thus, the RC frame models were supported by reaction buttresses at the back. Five models were tested against blast loads of 15.625 lb (~7.1 kg) located at stand-off distance *R* 3.5 feet (~1.07m); two similar open frames (one with larger *R* of 5 feet ~1.52 m), one infilled frame, one infilled frame with openings in the wall, and one open frame. Among the models, the 2_{nd} model, open frame with stand-off distance *R* equal to 1.07m as shown in Figure 2.14, is the most relevant to the present study. It may shed light on some important considerations of the present study on the dynamic response of ground floor RC columns of typical ground floor void decks in Singapore. The experimental results of the 2_{nd} model provided a displacement time history curve measured using accelerometer mounted on the distal face of an observed RC column as well as post test

measurements of residual displacements. During the experiment, reflected pressure and impulses on the observed RC column were also recorded by locating pressure gauges at several locations on the observed column.

Woodson and Baylot also performed numerical analyses using LS DYNA FE code. The displacement results, especially the peak lateral displacement of the observed column, obtained from the numerical analysis showed significant differences when compared to the experimental data (line 2) as shown in Figure 2.15. It provides a lower bound estimate in terms of peak and residual displacements. Such data will be discussed further and compared with those obtained from numerical analysis in Chapter 5.

2.5 ECC as Protective Material

Many blast field tests have been conducted on strengthened structural elements and structures (Hayes et al., 2005, Crawford et al., 1997, 2001, Mosalam and Mosallam, 2001, Muszynski and Purcell, 2003). Most of the aforementioned papers used CFRP strips in jacketing the structural elements tested. Crawford et al. (1997) modeled the behavior of CFRP-wrapped RC columns subjected to blast using the PRONTO 3D FE package. It was concluded that CFRP wrapped RC columns provide better resistance when compared to conventional RC columns in terms of flexure, diagonal shear and direct shear capacity. Field tests have also been conducted on the CFRP wrapped RC columns. However, again, full information on the test specimens and test data was not available due to confidentiality issues.

Another type of retrofitting was studied by Crawford et al. (1997) investigating steel jacketed, CFRP composite wrapped and conventional RC columns subjected to blast

numerically modeled using the DYNA 3D FE package. Mid-span displacements of all three cases were presented. From the results it was reported that the steel jacketed RC columns provide better resistance when compared to the CFRP composite wrapped and conventional RC columns.

Engineered cementitious composite (ECC) is a kind of cement-based material mixed with short-random fibers that undergoes pseudo strain-hardening instead of softening after the first crack is formed. It has some advantages compared to other materials in providing resistance to dynamic and impulse load. Maalej et al. (2005) studied the response of hybrid – fiber ECC targets subjected to dynamic tensile loading and high velocity impact. From the dynamic tensile tests under high strain rate, a significant increase in the ultimate tensile strength with increasing strain rate was observed. As shown in Figure 2.16, the tensile dynamic increase factor (DIF) of ECC is greater than that of concrete. This condition may due to the differences in micro-cracking distribution, which appears in the concrete and the ECC when subjected to such loads.

Under high velocity impact test, the penetration resistance of plain concrete targets decreased very quickly after the first crack occurred which may lead to the strain-softening behavior of a target when rapid perforation occurs. Meanwhile in the case of hybrid-fiber ECC targets, it was found that only a small area localized near the impact point was crushed with the other parts remaining intact. ECC possesses higher shatter resistance through the occurrence of microcracks and thus exhibits better energy absorption. The schematic of strain hardening behavior of ECC due to micro cracks is shown in Figure 2.17.

Low velocity impact on hybrid-fiber ECC panels was studied by Zhang et al. (2005, 2007). This experimental study concluded that ECC performs better than conventional RC materials when subjected to impact loading. The ECC specimen can withstand more impact and accommodate larger crater depth before perforation as shown in Figures 2.18 and 2.19. It suffered less damage per impact, retained more energy absorption capacity after multiple impacts and had less debris at failure. Also, the behavior of multiple cracking resulted in more effective distribution of impact energy. Thus, as compared to concrete, ECC is observed to be more suitable for use as a protective material.

Lee (2006) studied the effects of single blast load and multiple blast loads on steel bar reinforced hybrid fiber ECC (SRHFECC) panels and RC panels. This numerical study was carried out using LS DYNA. For the single blast load case the results showed that the SRHFECC panels exhibited smaller peak displacement and less visible damage compared to RC panels. For the case of multiple blast loads, it was discovered that no severe element distortion was observed in the SRHFECC panels when subjected to a second blast loading. In the case of SRHFECC panels, the second blast had less effect than the first blast for the same amount of explosives. As shown in Figure 2.20, the peak displacement measured during the second blast is smaller than that of the first blast. In the case of RC panels, the second blast resulted in higher peak displacement when compared to that of the first blast.

To summarize, no comprehensive field test data on blast loads on Reinforced-ECC structural element has been is available for benchmarking results from the numerical modeling. Moreover, the numerical modeling of RC structural elements strengthened by encasement with ECC subjected to blast load seems very limited in available literature.

Herein, numerical analysis and experimental study on the response of ECC encased RC column when subjected to close-in blast loads will be studied. The results obtained were then compared with those of similar conventional RC columns.

2.6 Observations Arising from Literature Review

The above literature review revealed that numerical modeling can be utilized to provide a better approach to predict blast loads acting on structure with specific geometry and dynamic response of structure under blast loading. Numerical modeling is a useful tool that provides practical complement to knowledge gained from experimental and theoretical studies. However, accurate nonlinear behavior of the materials involved must be simulated in order to obtain reliable results. The model should also be able to represent the dynamic behaviors of material through appropriate modeling of the tensile and compressive dynamic increase factor (*DIF*). Benchmarking of the numerical results with experimental data or analytical solutions, whenever possible, is also necessary.

As stated previously, no literature is available on blast propagation on RC structures with a void deck on the ground floor. The typical void deck at the ground floor has specific configuration of closely spaced columns having dimensions with *B/H* ratios more than two. Such wide columns may act as walls when the blast is directed parallel to its minor axis. The blast waves may be more dispersed onto its surroundings when the direction is parallel to column's major axis. Such columns together with ground floor and 1st storey‘s soffit slabs may provide reflective surfaces for blast waves to be amplified. It may result in very much larger reflected pressure P_R and impulse I_R measured at the incident face of the ground floor columns and at the soffit of the 1st storey slabs as compared to normally

reflected pressure and impulse. This phenomenon is known as shielding effect and it is one of the main interest of this study.

Although many numerical studies on RC columns have been carried out by a number of researchers, the dynamic response of RC column having dimensions with *B/H* ratio of more than 2 is less well understood. Therefore, numerical FE method is adopted to study the behavior of such column when subjected to blast loading. This study would also shed light on whether measures may be taken to enhance the resistance of such columns against close-in blast loads and potential retrofit technique.

In view of retrofit method on existing columns, no available literature on numerical and experimental study of ECC encased RC column has yet reported. Herein, such strengthening method is proposed to strengthen the existing RC columns of typical Singapore's apartment block with *B/H* ratio of more than 2. Such encasement may provide extra confinement to RC columns that in turn increases the column's capacity when subjected to blast loads.

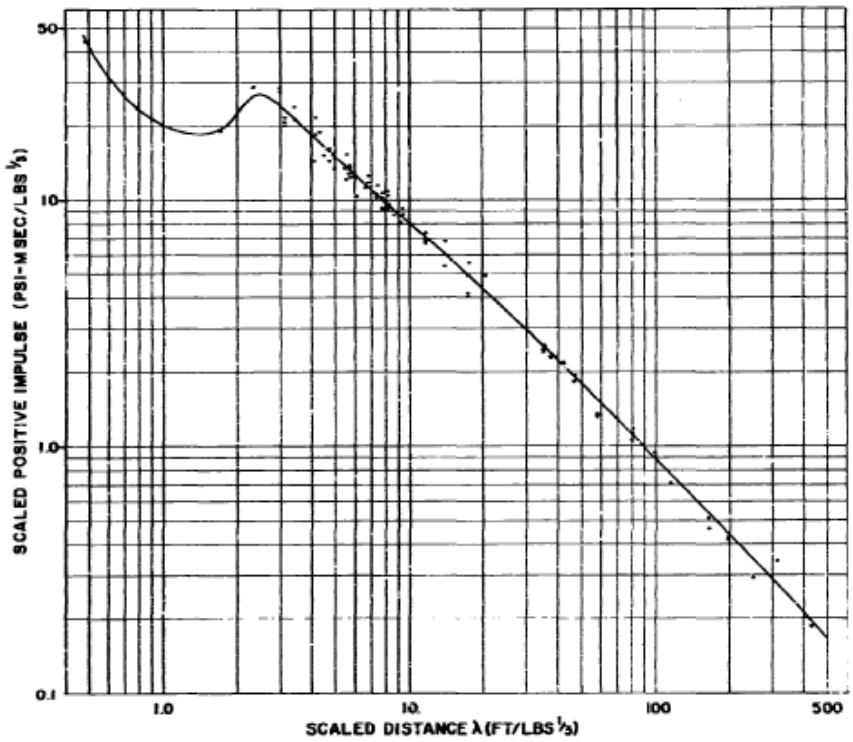

Figure 2.1 Scaled positive phase reflected impulse vs. scaled distance *Z* for 5, 20, 100 and 500 ton TNT detonations (Kingery, 1966)

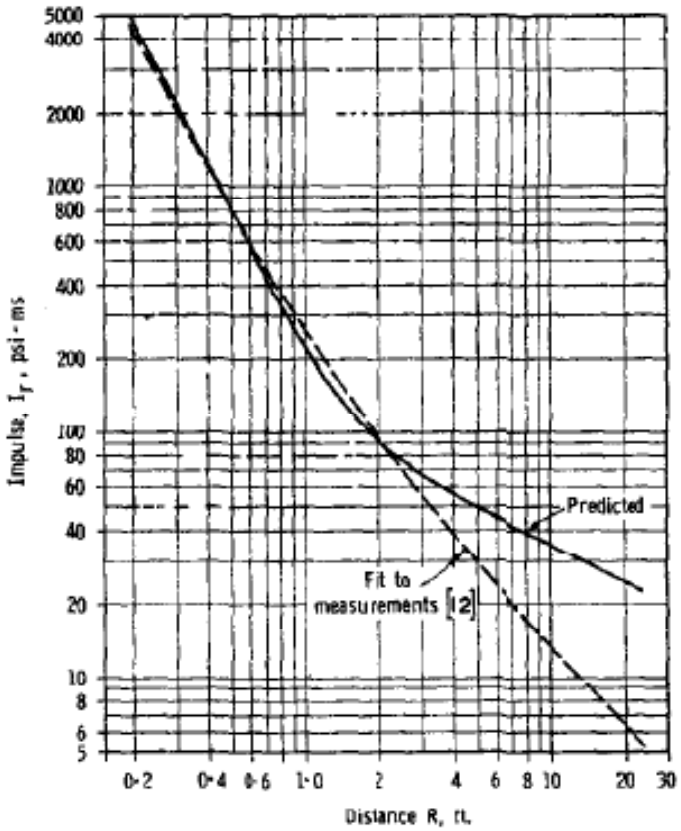

Figure 2.2 Comparison of predicted reflected impulse with smooth fit of experimental data (Baker, 1967)

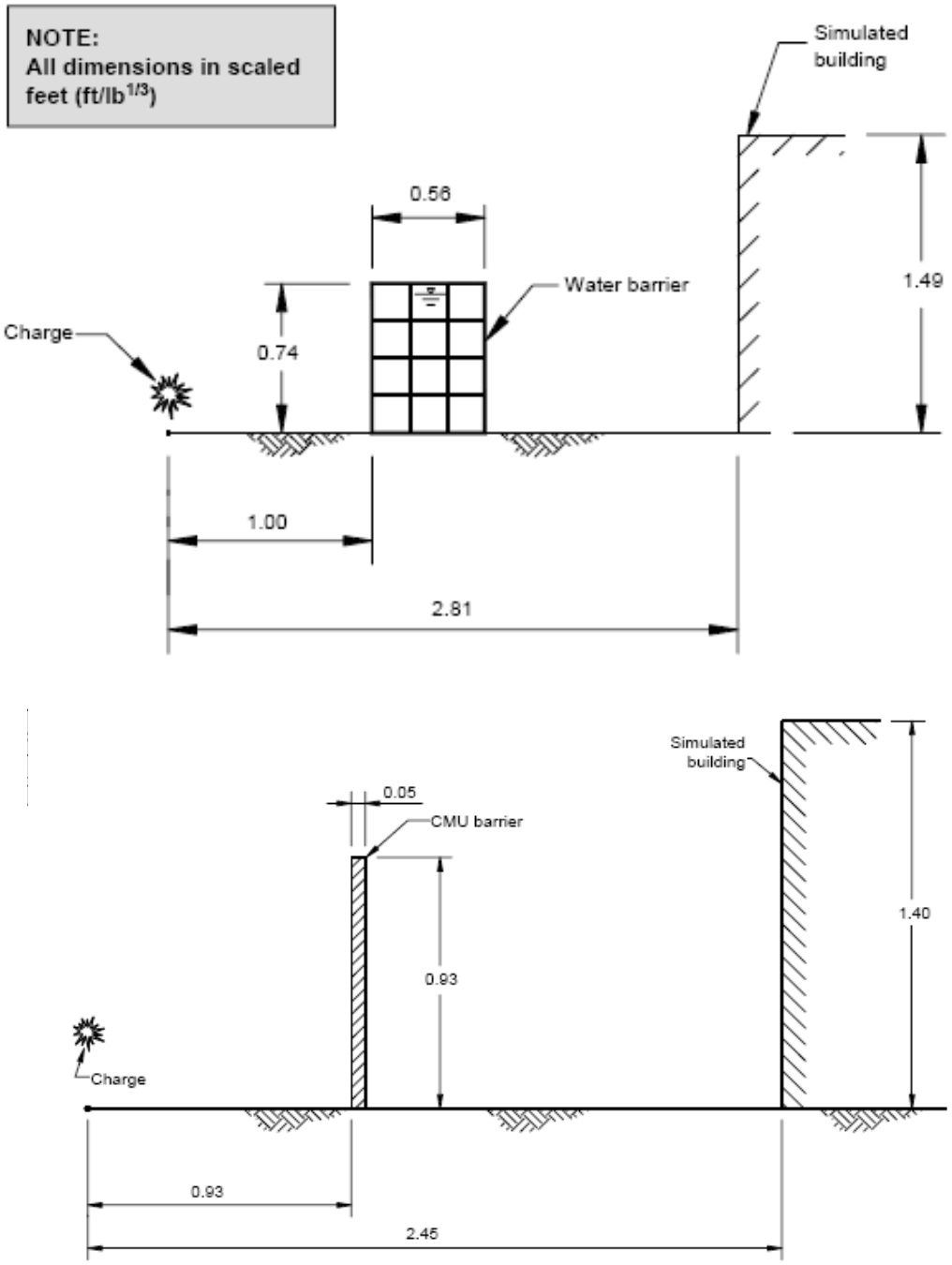

Figure 2.3 Configuration of water and CMU barriers of various width *B* and height *H* (Bogosian and Piepenburg, 2002)

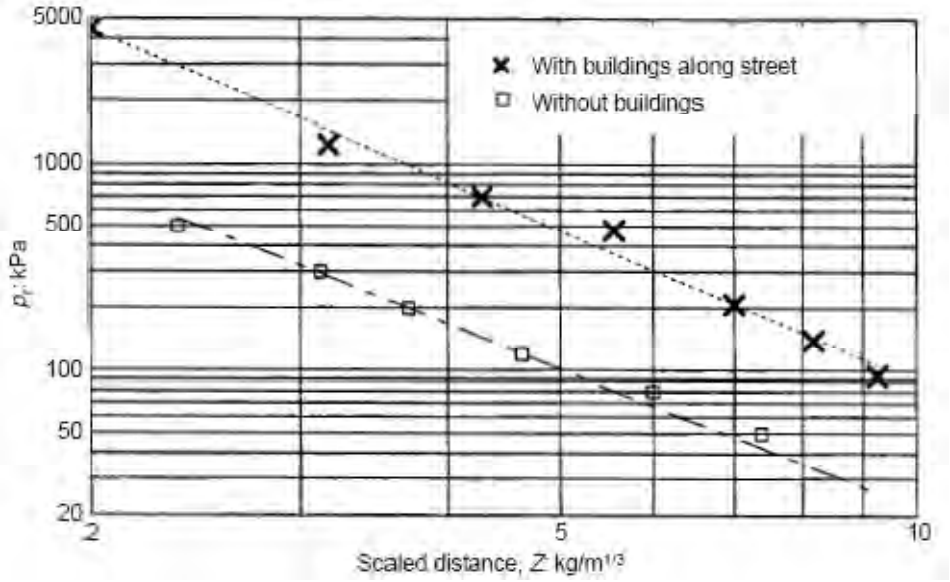

Figure 2.4 Peak reflected pressure on observed buildings with and without street buildings (Smith et al., 2001)

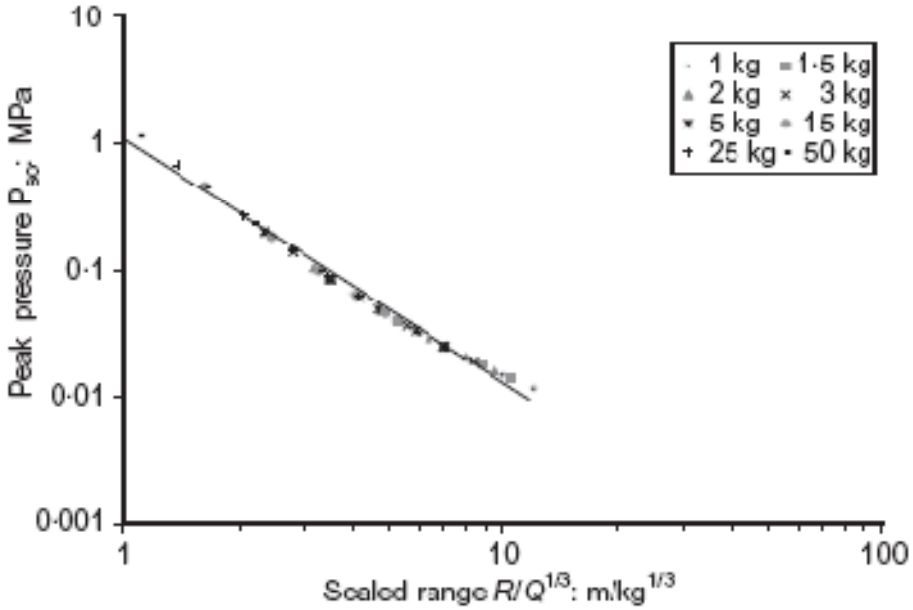

Figure 2.5 Peak overpressure as a function of scaled distance Z (Siddiqui and Ahmad, 2007)

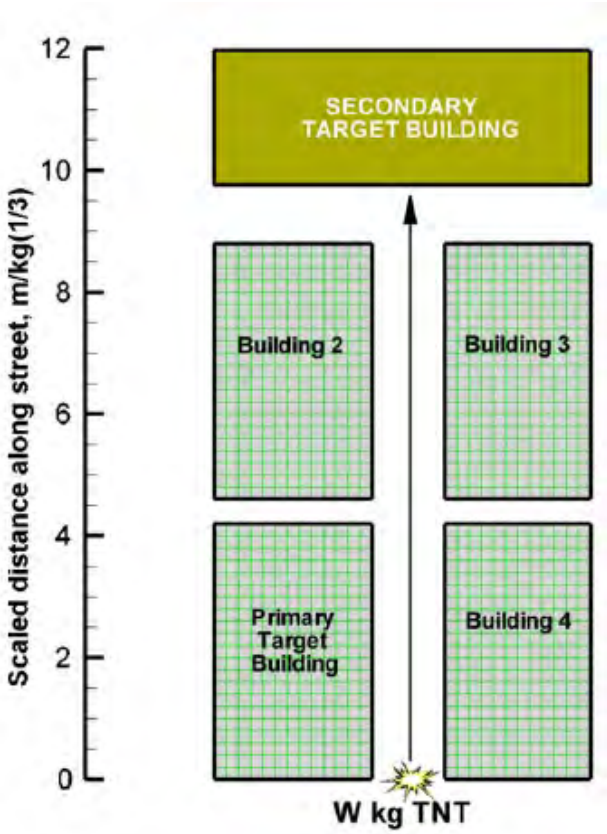

Figure 2.6 Simulation model for collateral blast effects on a building in city layout (Remennikov and Rose, 2005)

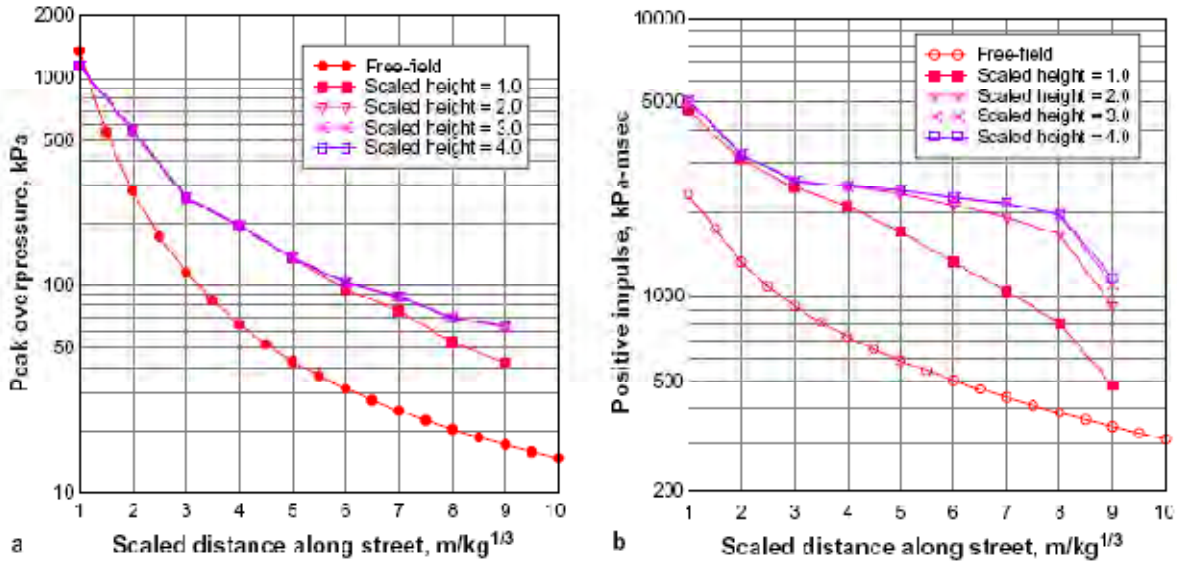

Figure 2.7 Distributions of peak overpressures and impulses enhanced by shielding effects and reflections from adjacent buildings along the street (Remennikov and Rose, 2005)

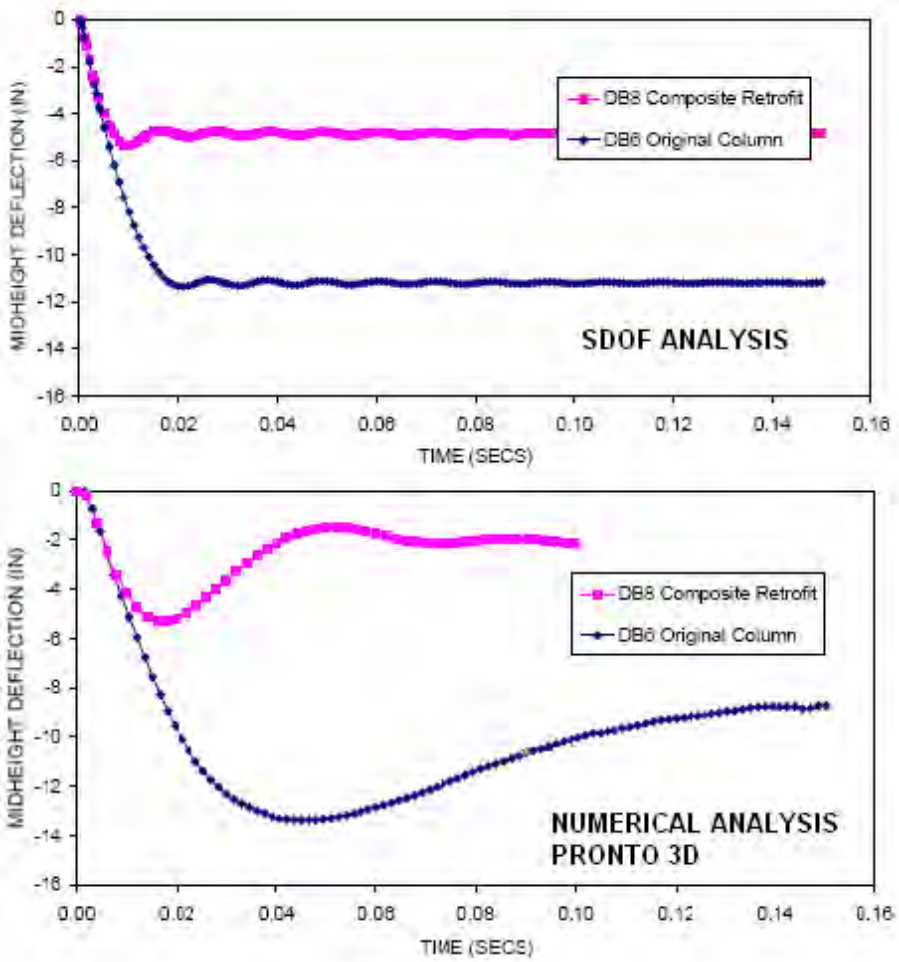

Figure 2.8 SDOF vs. numerical analyses of RC column subjected to blast loads (Crawford et al, 2001)

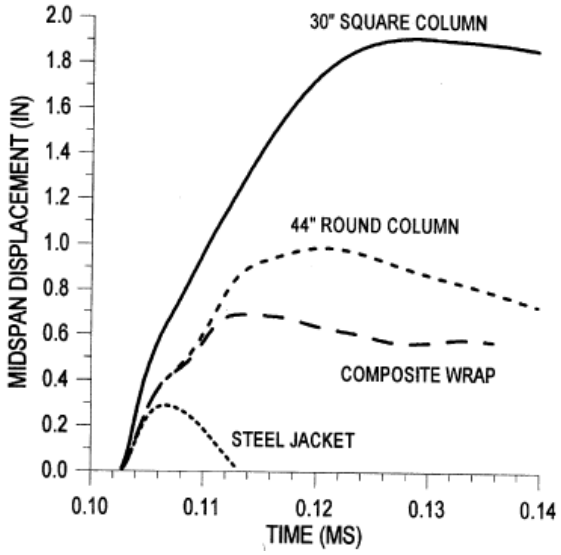

Figure 2.9 Midspan lateral displacements of four column types subjected to 682 kg explosive charge at stand-off distance *R* of 6.1 m and *HOB* 1.83m (1 inch = 25.4 mm) (Crawford et al., 1997)

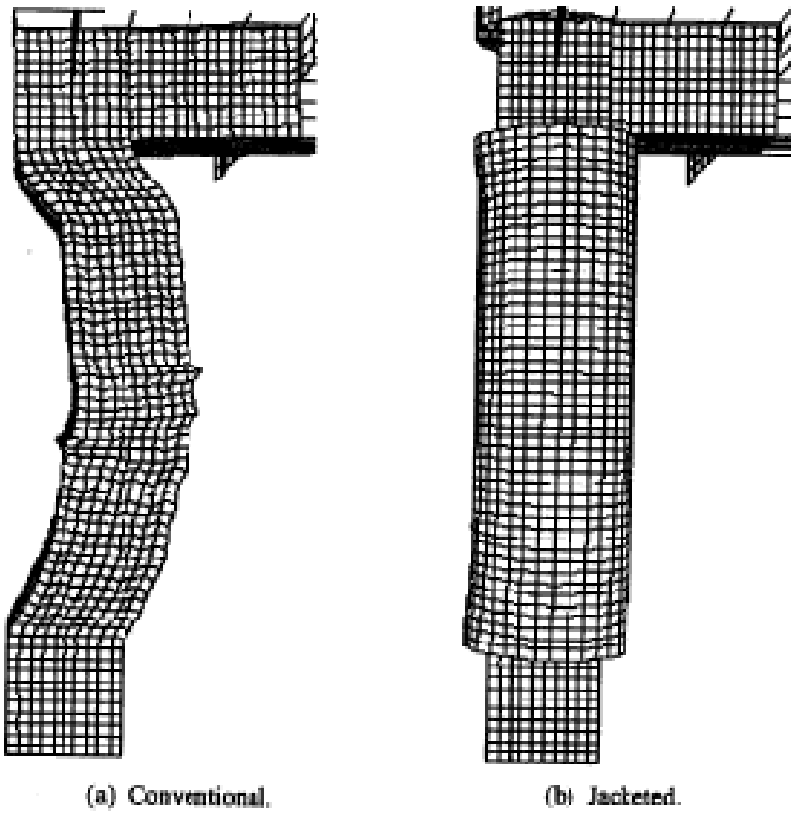

Figure 2.10 Numerical results on dynamic response of conventional and jacketed RC columns subjected to 1764 kg explosive charge at stand-off distance *R* of 6.1 m and *HOB* 1.83m (Crawford et al., 1997)

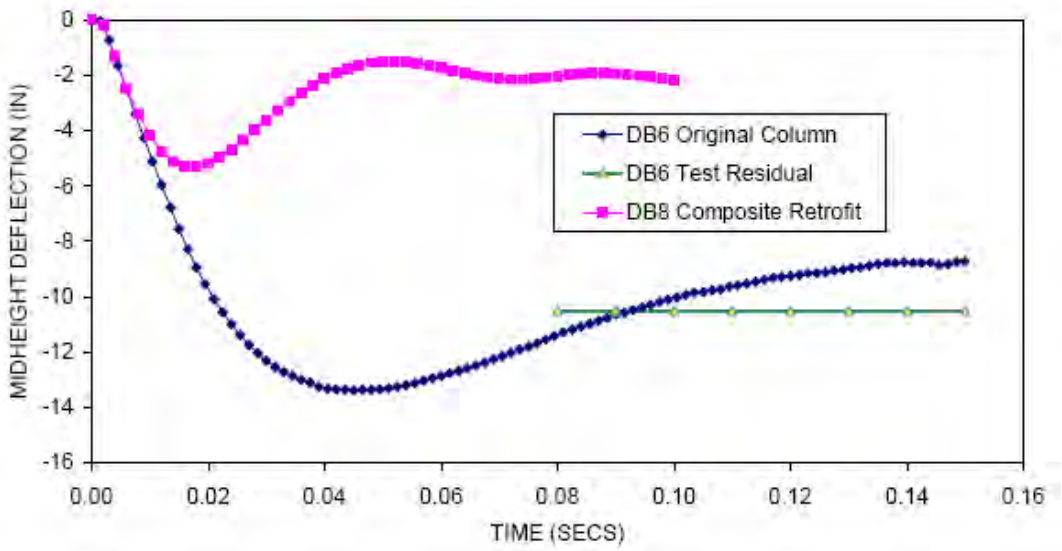

Figure 2.11 PRONTO 3D mid height displacement vs. residual displacement from experiment (Crawford et al., 2001)

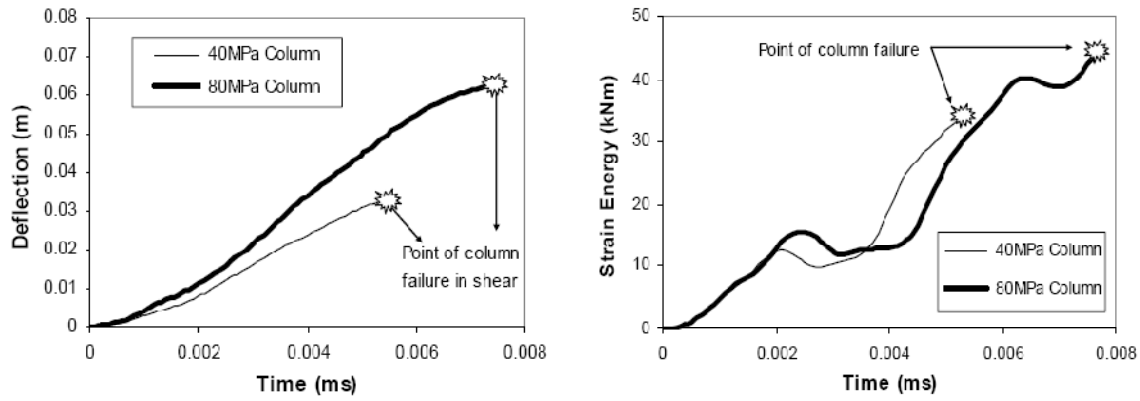

(a) (b)

Figure 2.12 Lateral displacements and energy absorption capacities of NS and HS RC column (Ngo et al., 2003)

(a) (b)

Figure 2.13 Post-test conditions of (a) Conventional (b) CFRP wrapped RC column after subjected to blast loads (Crawford et al, 2001)

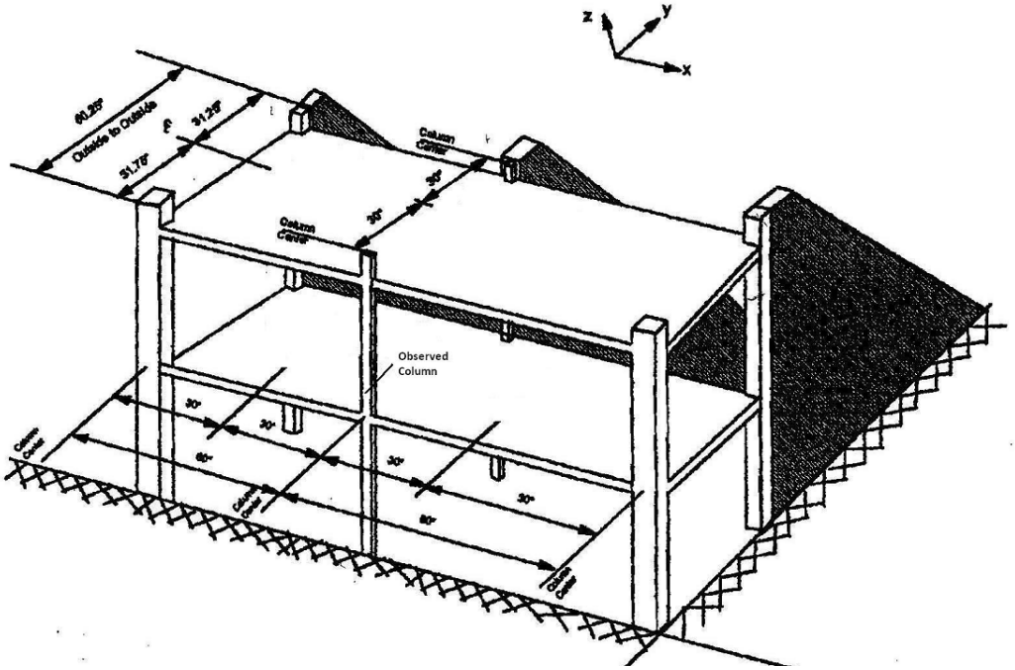

Figure 2.14 Layout of open RC frames quarter scale model
(Woodson and Baylot, 1999)

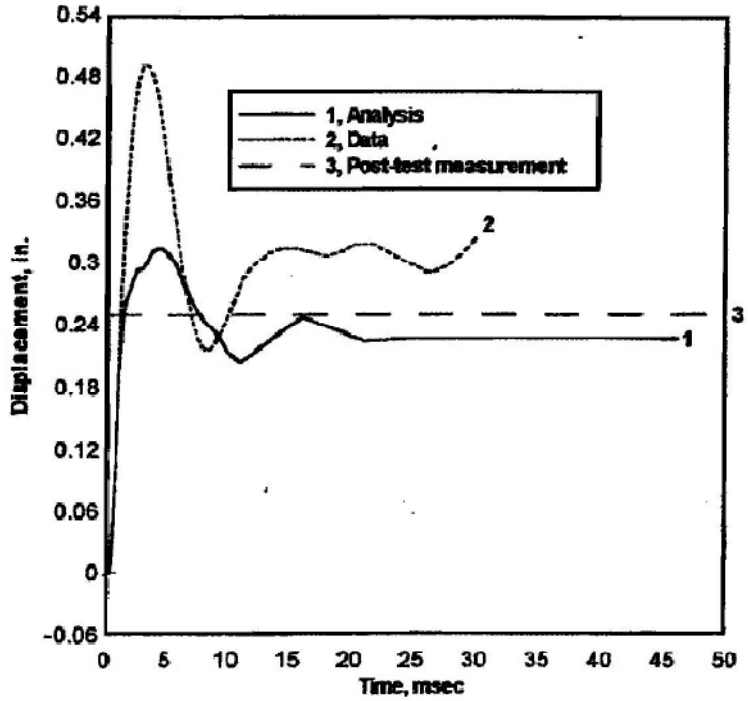

Figure 2.15 Lateral displacement of observed RC volumn from open RC frames quarter scale model subjected to blast loads of W= 7.1 kg C4 at R=1.07 m and HOB=0.23 m
(Woodson and Baylot, 1999)

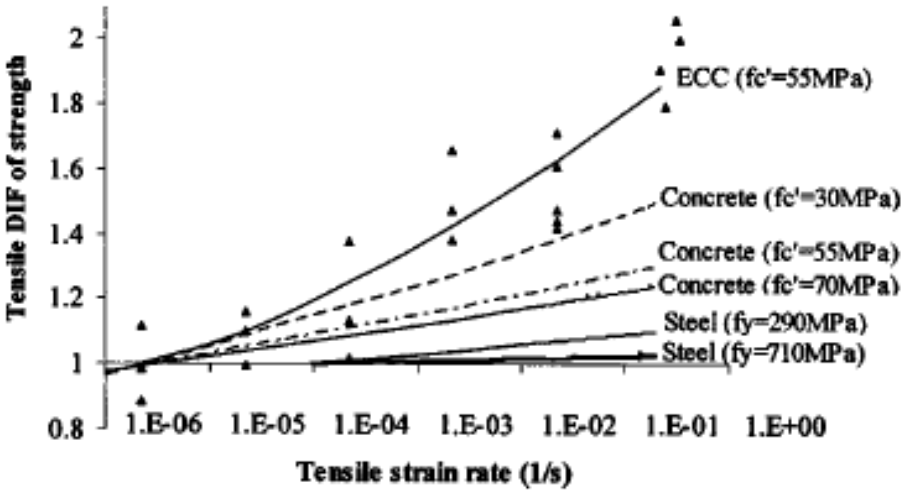

Figure 2.16 Tensile DIF of different materials as a function of strain rate (Maalej et al., 2005)

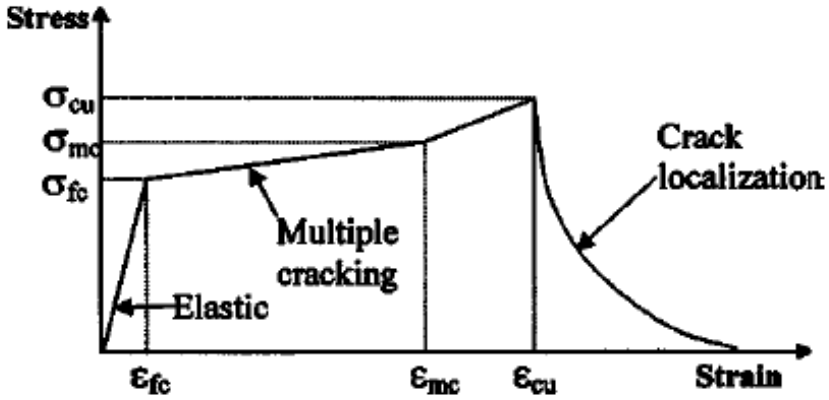

Figure 2.17 Schematics of strain hardening behavior of ECC (Maalej et al., 2005)

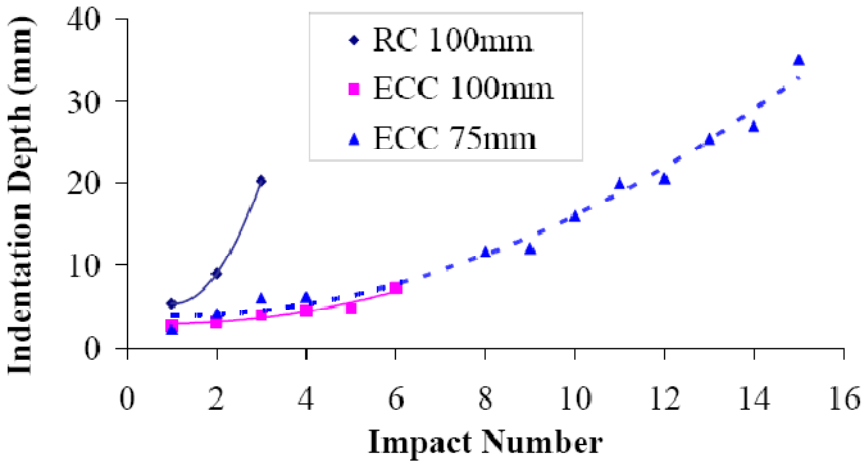

Figure 2.18 Indentation depths against numbers of impact (Zhang et al., 2005)

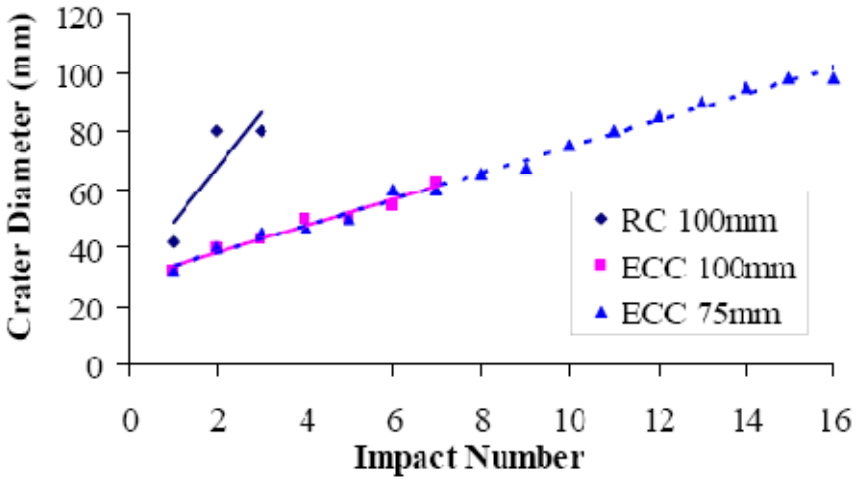

Figure 2.19 Crater diameters against numbers of impact (Zhang et al., 2005)

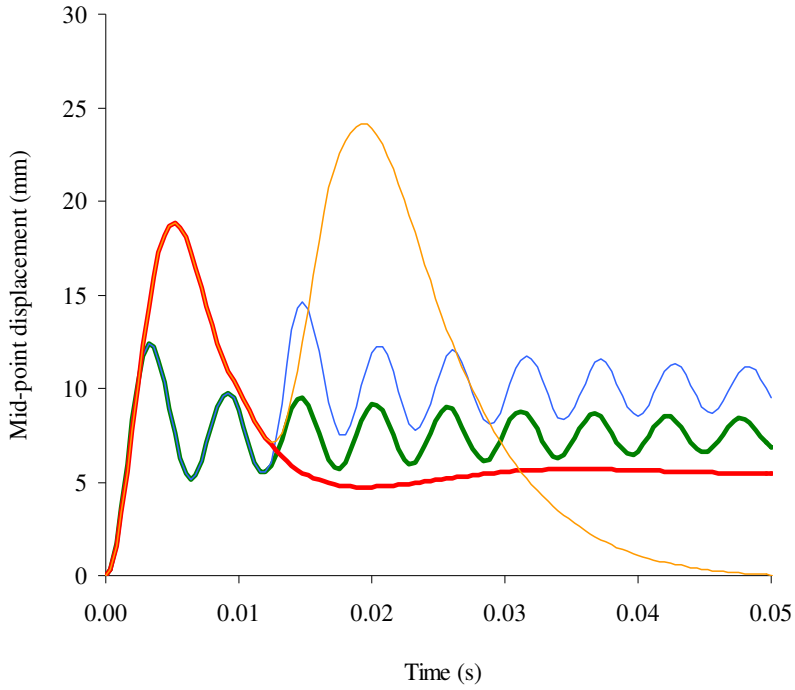

Figure 2.20 Midpoint displacement of the 100 mm thick RC and SRHFECC panels subjected to multiple blast loading (200 kg TNT followed by 100 kg TNT) at *R*= 10m (Lee, 2006)

3 Blast Loads on Structure

3.1 Introduction

In the study of the dynamic response of structures under blast loading, the definition of explosion, the range of explosions considered, and the magnitude of blast loads applied on the structure should be identified in advance. Therefore in this chapter, a common definition of explosions, the fundamental theory underlying explosions, blast loads, and the effects of a structure's configuration on the blast propagation are discussed.

3.2 Explosions, Characteristics and Its Products

An explosion is an exothermic process with a sudden-release of energy from the reaction of reactive compounds that, in turn, is dissipated in various forms of explosion products. In this study, the explosion refers to the chemical explosion from the ignition of flammable high explosive materials. During the ignition process of chemical explosions, one-third portion of the chemical energy available in most high explosives is discharged. The rest, the remaining two-third portion, is discharged slowly as the detonation products are mixed with air and burnt.

In general, there are four products associated with hemispherical explosions (Figure 3.1), i.e. blast waves, fireball, ground shock and flying debris. The very first mechanical effect of a blast is a vigorous blow from the pressure jump in its shock front, followed by the crushing effect of the blast waves overpressure and a blast wind of extremely high velocity. The blow force associated is proportional to the blast wave pressure and the reflected area.

As the shock waves spread out, the overpressure then decrease quasi-exponentially with time until atmospheric pressure is reached, owing to the geometric divergence and the consumption of energy in heating the air. Such a positive phase is then followed by a slight negative blast phase along with a reverse blast wind. The typical pressure-time history of blast loads accompanying both positive and negative phases is shown in Figure 3.2.

The fireball is formed due to a process of ignition of flammable high explosive materials. Such a fireball expands outwards following the blast wave bringing along some of the undischarged explosives until it reaches a certain radius from the source of explosion when all the undischarged explosives are burnt.

Blast wave travels through the air and when it meets the ground, it is transmitted into the ground as a form of ground shock. This phenomenon is typical of a hemispherical explosion, which is placed just at or slightly above the ground. However, the effect of ground shock on the dynamic response of a structure is insignificant as compared to the blast waves effect for close-in explosions (Wu and Hao, 2007).

The type of ground also affects the amount of ground shock transmitted and the resultant reflected blast wave overpressure. When the ground is fully a reflective surface, there will be no cratering and the analysis is conducted by assuming that all the blast waves are fully reflected. Generally, the ground never acts as a fully reflective surface and some of the energy of the explosion is consumed in the formation of a ground crater. When this occurs, flying debris in the form of loose material from the ground are carried along by the high velocity blast winds.

When the explosive is placed at a height above the ground, the formation of ground shock decreases and the blast waves may impact the structure in a form of incident waves rather than reflected blast waves, depending on the amount of charge weight W, height of burst HOB, and stand-off distance R. This type of explosion is known as a spherical explosion.

In this study, the explosion considered is a hemispherical close-in explosion with zero HOB that the explosion is located just above the ground level. The range of stand-off distance R and charge weight W of explosion considered are given in Sections 3.3 and 3.4, respectively. Since the effect of ground shocks on the dynamic response of the structure is generally insignificant, herein, such effects are neglected.

3.3 Magnitude of Explosion and Its Calculation

The magnitude of explosion is established by the amount of energy released, namely a mass specific energy (Mays and Smith, 1995). The standard accepted is the energy released in terms of TNT, an explosive selected due to it being a chemically pure material that is readily available for calibration purposes (Kinney and Graham, 1985).

The magnitude of explosion is a function of charge weight *W* and its stand-off distance *R*. Stand-off distance *R* is the distance between the explosive charge and the structure. As briefly described in Chapter 1, in this study the structure investigated is a conventional RC apartment block typical found in Singapore. Such structures typically have a void deck on the ground floor in close proximity to the adjoining car park as shown in Figure 3.3. The void deck is provided for residents to held social functions.

In terms of stand-off distance *R*, as shown in Figure 3.4, the range of *R* considered in this study is within 3 to 10 meters, representing the available stand-off distance of a typical apartment block in Singapore.

3.4 Range of Explosion Considered

An explosion does not provide any advance warning of impending destruction, as the blast travels faster than the speed of sound and may have severe implications on the structural integrity and stability of the affected structure, leading to possible structural failure and loss of life. Nowadays, the main sources of explosion threats to structures are from terrorist attacks. The recent attacks as listed in Table 3.1 show that the most common explosive devices used by terrorists is in the form of vehicular bombs, which the US military and law enforcement agencies named it as Vehicle Borne Improvised Explosive Device (VBIED). On the basis of the explosives standard provided by the Bureau of Alcohol, Tobacco, Firearms and Explosives (BATF), the VBIED is divided into 6 categories as summarized in Figure 3.5. The BATF explosive standard provides various categories of vehicular explosives that may occur. In this study, the explosive range considered is within the weight of 100 kg to 3 tons of TNT.

Table 3.1 Recent Terrorist Attack by VBIED

No.	Country, City	City	Date	Target	VBIED	Predicted Charge Weight (*W*)	Casualties (Died/Wounded)	Conditions of Target
1	Indonesia	Bali	10/12/2002	Paddy's pub & Sari Club Night clubs	Pick-up van	1.125 tons of explosives: mixture of potassium chlorate, aluminum powder, sulfur and TNT	202 died, 209 wounded	destroyed & similarly for the nearby buildings
2	Turkey	Istanbul	11/20/2003	HSBC Bank AS and the British Consulate	2 Trucks	-	30 died, >400 wounded	failure of façade, shattered glass
3	Iraq	Balad	2/10/2008	Iraqi army checkpoint	Pick-up truck	6 barrels of explosives: mixture unknown	25 died, >40 wounded	collapse of some buildings nearby
4	Pakistan	Islamabad	6/2/2008	Danish embassy	Car	-	6 died, 27 wounded	significant structural damage & similarly for the nearby residential buildings
5	Spain	Ondarroa	9/21/2008	Police station	Car	100 kg of explosives: mixture unknown	10 wounded	heavy structural damage
6	Pakistan	Islamabad	9/22/2008	Marriot Hotel	Six-wheeled dumper truck	600 kg of RDX mixed with TNT (Torpex or H6)	53 died, >250 wounded	failure of façade & the explosion caused a leakage of natural gas pipe, causing fire
7	Syria	Damascus	9/27/2008	Sidi Kadad suburban residential buildings	Car	200 kg of explosives: mixture unknown	17 died, 14 wounded	damaged, shattered glass
8	Spain	Pamplona	10/30/2008	Carpark of The University of Navarra	Car	100 kg of explosives: mixture unknown	17 wounded	shattered glass
9	Pakistan	Lahore	5/27/2009	Police headquarter	Car	-	70 died, >200 wounded	destroyed & similarly for the nearby buildings
11	Pakistan	Peshawar	6/9/2009	Pearl Continental Hotel	Pick-up truck	500 kg TNT	11 died, 52 wounded	destroyed

3.5 Blast Load vs. Other Hazards

On the basis of the ratio of the positive phase duration of blast loads, t_D, to the natural period of the structure, T, or the ratio of the t_D to the time for the structure to reach its maximum response, t_M, there are three regimes of loading (Cormie et al., 2009), i.e.:

a. Quasi-static Loading

When $10 < \frac{t_D}{T}$, the structure has reached its maximum response before the load is totally applied $\left(\frac{t_M}{t_D} < 0.3\right)$. Herein, the displacement of the structure is a function of pressure, P and stiffness, K.

$$f_{quasi-static} = f(P, K) \tag{3.1}$$

b. Impulsive Loading

When $\frac{t_D}{T} < 0.1$, the load has finished acting before the structure responds $\left(3 < \frac{t_M}{t_D}\right)$. Most of the deformation appears after time t_D. The displacement of the structure is therefore a function of stiffness, K, mass, M, and impulse, I (the area below the load curve). The change in the magnitude of peak pressure, P is insensitive to the dynamic response of the structure.

$$f_{impulsive} = f(I, K, M) \tag{3.2}$$

c. Dynamic Loading

When $0.1 < \frac{t_D}{T} < 10$ or $0.3 < \frac{t_M}{t_D} < 3$, the analysis is more complex. The dynamic response of the structure is influenced by a combination of $f_{quasi\text{-}static}$ and $f_{impulsive}$ that all the following parameters (pressure, P, impulse, I, stiffness, K and mass, M) affect the dynamic response of structure.

$$f_{(dynamic)} = f(P, I, K, M) \tag{3.3}$$

The aforementioned three regimes are plotted into an exponential curve with respect to the logarithmic values of impulse, I and pressure, P as shown in Figure 3.6. Such a curve may be used to indicate the damage threshold of the structure. Below the curve, such P and I combinations will not induce failure of structure. However, when the P and I combination lies above the curve, they may cause structural failure.

In general, as the blast load occurs within miliseconds, most cases of RC structure subjected to blast load fall into the last two regimes, i.e. dynamic and impulsive loading schemes. These two regimes are discussed further in Chapters 7 and 8. The characteristics of blast load are compared to loads arising from other hazards such as cyclones (strong wind), earthquakes, persistent wind, and floods and the differences in terms of its characteristics are schematically summarized in Table 3.2.

Table 3.2 Load Characteristics of Blast and Other Hazards

Load Characteristics	Blast Load	Cyclone	Earthquake	Persistent Wind	Floods
Forcing function	P (R, W), I (R, W)	P (wind speed v^2, ρ)	Force F (mass m, acceleration a)	P (wind speed v^2, ρ)	F (flow rate Q^2, contact area A, ρ)
Duration	*miliseconds*	*seconds*		*hours*	
Loading Time History	Exponential	Random	Combined sinusoidals	Random	Sinusoidal
Damage on Structure	Localized	Global			
Loading Regime	*Impulsive* or *Dynamic*	*Dynamic*		*Quasi-static*	

3.6 Prediction of Blast Load

In order for this study to provide an accurate prediction of the dynamic response of RC structures when subjected to blast loads, the first step is to correctly estimate the blast loads likely to be applied on the structure. Herein, the formulations of incident blast

overpressure, P_{SO}, reflected pressure, P_R, and other parameters of blast loads obtained from TM5-855 code, Conwep, and empirical analysis proposed by a number of researchers are presented.

From available literature, Sadovskyi (1952) reported on a formulation of the incident overpressure, P_{SO} as a function of scaled distance, Z and atmospheric pressure, P_O for a spherical blast.

$$Z = \frac{R}{W^{1/3}} \left[\mathrm{m/kg^{1/3}}\right] \tag{3.4}$$

R is the stand-off distance in meters whereas W is the charge weight in kg.

$$P_{SO} = P_O + \underbrace{0.0981\left(\frac{10.7}{Z^3} - 1\right)}_{\Delta P_{SO}} \text{[MPa] for } Z \leq 1 \tag{3.5a}$$

$$P_{SO} = P_O + 0.0981\left(\frac{0.76}{Z} + \frac{2.55}{Z^2} + \frac{6.5}{Z^3}\right) \text{[MPa]} \quad \text{for } 1 \leq Z \leq 15 \tag{3.5b}$$

The specific shockwave impulse, I_{SO} and the positive phase duration, t_D formulations were also derived and given as follows:

$$I_{SO} = 0.1\left(\frac{0.975}{Z} + \frac{1.455}{Z^2} + \frac{5.85}{Z^3} - 0.019\right) \text{[MPa]} \quad \text{for } 0.01 < P_{SO} \leq 1 \tag{3.6}$$

$$t_D = B\sqrt[6]{W^2}\sqrt{R} \quad \text{[msec]} \quad \text{where } B = 1.0, 1.3 \text{ or } 1.5 \tag{3.7}$$

Brode, in 1955, reported on a spherical blast that, in turn, is used as the base for further studies on blast. His formulation on incident overpressure, P_{SO}, is given as follows:

$$P_{SO} = 0.1\left(\frac{0.975}{Z} + \frac{1.455}{Z^2} + \frac{5.85}{Z^3} - 0.019\right) \text{[MPa]} \quad \text{for } 0.01 < P_{SO} \leq 1 \tag{3.8a}$$

$$P_{SO} = 0.1\left(\frac{6.7}{Z^3} + 1\right) \text{[MPa] for } P_{SO} > 1 \tag{3.8b}$$

Naumenko and Petrovskyi (1956) conducted another study on spherical blasts. Similar to the formulation proposed by Sadovskyi (1952), the incident overpressure's formula, P_{SO}, is given as a function of the delta overpressure, ΔP_{SO} and the atmospheric pressure, P_O.

$$P_{SO} = P_O + 0.0981\left(\frac{0.975}{Z} + \frac{1.455}{Z^2} + \frac{5.850}{Z^3} - 0.019\right) \text{[MPa]} \quad (3.9a)$$

$$\text{for } 0.01 \leq \Delta P_{SO} \leq 1.0$$

$$P_{SO} = P_O + 0.0981\left(1 + \frac{6.70}{Z^3}\right) \text{ [MPa] for } \Delta P_{SO} < 1.0 \quad (3.9b)$$

US Army Corps of Engineer in 1986 launched a TM5-855-1 code entitled "Fundamentals of Protective Design for Conventional Weapon". It provides a useful estimation for assessing blast loads especially when many combinations of explosives and locations are considered. Several graphs to obtain the incident overpressure P_{SO}, impulse I_S as well as the positive phase duration t_D of a spherical blast were given in TM5-855-1 code as a function of scaled distance Z and charge weight W.

Henrych (1979) conducted a more comprehensive study on spherical blasts and derived several empirical formulas to generate the blast parameters. Such formulas are given as follows.

In terms of the incident wave, the incident overpressure is a function of delta overpressure, ΔP_{SO}, and atmospheric pressure, P_O. The delta overpressure, ΔP_{SO}, itself is a function of scaled distance, Z.

$$P_{SO} = P_O + 0.0981\left(\frac{14.0717}{Z} + \frac{5.5397}{Z^2} - \frac{0.3572}{Z^3} + \frac{0.00625}{Z^4}\right) \text{ [MPa]} \quad (3.10a)$$

$$\text{for } 0.05 \leq Z \leq 0.30$$

$$P_{SO} = P_O + 0.0981\left(\frac{6.1938}{Z} - \frac{0.3262}{Z^2} + \frac{2.1324}{Z^3}\right) \text{[MPa] for } 0.30 < Z \leq 1.00 \quad (3.10b)$$

$$P_{SO} = P_O + 0.0981\left(\frac{0.662}{Z} + \frac{4.05}{Z^2} + \frac{3.288}{Z^3}\right) \text{[MPa] for } 1.00 < Z \leq 10 \quad (3.10c)$$

Incident impulse is derived as a function of scaled distance, Z and charge weight, W as:

$$I_{SO} = 0.00981\sqrt[3]{W\left(663 - \frac{1115}{Z} + \frac{629}{Z^2} - \frac{100.4}{Z^3}\right)} \text{ [MPa.msec] for } 0.40 \leq Z \leq 0.75 \quad (3.11a)$$

$$I_{SO} = 0.00981\sqrt[3]{W\left(-32 + \frac{211}{Z} - \frac{216}{Z^2} + \frac{80.1}{Z^3}\right)} \text{ [MPa.msec] for } 0.75 < Z \leq 3.0 \quad (3.11b)$$

In terms of the reflected wave, peak reflected pressure, P_R, is given as a function of delta overpressure, ΔP_R, and atmospheric pressure, P_O, and formulated as:

$$P_R = P_O + \underbrace{2\Delta P_{SO} \times 0.0981 + \frac{6 \times (0.0981 \times \Delta P_{SO})^2}{0.0981\Delta P_{SO} + 7.2}}_{\Delta P_R} \text{[MPa] for } \Delta P_R \leq 3.92 \quad (3.12)$$

Similar to the incident impulse formula, I_{SO}, given in Equation 3.11, the positive phase duration, t_D, is also a function of scaled distance, Z, and charge weight, W, and is given as:

$$t_D = \sqrt[3]{W(0.107 + 0.444Z + 0.264Z^2 - 0.129Z^3 + 0.0335Z^4)} \text{ [msec]} \quad \text{for } 0.05 \leq Z \leq 3.0 \quad (3.13)$$

Baker et al (1983) studied the effects of spherical explosions on incident and reflected blast waves parameters. Their findings are summarized into two main graphs as shown in Figures 3.7 and 3.8 for incident wave parameters consisting of incident overpressure (P_{SO}), incident impulse (I_{SO}), and time of arrival (t_A), and for reflected wave parameters (P_R, I_R and t_A) respectively. Such parameters are obtained as a function of scaled distance Z and charge weight W.

The aforementioned spherical blast formulas can generally be converted to obtain blast parameters arising from hemispherical explosions by considering the reflection phenomenon of the ground floor. In hemispherical explosions, the explosive is placed on or near the ground. Herein, the ground acts as a reflecting surface. Thus, the initial shock is very quickly reflected and the reflected wave merges with the incident wave so rapidly that a single, enhanced blast wave is formed.

The characteristics of such spherical waves are almost identical to the one formed by free-air burst of spherical explosions, except that the energy of the blast appears to be greater. The amount of energy reflected from the ground is dependent on the ground reflector condition, on how much energy is imparted to the ground in a form of cratering, for example. If the ground is a perfectly rigid surface, then the equivalent energy obtained would be twice as much as the spherical explosion's energy. However, if the ground is a perfect energy absorber, the equivalent energy may be similar to that obtained from spherical explosions. In general, for a hemispherical explosion, when a crater is created, the equivalent energy obtained is around 1.8 times that of a spherical explosion of similar charge weight.

A study on hemispherical explosion was first conducted by Kingery and Bulmash (1984). Blast parameters can be obtained from graphs that were plotted with respect to scaled distance, Z and equivalent TNT charge weight, W. Such graphs for hemispherical explosions were then incorporated into a software namely ConWep along with graphs for spherical explosions from TM5-855-1 code. In ConWep the blast parameters can be easily generated by inputting the type of explosion, type of explosive material, the charge weight W, and the stand-off distance R.

Another study on hemispherical explosions was done by Siddiqui and Ahmad (2007). They proposed formulas to generate the incident overpressure, P_{SO}, and reflected pressure, P_R, as follows:

$$P_{SO} = 1.017(Z)^{-1.91} \text{ [MPa]} \quad \text{for } 1 < Z \leq 12 \tag{3.14}$$

$$P_R = 1.8(P_{SO})^{1.3} \text{ [MPa]} \tag{3.15}$$

The time of arrival is formulated as:

$$t_A = \frac{400\ R^{1.2}W^{-0.2}}{C_a} \text{ [msec] in which } C_a = 340 \text{ m/s} \tag{3.16}$$

The positive phase duration, t_D, is usually a combination of two time duration, t_{RISE}, during which blast pressure increase to a maximum pressure, and $t_{DECREASE}$, during which the blast pressure reduces to the atmospheric pressure from the maximum pressure reached t_D is thus given as:

$$t_D = t_{RISE} + t_{DECREASE} \tag{3.17}$$

$$t_{RISE} = 2.6(Z)^{0.98} \text{ [msec]} \tag{3.18}$$

$$t_{DECREASE} = 0.3(Z)^{0.89}W^{0.47} \text{ [msec]} \tag{3.19}$$

Wu and Hao (2007) proposed several formulas to generate the hemispherical blast parameters. The incident overpressure, P_{SO}, is given as follows:

$$P_{SO} = 1.059\left(R/W^{1/3}\right)^{-2.56} - 0.051 \text{ [MPa] for } 0.1 < \frac{R}{W^{\frac{1}{3}}} \leq 1 \tag{3.20a}$$

$$P_{SO} = 1.008\left(R/W^{1/3}\right)^{-2.01} \text{ [MPa] for } 1 < \frac{R}{W^{\frac{1}{3}}} \leq 1 \tag{3.20b}$$

The reflected pressure, P_R, is formulated as a function of incident overpressure and is given as:

$$P_R = 2.85(P_{SO})^{1.206} \text{ [MPa]} \ \ for \ \ P_{SO} \leq 50 \tag{3.21}$$

The time of arrival is given as a function of stand-off distance R, charge weight W and the sound speed C_a.

$$t_A = \frac{340R^{1.4}W^{-0.2}}{C_a} \quad \text{[msec]} \quad \text{in which } C_a = 340 \text{ m/s} \tag{3.22}$$

Similar to Siddiqui and Ahmad (2007), Wu and Hao (2007) also formulated the positive phase duration as a function of rising and decreasing time duration on a pressure time history curve.

$$t_D = t_{RISE} + t_{DECREASE} \tag{3.17}$$

$$t_{RISE} = 1.9(Z)^{1.30} \quad \text{[msec]} \tag{3.23}$$

$$t_{DECREASE} = 0.5(Z)^{0.72}W^{0.4} \quad \text{[msec]} \tag{3.24}$$

The aforementioned formulas are herein compared for a specific hemispherical explosion of 100 kg TNT at 5 meters stand-off distance. Table 3.3 shows the values of blast parameters generated from the aforementioned formulas. The asterisk sign in Table 3.3 refers to the spherical blast formulas factored by *CF* equal to 1.8, an equivalent energy conversion factor to convert the pressure and impulse to those of a hemispherical blast. Generally such conversion factors also account for the ground reflection and cratering on the ground.

From Table 3.3, it is shown that incident overpressures, P_{SO}, from various empirical formulas for a hemispherical blast of 100 kg charge weight of TNT at 5 meters stand-off distance ranged between 0.868 (Wu and Hao, 2007) to 1.515 *MPa* (Sadovskyi, 1953). The discrepancies of P_{SO} are up to 1.75 times. In terms of reflected pressure, P_R, the discrepancies between the values obtained are around 1.05 to 3 times. Such discrepancies are rather significant. Henrych (1979), Siddiqui and Achmad (2007), and Wu and Hao (2007) proposed roughly similar values of reflected pressure, P_R, of around 2.278 to 2.488

MPa. In the mean time, Baker et al. (1983), and Kingery and Bulmash (1984) proposed P_R of around 6.65 to 7 MPa.

In terms of impulse, Baker et al. (1983), and Kingery and Bulmash (1984) proposed similar values of incident (I_{SO}) and reflected (I_R) impulses of around 1.0 and 3.7 *MPa*, respectively. However, Henrych (1979) proposed a value of an incident impulse more than twice of those proposed by Baker et al. (1983) and Kingery and Bulmash (1984), of around 2.5 *MPa*.

3.7 Effects of Structural Configuration to Blast Load

In order to accurately analyze any existing structure for its blast resistance or to design a new structure, the blast loads applied to the structural components should be estimated correctly in terms of peak reflected pressure P_R, reflected impulse I_R and the loading time history. In the empirical equations, blast parameters are found to be a function of charge weight, *W*, and stand-off distance, *R*. Such empirical equations provide a good estimate of blast parameters for far-field explosions acting on structures with simple geometry such as rectangular boxes with large reflection surfaces. When such equations are carried out to estimate the blast pressure applied on standalone RC columns with small reflection surfaces or structures with more complicated geometry and layout arising from close-in explosions, the accuracy may be diminished. Blast parameters may vary along the height, *H*, and along the width, *B*, of structure. Such variations are discussed in details in Chapter 5.

Table 3.3 Blast Pressure Calculation Based on Empirical Equations and Code for 100 kg TNT Explosion at 5 m Stand-off Distance

No	Parameter	Sym-bol	Unit	1952	1955	1956	1968	1979	1983	1984	2007	2007
				MA Sadov-skyi*	Brode*	IA Naumenko &GI Petrovskyi *	TM5-855-1 *	J Henrych *	WE Baker et al*	Kingery & Bul-mash	JI Siddiqui &S Ahmad*	C Wu & H Hao
a	Charge Weight	W	Kg	180	180	180	180	180	180	100	180	100
b	Stand-off distance	R	M	5	5	5	5	5	5	5	5	5
c	Scaled distance	Z	$m/kg^{1/3}$	0.886	0.886	0.886	0.886	0.886	0.886	1.077	0.886	1.077
d	Incident overpressure	P_{so}	MPa	1.515	1.136	1.216	1.330	1.146	1.025	1.157	1.283	0.868
e	Incident impulse	I_s	Mpa.msec					2.546	1.016	1.047		
f	Reflected pressure	P_{ro}	MPa					2.278	7.000	6.645	2.488	2.403
g	Reflected impulse	I_r	Mpa.msec						3.727	3.717		
h	Time of arrival	t_a	Msec						2.033	2.485	2.873	3.789
i	Positive phase duration	t_+	Msec	5.313				3.095		9.288	5.399	5.421
	Rising time	t_r	Msec								2.308	2.093
	Decreasing time	t_d	Msec								3.091	3.328
j	Shock front velocity		m/sec							1112		
k	Peak dynamic pressure	P_d	MPa							1.875		
l	Shock density		kg/m^3							5.198		
m	Decay coefficient									1.016		
n	Ground mat.compounds	*CF= 1.8		crater created	crater created	crater created	crater created	crater created	crater created	crater created	saturated sandy clay	granite
n1	Soil density	ρ	kg/m^3								1920	
n2	Soil seismic velocity	v	m/sec								1524	
o	Peak particle accel.	PPA	m/sec^2								80.339	53.244
p	Peak particle velocity	PPV	m/sec							849.300		

In the case of close-in explosions, a time lag, Δt_A, between the various parts of an incident surface that are loaded by a blast is an important parameter. Such time lag refers to the difference in terms of the arrival time of the blast waves to reach specific parts of a structure. An illustration of time lag calculation on RC column is given in Figure 3.9. Neglecting such time lag may result in a poor approximation of the dynamic response of a structure when subjected to blast loads. A structure with complex geometry, when subjected to blast, may experience multiple blast reflections and rarefactions. The aforementioned empirical equations do not take such phenomena into consideration, as some are not geared to provide predictions of the time of arrival, t_A.

Coping with close-in explosions acting on structures possesing complex geometry, numerical methods could be the solution. The 2D and 3D analysis of Computational Fluid Dynamics (CFD) may provide a better approach than the empirical formulas, in that actual physical model of the structure, no matter how complex it is, can be solved using such methods. The multiple blast reflection, rarefactions as well as the rapid expansion and the formation of blast wave are able to be captured by this method. Therefore, in this study, CFD analysis is carried out using AUTODYN ver.11. A detailed study on the effects of structural configuration on blast loads is reported in Chapter 5.

3.8 Summary

The aforementioned review on the prediction of blast loads by using empirical equations proposed by many researchers shows some significant discrepancies in terms of peak pressure, P_R, calculated. The largest discrepancy appears to be in the calculation of reflected pressures, P_R, up to 3 times. Good agreement was found between results

calculated using the empirical equations proposed by Baker et al. (1983) Kingery and Bulmash (1984).

The empirical equations presented in section 3.7, including those proposed by Kingery and Bulmash (1984), are generally derived for simple structural geometry such as rectangular infilled frame. For structures with complex geometry such as an apartment block with a void deck on the ground floor and infilled frames for the 1st storey and above, such empirical equations may not be applicable for predicting blast loads especially those acting on the interior columns and slabs. The structural layout and configurations needs to be taken into account. Generally, for hemispherical explosions, the empirical equations proposed only consider the effects of two reflective surfaces in the analysis of reflected pressure, P_R, and impulse, I_R, one from ground floor (hemispherical explosion) and the other from the incident face of the structure observed. Multiple reflections result from closely spaced columns and the soffit of the 1st storey slab. In the case of RC apartments with a void deck on the ground floor, numerical analysis of blast propagation using computational fluid dynamics (CFD) methods may be a better approach.

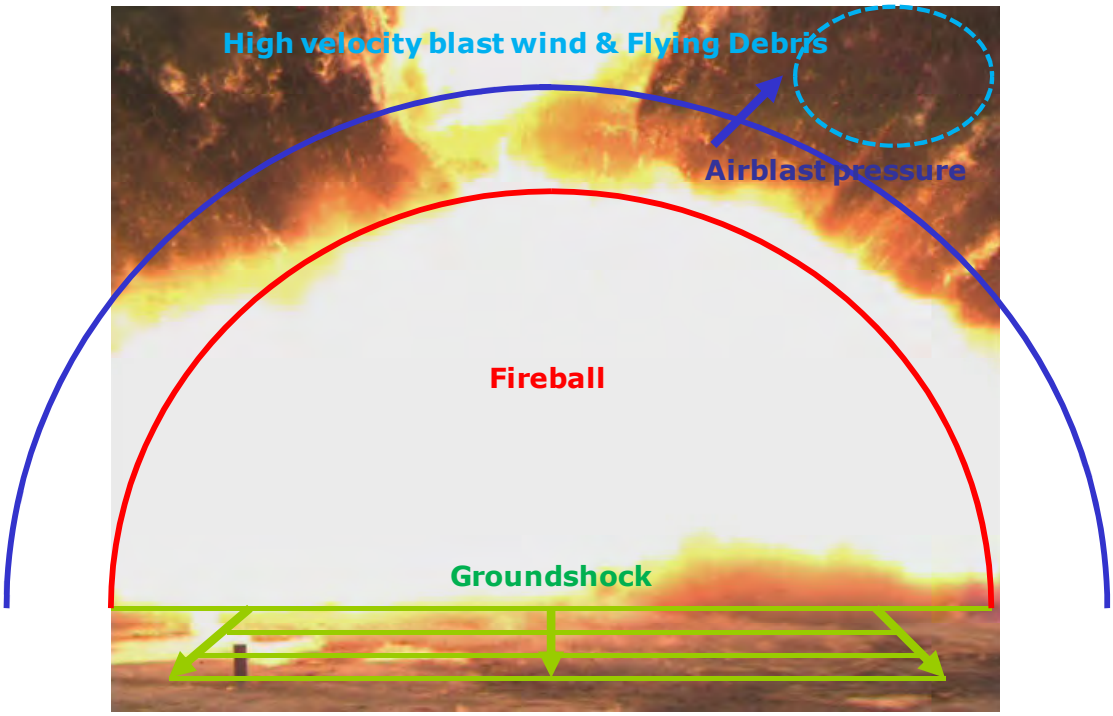

Figure 3.1 Products of explosion (ETSC2008, Courtesy: MINDEF-NUS)

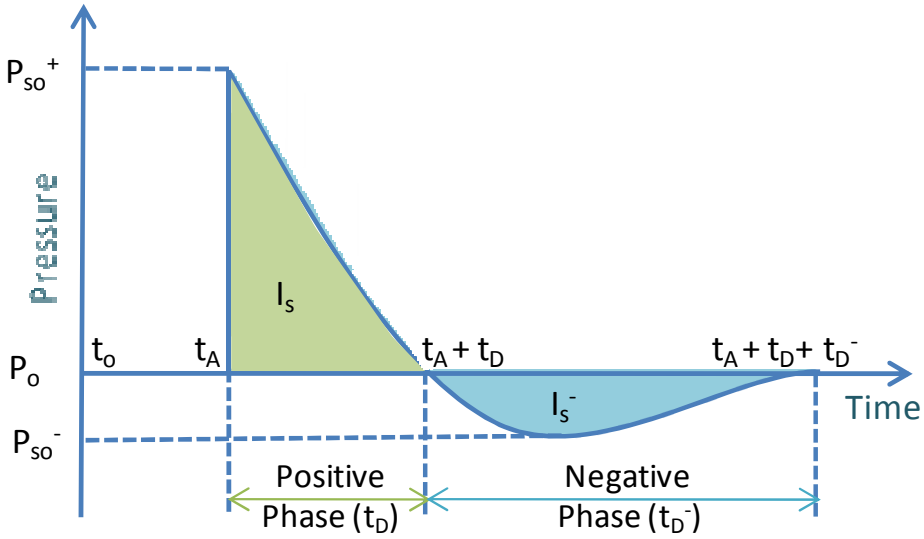

Figure 3.2 Typical blast overpressure time history (TM5-1300)

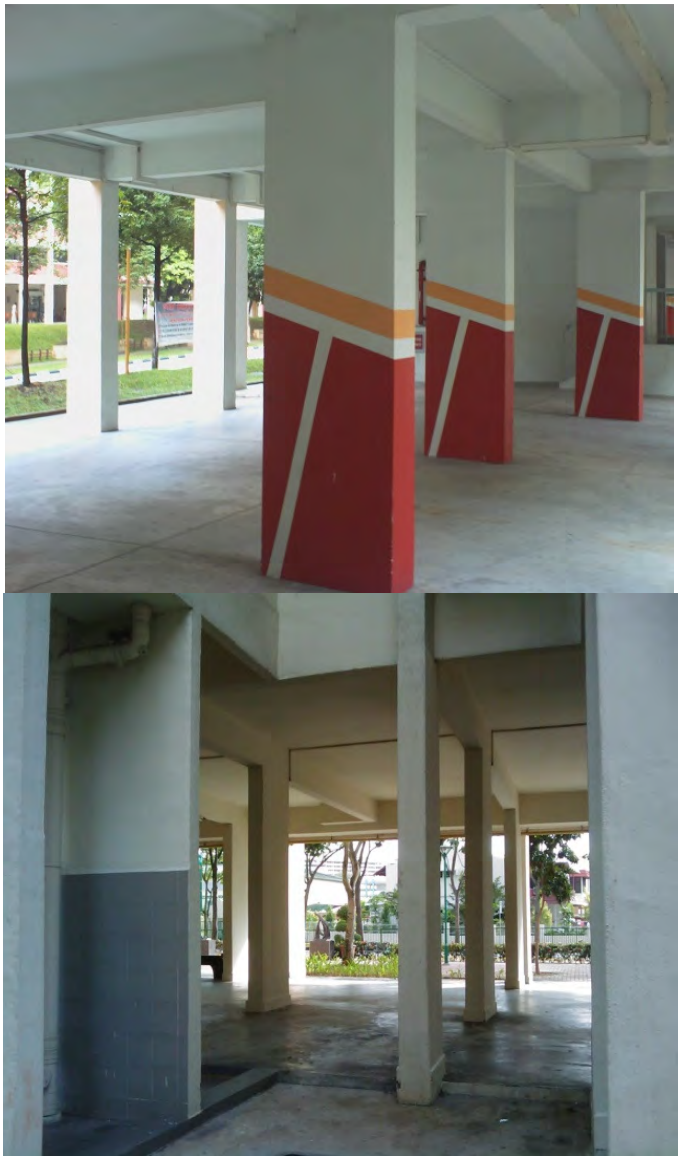

Figure 3.3 Void deck on the ground floor of yypical Singapore's apartment blocks

Figure 3.4 Available stand-off distance on typical Singapore's apartment block

ATF	Vehicle Description	Maximum Explosives Capacity	Lethal Air Blast Range	Minimum Evacuation Distance	Falling Glass Hazard
	Compact Sedan	500 pounds 227 Kilos (In Trunk)	100 Feet 30 Meters	1,500 Feet 457 Meters	1,250 Feet 381 Meters
	Full Size Sedan	1,000 Pounds 455 Kilos (In Trunk)	125 Feet 38 Meters	1,750 Feet 534 Meters	1,750 Feet 534 Meters
	Passenger Van or Cargo Van	4,000 Pounds 1,818 Kilos	200 Feet 61 Meters	2,750 Feet 838 Meters	2,750 Feet 838 Meters
	Small Box Van (14 Ft. box)	10,000 Pounds 4,545 Kilos	300 Feet 91 Meters	3,750 Feet 1,143 Meters	3,750 Feet 1,143 Meters
	Box Van or Water/Fuel Truck	30,000 Pounds 13,636 Kilos	450 Feet 137 Meters	6,500 Feet 1,982 Meters	6,500 Feet 1,982 Meters
	Semi-Trailer	60,000 Pounds 27,273 Kilos	600 Feet 183 Meters	7,000 Feet 2,134 Meters	7,000 Feet 2,134 Meters

Figure 3.5 BATF explosive standard

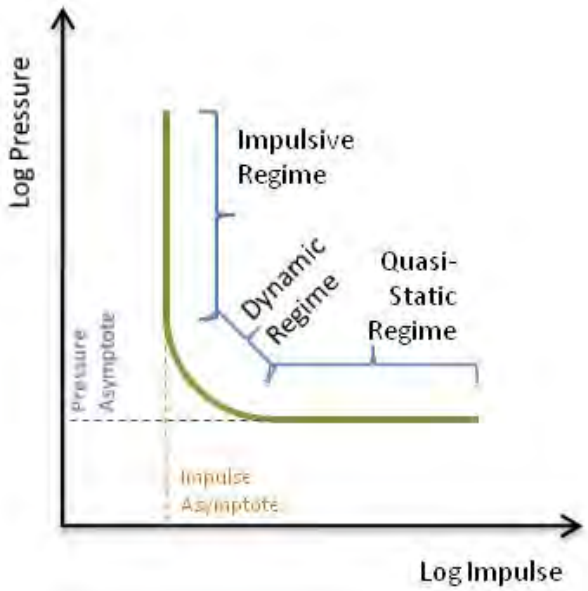

Figure 3.6 Pressure - impulse diagram

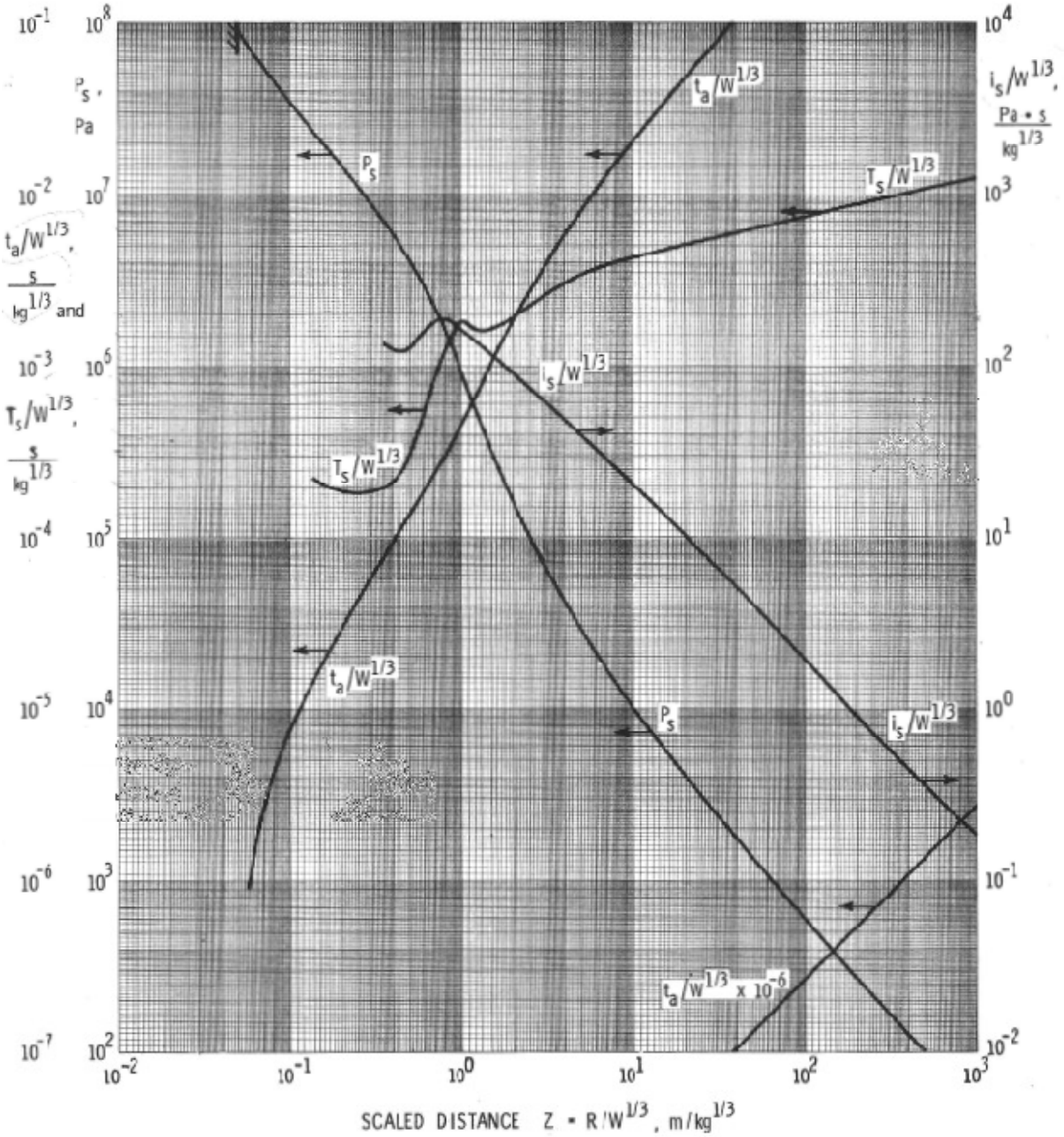

Figure 3.7 Incident wave parameters of blast loads from TNT explosive (Baker et al., 1983)

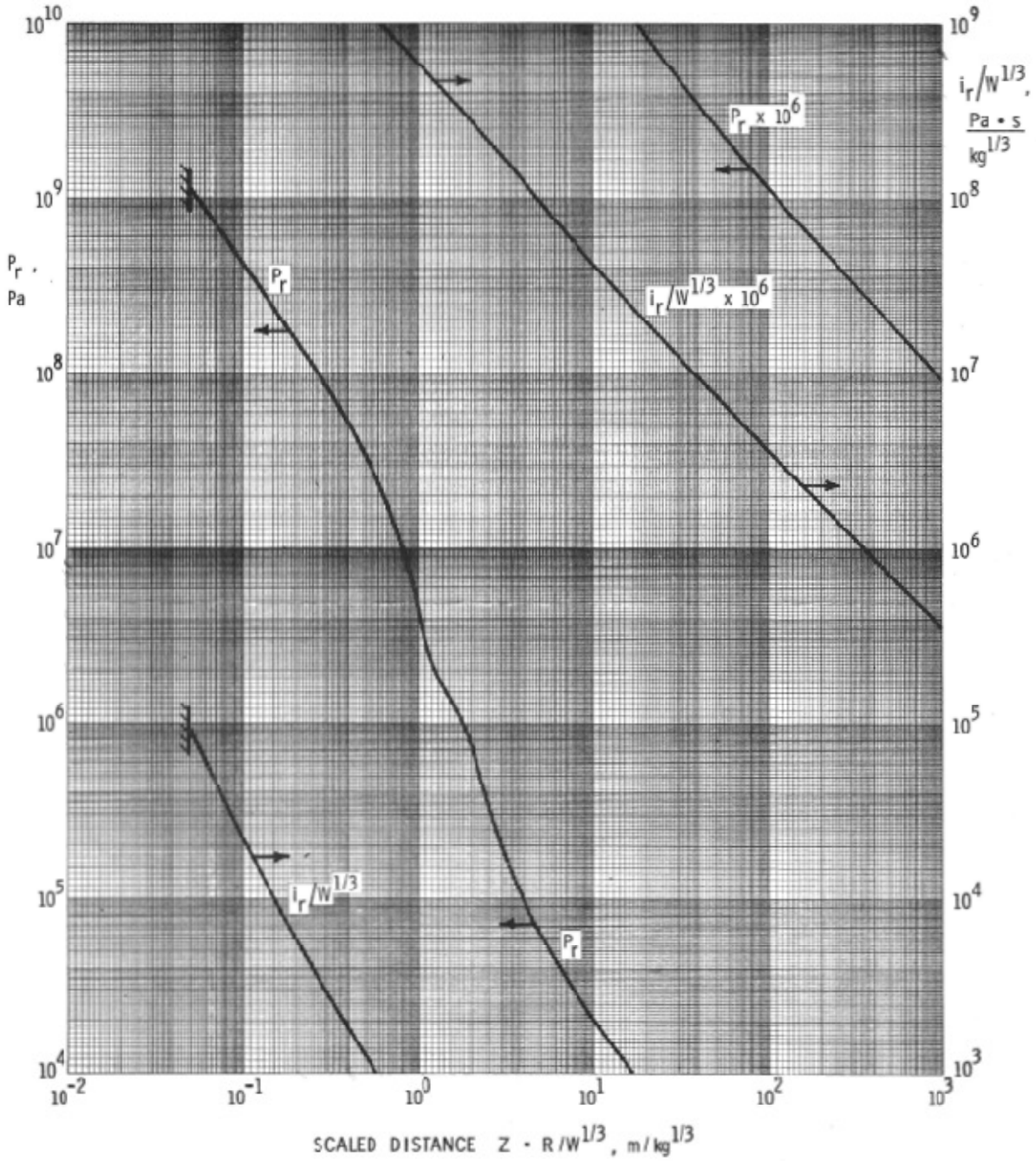

Figure 3.8 Normally reflected wave parameters of blast loads from TNT explosive (Baker et al., 1983)

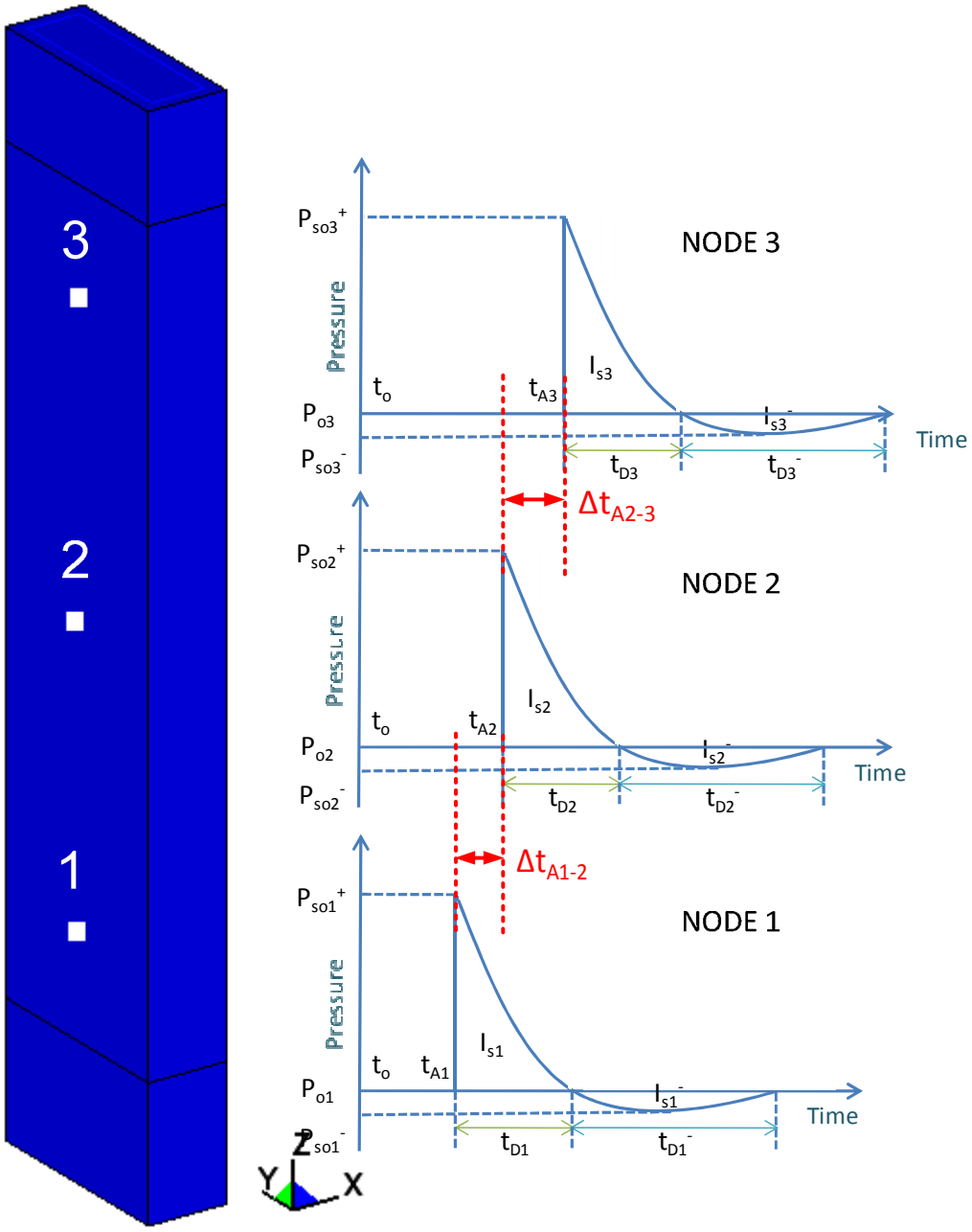

Figure 3.9 Illustration of time lag measurement on column

4 Experiment on Quarter Scale Standalone RC and ECC Encased RC Cantilever Columns

4.1 Introduction

In this chapter, actual blast loading of standalone RC cantilever and ECC encased RC columns conducted under MINDEF-NUS Joint Applied R&D Co-operation Programme are presented. The tests were carried out to further enhance the understanding of the blast performance of standalone RC columns typical of Singapore's apartment blocks and to study the effectiveness of ECC encasement as a potential strengthening method for blast resistance. The main objective of this experiment is to calibrate the results of and provide results for benchmarking against the numerical finite element (FE) study conducted with special focus on the performance of columns with *B/H* ratios exceeding 2.

Once the finite element (FE) model has been validated and the response of the column benchmarked against the experimental results, the response of typical apartment blocks subjected to various possible scenarios of such blast loads that may occur may be studied more comprehensively together with possible ways of mitigating and minimizing the impact of such loads on the structural integrity of such apartment blocks built over the last few decades in various parts of Singapore.

4.2 Background

This present study, as discussed briefly in Chapters 1, 2 and 3, is focusing on the dynamic response of RC ground floor columns typical of Singapore's apartment block comprising a void deck on the ground floor RC infilled frame from the 1st storey onwards. It is understood that the response of a structure depends on the direction of the blast in relation to the column geometry. For a column with a ratio of breadth to width (*B/H*) exceeding 2, its response to blast loads is rather different from one with a *B/H* ratio considerably less than 2. The latter is more commonly reported in available literatures. As the RC columns of typical apartment blocks generally have breadth to depth ratio, *B/H*, greater than two, this study is expected to shed light on the behavior of such columns when subjected to blast loads.

Bearing in mind that the typical apartment blocks are generally are located just next to the carparks, the blast loads considered is typical of explosions caused by vehicle borne improvised explosive device (VBIED) or the so called vehicular bomb located within the available stand-off distance typical of those found in Singapore's apartment block. The available stand-off distance, *R*, and the details of VBIED range of charge weight considered based on various types of vehicles were described in sections 3.3 and 3.4, respectively.

It is realized that if the effects of the close-in blast is severe such columns may be severely damaged which may compromise the structural integrity of the overall structure. Herein, a possible retrofit method via encasing the existing RC columns with a layer of engineered cementitious composite (ECC) is proposed.

Engineered cementitious composites (ECC) have been developed recently for retrofitting and strengthening purpose. It is a kind of cement-based material mixed with short-random fibers that undergoes pseudo strain-hardening instead of softening after the first crack is formed. From dynamic tests under high strain rates, a significant increase in the ultimate tensile strength with increasing strain rate as compared to normal concrete was observed (Maalej et. al, 2005). Recent studies on low velocity (Zhang et. al, 2005, 2007) and high velocity impact (Maalej et. al, 2005) on ECC specimens show that it possesses higher shatter resistance through the production of micro cracks, thus exhibiting better energy absorption. It suffered less damage per impact, retained more energy absorption capacity after multiple impacts and resulted in less debris at failure. Thus, the ECC material may be suitable for use as a protective material against blast loads. The proposed field test also includes RC columns encased in ECC to study their performance vis-à-vis conventional RC columns.

The results of this experimental study would yield valuable information on the performance of default and strengthened columns when subjected to blast loads to study the effectiveness of using ECC as encasement as an effective retrofit solution to mitigate against potential undesirable consequences such as explosions. The results obtained may also provide very useful supplementary information to an earlier study carried out and address some of the issues noted in the earlier study, in particular, direct shear failure at the construction joints of the specimens tested, inadequate restraint at supports and pressure relief around the edges of the test specimens.

4.3 Similitude Requirements of Quarter Scale Model

Theory of scale model has been introduced by Baker et. al. (1991) on dynamic analysis of reduced scale model by using similarity method. Harris and Sabnis (1999), in their book, discussed four components required of similitude requirements on similarity method to relate the scale model to the prototype (full scale) structure, i.e. dimensional and similarity analysis, geometric, loading and resistance conditions. In the present study, all four components of the similarity method for a quarter scale model of RC and ECC encased RC cantilever column are discussed briefly hereafter.

4.3.1 Dimensional and Similarity Analysis

In the physical modeling process in the similarity method, dimensional analysis is crucial in combining parameters into non-dimensional groups (π term) to decide on the parameters to be scaled down. In this study on quarter scale models of RC cantilever columns subjected to blast loads, the parameters considered as a function of displacement referring to the dimensional analysis using the similitude method briefly described in Appendix A are as follows:

- young's modulus, E_C
- column's inertia, $I = f\left(B, H, d', d, A_S, A_S', E_C, E_S\right)$
- column's length, L
- column's depth, B
- pressure and loading duration, $P, t_d = f(W, R)$
- time, t
- mass density, ρ

Since in this study the material parameters are kept the same as the prototype, only geometrical and loading parameters are scaled down. Thus, there are at least 7 parameters that need to be scaled down as shown in Figure 4.1. These are:

a. column's dimensions: breadth (B), width (H) and height (L)
b. reinforcements' detail: longitudinal reinforcements (LR=f (A_s, A_s')) and transverse reinforcements (TR= f (A_v, s))
c. charge weight of the explosive (W)
d. stand-off distance (R) from the location of the explosive charge

The descriptions of each parameter for geometric and loading conditions are given hereafter as a function of scaled factor (S_f) with respect to its respective prototype parameter (X_p).

4.3.2 Geometric Parameters

Herein, the geometries of a prototype are linearly scaled with a factor of S_f and the geometric parameters of the scale model are given as follows:

a. Height : $L_m = S_f L_p$
b. Breadth : $B_m = S_f B_p$
c. Depth : $H_m = S_f H_p$
d. Loading area : $A_{Lm} = S_f^2 A_{Lp}$
e. Cross section area : $A_{cm} = S_f^2 A_{cp}$

4.3.3 Loading Condition

By following a scaled distance concept of Hopkinson Scaling Law (Baker et al., 1991), the loading parameters are given as follows:

a. Scaled distance : $Z_m = Z_p$ (constant)$=R_p/W_p^{1/3}$

b. Blast pressure : $P_m = P_p$ (constant)

c. Total blast force : $F_m = P_m.A_{Lm} = S_f^2 F_p$

d. Loading duration : $t_{Dm} = S_f t_{Dp}$

e. Blast impulse : *(Force × time)*

- for $A_{Lm} = A_{lp}$ $\rightarrow I_m = S_f I_p$
- for $A_{Lm} = S_f^2 A_{lp}$ $\rightarrow I_m = S_f^3 I_p$

f. Resistance Condition

g. Material properties constant : (f_c', f_y)

h. % reinforcement constant : $A_{sm} = S_f^2 A_{sp}$

The scaled distance of the scale model Z_m is kept constant, similar to the loading condition of the prototype structure. Thus, the pressure acting on the scale model is identical to that of the prototype structure, with a scaled impulse.

4.4 Quarter Scale RC Cantilever Column - A Methodology

4.4.1 Design Concept

Based on the aforementioned description of similitude requirements and derivations on dimensional and similarity analyses on RC columns subjected to blast loads, in this experiment, quarter scale models of RC cantilever columns were proposed to be tested. A quarter scale model was chosen to be tested as in the blast experiment, as it allows more flexibility in the investigation of the effects of structure geometry and explosion charge positioning. Also the size selected correspond to the largest size of foundation possible within the limits of budget and transportation, crannage and installation requirements associated with fabrication yard on the main Singapore Island and the offshore test site.

The foundation is designed using the dynamic impulse concept as a shallow foundation block equipped with two shear keys aligned perpendicular to the blast direction to ensure minimal sliding of the foundation under the effects of the blast loads. The shear keys provided were cast monolithically with the foundation block (Figure 4.2) and the whole block is buried with only the column to be tested exposed above ground.

4.4.2 General Configuration

In this experiment, quarter scale RC cantilever columns were tested against close-in explosions. Two, out of four, specimens were encased with an ECC layer on the surface of each column. From the preliminary numerical analysis, based on the range of parameters considered in this study as described in Section 3.5, a combination of bare charge weight W and stand-off distance R equivalent to a scaled distance Z $\left(= R/W^{1/3}\right)$ of 1.08 $m/kg^{1/3}$ was selected. The performance of the default and strengthened RC columns are then compared.

The details of the quarter scale specimens are shown in Figure 4.2. The foundation is of dimension 2m x 2m with a depth of 1 m depth. The shear keys are 1.5 m deep. The shear keys were orientated perpendicular to the blast direction, parallel to the incident face of the column. The cross-sectional dimensions of column are of dimension 200 mm x 75 mm and of height 0.75 m. To provide fixity, the longitudinal reinforcement extends 1 m into the foundation. Out of four column specimens, two were encased by an ECC layer of 10 mm thickness. Longitudinal steel reinforcement provided (8T10) is as shown in Figure 4.3. Meanwhile the transverse reinforcement (2T6) is spaced 50 mm apart for the above ground portion of the column and 100 mm apart for the embedded portion of the column as shown in Figure 4.4.

In order to locate the instrumentations at the desired locations, an instrumentation stand is positioned directly behind the column specimen. The instrumentation stand was first designed as a steel-truss system, placed behind the column. However, the design was changed to a steel C channel 125x65x6. The purpose of using C channel is to enable the blast to engulf the whole section of the C channel. This minimizes the residual lateral load acting on the C channel. Several plate stiffeners were welded on the C channel at nominal intervals of 150 mm for buckling resistance.

4.4.3 Materials

The specimens comprised four materials: concrete, mortar, steel and ECC. Foundation was cast with concrete (30 MPa) ordered from Pan-United Concrete Pte Ltd. , a ready mix concrete supplier, consisting of cement paste, sand, coarse aggregate, water and superplasticizer Adva 181. The foundation is not the focus of attention as long as it is able impart fixity at the base of the column.

The column protruding from the foundation was cast using mortar mixture. Before construction, several trial mixes as shown in Table 4.1 were tested to achieve the desired mortar cylinder strength of 30 MPa. Since the column specimen is a quarter-scale model, mortar mix was chosen to replace the concrete in order to scale down the maximum aggregate size used. The maximum aggregate size is therefore around 6 mm achieved using sieved sand.

The hybrid fiber ECC composite used consist of 2% fibers and a mix proportion of 1 : 0.11 : 0.013 : 0.28 of cement, silica fume, SP and water. Two types of fibers were used herein, high modulus steel fibers (0.5%) and relatively low modulus PE fibers (1.5%), in

order to achieve the desired balance between the ultimate strength and the strain capacity for ductility purpose. The cube, compressive cylinder test and direct tensile test results of the ECC are shown in Table 4.2 and Figure 4.5.

Table 4.1 Trial Mix Design of Mortar

Trial Mix	Age (days)	Water / Cement Ratio	Cement/ Sand Ratio	Cube Test		Cylinder Test	
				fcu (MPa)	average	fc' (MPa)	average
A	3	0.50	0.25	27.9	28.5	26.7	27.3
				28.4		28.1	
				29.1		27.1	
	7	0.50	0.25	34.7	32.8	34.3	34.3
				29.6		33.6	
				34.0		35.1	
	28	0.50	0.25	36.6	38.4	30.3	27.2
				45.2		23.6	
				33.5		27.7	
B	3	0.50	0.33	21.6	23.3	10.1	10.0
				25.1		9.7	
				23.3		10.4	
	7	0.50	0.33	30.3	30.4	21.4	21.9
				29.8		22.0	
				31.1		22.2	
	28	0.50	0.33	35.6	35.6	27.8	27.1
						26.4	
				Split cylinder test = 2.9			
C	3	0.50	0.286	25.5	26.5	13.0	14.2
				26.2		14.4	
				27.7		15.1	
	7	0.50	0.286	33.1	32.7	29.6	29.8
				31.3		31.0	
				33.6		29.0	
	28	0.50	0.286	35.5	39.3	37.2	38.3
				41.9		39.4	
				40.5			
				Split cylinder test = 4.1			
D	3	0.485	0.286	21.2	21.9		
				22.1			
				22.5			
	7	0.485	0.286	29.8	30.7		
				31.6			
				30.8			
E	3	0.485	0.278	28.9	29.0		
				29.2			
	7	0.485	0.278	37.6	35.1		
				32.4			
				35.4			

Table 4.2 Uniaxial Compressive Test of ECC

Specimen		
Age	Cube	Cylinder
	f_{cu}	f_c'
days	MPa	MPa
7	56.09	52.65
14	65.92	56.28
17	72.50	60.15
28	71.73	63.11

4.4.4 Construction Methodology

Fabrication of the test specimens was carried at the contractor's site. The foundation of each column (Figure 4.6a) was first cast with a rectangular void reaching the full depth of the foundation, formed using styrofoam strengthened by thin plywood (Figure 4.6c), to accommodate the above ground column to be cast later. The required amount of longitudinal reinforcement projected from the foundation to ensure continuity of the column's longitudinal reinforcement at the column base, thus ensuring adequate resistance against direct shear failure when acted on by the blast.

The second stage was to construct the column as shown in Figure 4.7. The column was 1.75 m in height.

The third stage, only for ECC encased RC specimens, is to encase the two columns with a 10 mm thick ECC layer (Figure 4.8). The details on the method of application of ECC layer are given in section 4.4.5.

4.4.5 Methods of Application of ECC Layer

On the front surface of the column facing the blast, the ECC layer is recessed 200 mm into the foundation at the base of the column as shown in Figure 4.9. This was allowed for during casting of the foundation, formed using 10 mm thick Styrofoam. The intention is to ensure fixity of the ECC layer applied at the base of the column. Before the ECC layer is applied onto the column, all the four surfaces of RC column was poured by water to eliminate the occurrence of creep due to water absorption of the dry RC column surface from the ECC mix. The 10mm thick ECC layer containing dispersed fibers was then applied vertically (manual) onto the surfaces of RC cantilever columns as shown in Figure 4.9.

4.4.6 Transportation and Installation

A trailer truck and a barge were needed to transport the four specimens from the contractor's site to the offshore test site. Since each of the specimen weigh around 13 tons, a heavy duty crane is needed for lifting the specimens as shown in Figure 4.10.

On the test site, the foundation was buried in pits excavated using excavator. Firstly the 3 m x 3 m pits were excavated (Figure 4.11), 1 meter wider than the foundation for positioning purpose. The specimen was then aligned using the lifting crane to its final position after which the excavation was backfilled and compacted as shown in Figures 4.12 and 4.13.

4.5 Instrumentation

Several sensors consisting of concrete and steel strain gauges, accelerometers, potentiometers, and radio antenna were installed. The sensors, except strain gauges on the

steel rebars were located at the desired positions on the distal face of the column as summarized in Table 4.3 and shown in Figure 4.14.

Table 4.3 Location of Instrumentation

No.	Type of Strain Gauge	Location	Minimum Channels	
			Amount	Total Amount
1	Concrete Strain Gauge	L	1	2 MC
		1/2 L	1	
2	Steel Strain Gauge	Base – 1	1	2 MC
		Base – 2	1	
3	Potentiometer	L	1	2 MC
		1/2 L	1	
4	Accelerometer	L	1	1 BNC
Total channels needed per specimen				6 MC, 1 BNC

Except for the accelerometer, the physical setting up of all sensors was done by the NUS team. Meanwhile, connection settings between the sensors and data acquisition system (DAQ), connectivity and configuration checking of DAQ-sensor response and provision as well as configuration of DAQ during the tests were done by Singapore Technology Kinetics (ST Kinetics).

The instrumentation stand as shown in Figure 4.15 was constructed directly behind the column to mount the potentiometer sensors and radio antennas. Meanwhile, to prevent the cables from direct exposure to the fire ball and airblast pressure and to eliminate disturbance of signal readings, the cables are housed in two PVC pipes cast into the foundation. Both extend all the way from the middle to the edge of the foundation. The PVC pipes are shown in Figure 4.15.

4.5.1 Strain Gauges

Two types of strain gauges were used: concrete and steel strain gauges. Two steel strain gauges of type YFLA 5 (15-20%) 120Ω from TML were installed on the longitudinal reinforcements at the base of the column's distal face for the purpose of measuring the strain in the steel reinforcement. The steel strain gauges were installed before casting of the column. In order to protect the steel strain gauge from damage due to concrete pouring, coating with an epoxy layer was provided.

Two concrete strain gauges of type PFL 30-11 120Ω from TML were installed at the tip and at mid height on the column's distal surface. To prevent the concrete strain gauge from damage, an epoxy coating was applied over its surface. Shielded vinyl lead wire cables (3mm dia 3 cores) were used to connect the strain gauges to the data logger.

4.5.2 Accelerometer

One PCB 350B04 shock ceramic ICP accelerometer of $\pm$ 5g provided by ST Kinetics was attached at the tip of each specimen. The intention is to measure acceleration at the column tip to obtain the displacement. The displacement obtained can later, be evaluated and benchmarked against results obtained from potentiometer and radio antenna

4.5.3 Potentiometer and Radio Antenna

Two potentiometers S 13 FLP 100A 5KΩ were mounted on each specimen, at the tip and at mid height of specimen's distal face, to obtain the displacement time history. Overall shielded 24AWG cables (4 cores) by Farnell were used to connect the potentiometer to the data logger. As a backup, the radio antenna was mounted at each column tip, to measure the maximum static displacement of the column due to the blast load.

4.6 Results and Discussions

The experiments went well and the four specimens as summarized in Table 4.4 were tested successfully. As explained earlier, each specimen was subjected to close-in blast loads of scaled distance Z equals to 1.08 $m/kg^{1/3}$. The arrangement of the explosive charges is shown in Figure 4.16.

Table 4.4 Quarter Scale Columns of Size 200x75mm

Specimen	Type of Encasement	Thickness of Encasement, t	Column Axis	Scaled Distance, Z
Q-ABCt-MI/MA		t	MI/MA	1.08 $m/kg^{1/3}$
Q-UC-5-MI	-	-	Minor	
Q-UC-5-MA	-	-	Major	
Q-ECC10-5-MI	ECC	10 mm	Minor	
Q-ECC10-5-MA	ECC	10 mm	Major	

The first explosion was for testing the RC and ECC encased RC cantilever specimens aligned with their minor axis parallel to the blast direction and labeled as Q-UC-5-MI and Q-ECC10-5-MI, respectively. For the second blast, the Q-UC-5-MA and Q-ECC10-5-MA specimens were aligned with their major axis parallel to the blast direction. However, for the two explosions, the instrumentation data retrieval system did not work properly due to malfunctioning of the trigger system. Thus, the only data recorded was the back-up data, which seemed rather unreliable, e.g. the recorded acceleration data registered a shape similar to that of the pressure data. The only useful data extracted is the residual displacements which are measured manually on site. The latter was confirmed using digital image analysis of the images captured using a high resolution digital camera.

4.6.1 Minor Axis Study

In the first round, two specimens were tested against scaled distance Z of 1.08 $m/kg^{1/3}$ aligned parallel to the column's minor axis. As observed in Figure 4.17, the Q-UC-5-MI specimen virtually collapsed in the bending mode. Also as noted in Figure 4.17b it seemed to have experienced some torsion. This was due to the much larger deformation occurring on one side of the column causing it to rest against the instrumentation stand behind the column. Not only had the airblast pressure hit the column façade, evidence of impacts from soil debris was clearly visible. Figure 4.16b shows clearly the evidence of soil debris impact on the exposed steel reinforcement after the blast test.

Meanwhile, the Q-ECC10-5-MI specimen still stood (Figure 4.18) after the blast, although large deformation had occurred. Figure 4.18 shows that, although delamination and gouging were observed at the sides and at the front face of ECC encasement layer, the application method of ECC layer by recessing it to a depth of 200 mm into the foundation works well, resulting in a higher blast resistance as compared to the default Q-UC-5-MI specimen. Herein, ECC is found to have several functions as follows,

a. provides additional confinement to the concrete resulting in higher blast resistance
b. enhances energy dissipation through multiple cracking
c. prevents concrete from spalling and crushing
d. affords some protection against high velocity debris propelled along by the blast.

The overall increase in size of the column also contributes to the enhancement in performance of the Q-ECC10-5-MI specimen as compared to that of the default Q-UC-5-MI specimen. The increase in column size results in a higher moment of inertia and larger

flexural moment capacity. The effect of an increase in column size will be dealt with more fully in Chapter 8.

4.6.2 Major Axis Study

The second round was to test the Q-UC-5-MA and Q-ECC10-5-MA specimens with blast loads orientated parallel to column's major axis. As compared to the first round test directed along the column's minor axis, the structure is now stronger due to the larger moment of inertia and has smaller loading area.

After the blast, as shown in Figure 4.19, there was no significant damage on the Q-UC-5-MA specimen except for localized spalling of concrete cover at some corners and localized gouging of the front face due to impact from high velocity debris propelled along by the blast. From the observation of the Q-ECC10-5-MA specimen (Figure 4.20), ECC is found to provide several enhancement effects i.e. act as a protective layer against delamination of concrete cover and localized gouging, and provide additional confinement to the concrete resulting in better performance against blast loads. The size of the column is also increased as mentioned previously in section 4.6.1.

4.6.3 Instrumentation Reading

During the two tests, unfortunately, the data acquisition system of the instrumentation sensors did not work properly due to malfunctioning of the triggering device of the data acquisition (DAQ) system. Thus, data recorded was only the back-up data, which seemed to be unreliable. The recorded data plots were summarized in Figures B1 to B12 in the Appendix B.

The only useful data is the residual and maximum displacements that are measured manually on site. The maximum displacement is determined by the change in length of the radio antenna (static measurement). The residual displacement is determined by measuring the distance between the column tip of the initial profile having perpendicular direction to the slab with the deformed column profile, confirmed using digital image analysis of the images captured using a high resolution digital camera as summarized in Table 4.5. The manual measurement of specimens loaded parallel to its major axis (Q-UC-5-MA and Q-ECC10-5-MA) was difficult due to the significant effects of localized spalling and gouging relative to the displacement measured which is very small.

Table 4.5 Summary of Residual and Maximum Displacements Obtained

Specimen	δ residual (mm)		δ max (mm)
	DIA	Manual	Manual
Q-UC-5-MI	Collapsed		
Q-ECC10-5-MI	83.4	84	150
Q-UC-5-MA	10.9		
Q-ECC10-5-MA	9.1		

Digital Image Analysis (DIA) was performed on several images captured as shown in Figure 4.21. The DIA calculations as given in Table 4.6 is based on pixels measurement using Image Pro Plus software and distances as well as geometries that have been measured before the blast.

The residual and maximum displacements obtained will be used to benchmark against the numerical results obtained from FE codes and the analytical solution using Equivalent SDOF system.

Table 4.6 Digital Image Analysis for Displacement and Geometry Measurement

Specimen	Image	Image Point of View (Taken From)			Condition (Before / After)	Geometric Measurement using Image Analysis (Pixels)							
						Upper Measurement				Bottom Measurement			Notes
		L/R Side Facing Blast	U/M	F/M/B		T1	T1'	T2	T3	B1	B2	B3	
NC1	IMG 2055	Right	Upper	Back	Before	236.0	259.8	568.5	464.3	248.5	470.9	416.5	
	IMG 2063	Right	Upper	Front	After	C R U S H E D							
EC1	IMG 2053	Right	Middle	Back	Before	292.2	359.4	599.9	489.7	278.0	569.8	466.4	
	IMG 2070	Right	Upper	Middle	After	437.1	400.2	298.1	513.1	342.3	513.0	412.0	
NC2	IMG 2203	Right	Upper	Front	Before	483.5		335.3		464.9	344.8		Rotated 30 degree
	IMG 2235	Left	Middle	Middle	After	877.0		659.0	566.0	852.4	635.3	532.2	Rotated 0 degree
EC2	IMG 2209	Right	Upper	Front	Before	650.0		378.0		677.2	400.7		Rotated 20 degree
	IMG 2212	Left	Upper	Middle	After	832.1		462.1	448.9	776.4	470.2	431.2	Rotated 15 degree

Specimen	Image	Geometric Dimensions			Condition (Before / After)	Simple Calculation						Checking (T3=B3=125 mm)				
						Upper		Bottom		Δ = B2-T2	Displa-cement	T3	B3	Errors		
		B or H	L	H steel		(B or H)/T1	T2	(B or H)/B1	B2					eT3	eB3	Average
		(mm)	(mm)	(mm)		(mm)	(mm)	(mm)	(mm)	(mm)	(mm)	(mm)	(mm)	(mm)	(mm)	(mm)
NC1	IMG 2055	75	775	125	Before	E M P T Y										
	IMG 2063	75	775	125	After											
EC1	IMG 2053	95	750	125	Before											
	IMG 2070	95	750	125	After											
NC2	IMG 2203	200	765	125	Before	0.4	138.7	0.4	148.3	-9.6	10.9					
	IMG 2235	200	765	125	After	0.2	150.3	0.2	149.1	1.2		129.1	124.9	4.1	-0.1	2.1
EC2	IMG 2209	225	785	125	Before	0.3	130.8	0.3	133.1	-2.3	9.1					
	IMG 2212	225	785	125	After	0.3	124.9	0.3	136.3	-11.3		121.4	125.0	-3.6	0.0	1.8

Specimen	Image	Geometric Dimensions			Condition (Before / After)	Simple Calculation						Checking		Analysis		
						Upper		Bottom		Δ = B2-T2	Displa-cement	T1'	Errors			
		B or H (mm)	L (mm)	H steel (mm)		H steel/T3 (mm)	T2 (mm)	H steel/B3 (mm)	B2 (mm)	(mm)	(mm)	(mm)	eT1' (mm)	U/M	F/M/B	Notes
NC1	IMG 2055	75	775	125	Before	0.3	153.1	0.3	141.3	-11.7		72.6	2.4		Back	L back > L front
	IMG 2063	75	775	125	After	C R U S H E D									Front	L front > L back
EC1	IMG 2053	95	750	125	Before	0.3	153.1	0.3	152.7	-0.4	83.4	94.3	-0.7	Middle	Middle	L front ≈ L back
	IMG 2070	95	750	125	After	0.2	72.6	0.3	155.6	83.0		97.5	2.5	Upper		H top > H bottom
NC2	IMG 2203	200	765	125	Before	E M P T Y								Middle		H top ≈ H bottom
	IMG 2235	200	765	125	After											
EC2	IMG 2209	225	785	125	Before											
	IMG 2212	225	785	125	After											

4.7 Summary

It is clear that RC columns having B/H>2 is more vulnerable when subjected to close-in blast loads in the direction parallel to its minor axis. This vulnerability may translate into localized failure of the individual column when subjected to blast loads. The way the individual column responds to the blast load may trigger undesirable response from adjoining structural elements and may compromise the structural integrity of the overall structure.

As mitigation against loss of structural integrity, some strengthening may be needed. One possible strengthening method is by encasing the column with ECC layers. The method of application and application details, e.g. recessing the ECC layer 200 mm deep into the column base performed well. The method significantly increases the column's strength and encased columns did not show signs of collapse. The ECC layer:

a. increase the size of the column
b. provides additional confinement to the concrete resulting in higher blast resistance
c. enhances energy dissipation through multiple cracking
d. prevents concrete from spalling and crushing
e. affords some protection against high velocity debris propelled along by the blast.
f. acts as a protective layer against delamination of concrete cover and localized gouging

The results obtained experimentally will be used to benchmark against those obtained through numerical analysis carried out using LS Dyna FE codes. Equivalent SDOF analysis is performed analytically incorporating the step by step integration method.

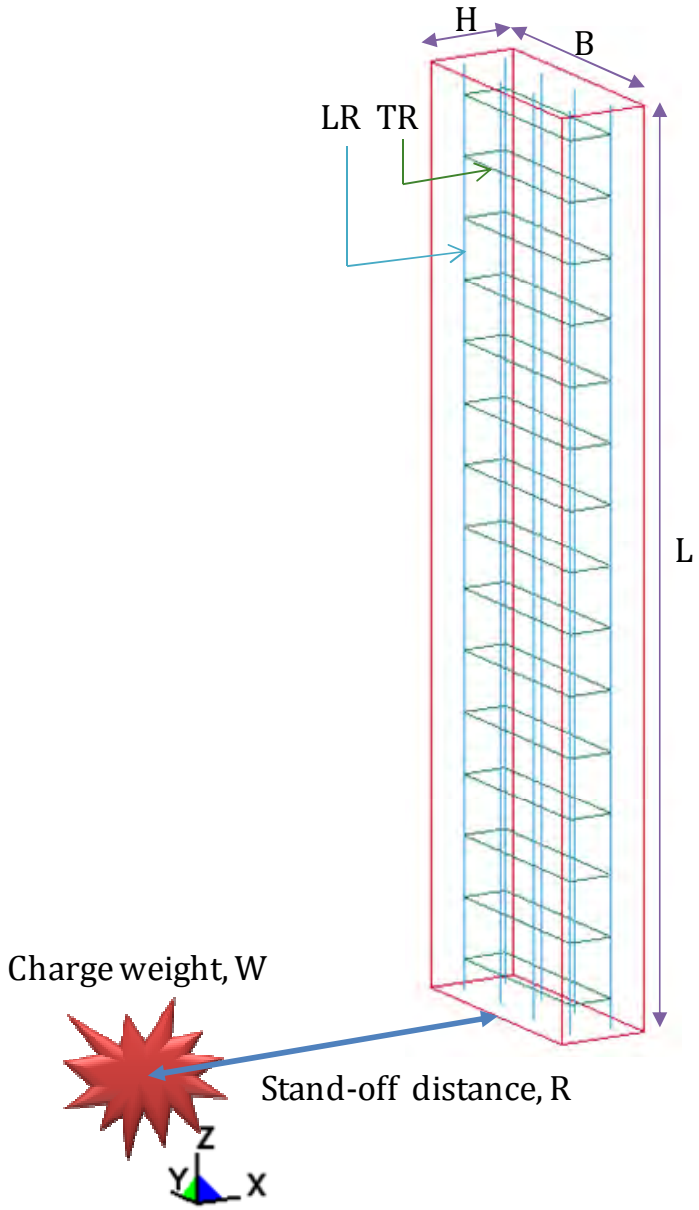

Figure 4.1 Illustration of independent parameters

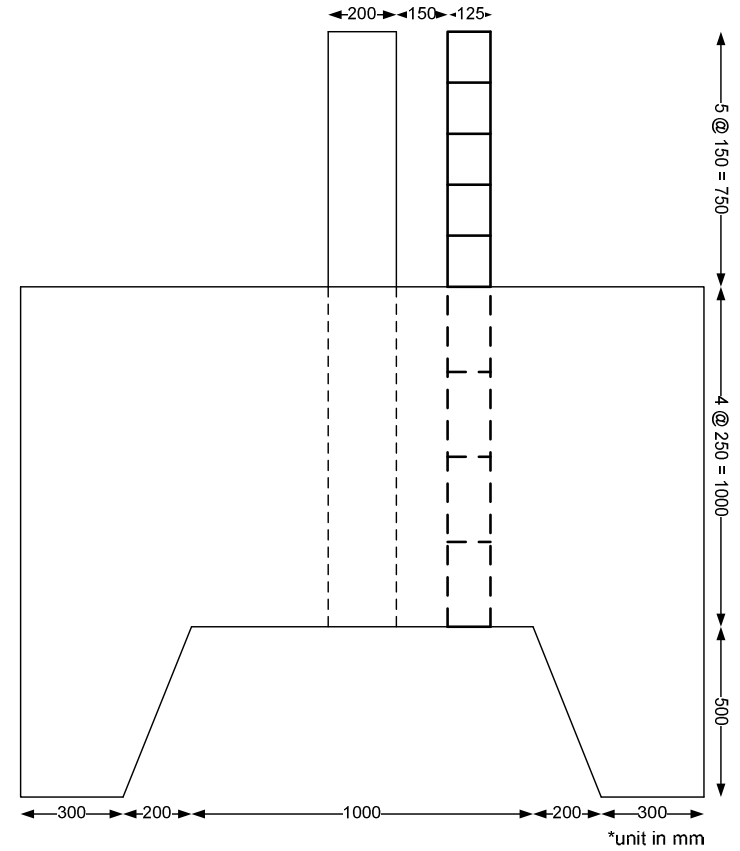

(a)

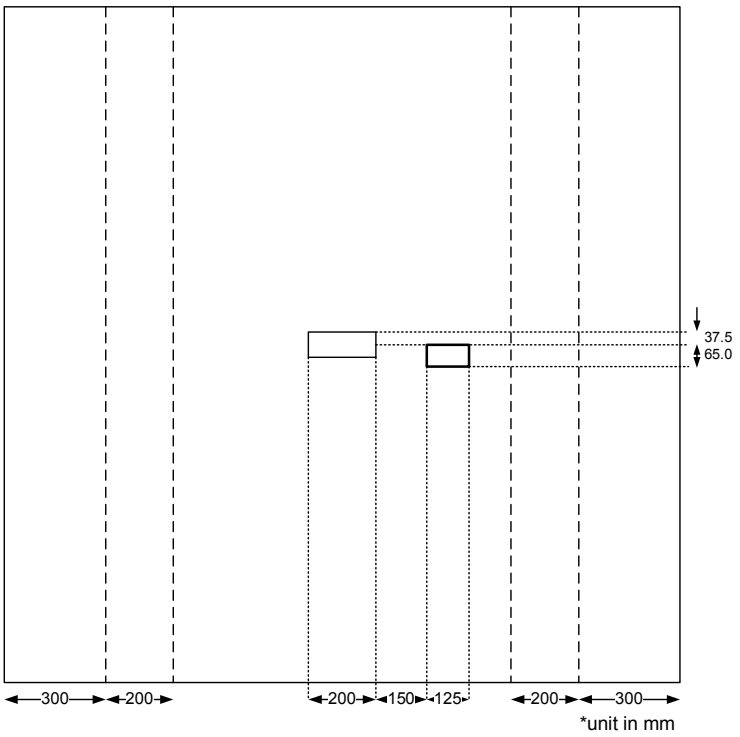

(b)

Figure 4.2 Quarter scale specimen (a) Side view (b) Plan view

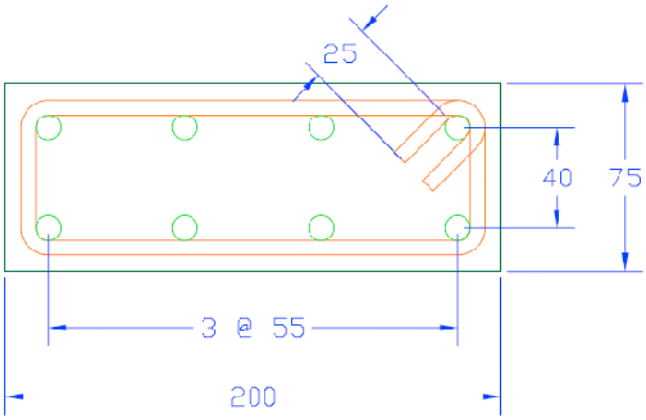

Figure 4.3 Cross section of quarter scale RC column

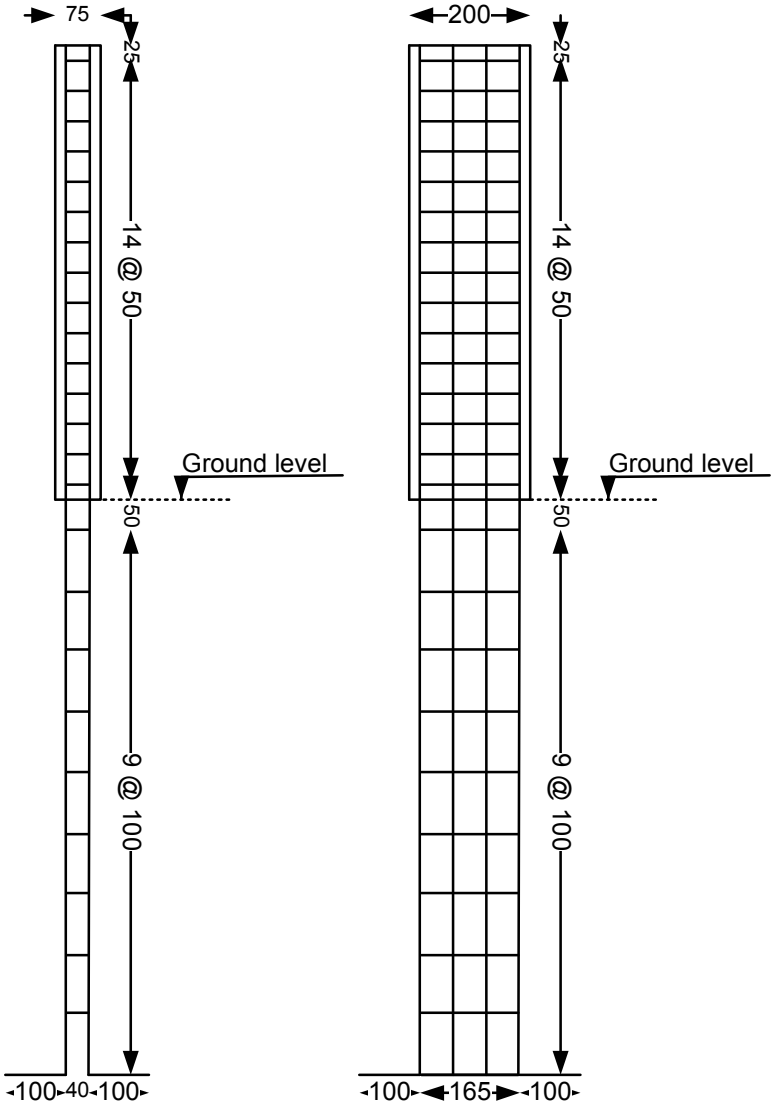

(a) (b)

Figure 4.4 Side view of RC column (a) Minor axis view (b) Major axis view

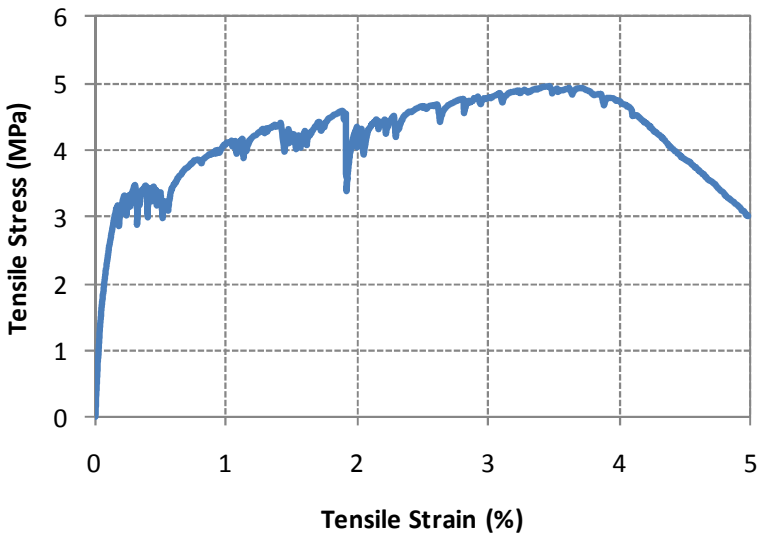

Figure 4.5 Direct tensile stress-strain curve of ECC of f_c=55MPa

(a) (b) (c)

Figure 4.6 Construction of foundation (a) Foundation reinforcement (b) Formwork (c) Column stopper

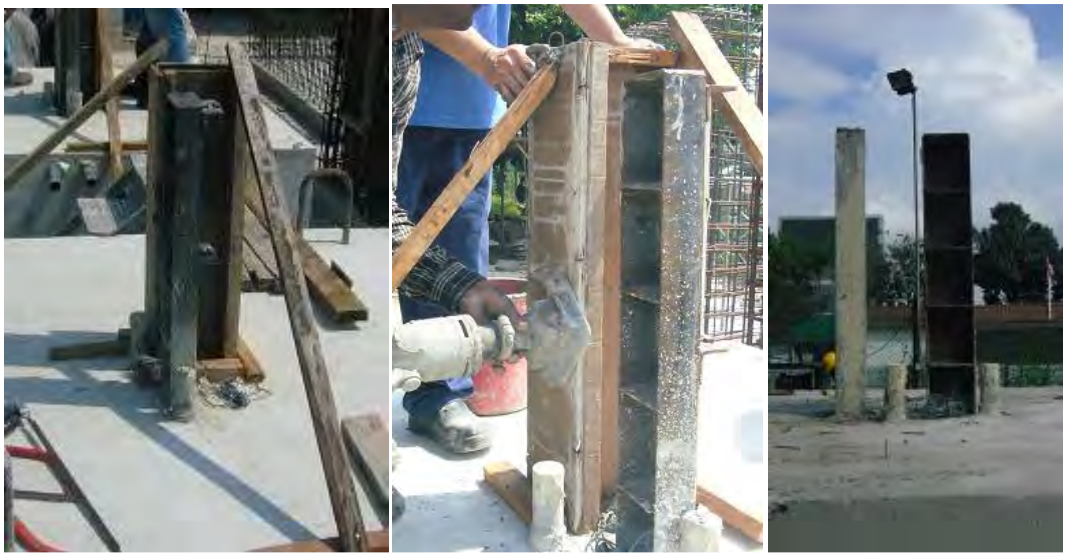

(a) (b) (c)

Figure 4.7 Construction of column, (a) Formwork (b) External vibrator (c) Hardened column

(a) (b)

Figure 4.8 ECC layering (a) Process (b) Final condition

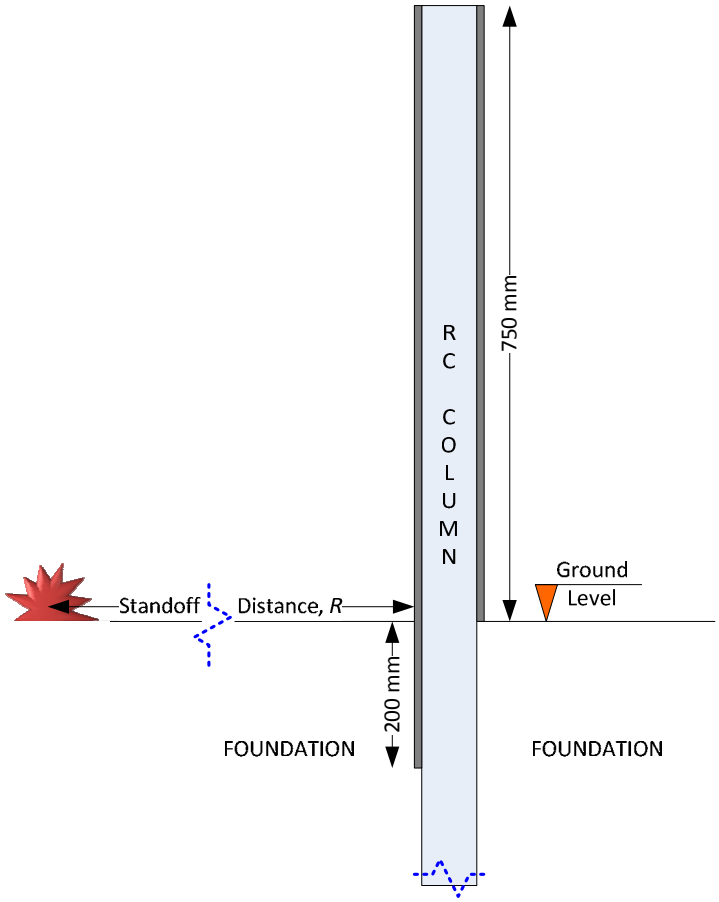

Figure 4.9 Method of application of ECC layer

Figure 4.10 Transportation

Figure 4.11 Soil excavations for foundation part

(a) (b)

Figure 4.12 (a) Installations and (b) Positioning of specimens on site

Figure 4.13 Backfilling and compaction of soil

Figure 4.14 Instrumentation

Figure 4.15 PVC pipes positioning

Figure 4.16 Explosives arrangement

(a) (b)

Figure 4.17 Q-UC-5-MI specimen (a) Before (b) After explosion

(a) (b)

Figure 4.18 Q-ECC10-5-MI specimen (a) Before (b) After explosion

(a)

(b)

Figure 4.19 (a) Q-UC-5-MA and (b) Q-ECC10-5-MA specimens after explosion - Plan view

(a)

(b)

Figure 4.20 (a) Q-UC-5-MA and (b) Q-ECC10-5-MA specimens after explosion - Front view

Figure 4.21 Images used in digital image analysis for geometry and displacement measurement

Effects of Structural Layout and Configuration on Blast Propagations

5

5.1 Introduction

Besides natural field tests, blast loads acting on structures may be studied via empirical and numerical methods. Field tests are expensive and require much time and effort, aside from safety issues that must be addressed and planned for. The results obtained are however, reliable only for the actual configuration that was being tested. The empirical method utilizes results from field tests for correlation to arrive at empirical equations and with more parameters considered may provide useful guidelines for design purposes. A number of empirical equations have been proposed earlier (Sadovskyi, 1952, Brode, 1955, Naumenko and Petrovskyi, 1956, Henrych, 1979, Baker et al., 1983, Kingery and Bulmash, 1984, Siddiqui and Ahmad, 2007, Wu and Hao, 2007) as presented in Chapter 3. Similarly, although such equations are accurate when applied specifically to the respective cases reported by individual researchers, the accuracy, however, may be diminished when applied to other scenarios. On the other hand, numerical methods involve the solution of a set of partial differential equations (PDEs) which govern the flow field of the blast waves using computational fluid dynamics (CFD). This method overcomes some of the limitations of the experimental and empirical methods as it is applicable for a diverse range of situations and scenarios.

Numerous studies on the effects of structural layout and configuration on blast propagation have been carried out by many researchers both experimentally and numerically. However, such studies are generally limited to rectangular standalone structure or rectangular buildings in city streets model. As far as the author is aware, none has dealt with structures with a void deck on the ground floor. Herein, a numerical approach based on computational fluid dynamics (CFD) to study the effects of a blast on a typical apartment block with a ground floor void deck is carried out using ANSYS AUTODYN ver.11.

In this chapter, the numerical technique incorporated into AUTODYN is briefly described. In order to verify the numerical approach applied, experimental data from available previous studies (Chapman et al., 1995, Lan et al., 1998, Woodson and Baylot, 1999, and Watson et al., 2006) are reviewed. Moreover, a simplified approach proposed by Remmenikov (2003) for predicting bomb blast effects on building is also evaluated.

5.2 Numerical Methods and Element Formulations

5.2.1 Numerical Methods

Typically, the numerical methods incorporated to simulate blast propagations and dynamic responses of structure are based upon finite difference, finite volume or finite element approaches by utilizing the explicit time integration (Šoln, 1996). Another numerical method available is known as the boundary element method (BEM).

Finite difference method (FDM) is used to solve the partial differential equations (PDEs) by discretizing the problem's domain, dividing the domain into a uniform grid and

replacing the derivative equations with a series of equivalent difference quotients namely finite difference equation. It makes use of either embedded boundary or overlapping grids for handling complex geometries to ensure its efficiency and accuracy. Forward difference and central difference equations are generally used to solve the explicit problems.

In the finite volume method (FVM), the governing equations are solved on discrete volumes within a meshed geometry. Such discrete volume refers to a small volume surrounding each node on a mesh. In the finite volume method, integrals of volume in a PDE that contain a divergence term are converted to surface integrals using the divergence theorem. The average values of a function over local mesh cells (discretized volume) are taken as unknowns while the discrete approximations of the divergence, gradient and the operators are defined using the general form of Navier-Stokes theorem. This method is easily formulated to allow for unstructured meshes and is generally applicable for solving computational fluid dynamics (CFD) problems as it is sensitive to distorted elements which can cause non-convergence if such elements are in the critical flow region.

The finite element method (FEM) may be used to solve the PDEs by discretizing the structural domain into smaller region/element of finite dimensions known as Finite Element in which the PDE are approximately solved. The elements are locally connected by a finite numbers of joint called Nodal Points/Nodes. Since the continuity is ensured at each node, the matrices of FEM are typically banded. Thus, the storage requirements for computational analysis follow a linear function with respect to the problem size. In terms

of stability and robustness of the solution, FEM is better although a larger memory size is needed vis-a-vis FVM (Huebner et al, 1995).

The boundary element method (BEM) is used to solve PDE by formulating integral equations. Such equations may be regarded as an exact solution of the governing PDE. The BEM attempts to use the given boundary conditions to fit boundary values into the integral equation, rather than fitting the boundary values throughout the space defined by PDE. For problems having a small ratio of the area over volume, BEM is computationally more efficient than other methods. Otherwise, generally BEM is less efficient as it gives rise to fully populated matrices. The storage requirement for computational analysis grows in accordance to the square of the problem size. This method can be used to solve the steady state flow, transient fluid flow, and unsteady flow with arbitrary body motion. However, this method is restricted to solving problems with inviscid, incompressible fluid flow. It cannot be used to analyze flows where shocks or cavitation exist (Hallquist, 2006).

5.2.2 Element Formulations

Besides the numerical methods, element formulations also play an important role in the simulation of multidimensional problems in fluid dynamics and nonlinear solid mechanics such as blast propagation and dynamic response of structure subjected to blast loads. There are at least four types of element formulations available:

- Eulerian formulation
- Lagrangian formulation
- Arbitrary Langrangian Eulerian (ALE) formulation
- Smooth Particle Hydrodynamics (SPH) formulation

In the Eulerian formulation, a control volume method is used to solve the equations that govern the conservation of mass, momentum and energy. The integral and discrete forms of these equations are expressed in conservation form to obtain accurate and stable solutions. In this formulation, a two steps numerical procedure is involved. First is a Lagrange step. In the Lagrange step, the Lagrangian equations are updated at every time interval. The next step is the Euler step. It maps the updated variables onto the Euler mesh. Such numerical mesh is fixed in space while the physical material flows through the mesh (Figure 5.1). The multiple materials are handled either through a volume fraction technique or an interface technique (Youngs,1982). The variables are all cell centered to allow arbitrary shaped control volumes to be formed at the interface between Euler and Lagrange grids. Eulerian formulation is suitable to handle large deformations and fluid flow. However, this formulation has difficulties in tracking the free surfaces and the material interfaces.

In Lagrangian formulation, each individual node of the numerical mesh follows the associated material during the motion. No transportation of material between the elements exists, rendering this formulation computationally faster than Eulerian formulation. As shown in Figure 5.2 the material remains within its initial mesh, allowing free surface tracking and tracking of the interfaces between different materials. This formulation is mainly used in structural mechanics problem to model solid materials. However, this formulation has a weakness due to its inability to allow for large distortions of the computational domain. This may lead to inaccurate solutions, computational time increment or even premature termination of the analysis. These shortcomings can be overcome using various methods described by Schwer and Day (1991) such as re-zoning,

erosion, tunnel and local modified symmetry constraint. Among the aforementioned methods, for a severe distortion problem like modeling a RC structure subjected to blast loads, the erosion method is generally applied and defined limit sets for certain predefined erosion parameters to remove elements from the calculation when they have failed. The erosion method is described in detail in Chapter 6.

Arbitrary Lagrangian Eulerian (ALE) formulation, as shown in Figure 5.3, is a combination of Lagrangian and Eulerian formulations. The Lagrange grid overlaps the Euler grid and offers constraints to the material flow in the Euler grid. At the interface between Euler-Lagrange grids, the Lagrange grid serves as a geometric flow boundary to Euler grid, whereas the Euler grids provide a pressure boundary to the Lagrange grid. This formulation allows for the solution of complex fluid-structure interaction problems including large displacement of a structure occurring within a single numerical simulation. For each computational time step, there are two phases of ALE formulation (Hallquist, 2006). The first step is the Lagrangian phase. In this phase the increment of the material's motion is computed. At the end of this step, the position of the material surface is known since the material motion and mesh motion are identical. The Lagrangian scheme is very accurate as long as the mesh remains regular. Once large material deformation appears, its accuracy reduces as well as the critical time step. The second step is the Eulerian phase. This step remaps the updated variables onto the Euler mesh. During that process, a transport of material between cells exists. Such transport of material through the element grid complicates the governing equations by introducing nonlinear transport terms. As mass conservation is not automatically satisfied, a new remapping algorithm (advection algorithm) needs to be implemented for mass, momentum and energy conservation to re-configure the frontier nodes along the material

surface determined in the Lagrange step so that the position of the material surface may be tracked.

Smoothed Particle Hydrodynamics (SPH) is a computational method developed to avoid the limitation of mesh tangling that is encountered in extreme deformation problems analyzed using the finite element method. This method is a mesh-free Lagrangian method generally used to simulate the hydrodynamic flows in which the coordinates move with the fluid. The method works by dividing the fluid into a set of discrete elements known as particles. Each particle has smoothing length with respect to Kernel function. The particles work as the computational framework on which the governing equations are resolved. The advantage of this method is the ability to adjust the resolution of the current local set of distributed particles with respect to variables (i.e. density) at each time step. On the basis of the advantage of this method, problems involving large deformation can be easily handled.

The aforementioned numerical methods and element formulations are now widely used in many commercial softwares. The three most common commercial softwares used to simulate blast propagation and its effects on dynamic response of structure are ANSYS AUTODYN, LS-DYNA, and Abaqus. In this study, only the first two softwares are used. AUTODYN is carried out to computationally model the fluid dynamics of an explosion and the propagation of the blast loads as its travels through the air to reach the structure. The blast loads obtained from AUTODYN is then applied onto the structural model built using LS DYNA FE software to obtain the dynamic response of the RC structure observed.

5.3 AUTODYN

AUTODYN is a numerical software established by Century Dynamics as part of the ANSYS suite. Finite element (for computational structural dynamics) and finite difference/finite volume (for fast transient CFD) solvers are incorporated into this software. This software also allows multi-solver coupling enabling a wide range of multi-physics solutions. The numerical method incorporated is a coupled finite difference/finite volume method proposed by Cowler and Hancock (1979). This proposed approach allows users to carry out the selected numerical solvers to model different components or regimes of a problem. The coupling of individual structured meshes operating on different numerical solvers with respect to time and geometry results in a more efficient computational analysis of structural, or fluid dynamic problems, including coupled problems. AUTODYN has been shown to be able to model extreme loading such as impact and penetration problems, and blast loading and explosion mechanisms (Quan, 2006; Chen et al., 2007). It also has a Euler remapping facility that involves establishing a fine, wedge-shaped grid at the apex of which the TNT is located. The grid is 2D. However, due to axial symmetry, it is effectively a 1D grid with spherical blast propagation. Thus, in general, the explosion is run as a 1D grid until a reflecting surface is encountered. It is then remapped into a 2D or 3D grid by taking into account the reflective obstacles (Century Dynamics, 2006).

Since the blast propagation may involve large displacements of fluid flows, the numerical analysis is well suited when it is carried out using Eulerian formulation. Lagrange formulation is not appropriate for this problem as severe distortions of air elements may occur. When dealing with distorted elements, an erosion algorithm is generally used in the Lagrange formulation. However, for fluid flow cases, such erosion algorithm is not

appropriate for solution. Thus, in this study, a CFD analysis incorporating Eulerian formulation embedded in the AUTODYN software is carried out to simulate the effects of structural layout and configuration on blast propagation.

5.3.1 Euler - Flux Corrected Transport (FCT) Processor

Euler - FCT processor has been designed to solve gas dynamic problems, in particular blast simulations. The algorithm is a multi-dimensional implementation of the explicit FCT formulation of Boris and Book (Century Dynamics, 2005). The Euler method solves problems by replacing the PDE for conservation of mass, momentum and energy with finite difference equations solved using an explicit central difference scheme. The computational cycle steps of Euler processors are given in Figure 5.5.

Euler - FCT processor allows only one element in each sub-grid and only an ideal gas equation of state (EOS) to define the material element. Besides its disadvantages, Euler-FCT is an accurate higher order method optimized for solving blast problems.

5.3.2 Material Models and Equations of State (EOS)

In this study, two material models are utilized: air and TNT explosives. The air material is assigned to follow Ideal Gas equation of state. The Ideal Gas EOS relates the pressure p to the specific internal energy e in such a way that it follows the following equation.

$$p = (\gamma - 1)\rho e \qquad (5.1)$$

where γ is the adiabatic constant (ratio of specific heats) and ρ is the density of the gas. For the ideal gas, the values of γ and ρ as well as specific heat, $H_{specific}$, and reference temperature, T_{ref}, are given in Table 5.1.

Table 5.1 Parameters of Ideal Gas EOS

Parameter	Unit	Value
γ	-	1.4
ρ	kg/m^3	1.225
$H_{specific}$	J/kgK	717.6
T_{ref}	K	288.2

The TNT explosives is defined using John-Wilkins-Lee (JWL) EOS which defines the explosive shock wave pressure, p, as a function of the specific volume, V, and specific internal energy, e, such that

$$p = C_1\left(1 - \frac{\omega}{r_1 V}\right)e^{-r_1 V} + C_2\left(1 - \frac{\omega}{r_2 V}\right)e^{-r_2 V} + \frac{\omega e}{V} \qquad (5.2)$$

where variables $\omega, C_1, C_2, r_1,$ and r_2 are constants for a specific explosive. For TNT, the values of these constants are as given in Table 5.2. Such constants are determined from Cylinder tests.

Table 5.2 Parameters of JWL EOS for TNT Explosive

Parameter	Unit	Value
ω	-	0.35
C_1	kPa	3.738E+08
C_2	kPa	3.747E+06
r_1	-	4.15
r_2	-	0.90
$v_{CJ\ Detonation}$	m/s	6930
E/V_{CJ}	kJ/m^3	6.0E+06
P_{CJ}	kPa	2.1E+07

In modeling the blast as it travels up to the time it reaches the incident surface of the structure, the structure in the path of the blast is modeled using its dimensions encased with a fully reflective surface. The effects of the deformation of the structure with respect to blast pressure and loading duration are negligible.

5.3.3 Time Zero Reference

The time zero, t_o, in the pressure - impulse curve as shown in Figure 3.2 refers to the ignition time, the time where the explosion starts at ignition. It is different from the time zero on the displacement time history curve plotting the dynamic analysis of the structure as given in Chapters 7 to 10. The time zero of the dynamic response analysis refers to time of arrival, t_a, the time where blast loads reach the incident face of a structure, as shown in Figure 3.2.

5.3.4 Basic Assumptions

In this present study, several assumptions with respect to the propagation of blast waves through air and its interaction with the structure are made and as follows:

1. The air is simulated as an ideal gas.
2. Unless otherwise stated, only hemispherical explosion is considered. Thus, in the 2D axial symmetry explosion model, the charge weight W TNT is modeled as 2W TNT to account for the perfect reflection of the surface burst explosion from the ground floor slabs.
3. The structures (walls, slabs, columns) are assumed rigid. Thus, all the surfaces of the structure are assumed to be fully reflective surfaces.

5.4 Experimental and Empirical Validations of the Proposed Approach using AUTODYN on Rectangular Structures by Experiments and Code

5.4.1 Experiment Done by Chapman et al. (1995) on Reflected Blast Wave Resultants behind Cantilever Walls

An extensive experimental study on a one-tenth scale target structure protected by a blast wall of height H_1 located at distance d_w from the detonation of a charge weight of W (kg

TNT) was conducted by Chapman et al. (1995). As shown in Figure 5.6 and Table 5.3, the variations in stand-off distance, R, distance from explosion charge to blast wall, d_w, height of burst, HOB and charge weight, W were examined. Herein, only results from two blast tests are presented and compared to the results obtained by numerical analysis.

Table 5.3 Experiment – Dimensional Details

Parameter	Unit	Test 1	Test 2
W	kg	0.06	0.06
HOB	m	0.15	0.15
d_w	m	0.60	0.45
H_1	m	300	300
R	m	1.20	1.05
H_t	m	300	300

In modeling the blast simulation using AUTODYN, the explosive is first analyzed as a 1D explosion. The 1D analysis is stopped before the blast reaches the ground floor. It is then remapped into a 2D-axial symmetry explosion model. Since a steel plate is positioned on the ground, laid under the charge, a fully reflective surface is assumed. In this numerical study, a mesh size of 5 mm is utilized.

Figure 5.7 shows the Pressure – Impulse (PI) curves from the experiment and the numerical results of Test 1. From the data from Test 1, the difference in terms of peak pressures between numerical analysis (106.7 kPa) and experiment (131.6 kPa) is about 19%. Moreover, there is a slight difference in terms of the time duration of the positive phase. The experimental results registered a shorter duration than the numerical results. Other than that, the overall positive phase impulse is similar. The difference between numerical (39.5 *kPa.msec*) and experimental data (36.84 *kPa.msec*) is only 7%, which is not significant.

The numerical analysis is also carried out by disregarding the blast walls on Test 1. This is to shed light on how the blast wall could affect the *P* and *I* measured on the structure, as the blast walls diffract the blast waves away from the target structure. As shown in Figure 5.8, the blast wall reduced the peak pressure by 70% ($P_{w/o\ BW}$= 353.74 *kPa*) and impulse by 60% ($I_{w/o\ BW}$=100 *kPa.msec*). The decrease is very significant and reduces the impact of the blast loads on the structure and may help in avoiding structural collapse.

A comparison of the *P* and *I* curves from the experiment and the numerical results of Test 2 is shown in Figure 5.9. The peak pressures differ by about 2.5% ($P_{experiment}$ = 145.6 *kPa*, $P_{numeric}$ = 141.9 *kPa*) while the impulses registered a 2% difference ($I_{experiment}$ = 42.4 *kPa.msec*, $P_{numeric}$ = 41.5 *kPa*). Moreover, the time durations of the positive phase are similar. Thus, this shows that the aforementioned numerical method is applicable and reliable in modeling the blast.

The effect of the blast wall on Test 2 is also demonstrated by comparing the PI obtained from numerical models with and without blast walls. As shown in Figure 5.10, the blast wall reduces the peak pressure by 71% ($P_{w/o\ BW}$ = 493.6 *kPa*) and the impulse by 65% ($I_{w/o\ BW}$ = 117.2 *kPa*). Thus, it is obvious that the blast walls deflect the blast waves preventing the full impact of the blast waves from reaching the target structure and significantly reduce the *P* and *I* obtained.

5.4.2 Experiment Done by Lan et al. (1998) on Composite RC Slabs

Lan et al. (1998) studied the effects of blast loads on composite RC slabs. Different from the previous experiment done by Chapman et al. (1995), this experiment was conducted

on full-scale composite RC slabs. The slabs were positioned vertically on the support structure at 5 m stand-off distance *R* from the source of explosion. The explosive was placed at a height of 1.1 m above ground (*HOB*), thus, the slabs were considered to be subjected to a spherical blast.

The following comparative study was carried out from experimental data D3-1 with a slab thickness of 150 mm. The slab was of dimension 2200x1200x150 mm, clamped on a vertical support structure with an incident face of dimension 2600x2200 mm.

The numerical analysis is carried out using AUTODYN by using the remapping function to map a 1D explosion into a 3D analysis. Since in this case the explosion was placed 1.1 m above ground, the 1D analysis is stopped before the blast reaches the ground level. In this study on blast simulation on composite slab, a mesh size of 50mm is utilized.

Figure 5.11 shows a comparison of the *P* and *I* curves of the reflected pressure and impulse curves obtained numerically compared to those generated from ConWep (Kingery and Bulmash, 1984) and the experimental data. With respect to the experimental results ($P_{experiment}$ = 5139 *kPa*; $I_{experiment}$ = 2165 *kPa.msec*), the peak pressure obtained from the numerical results differs by 3.4% (4965 *kPa*) while in the case of the impulse the difference is 10% (1941 *kPa.msec*). For peak pressure, within 0.5 msec from the time of arrival, the pressure curves obtained numerically and experimentally are shown to follow a similar shape, although some spikes are observed experimentally. On the basis of the spherical blast *P* and *I* calculation on ConWep (P_{Conwep} = 4031 kPa; I_{Conwep} = 2359.5 kPa.msec), the difference in the P and I values obtained numerically are 23% and 17.7%, respectively. Thus, ConWep seems to provide an overestimate of the impulse.

The times of arrivals t_a obtained numerically and experimentally are earlier than the one generated using ConWep. The loading duration of the experiment is shorter than that obtained numerically, leading to a smaller reflected impulse being obtained. This phenomenon could be due to cratering which absorbed some of the energy of the explosion leading to a reduction in the blast waves reflected by the ground.

5.4.3 Experiment Done by Watson et al. (2006) on Shock Waves in Explosion Measured using Optic Pressure Sensors

Watson et al. (2006) conducted blast experiments on reduced scale rectangular structure. The structure was of dimension 260x270x100 mm dimension, located at stand-off distance R of 1.010 m from the explosive source. The explosive used was PE4 which has a TNT equivalent factor of 1.37 (Weckert and Anderson, 2005). Herein, the reflected pressures P_r recorded at the front face from two different charge weights W of 30 g (Test A) and 80 g (Test B) of PE4 were analyzed.

In the experiment done by Watson et al. (2006), hollow rectangular steel boxes of dimension 260x270x100 mm was spot-welded on the plate diagonals at stand-off distance R of 1.010 m. Since the structure was situated very close to the blast source, it was instrumented with electrical sensors rather than the optical sensors, to ensure the accuracy of data capturing, especially the peak pressure. Two optic pressure sensors were located in a symmetrical way at mid-height of the structure.

The numerical analysis is carried out using AUTODYN with remapping function from 1D explosion into 3D analysis. Since the explosion is located at ground level and the

ground is a steel plate, a fully reflective ground surface is assumed. In this numerical model, a mesh size of 5 mm is utilized.

Figure 5.12 shows the reflected pressure and impulse curves of Test A (30g PE4 explosion). The peak reflected pressures P_r of the 3 sets of data (experiment, numerical analysis and TM5-1500 code) are found to be similar. With respect to pressure obtained experimentally of 320 kPa, the differences in peak pressure obtained numerically and TM5-1500 generated are 2.4% (327.6 *kPa*) and 3.7% (340.1 *kPa*), respectively. With regards to the impulse generated experimentally of 65.52 *kPa.msec*, the impulse obtained numerically and generated from TM5-1500 showed a 7% (70.08 *kPa.msec*) and 12% (79.67 *kPa.msec*) difference, respectively.

Figure 5.13 shows the reflected pressure and impulse curves of Test B (80g PE4 explosion). Again, it is shown that the peak reflected pressures P_r of the 3 sets of data (experiment, numerical analysis and TM5-1500 code) are found to be similar. With respect to pressure obtained experimentally of 782.61 *kPa*, the difference in peak pressure obtained numerically and TM5-1500 generated are 4.0% (814.2 *kPa*) and 4.6% (853.5 *kPa*), respectively. With regards to the impulse generated experimentally of 160.7 kPa.msec, the impulse obtained numerically and generated from TM5-1500 showed a 3.4% (166.14 *kPa.msec*) and 1.9% (163.1 *kPa.msec*) difference, respectively.

5.4.4 Empirical and Simplified Approach by Remennikov (2003) on Methods For Predicting Bomb Blast Effects on Building

In 2003, Remennikov conducted a comparative study on the prediction of pressure and impulse applied on a standalone building of dimension 20x20x10m. The building was

located 15m away from the explosion source. The explosion was considered as a hemispherical surface explosion as the explosives, 100 kg TNT, was placed at ground level.

A simplified approach was proposed by Remennikov (2003) to predict the bomb blast effects on the building by considering the relationship of an angle of incidence α and the reflection of the blast wave. The angle of incidence α is the angle between the outward normal and the direct vector from the explosive charge to the point observed (Figure 5.14)

The numerical analysis is carried out using AUTODYN with remapping function from a 1D explosion into a 3D analysis. Herein, a fully reflective ground surface is assumed and a mesh size of 250 mm is utilized. The mesh size is chosen based on a mesh sensitivity study with a constraint of the maximum number of elements allowed in AUTODYN 3D.

Fig 5.15 shows the results of the numerical analysis of blast waves propagation on the standalone building with respect to time. Once blast waves are obstructed by the building's facade, reflected waves are formed and applied onto the incident face of the building. Some of the waves are then diffracted back towards the direction of blast source, and some are refracted to the sides.

The results obtained from the numerical analysis (P, I, t_A, and t_D) are then compared to those obtained from the simplified approach and ConWep (Kingery and Bulmash, 1984). Table 5.4 shows a comparison of several blast parameters obtained from the four different methods. In this comparative study, ConWep is used as a reference. For impulse, with

respect to ConWep, the numerical results obtained herein are better than those obtained using the simplified approach and those obtained by Remennikov (2003). The peak pressures obtained numerically are found to be similar to those obtained by Remennikov, while the peak pressures obtained using the simplified analysis are relatively close to the default pressure generated using ConWep. In this case study, the differences between the numerical results and those obtained using ConWep are less significant due to the large incident area of the observed structure. The calculation of the pressure and impulse via ConWeb is based on the assumption of an infinite reflective surface area.

5.4.5 Experiment Done by Liew et al. (2008) on Concrete Supporting Structure of SCS Specimens

In 2008, blast tests on steel-concrete-steel (SCS) composite sandwich panels were carried out by Liew et al. Two pressure gauges were mounted at the incident face of the concrete supporting structure as shown in Figure 5.16. The incident face is of dimension 2m x 2m. A 100kg TNT explosive was located on the ground, 5 meters away from the front face, resulting in a hemispherical explosion.

The numerical analysis is carried out using AUTODYN with remapping function from a 1D explosion into a 3D analysis. Herein, a fully reflective ground surface is assumed and a mesh size of 40 mm is utilized. The mesh size is chosen based on a mesh sensitivity study with constraints imposed on of the maximum number of elements allowed in AUTODYN 3D.

Table 5.4 Comparison of Blast Parameters Due to The Effects of a Hemispherical Explosion on a Standalone Building

Level		@ Ground - Peak Reflected Pressure				@ 12 meters Above Ground				@ Roof			
Applied Method*		**A**	**B**	**C**	**D**	**A**	**B**	**C**	**D**	**A**	**B**	**C**	**D**
W	Kg	100	100	100	100	100	100	100	100	100	100	100	100
R	M	15	15	15	15	15	15	15	15	15	15	15	15
Z	$m/kg^{1/3}$	3.232	3.232	3.232	3.232	3.232	3.232	3.232	3.232	3.232	3.232	3.232	3.232
P_r	kPa	262.80	202.09	270.00	190.00	147.85	137.83	146.00	140.00	96.25	90.32	88.00	92.00
I_r	kPa.msec	955.00	968.80	955.00	970.00	621.30	662.80	715.00	670.00	402.30	347.43	536.00	480.00
t_A	Msec	18.73	16.75	18.70	17.40		26.88	28.30	26.50		41.01	42.80	41.00
$t_{end}= t_A+t_D$	Msec	32.66	29.47	35.90	29.50		40.25	47.00	41.30		54.05	62.90	57.20
t_D	Msec	13.93	12.72	17.20	12.10		13.37	18.70	14.80			20.10	16.20
diff P_r	%	default	23.10	2.74	27.70	default	3.81	0.70	2.99	default	2.26	3.14	1.62
diff I	%		1.44	0.00	1.57		4.35	9.81	5.10		5.75	14.00	8.14

Note on Methods Applied*
A : CONWEP (Kingery and Bulmash, 1984)
B : Proposed Numerical Analysis
C : Simplified Approach (Remennikov, 2003)
D : Remennikov's Numerical Analysis (Remennikov, 2003)

Figure 5.17 shows the maximum reflected pressure and impulse curves obtained from numerical results and obtained using ConWep. The numerical data was collected from the middle node at the ground having (5, 0, 0) coordinate from the blast source. The two sets of data show almost similar pattern, with similar time of arrivals and time durations as shown in Figure 5.17. With respect to pressure obtained numerically as 5.3 *MPa*, the difference in peak pressure generated from ConWep generated is 25.5% (6.65 *MPa*). The difference in terms of impulse is of 12.7% comparing I_{R_num} (3.3 *MPa.msec*) and I_{R_ConWep} (3.717 *MPa.msec*). Such significant differences in terms of reflected pressure and impulse obtained between numerical results and those obtained from ConWep are due to the smaller area of the incident face as compared to those described in Section 5.4.4.

Figure 5.18 shows the reflected pressure and impulse curves obtained numerically and experimentally. Since the pressure gauges are located at the sides on the incident face, the numerical data was collected on the coordinates of (5, 0.75, 1) from the blast source. The two sets of data show almost similar pattern, with similar time of arrivals and time durations and pressure decay as shown in Figure 5.17. The differences in terms of pressure and impulse obtained are, however, significant. With respect to pressure obtained numerically as 5.3 *MPa*, the difference in peak pressure vis-à-vis experimental data is 150 % (12.7 *MPa*). The difference in terms of impulse is 32.5% comparing I_{R_num} (3.3 *MPa.msec*) $I_{R_{Experiment}}$ are (3.65 *MPa.msec*).

5.5 Experimental Validation of the Proposed Approach using AUTODYN on RC Frames and Columns

Woodson and Baylot (1999) conducted an extensive experimental study on Quarter Scale Models of RC Frames with different cladding conditions. Herein only two sets of experimental data on RC frames with no cladding (open-frame) are employed to verify the proposed numerical analysis in the case of the effects of blast propagation on RC structural elements, in particular, columns. The target column was of dimension 89x89 mm (3.5x3.5 inch) with a 1st storey height of 1.52m (5 feet). The explosive used was 7.1 kg (15.625 pounds) of C4 charge located 0.22 m (9 inches) above the ground within a stand-off distance *R* of 1.52 m (5 feet) for Test 1 and at 3.5 feet (~1.07 m) for Test 2. During the experiment two pressure gauges were installed at a height of 300 and 750mm on the incident face of target column.

Similarly, the numerical analysis is carried out using the AUTODYN using the remapping function from a 1D explosion to a 3D analysis. Herein, based on mesh sensitivity study, a mesh size of 10mm is selected.

Figures 5.19 and 5.20 show the pressures and impulses obtained from the two experiments plotted against the height of the observed nodes on the target column. Based on the figures, the proposed numerical analysis is shown to be better than the CTH analysis carried out by the US Army Corps of Engineer when compared to the experimental results. The CTH code is a multimaterial, large deformation, strong shock-wave, solid mechanics code developed at Sandia National Laboratories that uses eulerian second-order formulation to reduce dispersion and dissipation and to produce more efficient results.

In Figure 5.19, on Test 1 pressure gauge PG1 located at the height of 300 mm above ground registered a lower impulse, *I*, and pressure, *P*, than pressure gauge PG2 that was located at a height of 750 mm. This seems to be incorrect, since PG1 should register larger *P* and *I* values. Thus, on Test 1, the *P* and *I* registered by PG1 is ignored. At the location of PG2, the proposed numerical analysis resulted in similar *P* and *I* values when benchmarked against the experimental data.

On Test 2, as shown in Figure 5.20, the numerical results showed similar values of *P* and *I* as when compared to the experiment data, except for *P* at the location of PG2. The CTH analysis proposed by US Army Corps of Engineers seems to underestimate the peak pressure *P*, and overestimate the impulse *I* at $H \geq 450$ mm.

5.6 Case Studies on RC Frames and Columns

The aforementioned validation study on blast propagation on buildings and RC frames as presented in Sections 5.4 and 5.5 shows that the proposed numerical analysis using AUTODYN agrees well with available experimental data and code. The proposed numerical method is, thus, carried out further to study the effects of RC frame layout and RC column configuration, typical of Singapore's apartment block, on blast propagation.

As described in Chapters 1 and 3, a typical apartment block in Singapore has an open, unoccupied ground floor with the 1st storey and above as infilled frames (Figure 1.1). Based on the field observations, the ground floor columns of such blocks are closely spaced with dimensions of breadth to depth ratio (*B/H*) mostly exceeding 2.0. These aforementioned conditions may, in turn, result in channeling of the blast wave when it propagates through the void deck on the ground floor.

On the basis of the ground floor columns, a number of commonly used columns' configurations are shown in Figure 5.21. In this study, two such configurations of ground floor columns are presented and used in the present study.

The main purpose of this study is to observe whether the ground floor, the soffits of the 1st storey slabs or typical closely spaced ground column configurations may result in significant reflection of the blast waves leading to higher reflected pressure and impulse at some critical locations in the structural layout.

In this section, the effect of the presence of an upper reflecting surface and closely spaced columns on blast propagation is first studied. In the analysis of the effects of an open ground floor void deck on blast propagation, the upper reflecting surface, representing the soffit of the slab above the void deck is assumed to be fully reflective.

Two cases were dealt with, viz. case A and case B, both with a stand-off distance R=5m to the critical column. Case A (Fig 5.22a) involves one column between the upper and lower reflecting surface. Case B (Fig 5.22b) on the other hand involves three columns arranged as shown.

All columns are 4 meters high with dimensions of 1000x300 mm. The critical column is subjected to blast loads along its minor axis as shown in Figure 5.23. The dimension of air modeled is 9x3x3 meters for d_x, d_y, d_z, respectively.

Cases A1 to A3 (Figure 5.22a) involves three scenarios with respect to the upper reflecting surface as follows:

- Case A1 : No upper reflecting surface (Figure 5.24a)
- Case A2 : The reflecting surface comes at the outer surface of the critical column, $R_{soffit} = R_{column}$ (Figure 5.24b)
- Case A3 : The reflecting surface projects 1m in front of the critical column's outer surface , $R_{soffit} < R_{column}$ (Figure 5.24c)

Likewise cases B1 to B3 (Figure 5.22b) involves a critical column at a stand-off distance R=5m. The three scenarios are as follows:

- Case B1 : No upper reflecting surface (Figure 5.25a)
- Case B2 : The reflecting surface comes at the outer surface of the critical column, $R_{soffit} = R_{column}$ (Figure 5.25b)
- Case B3 : The reflecting surface projects 1m in front of the critical column's outer surface, $R_{soffit} < R_{column}$, in line with the outer surfaces of the adjacent columns (Figure 5.25c)

Numerical analysis is also carried out using AUTODYN utilizing a remapping function from a 1D explosion into a 3D analysis. On the basis of mesh sensitivity study, a mesh size of 50mm is selected. The columns are assigned solid by assuming that the deformations of columns do not affect the pressure and impulse obtained. The orange color in Figures 5.24 and 5.25 represents outflow boundary conditions (BCs), whereas the blue color characterizes reflective BCs. To reduce the computational time, only half a model is built. Vertical reflective BC is applied to achieve a symmetrical condition. The

horizontal BC at the top of the model is assigned to represent the soffit of the 1st storey slab.

Figure 5.26 shows the reflected pressures *P* and impulses *I* at the incident face of Case A (A1, A2 and A3). Cases A1, A2, and A3 have similar pressure *P* obtained at the nodes within the height of *h*=0 to 2.5m. At nodes within a 0.5m wide band adjacent to the column's tip (*h*=2.5 to 3m), Case A3 results in higher *P* of up to 2.25 times of Cases A1 and A2 due to blast waves that are reflected by the 1st storey slabs' soffit located in front of the target column (R_{soffit}=4m). Similar reflected impulse is also observed for Cases A1 and A2 along the height of the incident face. Meanwhile, Case A3 results in 25% lower impulse at nodes within *h*=0 to 1.75m, and up to 2.25 times higher impulse at nodes within *h*=1.75 to 3m than Cases A1 and A2. The results show that the configuration of the upper reflecting surface affects the pressure and impulse obtained at the incident face of the target column when it is located at the front of the target column ($R_{soffit} < R_{column}$). The significance of the effects of 1st storey slab's soffit is a function of R_{soffit} and R_{column}.

Figure 5.27 shows the pressures *P* and impulses *I* at the distal face of Case A. Similar pressures are observed in the three cases at the nodes within a height of *h*=0 to 2m. At *h*=2 to 3m, Case A3 results in higher *P*, followed by Cases A2 and A1 respectively. In terms of impulse, at nodes within 0.5m wide band adjacent to the column's base ($h \leq 0.5$m) Case A3 experiences the largest impulse, of up to 1.43 times of Case A1, while at the middle portion and the top end of the target column ($h > 0.5$m) Case A2 leads in achieving the largest impulse up to 1.78 times of Case A1, followed by Case A3 (up to 1.24 times). This indicates that the configuration of the upper reflecting surface also affects the pressure and impulse obtained at the distal face of the target column.

The impulse obtained from Case A are then compared to those obtained from Case B as shown in Figures 5.28a and 5.28b. At the incident face of the target column, impulse from Case B are up to 1.2 times higher than those of Case A ($I_{B1}>I_{A1}$, $I_{B2}>I_{A2,}$ $I_{B3}>I_{A3}$). Meanwhile, the impulse at the distal face of Case B are more likely to be less by 27% than Case A ($I_{B1}<I_{A1}$, $I_{B2}<I_{A2}$) except for Case B3 that I_{B3} is up to 1.37 times larger than I_{A3}. This indicates that the columns nearby may have acted as an additional reflection surface and channel the blast waves resulting in a higher impulse obtained at the incident face of the target column.

The second study is on the effects of ground floor columns' configuration of a typical existing Singapore apartment block as shown in Figure 5.29 on blast propagation. The available stand-off distance *R*, as in Figure 5.30, is around 5 meters from the perimeter of the building. All the five columns are of dimension 1000x300 mm, with a storey height of 3 m.

In this case study, the explosive is assumed to be located on the ground at coordinates of (4000,0,0mm) as shown in Figure 5.31, with a stand-off distance *R* of 5 meters in front of Column 2. An explosive charge weight of 100 kg of TNT is utilized. Similar to the previous section, numerical analysis is carried out using AUTODYN by utilizing a remapping function from a 1D explosion into a 3D analysis. Based on mesh sensitivity study, a mesh size of 100mm is selected. The columns are assumed solid since the deformations of columns do not significantly affect the pressure and impulse obtained.

The pressure contours at three different time after the blast of the open ground floor are shown in Figure 5.32. The hemispherical blast waves first strike the bottom of Column 2 (Figure 5.32a). The blast waves then engulf Column 2, strike Column 1 (Figure 5.32b) and are channelled through the open ground floor void deck via the "windows" between columns (Figure 5.33c). They are also reflected by the soffit of 1st storey slab.

Table 5.5 and Figure 5.33 show the pressure and impulse obtained at the incident faces of Columns 1 to 5. As expected, Column 2 experiences the highest reflected pressure and impulse as the column is nearest the blast source, followed by Columns 1, 4, 3 and 5, consecutively. Columns 1 and 2 are not affected by the blast waves reflection from the 1st storey slab's soffit since they are located at the incident face of the structure. Thus, the pressures and impulse obtained on the nodes of Columns 1 and 2 reduce with the height above the base of the column. On the other hand, the blast waves reflected by the 1st storey slab's soffit affect Columns 3, 4 and 5 and result in an increase in pressures and impulses obtained as the observed node is nearer to the soffit of the 1st storey's slab.

Table 5.5 Reflected Pressures and Impulses Observed at Incident Face of Columns

P/I	Column	observed height (m) at incident face					
		0	0.6	1.2	1.8	2.4	3
Pressure (kPa)	1	2205.5	2191.9	2157.5	2111.9	2065.8	1967.3
	2	3894.3	3860.4	3758.5	3644.7	3534.3	3443.3
	3	606.7	605.7	602.9	604.9	836.7	1108.4
	4	913.0	914.4	914.1	917.7	927.6	918.9
	5	654.6	671.5	715.6	1069.4	1059.7	1054.2
Impulse (kPa.msec)	1	1812.9	1802.2	1781.3	1765.8	1731.2	1720.6
	2	2726.4	2703.4	2591.5	2429.6	2237.3	2038.0
	3	1133.9	1126.8	1168.3	1225.2	1336.0	1456.9
	4	1440.4	1436.8	1423.2	1403.7	1420.1	1470.9
	5	1092.3	1036.2	1080.3	1281.9	1349.4	1381.0

5.7 Summary

To summarize, the experimental and empirical validation studies show us that the proposed numerical analysis using AUTODYN3D with its remapping function agrees well with the available experimental data and code. This numerical method may then be used to study the effects of more complex structural configuration, such as an apartment block with open, unoccupied ground floor, on the blast wave propagation as a result of explosion. The aforementioned case studies simulating the effect of a ground floor void deck indicate that, besides the location of the target column, the configuration of the upper reflecting surfaces representing the soffit of the slab above the void deck and columns nearby also affects the pressure and impulse acting on the incident and distal faces of the target column.

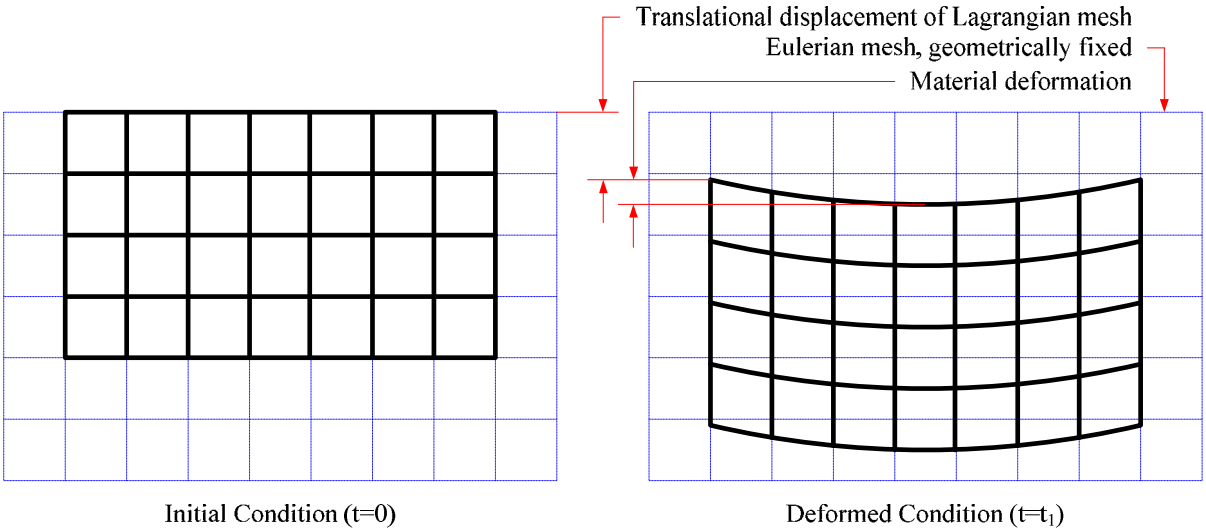

Figure 5.1 Schematics of Eulerian formulation

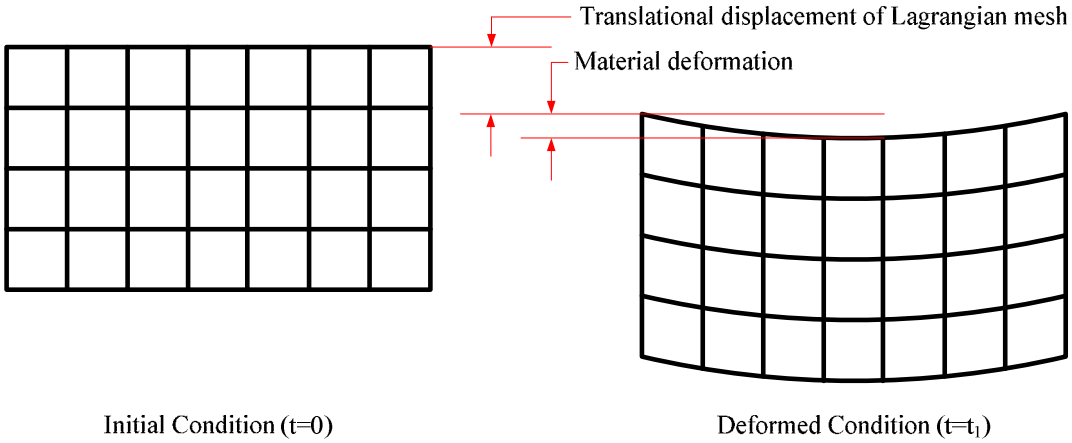

Figure 5.2 Schematics of Lagrangian formulation

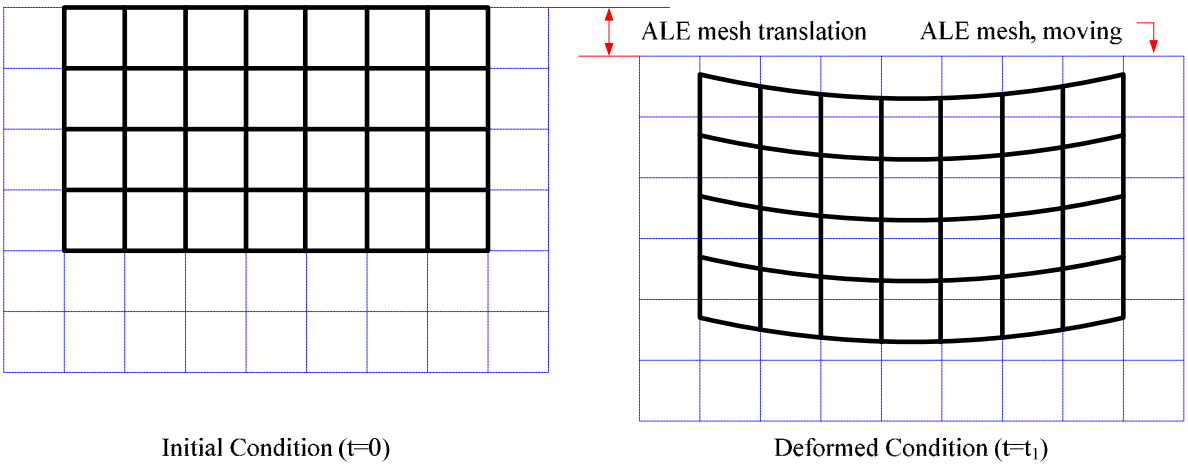

Figure 5.3 Schematics of ALE formulation

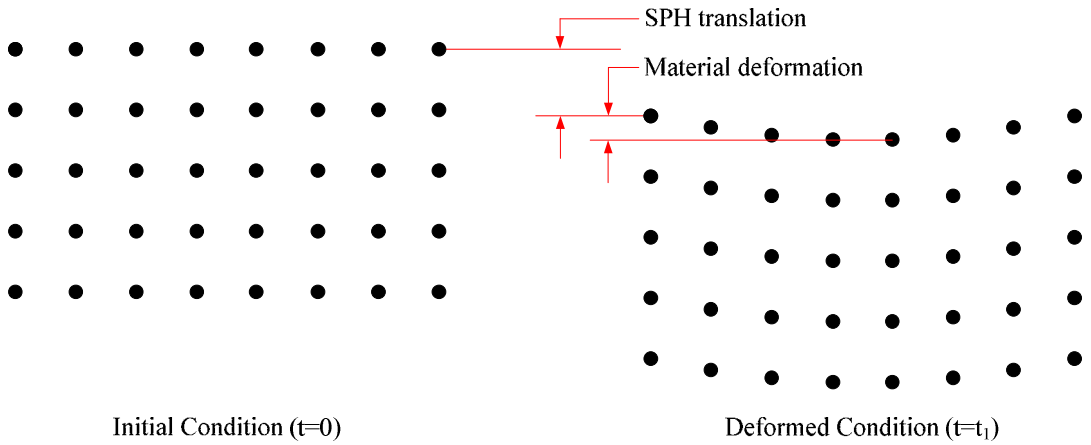

Figure 5.4 Schematics of SPH formulation

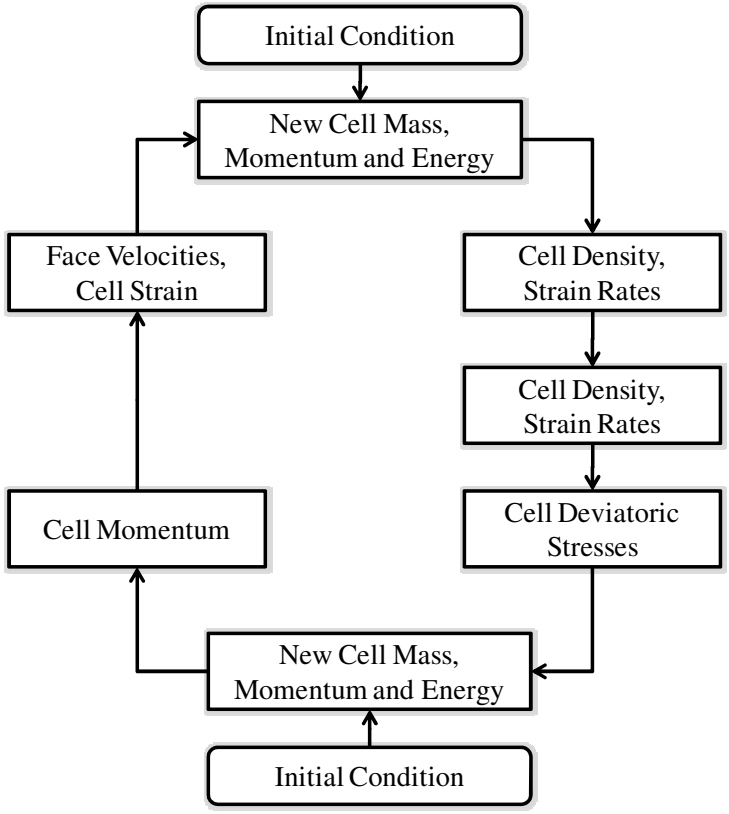

Figure 5.5 Eulerian computational cycle (Century dynamics, 2006)

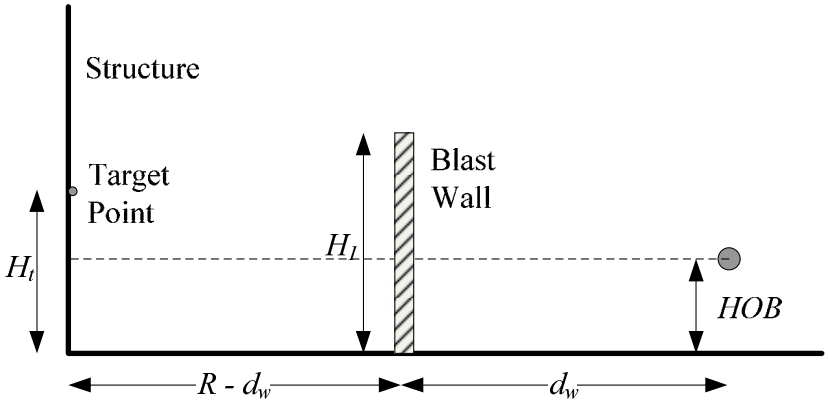

Figure 5.6 Experiment set-up (Chapman et al., 1995)

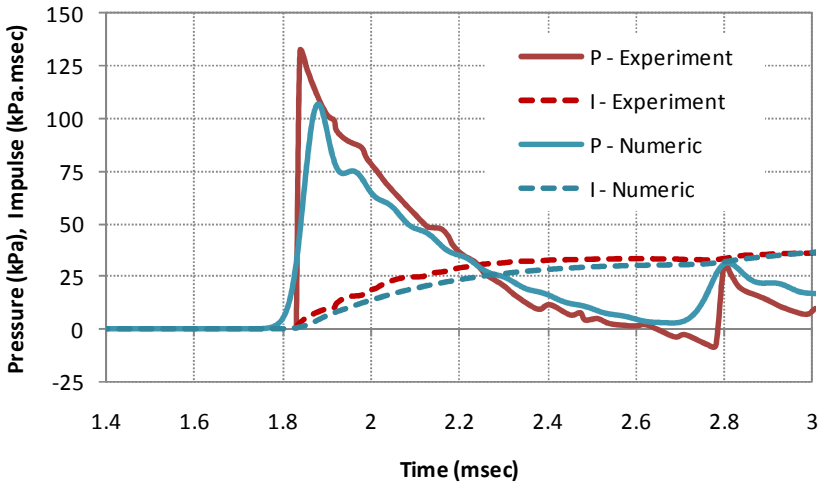

Figure 5.7 Pressure - impulse curve of Test 1 - numerical vs. experiment

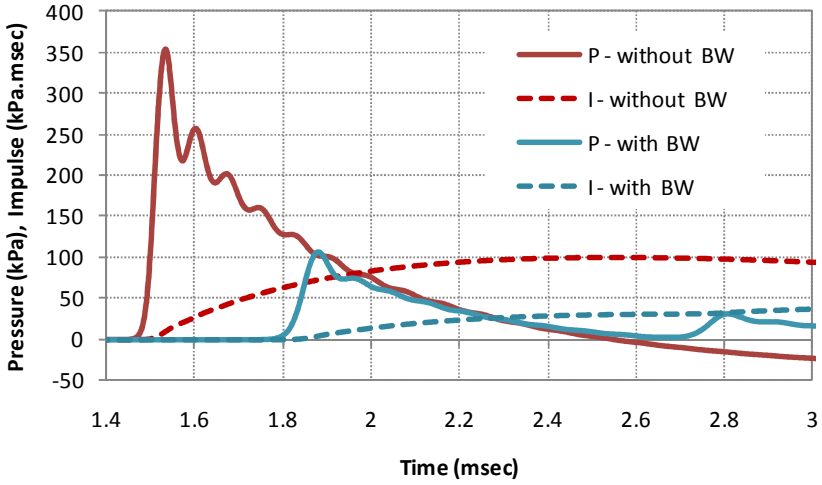

Figure 5.8 Numerical results of Test 1 - with and without blast wall (BW)

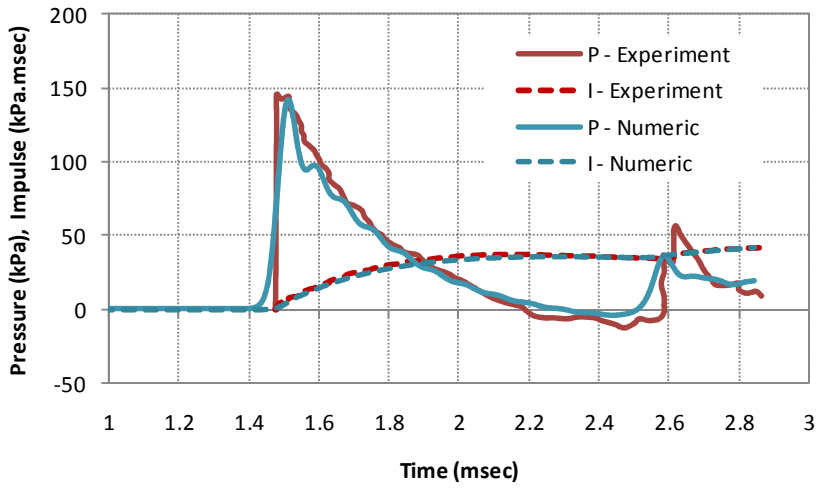

Figure 5.9 Pressure - impulse curve of Test 2 - numerical vs. experiment

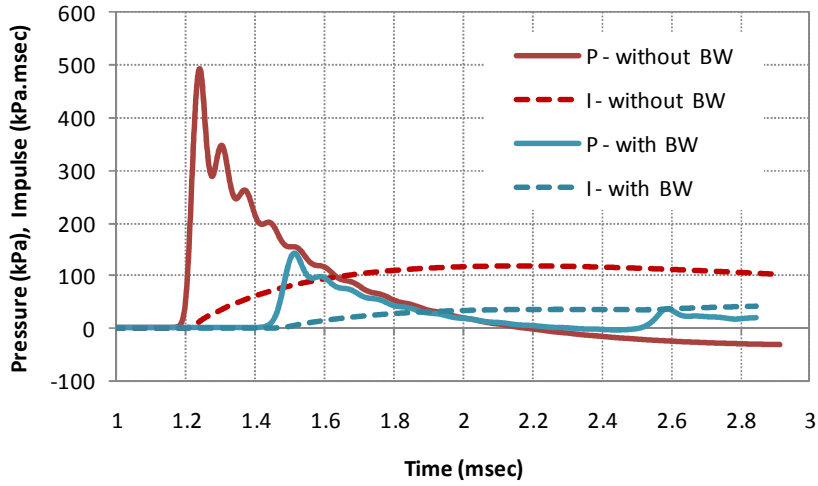

Figure 5.10 Numerical results of Test 2 - with and without blast wall (BW)

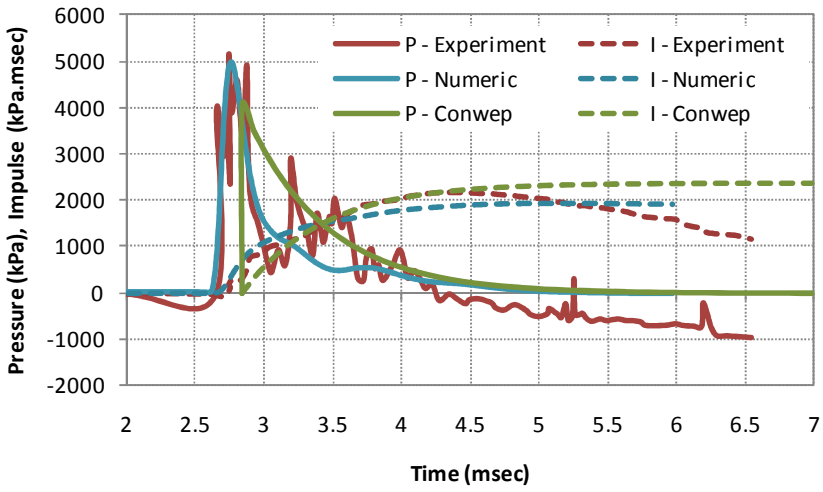

Figure 5.11 Spherical explosion of 100 kg TNT at 5 m stand-off distance

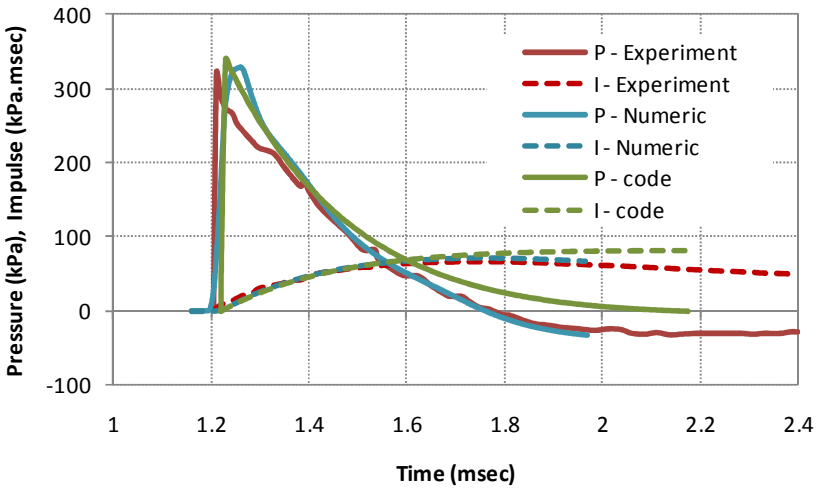

Figure 5.12 PI curve of reflected pressure of Test A (30g PE4)

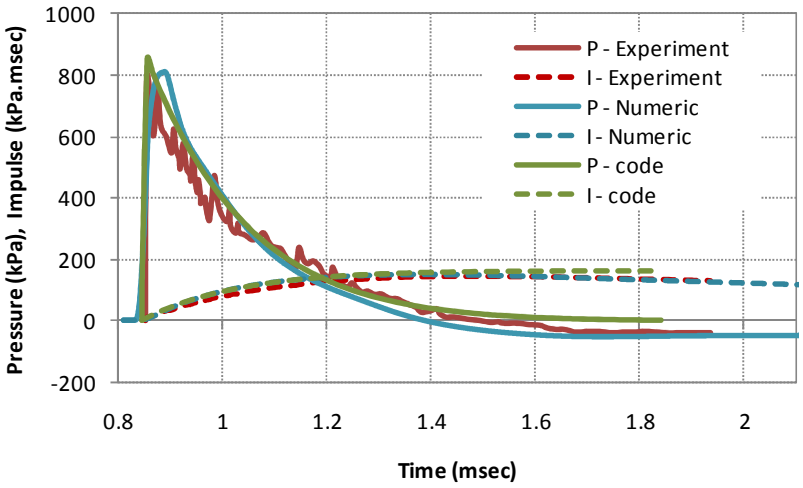

Figure 5. 13 PI Curve of reflected pressure of Test B (80g PE4)

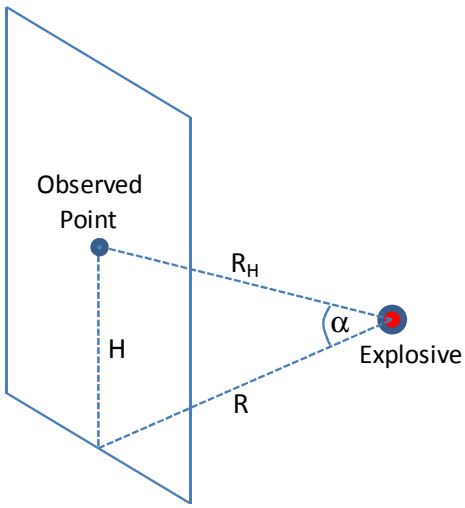

Figure 5.14 Angle of incident w.r.t. explosive charge and observed point locations

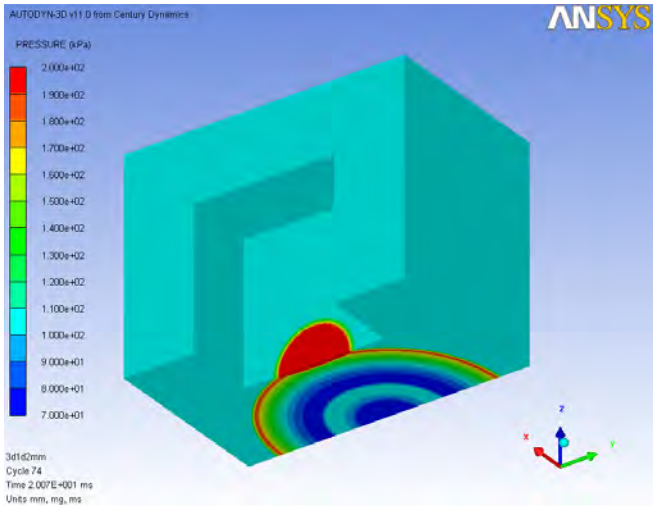

(a)

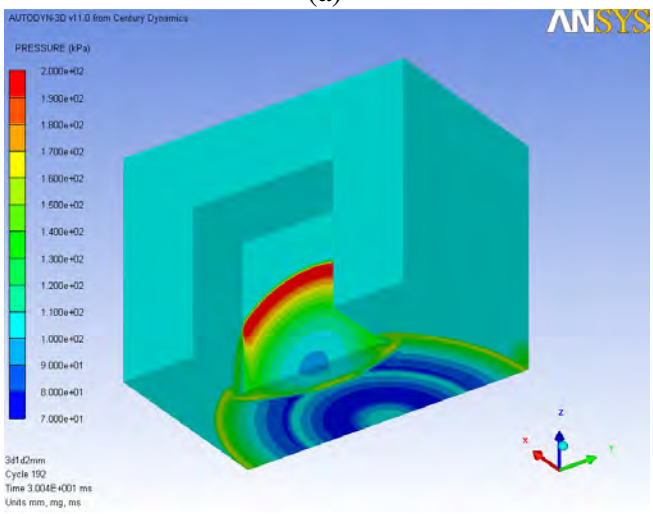

(b)

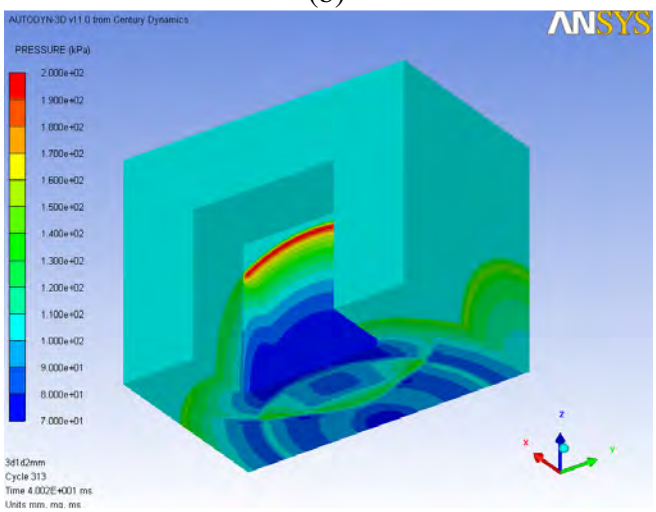

(c)

Figure 5.15 Blast pressure contours on standalone building after (a) 20, (b) 30, (c) 40 msec

Figure 5.16 Configuration of concrete supporting structure of SCS specimens

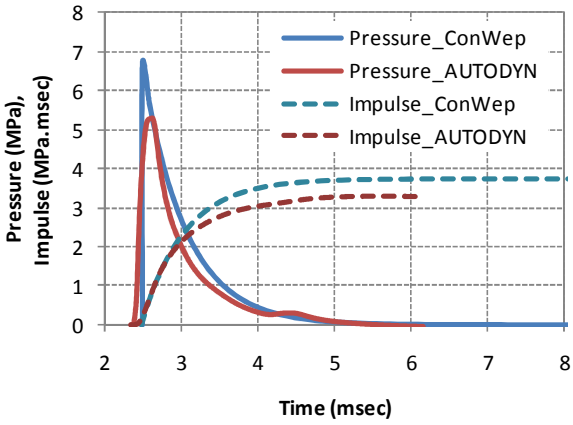

Figure 5.17 Reflected pressure and impulse time histories of blast loads from 100 kg TNT at 5 meters stand-off distance

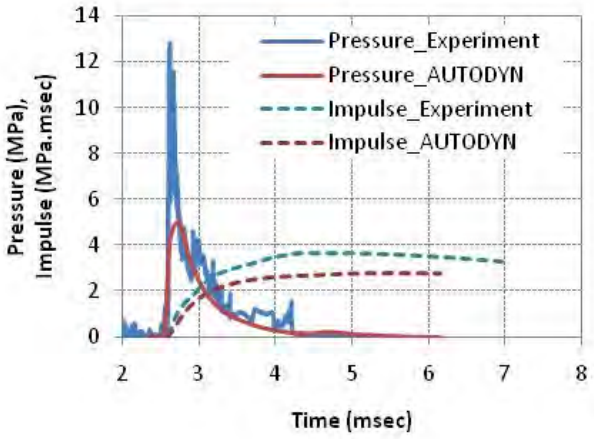

Figure 5.18 Experimental vs. numerical pressure and impulse histories of blast loads from 100 kg TNT at 5 meters stand-off distance

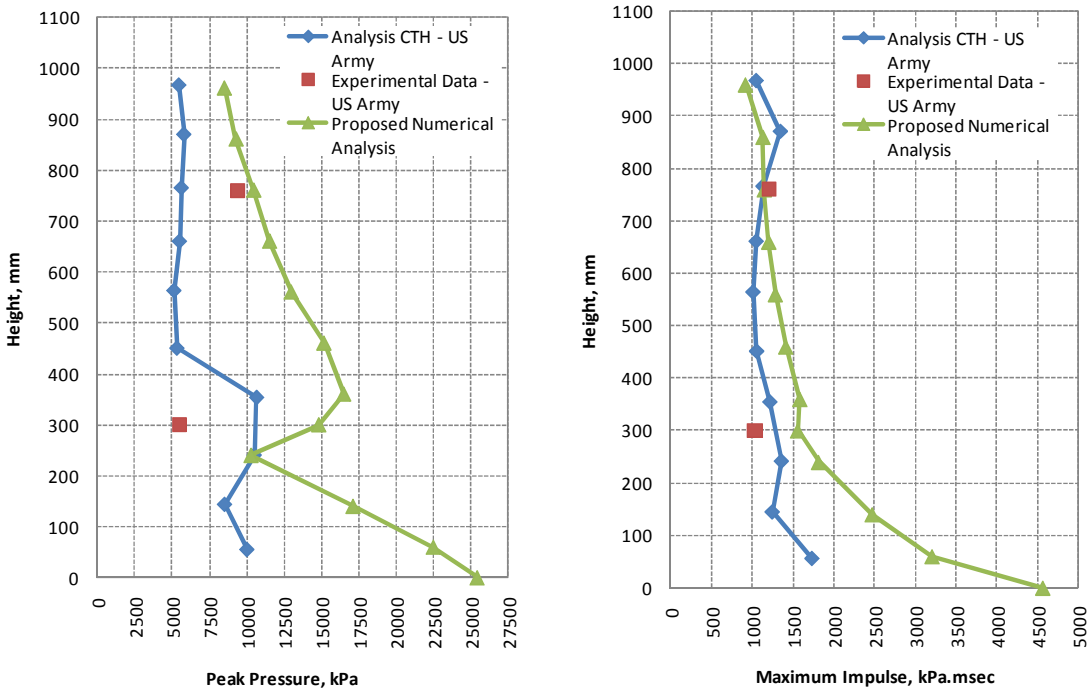

Figure 5.19 Pressure and impulse w.r.t. height of target column - Test 1

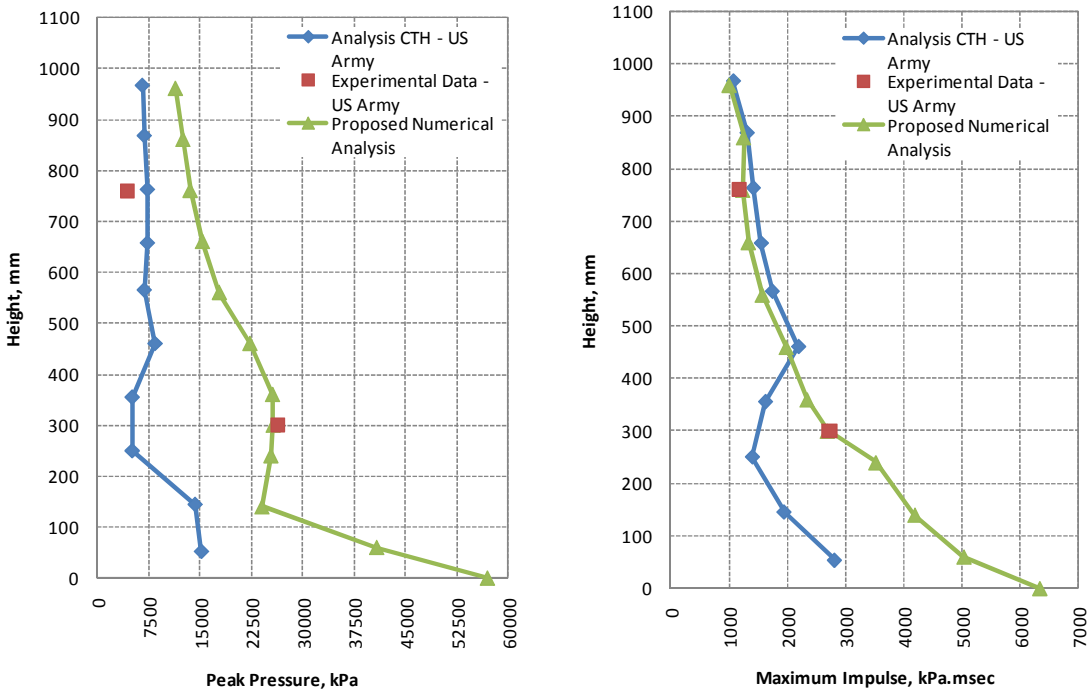

Figure 5.20 Pressure and impulse w.r.t. height of target column - Test 2

(a) (b)

(c) (d)

(e)

Figure 5.21 Typical configurations of ground floor RC columns

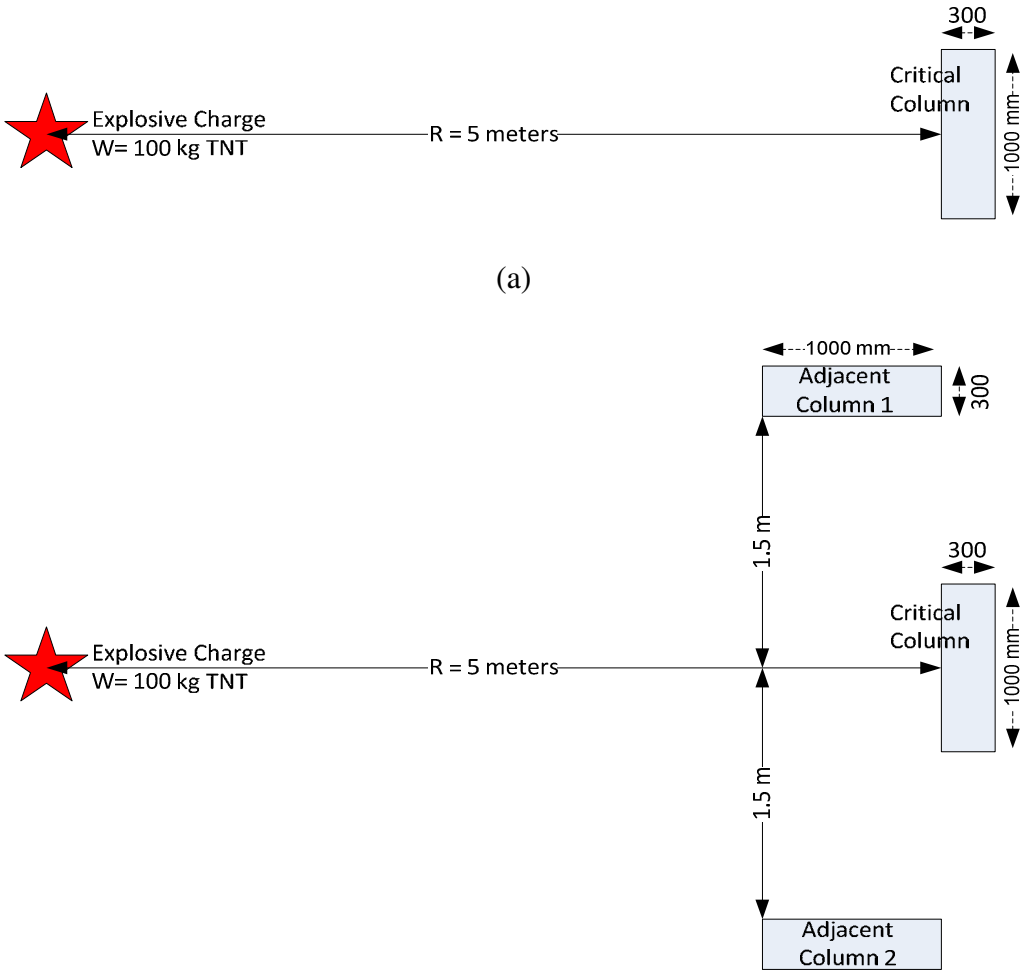

Figure 5.22 (a) Single column (Case A) and (b) Three closely spaced columns (Case B)

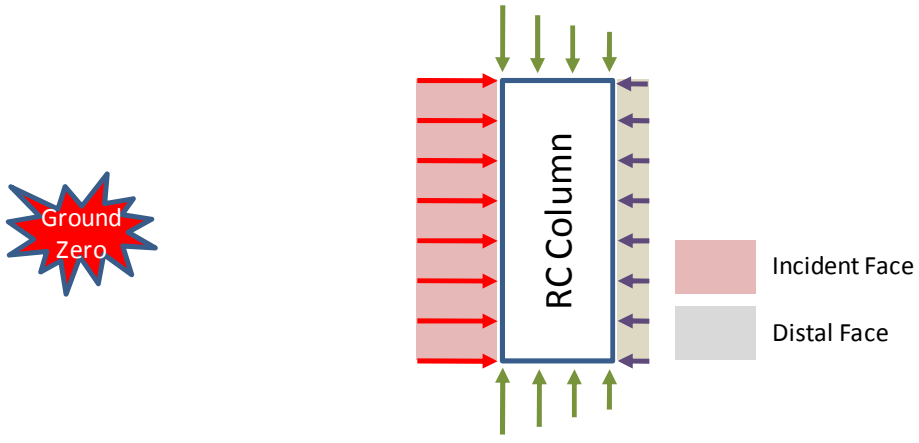

Figure 5.23 Direction of pressure and impulse on critical column subjected to blast loads along its minor axis

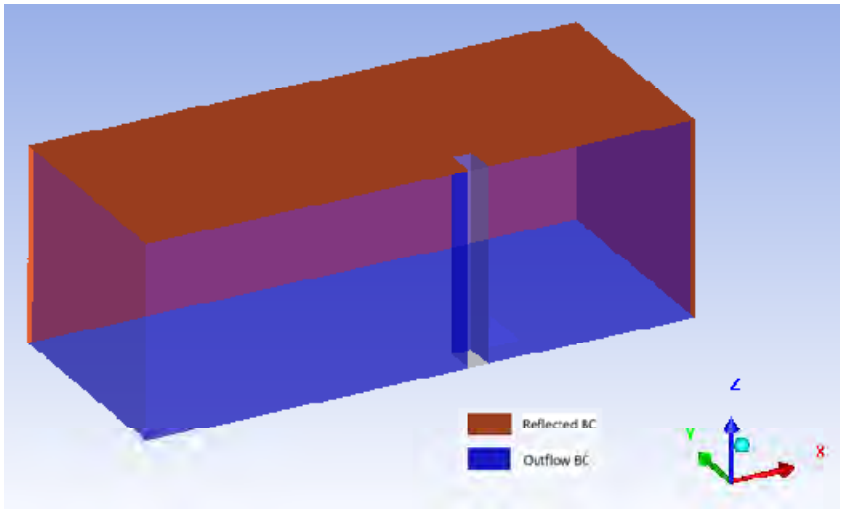

(a)

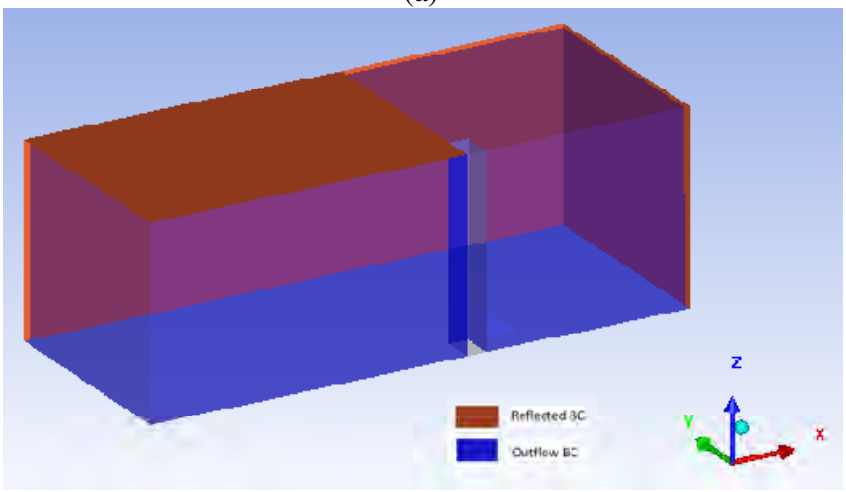

(b)

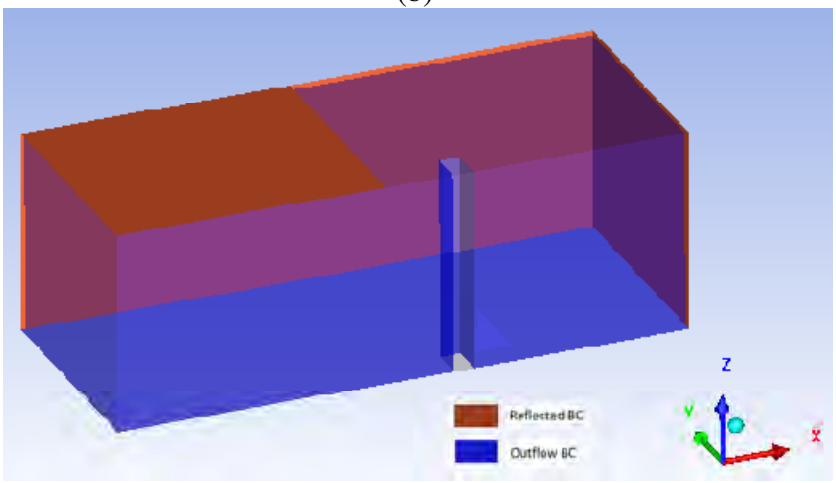

(c)

Figure 5.24 Case A: Single column model (a) A1, (b) A2, (c) A3

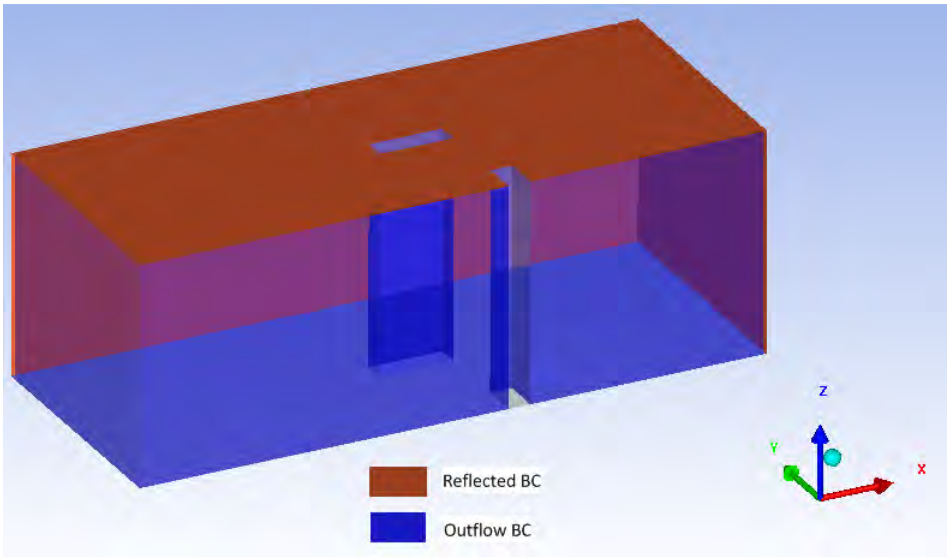

(a)

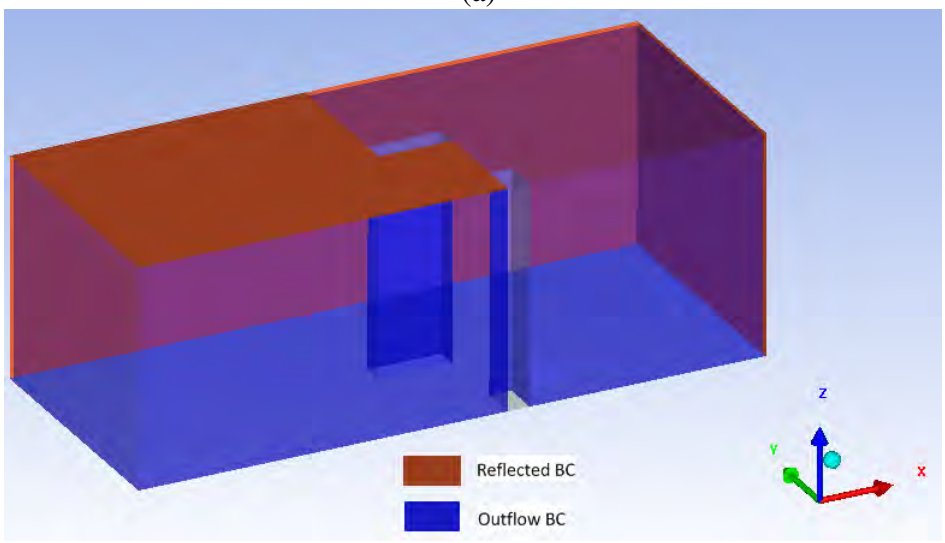

(b)

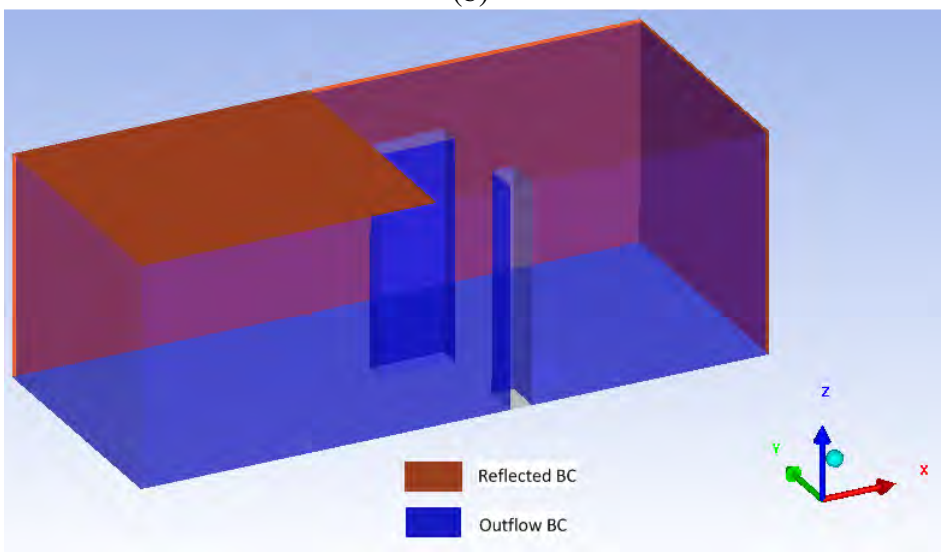

(c)

Figure 5.25 Case B: Three column model (a) B1, (b) B2, (c) B3

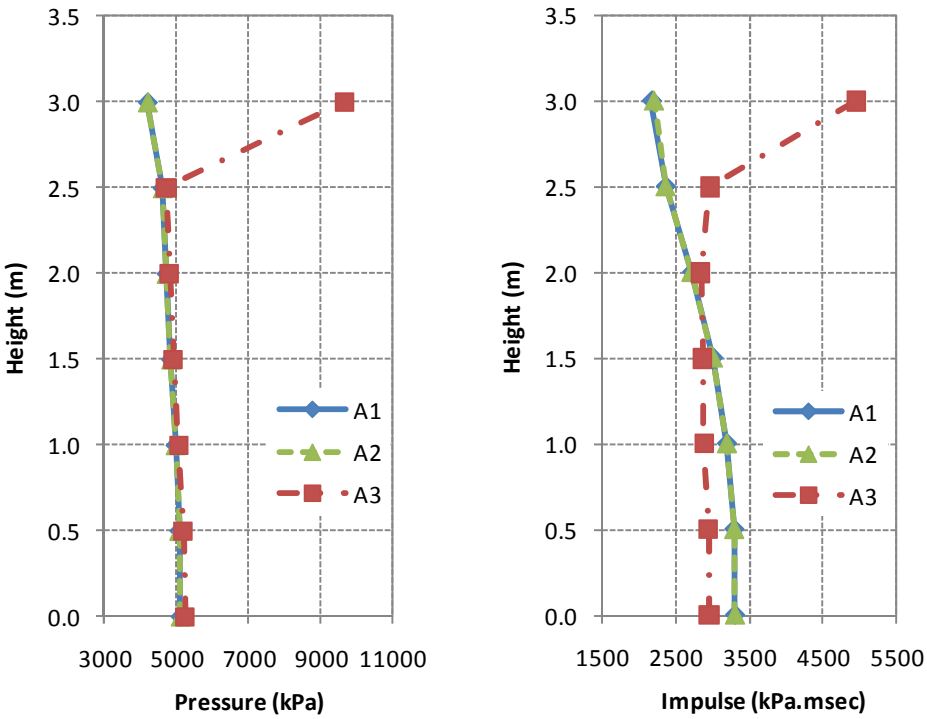

(a) (b)

Figure 5.26 (a) Pressure and (b) Impulse at incident face of Case A

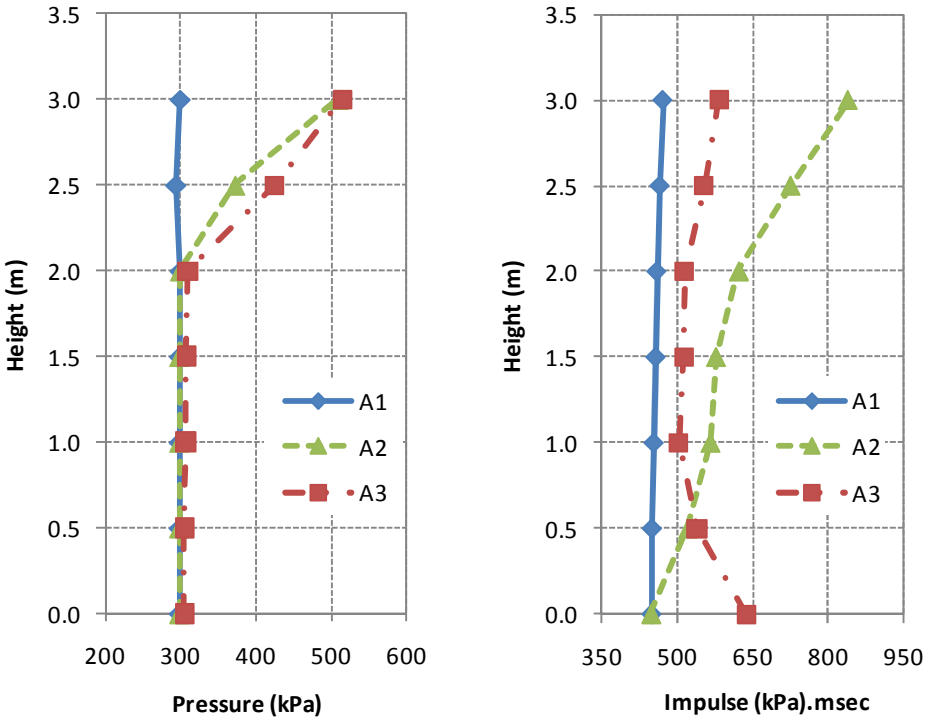

(a) (b)

Figure 5.27 (a) Pressure and (b) Impulse at distal face of Case A

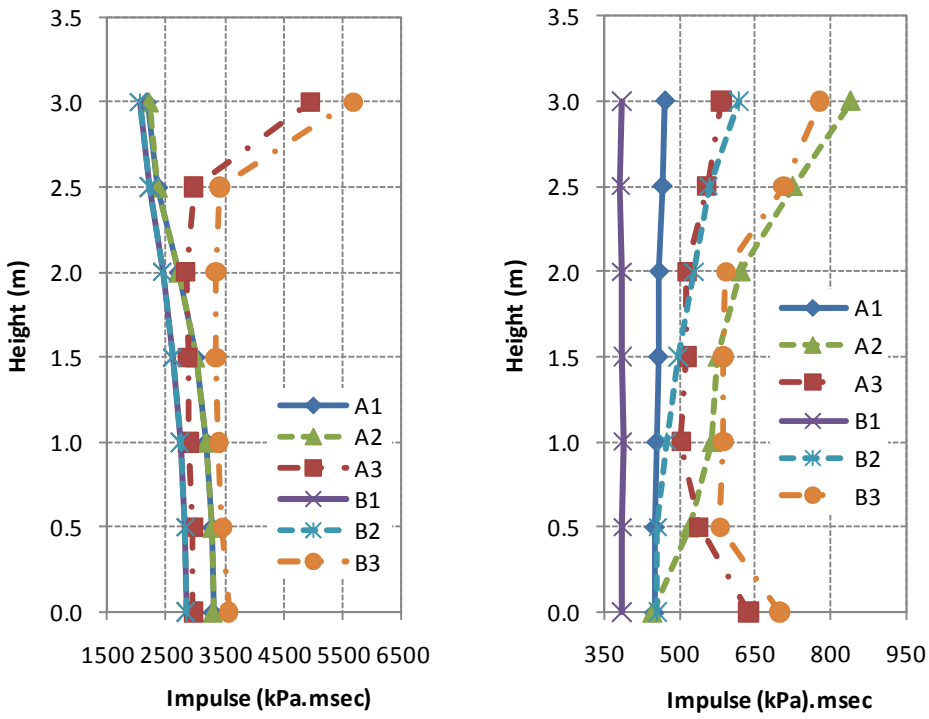

(a) (b)

Figure 5.28 Impulse at (a) Incident and (b) Distal faces of Cases A and B

Figure 5.29 Open ground floor void deck with its columns configuration

Figure 5.30 Available stand-off distance *R*

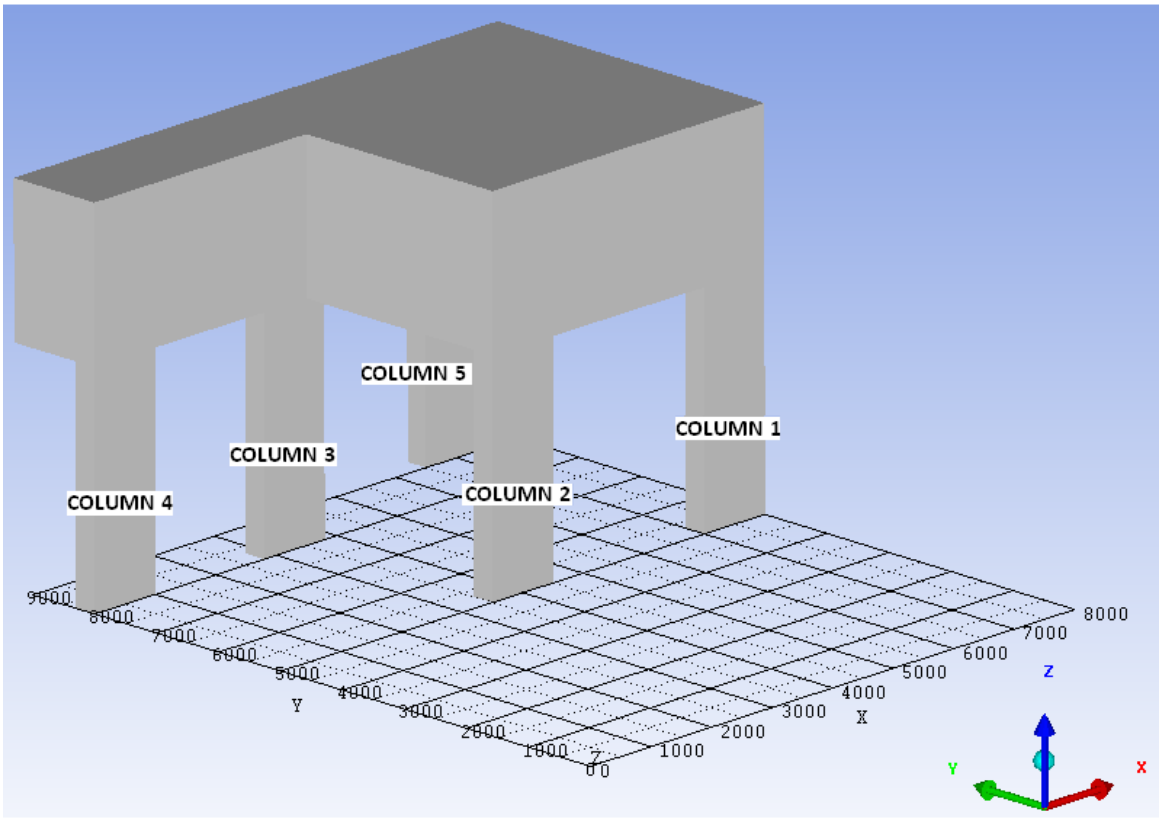

Figure 5.31 Numerical model of open ground floor void deck

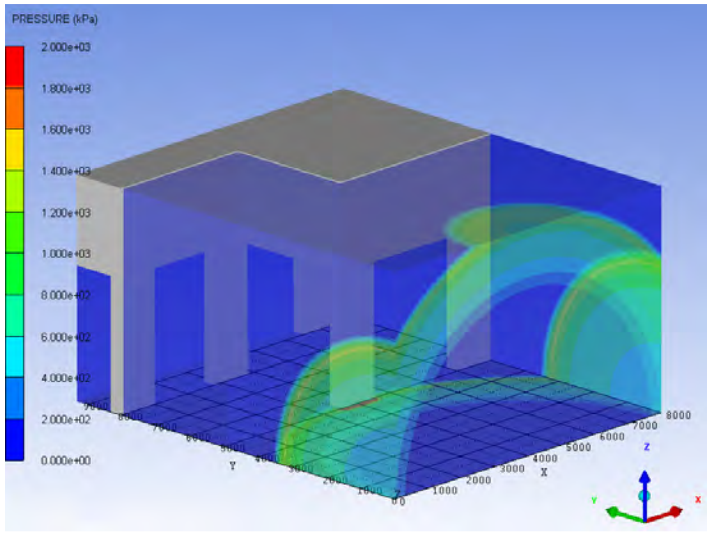

(a)

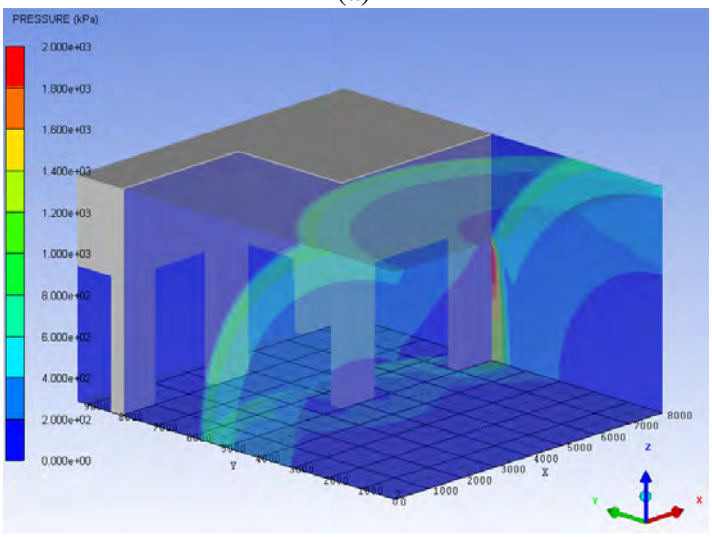

(b)

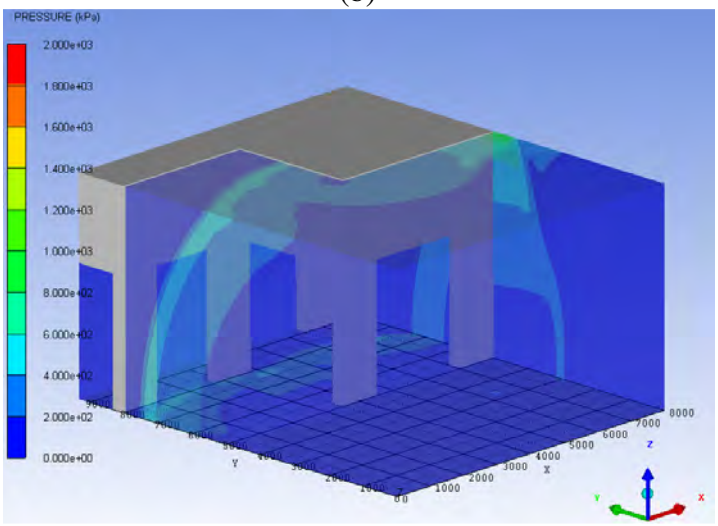

(c)

Figure 5.32 Pressure contours of ground floor columns subjected to 100 kg TNT at stand-off distance R=5m at time (a) t=2.5ms, (b) t=4.25ms and (c) t=6.25ms

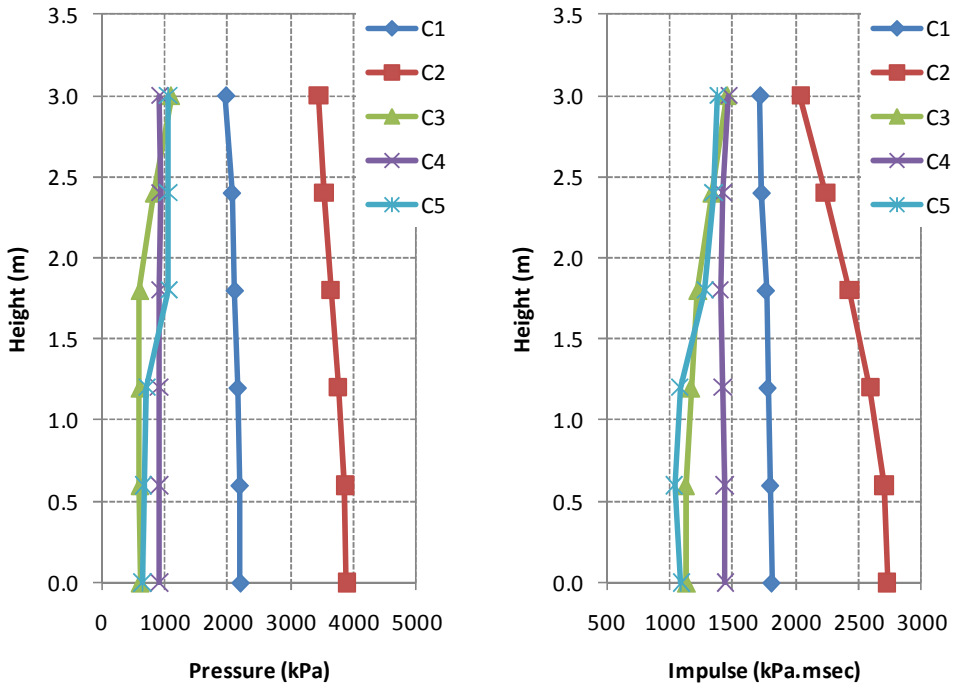

(a) (b)

Figure 5.33 (a) Pressure and (b) Impulse at incident faces of Columns 1, 2, 3, 4 and 5

6 Numerical Modeling using LS DYNA

6.1 Introduction

In this present study, the dynamic response of RC column subjected to blast loads is analyzed. Both analytical and numerical solutions are discussed and presented. The analytical solutions or RC cantilever column subjected to blast load are obtained f using equivalent SDOF analysis, while the numerical solutions for RC columns are obtained using LS DYNA FE software version 971 developed by LSTC Livermore. Numerical modeling of the blast loads acting on the structures is more widely reported compared to actual field tests as the latter involve more time and costs in preparations and in executing the tests. Moreover, numerical modeling may be able to provide a more comprehensive array of results covering a wider range of influencing parameters which may not be available from a limited number of field tests. Generally experimental data from field tests may be used to validate the results obtained from numerical analysis.

In numerical modeling, the material models are the foremost important aspects to be considered in achieving the desired behavior of structures under blast loading. Steel, concrete and hybrid fiber ECC composites are used in this study. Herein, a theoretical study on the material models and their influencing parameters are carried out.

Another important aspect in modeling the structure using LS DYNA is the hourglass problem. This problem may arise due to a lack of integration point introduced in the system. Most FE softwares incorporate reduced integration points on their system for the computational efficiency. To overcome such problems, control hourglass may be applied in the models as appropriate. Details of the hourglass problem and its control are discussed hereafter.

6.2 LS DYNA

Numerous finite element packages are now available worldwide; each with its own specialty applications. For the case of structures subjected to blast load, LS DYNA, ABAQUS and PRONTO are some of the numerical softwares generally used that incorporate finite element formulation. LS DYNA is used in the present study of the dynamic response of RC columns subjected to blast loads.

Incorporating Lagrangian formulation in the explicit time integration scheme of LS DYNA, very small time steps are required to maintain stability of the central difference method and its convergence. The stability of the central difference method is determined by controlling the stability of a set of linear equations of motion. These equations are then uncoupled and normalized into mass and stiffness modal equations. The concept of the central difference method is briefly discussed herein.

The matrix forms of the equation of motion is obtained as a function of Mass M, damping C, stiffness K, force F and displacement u matrices.

$$M\ddot{u} + C\dot{u} + Ku = F(t) \tag{6.1}$$

Normalizing the above form by introducing modal coordinates x_i, the displacement u is obtained in terms of deflection function ϕ_i and becomes $u_i = \Sigma \phi_i x_i$. Thus, the equation of motion is obtained as follows.

$$\phi^T M \phi \ddot{x} + \phi^T C \phi \dot{x} + \phi^T K \phi x = \phi^T F \tag{6.2a}$$

$$M_m \ddot{x} + C_m \dot{x} + K_m x = \phi^T F \tag{6.2b}$$

Multiplying the mass, damping and stiffness matrices with ϕ will provide diagonal matrices of mass M_m, damping C_m and stiffness K_m as shown in Equations 6.2. These equations can then be solved easily as they are uncoupled.

$$\phi_i^T M \phi_i = M_{mi} = m_i$$

$$\phi_i^T C \phi_i = C_{mi} = c_i \tag{6.3a}$$

$$\phi_i^T K \phi_i = K_{mi} = k_i$$

$$\omega_i^2 = \frac{k_i}{m_i}$$

$$\xi_i = \frac{c_i}{c_{cr\,i}} = \frac{c_i}{2 m_i \omega_i} \Leftrightarrow \frac{c_i}{m_i} = 2 \xi_i \omega_i \tag{6.3b}$$

m_i, k_i and c_i respectively represent modal mass, modal stiffness and modal damping, ω_i is the natural frequency of the i^{th} mode and ξ_i is the damping ratio of the i^{th} mode with respect to the critical damping $c_{cr\,i}$. Using the two correlation functions as given in Equation 6.3, Equation 6.4 can be written in non matrix form as follows. (Noted that $\phi^T F = P$).

$$\ddot{x} + 2 \xi \omega \dot{x} + \omega^2 x = P \tag{6.4}$$

Velocity $\dot{x}$ and acceleration $\ddot{x}$ may be obtained using the central difference method as functions of time step Δt.

$$\dot{x}_n = \frac{x_{n+1} - x_{n-1}}{2\Delta t}$$
$$\ddot{x}_n = \frac{x_{n+1} - 2x_n + x_{n-1}}{\Delta t^2} \tag{6.5}$$

Substituting Equation 6.5 into the equation of motion (Equation 6.4) leads to

$$x_{n+1} = \frac{2-\omega^2\Delta t^2}{1+2\xi\omega\Delta t^2} x_n - \frac{1-2\xi\omega\Delta t^2}{1+2\xi\omega\Delta t^2} x_{n-1} + \frac{\Delta t^2}{1+2\xi\omega\Delta t^2} P_n \tag{6.6}$$

In matrix form Equation 6.6 can also be written as

$$\begin{Bmatrix} x_{n+1} \\ x_n \end{Bmatrix} = \begin{bmatrix} \frac{2-\omega^2\Delta t^2}{1+2\xi\omega\Delta t^2} & -\frac{1-2\xi\omega\Delta t^2}{1+2\xi\omega\Delta t^2} \\ 1 & 0 \end{bmatrix} \begin{Bmatrix} x_n \\ x_{n-1} \end{Bmatrix} + \begin{Bmatrix} \frac{\Delta t^2}{1+2\xi\omega\Delta t^2} \\ 0 \end{Bmatrix} P_n \tag{6.7}$$
$$X_{n+1} = AX_n + BP_n$$

where A, B, and X are matrices representing the equation of displacement, equation of load, and displacement, respectively. When no load is applied to the structure, matrix B assumes a zero value, while A still exists.

The time step is controlled by the critical time step obtained from eigen-value analysis based on the smallest size of the elements. As the critical time step is a function of the mesh size, mesh sensitivity study needs to be done to eliminate errors due to element size.

$$\begin{aligned} &[A - \lambda I]X = 0 \\ &\det[A - \lambda I] = 0 \end{aligned} \tag{6.8}$$

For the undamped equation of motion, $\xi = 0$, the eigenvalues λ are obtained as

$$\begin{vmatrix} \frac{2-\omega^2\Delta t^2}{1+2\xi\omega\Delta t^2}-\lambda & -\frac{1-2\xi\omega\Delta t^2}{1+2\xi\omega\Delta t^2} \\ 1 & -\lambda \end{vmatrix} = 0$$

$$\begin{vmatrix} 2-\omega^2\Delta t^2-\lambda & -1 \\ 1 & -\lambda \end{vmatrix} = 0$$

$$\lambda^2 - \left(2-\omega^2\Delta t^2\right)+1=0$$

$$\lambda = \frac{2-\omega^2\Delta t^2 \pm \sqrt{\left(2-\omega^2\Delta t^2\right)^2-4}}{2} \tag{6.9}$$

A matrix should remain bounded as the *n+1* value approaches infinity. Thus, for stability purpose, it is required to restrain $|\lambda| \le 1$. Taking an eigenvalue of $|\lambda| = 1$, the only possible root is obtained from $\lambda = -1$:

$$-1 = \frac{2-\omega^2\Delta t^2 - \sqrt{\left(2-\omega^2\Delta t^2\right)^2-4}}{2}$$

$$\Delta t_{critical} = \frac{2}{\omega_{\max}} \tag{6.10}$$

To achieve $|\lambda| \le 1$, time step should be constrained to a value less than the critical time step.

$$\Delta t < \frac{2}{\omega_{\max}} \tag{6.11}$$

For the damped structure, the constraint of time step is as follows.

$$\Delta t < \frac{2}{\omega_{\max}}\left(\sqrt{1+\xi^2}-\xi\right) \tag{6.12}$$

In the numerical modeling of this study, the steel and concrete elements are assigned as beam-truss element and solid element, respectively. The beam-truss element is a 2-D line element that is only capable of restraining axial forces, tension–compression. In this

study, elastic – fully plastic steel material model with kinematic hardening constitutive model is selected for use and discussed hereafter.

The solid element is an eight-node hexahedron (H8) element. Theoretically, an exact integration of H8 element is achieved when 2x2x2 Gauss integration points are introduced in the model. However, applying exact integration to the model will reduce processing time efficiency as 3-D matrix should be applied to the *K* and *B* matrices of the element. Thus, the LS DYNA program reduces the Gauss integration points to 1x1x1 point noting that it is sufficient to guarantee convergence. The reduced integration point may lead to the occurrence of zero energy modes. To counter this problem, hourglass control is applied to the model and will be discussed in more detail in Section 6.6.

6.3 Steel Material Model

Steel is an isotropic material having the same initial yield stress for both uniaxial tension and uniaxial compression. The term steel refers to steel reinforcements present in reinforced concrete. In order to select a suitable material model for steel reinforcement, the material models generally used for metals in LS DYNA 971 were reviewed. These include MAT 3_PLASTIC KINEMATIC and MAT 24_PIECEWISE LINEAR PLASTICITY. Since the steel reinforcement is modeled as beam-truss elements capable of sustaining only tension - compression, MAT 3_PLASTIC KINEMATIC is found to be more efficient in terms of the computational time. Thus, the steel material is modeled using MAT 3_PLASTIC KINEMATIC. The elastic – fully plastic behavior with kinematic hardening plasticity is utilized in accordance to von Mises yield criterion. Herein, the so-called Bauschinger effect is also taken into account showing that when the steel material is subjected to cyclic loading of tension followed by compression, it

exhibits a compression yield point that is lower and occurs earlier than the first tensile yield point. The kinematic hardening is achieved by maintaining the radii of yield surface at a fixed value by allowing the centre to move in the direction of the plastic strain.

Ottosen and Ristinmaa in 2005 proposed a general formulation for initial yield or failure criterion that consists of three parameters; I_1 is the first invariant of hydrostatic stresses, σ_{ii}, J_2 represents the second invariant of the deviatoric stresses, s_{ij}, and θ refers to the angle that represents the direction of the deviatoric stresses.

$$\phi\left(I_1, J_2, \cos 3\theta\right) = 0 \tag{6.13}$$

The von Mises yield criterion assumes that the influence of $\cos 3\theta$ is negligible and the occurrence of initial yield or failure is independent of the hydrostatic stress I_1. It results in a convex shape of deviatoric plane and similar values for uniaxial yield tensile stress and uniaxial yield compressive stress as shown in Figure 6.1. σ_i is the principal stress acting in the i direction.

$$\begin{aligned} \phi\left(J_2\right) &= 0 \\ \sqrt{3J_2} - \sigma_y &= 0 \\ \frac{1}{2} s_{ij} s_{ij} - \frac{\sigma_y^{\,2}}{3} &= 0 \end{aligned} \tag{6.14}$$

Strain rate $\dot{\varepsilon}$ effect is also taken into account by using the Cowper Symonds model as given in Equation 6.15. This model introduced strain rate dependent factors to scale the yield stress. β parameter is occupied to distinguish the type of plastic hardening in the material model. For elastic fully plastic material with kinematic hardening ($\beta = 0$), the additional stress of the plastic hardening part which is $\beta E_p \varepsilon_{eff}^p$ is not considered. E_p is the plastic modulus of the material whereas ε_{eff}^p is the effective plastic strain of the material. Two constants of strain rate parameters are introduced; C and P. The C and P values are

obtained based on curve fitting of the DIF of steel reinforcements proposed by Malvar (1998) as described in Section 6.5. The material parameters of steel used in this study are given in Table 6.1.

$$\sigma_y = \left[1+\left(\frac{\dot{\varepsilon}}{C}\right)^{\frac{1}{P}}\right]\left(\sigma_o + \beta E_p \varepsilon_{eff}^p\right) \tag{6.15}$$

Table 6.1 Steel material properties

Type	Symbol	Units	Longitudinal Reinforcement	Transverse Reinforcement
Tangent modulus	E	MPa	207000	207000
Yield stress	f_y	MPa	460	365
Poisson ratio	v	-	0.3	0.3
Density	ρ	kg/m^3	7850	7850
Strain speed factor	C	-	1080.5	172.4
Ultimate strain factor	P	-	5.48	5.40

6.4 Concrete and ECC Material Models

Concrete is a porous and brittle material. When concrete is compacted, the micro-structural pores of the material collapse, and thus give rise to a inelastic compaction response. The plastic strains exist in the material and at the same time there is an increment in bulk modulus. Since concrete is an orthotropic material consisting of cement paste, aggregate and mortar, it is brittle in nature with different strengths in tension and compression. Therefore unlike steel, concrete cannot be characterized accurately using only a single parameter of f_c.

In modeling the concrete & hybrid-fiber ECC materials, well characterized cementitious parameters need to be obtained. Prior to that, a selection of material model capable of characterizing concrete and ECC behaviors when subjected to blast loading should be

made. In order to select a proper material model, concrete material models in LS DYNA version 971 were reviewed. These included 9 material models as follows,

- MAT 5_SOIL AND CRUSHABLE FOAM
- MAT 16_PSEUDO TENSOR
- MAT 17_ORIENTED CRACK
- MAT 25_GEOLOGICAL CAP MODEL
- MAT 72_CONCRETE DAMAGE Release III
- MAT 78_SOIL AND CONCRETE
- MAT 84_WINFRITH CONCRETE
- MAT 111_JOHNSON HOLMQUIST CONCRETE
- MAT 159_CONTINUOUS SURFACE CAP MODEL

MAT 16_PSEUDO TENSOR as regards to Malvar et al. (1997) and Lim (1999) appeared to be more appropriate to represent concrete as it is more robust as compared to MAT 5, MAT 17, and MAT 25. The material model incorporates the plasticity, hardening and softening characteristics of concrete/cementitious materials and has two non-intersecting failure surfaces (maximum and residual failure surfaces) capable of migrating the failure surface from one curve to another by incorporating damage scale factor. MAT 5_SOIL AND CRUSHABLE FOAM also incorporates two independent non-intersecting surfaces (maximum failure and residual failure surfaces) based on Drucker et al. (1957). MAT 17_ORIENTED CRACK is applicable for modeling brittle materials under significant tensile or shear loading when fracture is expected. However, strain rate effects could not be modeled using MAT 17. MAT 25_GEOLOGICAL CAP MODEL is a kinematic hardening cap model with two intersecting surfaces following Sandler et al. (1976) and Sandler and Rubin (1979). It consists of a non-softening convex yield surface defined by

a failure envelope and a hardening cap, and a plastic strain rate vector normal to the yield surface in stress pace. MAT 78_SOIL AND CONCRETE is defined by a deviatoric perfectly plastic, pressure dependent yield function. Cracking can be invoked by setting the residual strength factor *B* to a value between 0 and 1. The yield stress is multiplied by a factor *f* which reduces with plastic strain according to a trilinear law (Hallquist, 2007). This material model requires four curves: pressure - volumetric strain, yield stress - pressure, plastic strain at which fracture begins - pressure, and plastic strain at which residual strength is reached - pressure. Yonten et al. (2002) reported that MATs 25 and 78 were not able to predict the softening behavior of concrete, and thus provide significant limitations in modeling concrete behavior.

According to Malvar (1997), MAT 72_CONCRETE DAMAGE Rel. III is a significant modification of MAT 16_PSEUDO TENSOR. Some modifications to eliminate the shortcomings of MAT 16 are:

1. New pressure cut-off with an initial value of $-f_t$ that allows both the biaxial and triaxial tensile tests to reach a principal stress difference of f_t.
2. Implementation of an initial yield surface that is independent of the maximum and residual failure surfaces to represent initial yielding.
3. New shear damage accumulation by interpolating maximum failure surface with initial yield or residual failure surfaces to obtain the current failure surface.

Based on the aforementioned evaluation among the concrete material models, in this study, MAT 72_CONCRETE DAMAGE Rel. III is utilized. Schwer and Malvar (2005) have shown that MAT 72 Rel. III is able to characterize the behavior of concrete materials subjected to uniaxial, biaxial and triaxial loads. Moreover, the dynamic increase

factor (DIF) of concrete which is needed for high strain rate cases can also be considered. It has been shown by Lee (2006) to be able to model concrete under impact loading. The dynamic increase factor applied is presented in Section 6.5.

The ECC material tends to exhibit ductile behavior. It absorbs more energy due to its plasticity showing high failure strain due to the bridging effects arising from the fibers present therein as compared to concrete. In general, the ECC material may be modeled using similar parameters as those of the concrete material, only the numerical values are different. Therefore, MAT 72 Rel. III is also applicable for ECC.

In the concrete material, higher confinement effect results in higher material shear resistance. The deviatoric stress s_{ij} represents the shear resistance of the material and is obtained as follows.

$$s_{ij} = \sigma_{ij} - \tfrac{1}{3}\sigma_{kk}\delta_{ij} \tag{6.16}$$

σ_{kk} is the so called hydrostatic stress, whereas σ_{ij} is the shear stress.

MAT 72 Rel. III considers three failure surfaces (Figure 6.2) that should be defined to evaluate the flow variables. These variables are needed to correlate the stress – strain relationship of the material. The three failure surfaces are given as follows.

1. Maximum failure surface

   This failure surface is the primary surface that should be defined first to obtain the other two failures. There are three parameters of maximum failure ($\Delta\sigma_m$) surface as a function of pressure p: a_0, a_1 and a_2 (as shown in Equation 6.17) to be

obtained from laboratory test results for unconfined compression test and triaxial compression test.

$$\Delta\sigma_m = a_0 + \frac{p}{a_1 + a_2 p} \tag{6.17}$$

Three boundary conditions are needed to solve the three unknowns. They are:

- Unconfined uniaxial compression condition

  Under the uniaxial compression test–unconfined condition (Figure 6.3 a), the stresses applied to the specimen are $\sigma_1 = -f_c'$ and $\sigma_2 = \sigma_3 = 0$. Thus the pressure applied equals to $p = -\frac{1}{3}(\sigma_1 + \sigma_2 + \sigma_3) = \frac{1}{3} f_c'$. It should be noticed that stress is positive in tension and pressure is positive in compression. For the unconfined condition, $\Delta\sigma_m / f_c' = 1$. Concrete may achieve a higher compressive strength when confinement is provided, such as in a triaxial test wherein $\sigma_2 = \sigma_3 \neq 0$.

- Pure shear condition in plane stress

  This condition is achieved when the stresses applied to the specimen are $\sigma_1 = \tau$, $\sigma_2 = 0$ and $\sigma_3 = -\tau$ (pressure $p = 0$). Under pure shear condition (Figure 6.3b), deviatoric stresses obtained are similar to the applied stresses. These stresses are given as $s_1 = \tau, s_2 = 0$ and $s_3 = -\tau$. By using the deviatoric stresses obtained, the second invariant J_2 can therefore be derived as $J_2 = \tau^2$.

  Failure under the pure shear condition occurs when the maximum tensile stress f_t is achieved i.e. $\tau = f_t$. As hydrostatic pressure has no influence $(I_1 = 0)$ in the case of pure shear condition, based on Equation 6.13, by neglecting the effect of $\cos 3\theta$ the failure criterion is determined as

$$\begin{aligned} \phi(J_2) &= 0 \\ \sqrt{3J_2} - \Delta\sigma &= 0 \\ \Delta\sigma &= \sqrt{3} f_t \end{aligned} \tag{6.18}$$

- High confinement condition (Chen, 1994)

  One data point for concrete in the compressive meridian is utilized to obtain the maximum failure surface parameters of the material. The original data point is $(\rho/f_c' = 4.92, p/f_c' = 4.4)$. ρ is the length between point p ($\sigma_1, \sigma_2, \sigma_3$) and the hydrostatic axis and this equals to $\sqrt{2J_2}$. Thus, $\Delta\sigma_m$ equals to $\sqrt{3J_2} = \sqrt{1.5\rho} = 6.026$.

2. Initial yield surface

   Three parameters are implemented to achieve this failure surface: a_{0y}, a_{1y} and a_{2y} . Malvar et al. (1997) determined these three parameters by approximating the locus of points at $\Delta\sigma_y = 0.45\Delta\sigma_m$. Based on experiment data, the line slope connecting $(p_m, \Delta\sigma_m)$ and $(p_y, \Delta\sigma_y)$ is ⅓. Thus, $p_y = p_m - 0.55\Delta\sigma_m$.

$$\Delta\sigma_y = a_{0y} + \frac{p}{a_{1y} + a_{2y} p} \tag{6.19}$$

3. Residual failure surface

   There are three parameters that are needed to be obtained in achieving residual failure surface: a_{0f}, a_{1f} and a_{2f}. For the high residual stress difference $\Delta\sigma_r$ case, $\Delta\sigma_r$ should be limited to $\Delta\sigma_m$. Once it is exceeded, $\Delta\sigma_r$ should be reset to $\Delta\sigma_m(p_m)$. Maximum pressure p_m in this study is taken to be the same as that of Malvar et al. (1997) which is 3.878. Since for concrete the residual stress is taken to be zero, thus the parameter a_{0f} vanishes.

$$\Delta\sigma_r = a_{0f} + \frac{p}{a_{1f} + a_{2f} p} = \frac{p}{a_{1f} + a_{2f} p} \tag{6.20}$$

The current surface is obtained by interpolating the maximum failure surface with either initial yield surface or residual failure surface using parameter $\eta(\lambda)$. The parameter $\eta(\lambda)$ indicates the relative location of the current failure surface, while the damage parameter λ indicates the damage accumulation. The parameter λ is defined to be non- decreasing and depends upon strain rate enhancement factor r_f, effective plastic strain increment $\left(d\overline{\varepsilon^p} = \sqrt{\tfrac{2}{3}\varepsilon_{ij}^p \varepsilon_{ij}^p}\right)$ and b parameters which are given as follows:

- For the case of compressive pressure $(p \geq 0)$

  λ is obtained as given in Equation 6.21. Parameter b_1 is determined by assigning the G_{f_comp} obtained as the area under stress-displacement curve of the uniaxial compression tests for use in finite element modeling. The b_1 parameter is changed iteratively until G_{f_comp}/h of the uniaxial compression experiment is equal to the FE model stress strain curve.

$$\lambda = \int_0^{\overline{\varepsilon^p}} \frac{d\overline{\varepsilon^p}}{r_f \left(1 + p/r_f f_t\right)^{b_1}} \tag{6.21}$$

- For the case of tensile pressure $(p < 0)$

  In Equation 6.22, similar to the compressive pressure case, parameter b_2 of Equation 6.17 is determined by assigning the fracture energy $G_{f\_tensile}$ obtained as the area under stress-displacement curve of the uniaxial tensile tests for use in finite element modeling. The b_2 parameter is changed iteratively until the

$G_{f\_tensile}/h$ value for localization in one element width h from the uniaxial tensile test is equal to the area of the FE model stress strain curve.

$$\lambda = \int_0^{\overline{\varepsilon^p}} \frac{d\overline{\varepsilon^p}}{r_f\left(1+p/r_f f_t\right)^{b_2}} \tag{6.22}$$

- For triaxial compression condition

  In the triaxial compression test, in addition to λ there is an incremental damage parameter $\Delta\lambda$ which is given as

$$\Delta\lambda = b_3 f_d k_d \left(\varepsilon_v - \varepsilon_{v,yield}\right) \tag{6.23}$$

  where b_3 is obtained by the same procedure as b_1 and b_2 using triaxial tensile test results, k_d is the internal scalar multiplier, ε_v and $\varepsilon_{v,yield}$ are the volumetric strain and volumetric strain at yield respectively, and f_d is the incremental damage multiplier obtained as

$$f_d = \begin{Bmatrix} 1-\dfrac{\left|\sqrt{3J_2}\right|}{0.1} & for\ 0 \le \left|\sqrt{3J_2}/p\right| < 0.1 \\ 0 & for\ \left|\sqrt{3J_2}/p\right| \ge 0.1 \end{Bmatrix} \tag{6.24}$$

At $\eta = 1$, maximum failure surface is achieved when $\lambda = \lambda_m$ (Table 6.2). Therefore, the current failure surface is given as follows:

- For the condition after the initial yield surface, before the maximum failure surface is achieved $\left(\lambda < \lambda_m\right)$

$$\Delta\sigma = \eta\left(\Delta\sigma_m - \Delta\sigma_y\right) + \Delta\sigma_y \tag{6.25}$$

- For the condition after the maximum failure surface is achieved $\left(\lambda \ge \lambda_m\right)$

$$\Delta\sigma = \eta\left(\Delta\sigma_m - \Delta\sigma_r\right) + \Delta\sigma_r \tag{6.26}$$

Table 6.2 Values of damage parameter λ and failure surface parameter η

λ	$\eta(\lambda)$
0.00E+00	0.00E+00
8.00E-06	8.50E-01
2.40E-05	9.70E-01
4.00E-05	9.90E-01
5.60E-05	1.00E+00
7.20E-05	9.90E-01
8.80E-05	9.70E-01
3.20E-04	5.00E-01
5.20E-04	1.00E-01
5.70E-04	0.00E+00
1.00E+00	0.00E+00

Ottosen and Ristinmaa (2005) proposed a general formulation for initial yield or failure criterion that consists of three parameters; I_1 is used to characterize hydrostatic stress, while J_2 and $\cos 3\theta$ represent the influence of deviatoric stress. I_n and J_n are the n^{th} invariants of hydrostatic stress and deviatoric stress respectively.

$$\phi\left(I_1, J_2, \cos 3\theta\right) = 0 \tag{6.13}$$

The failure criterion proposed by Ottosen and Ristinmaa (2005) includes the $\cos 3\theta$ term that is given in Equation 6.13. As there are three principal stresses, the deviatoric plane is indeed periodic with a period of $120°$. There are three meridians which are obtained from the intersection of the failure surface with the hydrostatic plane and thus each has a constant θ.

- Tensile meridian

It occurs when the applied stresses in a specimen are such that $\sigma_1 > \sigma_2 = \sigma_3$. This condition corresponds to the hydrostatic stress state superposed by a tensile stress in the σ_1 direction. The tensile meridian is achieved when $\theta = 0°$. Malvar et al. (1997) found that for the case of pressure within a range of $-f_t \le p \le f_c/3$, the maximum tensile stress is limited to f_t. Thus, the tensile meridian is defined as follows:

$$\Delta\sigma = \frac{3}{2}(p + f_t) \tag{6.27}$$

Two boundary conditions are then obtained: at a point when $p = -f_t$ (triaxial tensile test condition) $\Delta\sigma = 0$ and at a point when $p = f_c/3$ (uniaxial tensile test condition) $\Delta\sigma = f_t$.

- Compressive meridian

  It occurs when the applied stresses in a specimen are such that $\sigma_1 < \sigma_2 = \sigma_3$. This condition corresponds to the hydrostatic stress state superposed by a compressive stress in the σ_1 direction. The compressive meridian is achieved when $\theta = 60°$.

  Malvar et.al. (1997) found that the compressive meridian can be obtained by multiplying the tensile meridian with a ratio $r' = r/r_c$. r' is defined as follows.

$$r' = \frac{2\left(1-\psi^2\right)\cos\theta + (2\psi - 1)\sqrt{4\left(1-\psi^2\right)\cos^2\theta + 5\psi^2 - 4\psi}}{4\left(1-\psi^2\right)\cos^2\theta + (1-2\psi)^2} \tag{6.28}$$

  $\psi = r_t/r_c$, where r_t and r_c are the radii of tensile and compressive meridian respectively as shown in Figure 6.4 $(r_t < r < r_c)$. Thus, the stress difference $\Delta\sigma$ of the compressive meridian is given as follows:

$$\Delta\sigma = \frac{3}{2\psi} r'(p + f_t) \tag{6.29}$$

- Shear meridian

  It occurs when the applied stresses in a specimen are such that $\sigma_1 > \sigma_2 = (\sigma_1 + \sigma_3)/2 > \sigma_3$. This condition corresponds to the hydrostatic stress state superposed by a positive stress τ in the σ_1 direction and a negative stress $-\tau$ in the σ_2 direction. The shear meridian is achieved when $\theta = 30°$.

In this study, the concrete and ECC material properties utilized is summarized in Tables 6.3. There are two types of concrete strength i.e. normal strength (NSC) and high strength (HSC) concrete with cylinder compressive strengths f_c' of 30 and 55 MPa respectively. The ECC material's f_c' is 55 MPa (Zhang, 2005). The three failure surfaces (initial yield, maximum failure and residual failure surfaces) are shown in Figure 6.5.

Table 6.3 NSC, HSC and ECC Material Properties

Type	Symbol	Units	NSC	HSC	ECC
Tangent modulus	E	*MPa*	25930	35100	17950
Compressive strength	f_c'	*MPa*	30.0	55.0	55.0
Tensile strength	f_t	*MPa*	2.90	4.35	4.95
Area under compressive stress - displacement curve	G_{f_comp}	*N/mm*	24.8	43.1	58.3
Area under tensile stress - displacement curve	$G_{f\_tensile}$	*N/mm*	0.066	0.105	21.1
Poisson ratio	v	-	0.2	0.2	0.2
Density	ρ	kg/m^3	2400	2400	2080

6.5 Strain Rate Effects

The dynamic increase factor (DIF) for use with concrete, as proposed in the CEB-FIP-1990 model for compression was adopted as follows:

$$DIF_C = \frac{f_{cd}}{f_{cs}} = \left(\frac{\dot{\varepsilon}_c}{\dot{\varepsilon}_{cs}}\right)^{1.026\alpha} \qquad \text{for } \dot{\varepsilon}_c \leq 30\ s^{-1}$$
$$DIF_C = \frac{f_{cd}}{f_{cs}} = \gamma\left(\frac{\dot{\varepsilon}_c}{\dot{\varepsilon}_{cs}}\right)^{1/3} \qquad \text{for } \dot{\varepsilon}_c > 30\ s^{-1} \tag{6.30}$$

where f_{cd} = dynamic compressive strength at strain rate $\dot{\varepsilon}_c$, f_{cs} = static compressive strength, $\dot{\varepsilon}_c$ = compressive strain rate ranging from 30×10^{-6} to 300 s^{-1}, $\dot{\varepsilon}_{cs} = 30 \times 10^{-6} s^{-1}$ = static compressive strain rate, $\log \gamma = 6.156\alpha - 2$, $\alpha = 1/(5 + 9f_{cs}/10)$.

In tension, the DIF of concrete was invoked as proposed by Malvar and Ross (1998) as follows:

$$DIF_T = \frac{f_{td}}{f_{ts}} = \left(\frac{\dot{\varepsilon}_t}{\dot{\varepsilon}_{ts}}\right)^{\delta} \qquad \text{for } \dot{\varepsilon}_t \leq 1\ s^{-1}$$
$$DIF_T = \frac{f_{td}}{f_{ts}} = \beta\left(\frac{\dot{\varepsilon}_t}{\dot{\varepsilon}_{ts}}\right)^{1/3} \qquad \text{for } \dot{\varepsilon}_t > 1\ s^{-1} \tag{6.31}$$

where f_{td} = dynamic tensile strength at strain rate $\dot{\varepsilon}_t$, f_{ts} = static tensile strength, $\dot{\varepsilon}_t$ = tensile strain rate ranging from 1×10^{-6} to 160 s^{-1}, $\dot{\varepsilon}_{ts} = 1 \times 10^{-6} s^{-1}$ = static tensile strain rate, $\log \beta = 6\,\delta - 2$, and $\delta = 1/(1 + 8f_{cs}/10)$.

The tensile DIF of ECC with a compressive strength of 55 MPa, as proposed by Zhang et al. (2005) for low strain rate is given as follows:

$$DIF_{ECC\_T} = \frac{f_{td}}{f_{ts}} = 2.0705\dot{\varepsilon}^{0.0575} \qquad \text{for } \dot{\varepsilon}_t \leq 1\ s^{-1} \tag{6.32}$$

It may be noted that the DIF values given in Equation 6.32 were rather close to those of concrete with a compressive strength of 23 MPa (Lee, 2006). Experimental data on the

DIF of ECC under high tensile strain rates and compression is not available at present. Thus, to be conservative, the tensile DIF values of ECC were calculated as recommended by Malvar and Ross (1998) for concrete with a compressive strength of 55 MPa for $\dot{\varepsilon}_t > 1\ s^{-1}$ as given by Equation 6.31. The compressive DIF equations as given by Equations 6.30 are adopted for the ECC material under compression. The DIFs of normal strength concrete (NSC), high strength concrete (HSC) and engineered cementitious composite (ECC) with respect to the respective strain rates are given in Table 6.4.

Table 6.4 Dynamic increase factor of concrete and ECC

$\dot{\varepsilon}$	DIF			$\dot{\varepsilon}$	DIF		
	NSC	HSC	ECC		NSC	HSC	ECC
	30 MPa	55 MPa	55 MPa		30 MPa	55 MPa	55 MPa
-1.000E+04	9.434	7.380	7.380	1.000E-06	1.000	1.000	1.000
-1.000E+03	9.434	7.380	7.380	3.000E-05	1.000	1.000	1.000
-1.600E+02	9.434	7.380	7.380	1.000E-04	1.039	1.023	1.023
-1.500E+02	9.233	7.223	7.223	1.000E-03	1.119	1.068	1.068
-1.000E+02	8.066	6.310	6.310	1.000E-02	1.205	1.116	1.116
-5.000E+01	6.402	5.008	5.008	1.000E-01	1.297	1.165	1.165
-1.000E+01	3.744	2.929	2.929	1.000E+00	1.396	1.217	1.217
-5.000E+00	2.972	2.324	2.425	5.000E+00	1.470	1.254	1.254
-1.000E+00	1.738	1.359	2.021	1.000E+01	1.503	1.270	1.270
-1.000E-01	1.585	1.292	1.770	5.000E+01	1.846	1.538	1.538
-1.000E-02	1.445	1.227	1.550	1.000E+02	2.326	1.938	1.938
-1.000E-03	1.318	1.166	1.358	1.500E+02	2.663	2.218	2.218
-1.000E-04	1.202	1.108	1.189	3.000E+02	3.355	2.794	2.794
-3.000E-05	1.146	1.079	1.109	1.000E+03	3.355	2.794	2.794
-1.000E-06	1.000	1.000	1.000	1.000E+04	3.355	2.794	2.794
0.000E+00	1.000	1.000	1.000				

The strain rate effect of the steel reinforcements, both the longitudinal and transverse reinforcement used was proposed by Malvar (1998) using linear approximation. The

adopted DIF formulation is valid for yield stress varying from 290 to 710 *MPa* and given as,

$$DIF_T = \left(\frac{\dot{\varepsilon}}{10^{-4}}\right)^{\alpha} \tag{6.33}$$

where $\dot{\varepsilon} =$ strain rate of rebar ranging between 1×10^{-4} to 10 s^{-1}, $\alpha = 0.074 - 0.040\left(f_y/414\right)$, and $f_y =$ rebar yield stress in *MPa*.

The DIFs of normal strength concrete (NSC), high strength concrete (HSC), engineered cementitious composite (ECC) and steel reinforcement used in this study are summarized in Figure 6.6.

6.6 Equation of State (EOS)

Equation of state (EOS) has a function to relate the hydrostatic pressure with the incremental volume change and the internal energy e_{internal} of the material. In this study, the EOS Tabulated Compaction (EOS 8) is applied to represent the material's response at the hydrostatic pressure level in accordance to MAT 72_release III. The pressure p is defined as follows.

$$p = C(\varepsilon_v) + \gamma T(\varepsilon_v) e_{\text{internal}} \tag{6.34}$$

ε_v, which is the volumetric strain, is given by the natural logarithm of the volume, $\ln(V/V_o)$. C and T are the coefficients tabulated against the volumetric strain ε_v, whereas γ is the ratio of specific heat. In this study, only the first term of Equation 6.30 is considered and generated automatically in MAT 72 Release III as recommended by Malvar et al. (1997) for the uniaxial compression test.

6.7 Erosion Material Model

The erosion material model is utilized to allow the material element to be eroded after it has failed. In LS DYNA, the erosion material model is applied using MAT_ADD_EROSION. Mainly, there are two types of erosion criterions; stress failure and strain failure. MAT_ADD_EROSION provides 7 failure criteria:

1. $p \geq p_{\max}$ where p is the pressure and $p_{\max}$ is the maximum pressure at failure.
2. $\varepsilon_3 \leq \varepsilon_{\min}$ where ε_3 is the minimum principal strain and $\varepsilon_{\min}$ is the minimum principal strain at failure.
3. $p \leq p_{\min}$ where p is the pressure and $p_{\min}$ is the minimum pressure at failure.
4. $\sigma_1 \geq \sigma_{\max}$ where σ_1 is the maximum principal stress and $\sigma_{\max}$ is the maximum principal stress at failure.
5. $\sqrt{\frac{3}{2}\sigma'_{ij}\sigma'_{ij}} \geq \bar{\sigma}_{\max}$ where σ'_{ij} are deviatoric stress components and $\bar{\sigma}_{\max}$ is the equivalent stress at failure.
6. $\varepsilon_1 \geq \varepsilon_{\max}$, where ε_1 is the maximum principal strain and $\varepsilon_{\max}$ is the maximum principal strain at failure.
7. $\gamma_1 \geq \gamma_{\max}$, where γ_1 is the shear strain and $\gamma_{\max}$ is the shear strain at failure.

Each of these erosion criterion is applied independently and once any of the stated failure criterions is exceeded, the particular material element will be deleted. It is necessary to ensure that correct erosion parameters are applied to the model. As this study deals with high strain rate due to blast loads, the stress in an element is a function of its strain rate. The higher the strain rate, the more the material is able to resist higher impulsive or

dynamic loads without failure. Based on the aforementioned condition, strain failure is the best solution to be applied as the failure criterion for use in this study.

6.8 Hourglass Control

In solid element analysis, the zero energy modes may appear due to reduced integration point. The reduced integration method, in LS DYNA finite element package, is occupied for efficiency. The zero energy modes appear when the displacement and strain measured from the integration point at the centre of each element are zero even though the rectangular elements are deformed as shown in Figure 6.7. As can be seen, the shape of the deformed elements resembled that of an hourglass with zero deformation, measured orthogonally along the dotted lines intersecting at the integration point at the centre of the element. For this reason, the zero energy mode is often called the hourglass modes.

As a consequence of zero displacement and strain measured, the strain energy $\frac{1}{2}\{u\}^T [K]\{u\}$ of the element is zero and this leads to the occurrence of zero energy modes. These modes reduce the ranks of the stiffness matrix K by n number of zero energy modes in addition to m number of rigid body modes. Rank deficiency may then occur.

A structure with elements experiencing undesired hourglass modes tends to have natural periods *T* that are typically much shorter than the periods of the structural response. In order to avoid zero energy modes in the solid elements, hourglass control function should be used. Dealing with spurious zero energy modes, hourglass control of the Flanagan – Belytschko viscous form type is applied to the model by incorporating exact volume integration method. This type of hourglass control is recommended by the LS DYNA

manual for problems involving high velocities and highly distorted elements. Beam elements, since it is essentially fully integrated, do not require hourglass control.

6.9 Summary

To summarize, concrete and hybrid fiber ECC are modeled using MAT 72 Concrete damage release III as solid elements with single integration points. Material parameters of concrete and ECC are obtained from available experimental data. To avoid the zero energy modes, hourglass control is applied in the model. Also, in order to properly capture the inelastic behavior of the RC structure, erosion is introduced into the material model using strains as the threshold. Reinforcement bars are modeled using MAT 3 Plastic Kinematic as beam-truss elements that can only resist axial loads. Concrete and steel are modeled as hybrid elements and are assumed to be fully bonded by merging the coincident nodes between adjacent concrete and steel elements.

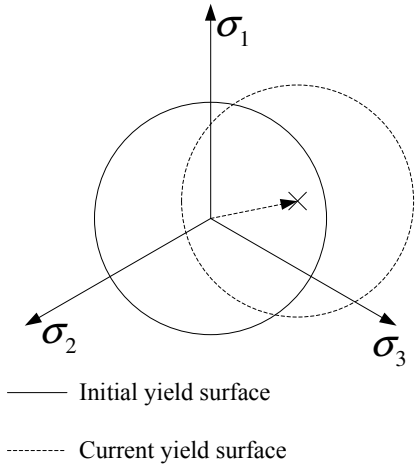

Figure 6.1 Kinematic hardening steel material yield surface in deviatoric plane

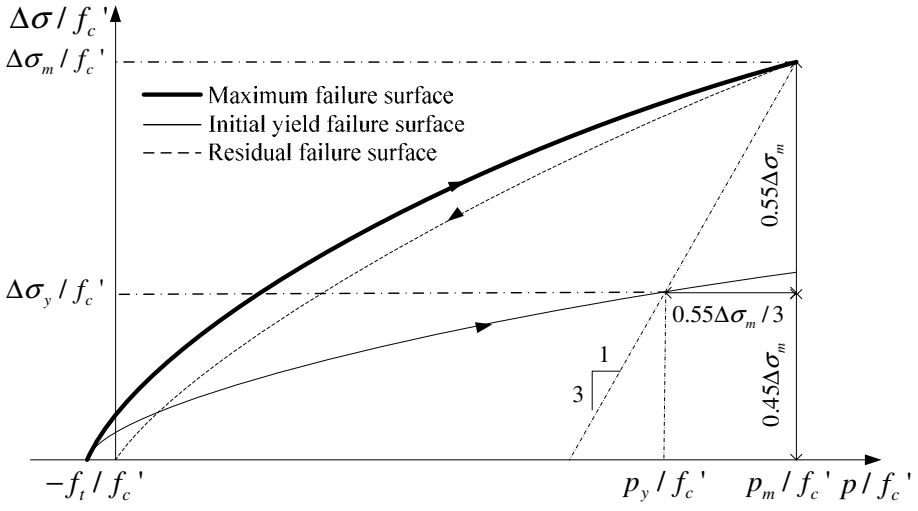

Figure 6.2 Failure surfaces of specimens subjected to triaxial compression tests

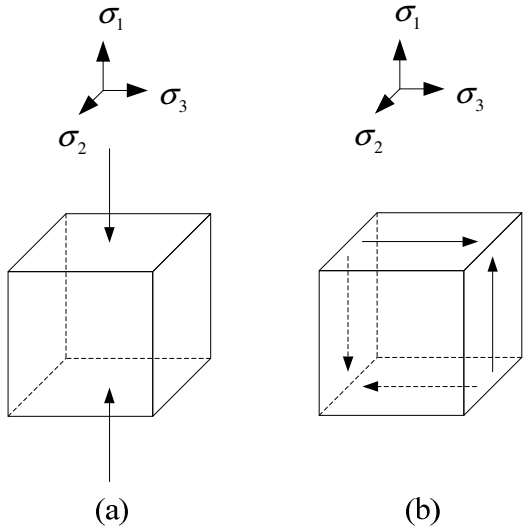

Figure 6.3 (a) Uniaxial compression and (b) Pure shear conditions

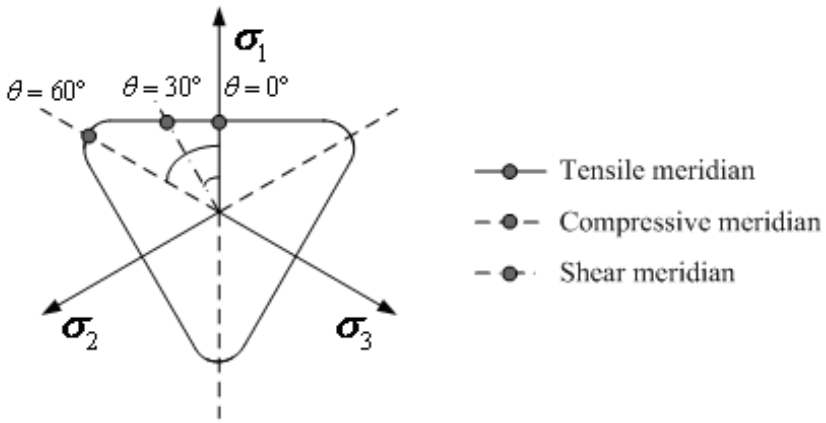

Figure 6.4 Deviatoric plane of concrete and ECC materials

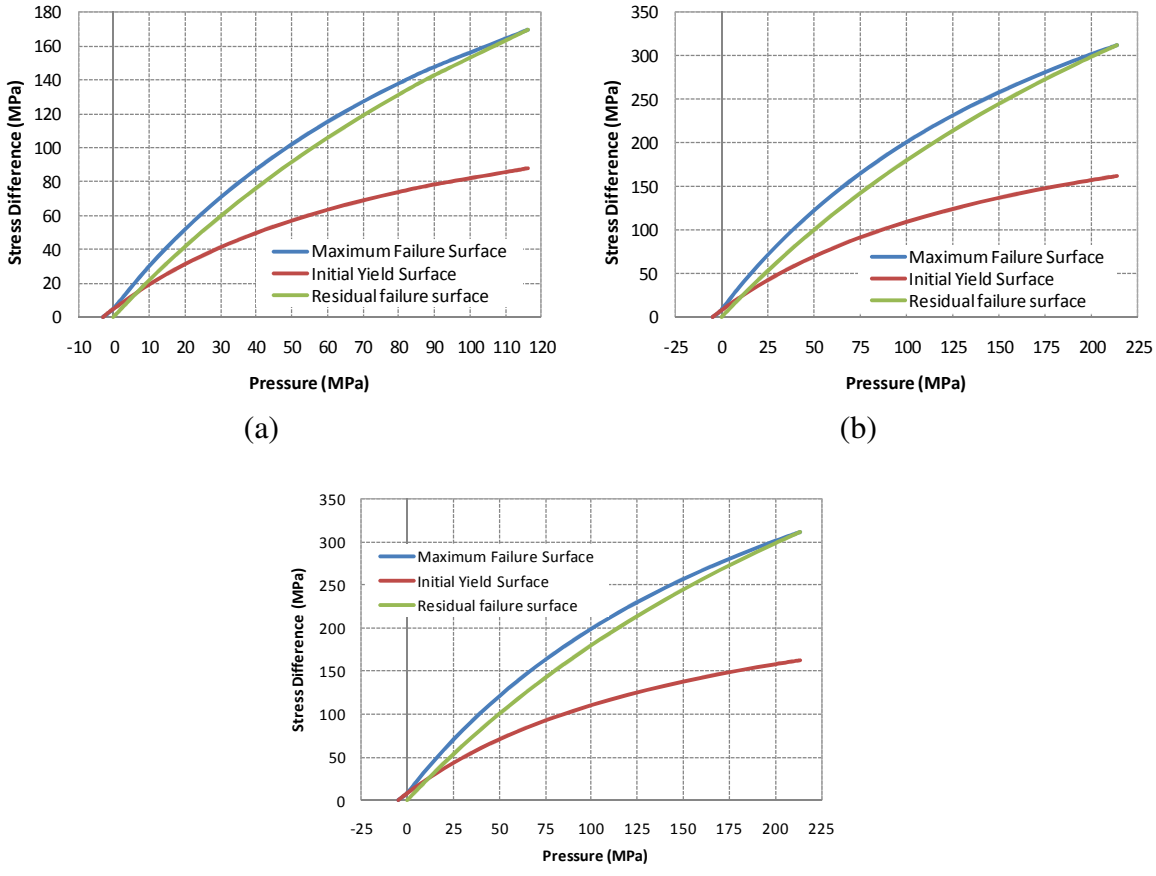

Figure 6.5 Failure surfaces of (a) NSC 30 MPa, (b) HSC 55 MPa, and (c) ECC 55 MPa

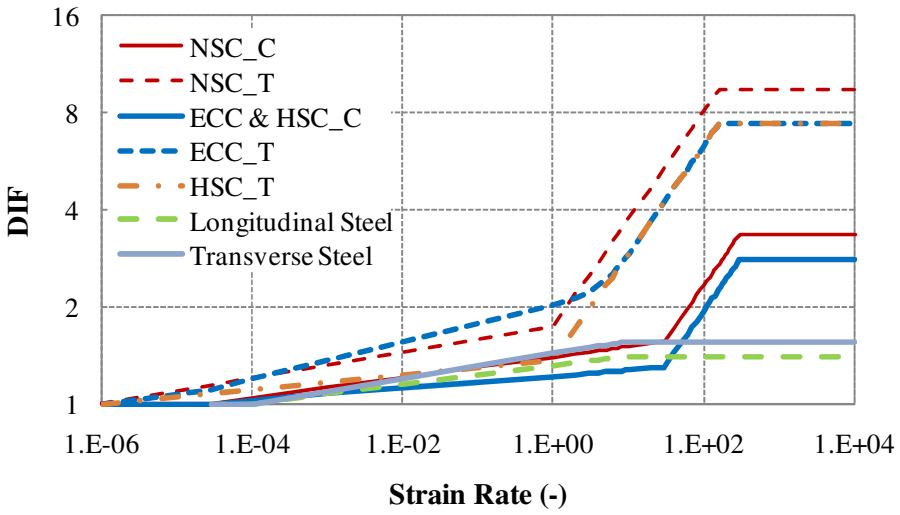

Figure 6.6 Strain rate enhancements (C: compression, T: tension)

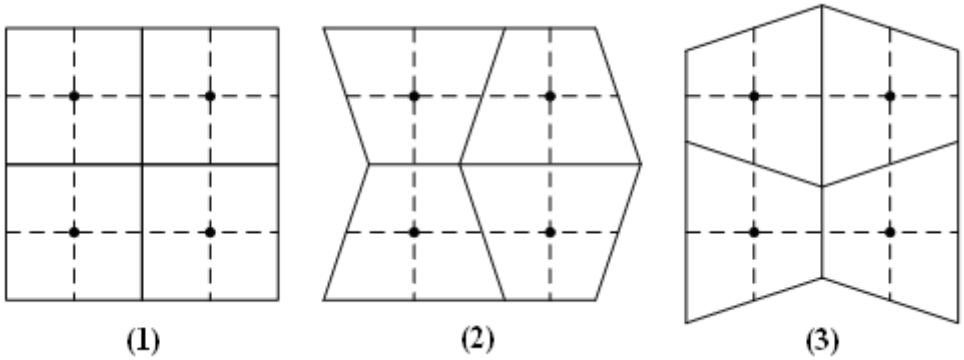

Figure 6.7 Zero energy modes of H8 element - Side view
(1) Initial condition, (2) and (3) Deformed conditions

7 Standalone Cantilever RC Column

7.1 Introduction

In recent years, some buildings were severely damaged and collapsed due to effects of blast explosions, causing numerous injuries and loss of life. To minimize the consequences associated with such external explosions, it is important to understand the response and vulnerability of critical structural elements present in a typical multi-storey structure when subjected to external blast loads. The structure investigated is a typical apartment block in Singapore. The ground floor of such apartment blocks is usually a void deck used for staging social events with car parks in close proximity. The present study is focused on the ground floor column, closest to the blast source considered as the most critical structural element in the structure. The study of ground floor RC column is preceded in this chapter by the study of standalone cantilever RC column. Numerical modeling of a standalone cantilever RC column subjected to blast load is examined for both elastic and inelastic condition. Theoretical solution using equivalent SDOF analysis is also carried out for both elastic and inelastic conditions.

Elastic condition may prevail when the RC column is subjected to low intensity blast. In this region, the displacement is dependent on the elastic stiffness of the column. When the blast is of a high intensity nature, inelastic response of RC column may be exhibited.

7.2 Elastic Analysis of Standalone Cantilever RC Column

In this study, elastic response analysis of standalone cantilever RC column is examined using both theoretical and numerical analysis. The theoretical analysis is carried out using equivalent SDOF - direct integration method, while the numerical analysis (MDOF) is done using LS DYNA finite element software. This study is aimed to validate the numerical results, to provide a benchmark for numerical methods.

7.2.1 SDOF Analysis using Direct Integration Method

The SDOF analysis is carried out using an equivalent SDOF system - direct integration method. The derivation and the results from the theoretical analysis for elastic cantilever RC columns are presented herein.

7.2.1.1 Derivation of Equivalent SDOF Method – Elastic Condition

Multi degree of freedom (MDOF) system can be represented using single degree of freedom (SDOF) system by introducing equivalent dynamic systems. In equivalent dynamic systems, three transformation factors (TFs) for the load, stiffness and mass are introduced into the system. The triangular blast pressure applied with respect to time as shown in Figure 7.1, is assumed to be uniformly distributed along the height of column (Figure 7.2). The blast pressure is then converted into a lateral load (Figure 7.3) applied at the column's tip after being multiplied by the load transformation factor (K_L).

Instead of using the equation of motion as shown in Equation 7.1, the equivalent approach stated in Equation 7.2 is carried out. Below are derivation steps of the equivalent SDOF system – direct integration method.

In the SDOF analysis, the column is modeled as a lumped mass connected to the base by the spring. The governing equation of the SDOF system may be given in terms of mass m, damping *c*, stiffness *k*, force *F* and displacement *u* as follows.

$$m\ddot{u} + c\dot{u} + ku = F(t) \tag{7.1}$$

while the governing equation of equivalent SDOF system is given as

$$m_e\ddot{u} + c\dot{u} + k_e u = F_e(t) \tag{7.2}$$

The equivalent terms of mass m_e, stiffness k_e and load F_e are as follows

$$\begin{aligned} m_e &= K_M.m \\ k_e &= K_S.k \\ F_e(t) &= K_L.F(t) \end{aligned} \tag{7.3}$$

K_M, K_S and K_L refer to the mass, the stiffness and the load transformation factors respectively. TM 5-1300 (1990) provides the values of K_M, K_S and K_L for one way elements based on the given edge conditions and loading diagrams of a specific problem.

The transformation factors, theoretically, are values used to transform the MDOF problems into SDOF system by modeling the deflection as a shape function of $\phi(x)$. The deflection functions of a cantilever RC column are determined from the boundary conditions. The deflection function assumed for the first mode is represented as

$$\phi(x) = 1 - \cos\left(\frac{\pi x}{2l}\right) \tag{7.4}$$

where x is the distance from fixed support whereas l is the column's length. This deflection function satisfies both geometry and force boundary conditions of the cantilever column subjected to uniform loads, and thus is appropriate for use herein. Now, the problem is reduced to one unknown parameter, u. The governing equation for equivalent SDOF analysis is given in Equation 7.2.

The equivalent mass, stiffness and force are as given in Equation 7.5. This equation is equal to Equation 7.3.

$$\begin{aligned} m_e &= \int_l m(x)\phi(x)^2\,dx \\ k_e &= \int_l EI(x)\phi''(x)^2\,dx \\ F_e &= \int_l q(x)\phi(x)\,dx \end{aligned} \tag{7.5}$$

Mass, stiffness, and load transformation factors, are obtained theoretically as

$$K_M = \frac{\int_l \phi(x)^2\,dx}{l} = \frac{\int_l \left(1-\cos\left(\frac{\pi x}{2l}\right)\right)^2 dx}{l} = \frac{3}{2}-\frac{4}{\pi} \approx 0.227 \tag{7.6}$$

$$K_S = \frac{\int_l \phi''(x)^2\,dx}{l^3} = \frac{\int_l \left(\left(\frac{\pi x}{2l}\right)^2 \cos\left(\frac{\pi x}{2l}\right)\right)^2 dx}{l^3} = \frac{\pi^4}{32} \approx 3.044 \tag{7.7}$$

$$K_L = \frac{\int_l \phi(x)\,dx}{l} = \frac{\int_l \left(1-\cos\left(\frac{\pi x}{2l}\right)\right) dx}{l} = 1-\frac{2}{\pi} \approx 0.3634 \tag{7.8}$$

Assuming that the excitation during the interval is approximated as a linear function having time step Δt for time duration of $t_i \le t \le t_{i+1}$, the load function is obtained as

$$F_e(t) = \left(1 - \frac{t - t_i}{\Delta t}\right) F_{ei} + \left(\frac{t - t_i}{\Delta t}\right) F_{e(i+1)} \tag{7.9}$$

Substituting Equation 7.9 into Equation 7.2, for time duration of $t_i \le t \le t_{i+1}$ the following is obtained.

$$m_e \ddot{u} + c\dot{u} + k_e u = \left(1 - \frac{t - t_i}{\Delta t}\right) F_{ei} + \left(\frac{t - t_i}{\Delta t}\right) F_{e(i+1)} \tag{7.10}$$

There are two sets of solutions to be obtained from Equation 7.10: complimentary (u_c) and particular (u_p) solutions.

$$u = u_c + u_p \tag{7.11}$$

Complimentary Solution

Solving the complimentary solution, the right hand side of Equation 7.10 is equated to zero.

$$m_e \ddot{u} + c\dot{u} + k_e u = 0 \tag{7.12}$$

A possible solution for Equation 7.12 that is applicable for all kinds of boundary conditions as follows:

$$u_c = e^{\xi \omega_e (t - t_i)} \left[A_i \cos \omega_{De} (t - t_i) + B_i \sin \omega_{De} (t - t_i) \right] \tag{7.13}$$

ξ is the damping ratio as given in Equation 2.3, A and B are constants of the complimentary solution, whereas ω_e and ω_{De} are the undamped and the damped natural frequency in radians given in Equations 7.14, respectively.

$$\omega_e = \sqrt{\frac{k_e}{m_e}} \tag{7.14 a}$$

$$\omega_{De} = \omega_e \sqrt{1 - \xi^2} \tag{7.14 b}$$

Particular solution

Particular solution takes into account the effect of loading. As the load function is approximated as a linear function, this solution may be assumed to follow a linear function.

$$u_p = C_i\left(t - t_i\right) + D_i \tag{7.15}$$

$$\dot{u}_p = C_i \tag{7.16}$$

From the substitution of Equations 7.15 and 7.16 in Equation 7.10, C and D which are constants of the particular solution are then obtained.

$$c.C_i + k_e\left[C_i\left(t - t_i\right) + D_i\right] = \left(1 - \frac{t - t_i}{\Delta t}\right)F_{ei} + \left(\frac{t - t_i}{\Delta t}\right)F_{e(i+1)}$$

$$C_i = \frac{F_{e(i+1)} - F_{ei}}{k_e \Delta t} \tag{7.17}$$

$$c.C_i + k_e.D_i = F_{ei}$$

$$D_i = \frac{F_{ei} - c.C_i}{k_e} \tag{7.18}$$

Therefore, the particular solution is obtained as follows:

$$u_p = \frac{F_{ei} - c.C_i}{k_e} + \frac{\left(F_{e(i+1)} - F_{ei}\right)}{k_e \Delta t}\left(t - t_i\right) \tag{7.19}$$

Total Solution

Compiling the complimentary solution and the particular solution, the total solution is obtained as follows:

$$u = \underbrace{\frac{F_{ei} - c.C_i}{k_e} + \frac{\left(F_{e(i+1)} - F_{ei}\right)}{k_e \Delta t}\left(t - t_i\right)}_{(1)} + \underbrace{A_i e^{-\xi\omega_e\left(t - t_i\right)} \cos\omega_{De}\left(t - t_i\right)}_{(2)} + \underbrace{B_i e^{-\xi\omega_e\left(t - t_i\right)} \sin\omega_{De}\left(t - t_i\right)}_{(3)} \tag{7.20}$$

In order to obtain the constants of integration, the boundary conditions should be known for the displacement and velocity. As the total solution for the displacement is governed by Equation 7.20, the equation of velocity is obtained herein.

Parts 1, 2 and 3 of Equation 7.20 are then differentiated with respect to time t and result in the following equations:

$$\frac{d\left(\frac{F_{ei}-c.C_i}{k_e}+\frac{\left(F_{e(i+1)}-F_{ei}\right)}{k_e\Delta t}\left(t-t_i\right)\right)}{dt}=\frac{F_{e(i+1)}-F_{ei}}{k_e\Delta t} \tag{7.21}$$

$$\frac{d\left(A_i e^{-\xi\omega_e(t-t_i)}\cos\omega_{De}\left(t-t_i\right)\right)}{dt}=A_i e^{-\xi\omega_e(t-t_i)}\left\{-\xi\omega_e\cos\omega_{De}\left(t-t_i\right)-\omega_{De}\sin\omega_{De}\left(t-t_i\right)\right\} \tag{7.22}$$

$$\frac{d\left(B_i e^{-\xi\omega_e(t-t_i)}\sin\omega_{De}\left(t-t_i\right)\right)}{dt}=B_i e^{-\xi\omega_e(t-t_i)}\left\{-\xi\omega_e\sin\omega_{De}\left(t-t_i\right)+\omega_{De}\cos\omega_{De}\left(t-t_i\right)\right\} \tag{7.23}$$

Therefore, the expression for velocity of the total solution is obtained as

$$\begin{aligned}\dot{u}=&\frac{F_{e(i+1)}-F_{ei}}{k_e\Delta t}+A_i e^{-\xi\omega_e(t-t_i)}\left\{-\xi\omega_e\cos\omega_{De}\left(t-t_i\right)-\omega_{De}\sin\omega_{De}\left(t-t_i\right)\right\}\\&+B_i e^{-\xi\omega_e(t-t_i)}\left\{-\xi\omega_e\sin\omega_{De}\left(t-t_i\right)+\omega_{De}\cos\omega_{De}\left(t-t_i\right)\right\}\end{aligned} \tag{7.24}$$

To obtain the constants of integration, the displacement and the velocity at time t_i are described as u_i and v_i. Thus, the relationships between the constants are as follows:

$$u_i=\underbrace{\frac{F_{ei}-c.C_i}{k_e}}_{=D_i}+A_i$$

$$A_i=u_i-D_i \tag{7.25}$$

$$\dot{u}_i = \underbrace{\frac{F_{e(i+1)} - F_{ei}}{k_e \Delta t}}_{=C_i} + A_i\{-\xi\omega_e\} + B_i\{\omega_{De}\}$$

$$B_i = \frac{\dot{u}_i - C_i + \xi\omega_e A_i}{\omega_{De}} \tag{7.26}$$

Compiling all the relations between the constants of integration as stated in Equations 7.17, 7.18, 7.25 and 7.26, the displacement equation over a time t_{i+1} is then obtained as

$$u_{i+1} = \underbrace{C_i \Delta t + D_i}_{(1)} + \underbrace{(u_i - D_i)}_{(2)} e^{-\xi\omega_e \Delta t} \cos\omega_{De}\Delta t + \underbrace{\left(\frac{\dot{u}_i - C_i + \xi\omega_e A_i}{\omega_D}\right)}_{(3)} e^{-\xi\omega_e \Delta t} \sin\omega_{De}\Delta t \tag{7.27}$$

Parts 1, 2 and 3 of Equation 7.27 result in the following equations

$$(1): C_i \Delta t + D_i = \frac{F_{ei}(2\xi) + F_{e(i+1)}(\omega_e \Delta t - 2\xi)}{\omega_e k_e \Delta t}$$

$$(2): u_i - D_i = u_i - \frac{F_{ei}(\omega_e \Delta t + 2\xi) - F_{e(i+1)}(2\xi)}{\omega_e k_e \Delta t}$$

$$(3): \frac{\dot{u}_i - C_i + \xi\omega_e A_i}{\omega_{De}} = \frac{\dot{u}_i k_e \Delta t - \left(F_{e(i+1)} - F_{ei}\right) + \xi\omega_e k_e \Delta t . u_i - \xi\left[F_{ei}(\omega_e \Delta t + 2\xi) - F_{e(i+1)}(2\xi)\right]}{\omega_{De} k_e \Delta t}$$

The total solution of the expression for displacement for time step *i+1* using the direct integration method of equivalent SDOF system is therefore obtained as a function of the displacement and the velocity at time step *i* and the applied forces at time step *i* and *i+1* as follows:

$$u_{i+1} = u_i\left[e^{-\xi\omega_e\Delta t}\left(\frac{\xi\omega_e}{\omega_{De}}\sin\omega_{De}\Delta t+\cos\omega_{De}\Delta t\right)\right]+\dot{u}_i\left[\frac{e^{-\xi\omega_e\Delta t}}{\omega_{De}}\sin\omega_{De}\Delta t\right]$$
$$+F_{ei}\cdot\left[\frac{1}{\omega_e k_e\Delta t}\left\{2\xi-(\omega_e\Delta t+2\xi).e^{-\xi\omega_e\Delta t}\cos\omega_{De}\Delta t\right\}+\left(\frac{1-\xi(\omega_e\Delta t+2\xi)}{\omega_{De}k_e\Delta t}\right)e^{-\xi\omega_e\Delta t}\sin\omega_{De}\Delta t\right] \quad (7.28)$$
$$+F_{e(i+1)}\left[\frac{1}{\omega_e k_e\Delta t}\left\{(\omega_e\Delta t-2\xi)+2\xi.e^{-\xi\omega_e\Delta t}\cos\omega_D\Delta t\right\}+\left(\frac{2\xi^2-1}{\omega_{De}k_e\Delta t}\right)e^{-\xi\omega_e\Delta t}\sin\omega_D\Delta t\right]$$

Using the same procedures as the displacement equation, it gives rise to expression for velocity as follows:

$$\dot{u}_{i+1} = \left\{\begin{array}{l} -u_i e^{-\xi\omega_e\Delta t}\left[\frac{\xi^2\omega_e{}^2+\omega_{De}{}^2}{\omega_{De}}\right]\sin\omega_{De}\Delta t+\dot{u}_i e^{-\xi\omega_e\Delta t}\left[\cos\omega_{De}\Delta t-\frac{\xi\omega_e}{\omega_{De}}\sin\omega_{De}\Delta t\right] \\ +F_{ei}\left[-\frac{1}{k_e\Delta t}+e^{-\xi\omega_e\Delta t}\left\{\frac{1}{k_e\Delta t}\cos\omega_{De}\Delta t-\left(\frac{\omega_e{}^2}{\omega_{De}k}+\frac{\xi\omega_e}{\omega_{De}k_e\Delta t}\right)\sin\omega_{De}\Delta t\right\}\right] \\ -F_{e(i+1)}\frac{1}{k_e\Delta t}\left[\cos\omega_{De}\Delta t+\frac{\xi\omega_e}{\omega_{De}}\sin\omega_{De}\Delta t-1\right] \end{array}\right\} \quad (7.29)$$

7.2.1.2 SDOF - Displacement Analysis of the Cantilever RC column Subjected to Blast Load

Making use of Equation 7.28, displacement results of cantilever RC columns of various dimensions can therefore be obtained. In this present study, 20 sizes of cantilever RC columns are investigated (Table 7.1). For each column, the amount of longitudinal reinforcements is kept to be the same (A=804.25 mm^2).

In terms of blast load, the uniformly distributed pressures applied to the column are varied from 0.01 MPa to 0.05 MPa provided that the column is still in elastic condition. Loading duration t_D is also varied from 5 msec to 15 msec to achieve various t_D/T ratios. The load transformation factor of 0.4 based on TM5-1300 US Army Corps of Engineer is first applied to the model.

Table 7.1 Model Description of Cantilever Column

Model	Model	Loading Direction	*B* (mm)	*H* (mm)	*L* (m)	*T* (msec)
1	1	x	400	400	2	19.242
2	2	x	250	650	2	30.887
	2	y	250	650	2	12.259
3	3	x	250	500	2	30.889
	3	y	250	500	2	15.493
4	4	x	250	400	2	30.868
	4	y	250	400	2	19.119
5	5	x	250	350	2	30.847
	5	y	250	350	2	19.119
6	6	x	250	300	2	30.812
	6	y	250	300	2	25.438
7	7	x	250	250	2	30.767
8	8	x	300	800	2	25.632
	8	y	300	800	2	10.326
9	9	x	300	600	2	25.611
	9	y	300	600	2	13.179
10	10	x	300	500	2	25.567
	10	y	300	500	2	13.179
11	11	x	300	400	2	25.489
	11	y	300	400	2	19.176
12	12	x	300	300	2	25.495
13	13	x	400	1000	2	19.317
	13	y	400	1000	2	8.699
14	14	x	400	800	2	19.312
	14	y	400	800	2	10.348
15	15	x	400	600	2	19.266
	15	y	400	600	2	13.22
16	16	x	400	500	2	19.216
	16	y	400	500	2	15.591
17	17	x	500	500	2	15.621
18	18	x	600	600	2	13.254
19	19	x	600	500	2	13.24
	19	y	600	500	2	15.638
20	20	x	250	600	2	30.89
	20	y	250	600	2	13.145

It is shown in Figure 7.4 to Figure 7.7 that for the case of a cantilever RC column subjected to blast load over a range of applied pressures, the peak displacement which

occurs at the tip of the column plotted against t_D/T follows a power function. Comparing the loading duration of the dynamic loading, the results show that for a longer loading duration T_d the peak displacement which occurs at the tip of cantilever is larger.

The displacement of columns subjected to the blast load is a function of the blast pressure, loading duration and natural period of structure. The blast pressure and loading duration correlate to the impulse of the applied blast pulse, in that the longer the loading duration the bigger the impulse applied. In an actual explosion, the blast pressure and loading duration depend upon the type of explosives, the charge weight and the stand-off distance where the explosive is placed.

Dynamic magnification factor (DMF) is the ratio of the displacement under dynamic loading $F(F_0,t)$ to the displacement under the static loading F_0. The DMF value of a column differs in time following a trigonometric function. A complete derivation of the DMF equation following structural dynamic theory is given in Appendix C.

There are two intervals of time based on loading duration t_D, as follows:

1. For the interval of $0 \le t \le t_D$, the DMF is obtained as

$$DMF = \frac{u}{u_{static}} = 1 - \cos \omega_e t + \frac{1}{\omega_e t_D} \sin \omega_e t - \frac{t}{t_D} \tag{7.30}$$

2. For the interval of $t \ge t_D$, the DMF may be obtained by

$$DMF = \frac{u}{u_{static}} = \frac{1}{\omega_e t_D} \left\{ \sin \omega_e t - \sin \omega_e \left(t - t_D \right) \right\} - \cos \omega_e t \tag{7.31}$$

As shown in Figure 7.8, the maximum value of DMF depends upon the ratio of t_D / T. The higher the ratio of t_D /T, the DMF obtained is greater. Once the ratio of t_D/T reaches a

value larger than 1, the slope of the curve reduces until the DMF reaches the maximum value of 2.

The DMF analysis can therefore be used as to validate the results obtained from either the theoretical equivalent SDOF analysis or numerical MDOF analysis. Figure 7.8 shows a comparison between the DMF value obtained from the structural dynamic theory and from SDOF analysis. It is observed that the DMF of SDOF results are in good agreement with the theoretical values.

7.2.2 MDOF Analysis using LS DYNA

Numerical modeling for the cantilever RC column under blast loading is carried out using LS DYNA FE software. By making use of the material models and material parameters described in Chapter 6, 20 models of cantilever RC columns as described in Table 7.1 are herein analyzed and discussed. For a brief description reference may be made to Chapter 6, MAT 72_CONCRETE DAMAGE Rel. III is utilized for modeling the normal strength concrete (NSC) material with cylinder compressive strength f_c' of 30 MPa. For the steel reinforcement, MAT 3_PLASTIC KINEMATIC is used. However, the erosion of the material is not activated at this stage as the model is still in an elastic condition.

7.2.2.1 MDOF - Displacement Analysis of the Cantilever RC column Subjected to Blast Load

Similar to the SDOF analysis, 20 sizes of RC column model are modeled numerically in LS DYNA. Provided that the column is still in an elastic condition, uniformly distributed triangular pressure loads applied to the column vary from 0.01 MPa to 0.05 MPa, and the loading durations range vary between 5 msec and 15 msec. It may be noted that some of

the models of the cantilever RC columns are no longer in an elastic condition when subjected to triangular pressure loads of 0.04 MPa and 0.05 MPa. For such cases the results are not shown here, neither for such cases in the SDOF analysis.

The results show that the behavior of columns when subjected to an equivalent blast load over a range of applied pressures obtained from MDOF analysis is very similar to that of the SDOF analysis (Figures 7.9 to 7.12). The peak displacement of the column plotted against t_D/T also follows a power function. Similar to the SDOF analysis, it is noted that the longer the loading duration t_D, the larger the peak displacement of the cantilever RC column.

Figure 7.13 shows a comparison between the DMF values obtained from the structural dynamic theory and from the MDOF analysis. It is noted that the DMF of the MDOF analysis shows good agreement with the theoretical values. Some discrepancies are also shown particularly in cases where the column is subjected to blast loading parallel to its major axis (y). Such discrepancies appear due to significant difference in percentage terms, although the relative difference in absolute terms between MDOF and SDOF analysis are very small, around 0.01 mm or less (Figures 7.14 to 7.17). Table 7.2 shows the percent and relative differences in absolute terms.

Table 7.2 Percent (%) and relative differences in some of the elastic analysis results

Model	Loading Direction	Loading duration t_D (msec)	Natural Period T (msec)	t_D/T	SDOF Displacement (mm)			MDOF Displacement (mm)			Errors	
					0.01 *MPa*	0.03 *MPa*	0.05 *MPa*	0.01 *MPa*	0.03 *MPa*	0.05 *MPa*	% Diff.	Relative Difference (mm)
8	y	5	10.33	0.48	0.022	0.067	0.111	0.024	0.073	0.121	8.84	0.0060
13	y	5	8.70	0.57	0.012	0.037	0.062	0.014	0.043	0.072	16.29	0.0064
14	y	5	10.35	0.48	0.022	0.067	0.111	0.025	0.073	0.122	10.03	0.0068
8	y	10	10.33	0.97	0.028	0.085	0.142	0.031	0.093	0.156	9.24	0.0082
13	y	10	8.70	1.15	0.015	0.045	0.076	0.018	0.056	0.091	20.29	0.0097
14	y	10	10.35	0.97	0.028	0.085	0.142	0.032	0.094	0.157	10.47	0.0092
8	y	15	10.33	1.45	0.031	0.093	0.154	0.034	0.102	0.171	10.31	0.0099
13	y	15	8.70	1.72	0.016	0.049	0.081	0.020	0.059	0.098	19.17	0.0099
14	y	15	10.35	1.45	0.031	0.093	0.154	0.035	0.104	0.173	11.55	0.0111

Examination of the transformation factors provided by the TM5-1300 US code is carried out without considering the TFs of 9 cases mentioned in Table 7.3. Load and mass transformation factors (K_L and K_M) obtained are plotted against the ratio of the loading duration to the natural period of columns (t_D/T) as shown in Figure 7.18.

On the basis of load transformation factors (K_Ls), TM5-1300 code with its proposed value of 0.40 slightly overestimates the average value of the obtained K_Ls. The K_L values obtained ranged between 0.368 and 0.421 with most of the values below 0.40. The structural dynamics theory provides a unique KL value equal to 0.363 as a lower bound to the K_L values obtained.

With regards to the mass transformation factors (K_Ms), TM5-1300 code proposed a K_M value for the cantilever RC column subjected to uniformly distributed load to be taken as 0.26. As shown in Figure 7.18, this code overestimates the K_M values obtained. The K_M values obtained are relatively similar to the K_M provided by theoretical structural dynamics given as 0.227. The obtained K_Ms range from 0.222 to 0.242.

As shown in Figure 7.19, the transformation factors are also plotted against B/H ratio by taking into account the TFs of 9 cases mentioned in Table 7.2. The outliers of the 9 cases mentioned in Table 7.2 are circled in red. The K_L outliers ranged in magnitude from 0.438 to 0.486 whereas K_M outliers ranged between 0.260 and 0.289. Figure 19 shows that significant difference in terms of percentage (larger than 8%) between displacements analyzed using the SDOF and MDOF methods leads to incorrect transformation factors obtained.

7.3 Inelastic Analysis of Single Cantilever RC column Subjected to Blast Load

7.3.1 Inelastic SDOF Analysis

The elastic behavior of a single cantilever RC column subjected to blast loads has been discussed in Section 7.2. When the intensity of the applied blast loads increases, elastic SDOF analysis may not be applicable for use in the analysis as parts of the structure behaves beyond their plastic yield point. Herein, inelastic SDOF analysis is carried out.

For inelastic modeling, the resistance vs. displacement curve of the structure needs to be obtained. The slopes of the resistance vs. displacement curve of a structure represent its structural stiffness. Typically after reaching its yield point the stiffness is assumed to reduce gradually. A typical simplified bilinear elasto-plastic resistance curve is employed herein as shown by the dotted line in Figure 7.20. K_1 is the elastic stiffness whereas K_2 is the plastic stiffness of the structure.

Obtaining The Resistance Curve

Theoretical values of the ultimate flexural resistance of the cantilever RC column can be calculated as shown in Figure 7.21.

Force in Equilibrium

When the top reinforced bars A_s' are not yet reaching their yield point, the compressive depth of concrete is governed by

$$x = \frac{f_y A_s - 700 A_s' + \sqrt{\left(700 A_s' - f_y A_s\right)^2 + 1688.4 f_{cu} b A_s' d'}}{1.206 f_{cu} b} \tag{7.32}$$

where f_y is the yield strength of the rebar, f_{cu} is the cube compressive strength of the concrete, A_s and A_s' are the area of bottom and top rebar respectively, d' is the concrete cover and b is the breadth of concrete cross section.

The top rebars A_s' could be under two possible stress conditions: compression or tension. When the depth of the neutral axis x is less than the thickness of concrete cover d', the top rebar is in tension. It is in compression if $x > d'$.

For the case when the top rebars A_s' have yielded, the neutral axis is obtained as follows.

$$x = \frac{f_y.\left(A_s' + A_s\right)}{0.603 f_{cu} b} \tag{7.33}$$

The compression force of concrete C_c, the rebars forces $T_{s1,2}$ and the ultimate moment M_u are therefore formulated as follows.

$$\begin{aligned} C_c &= 0.67 f_{cu} b \times 0.9x \\ T_{s1} &= f_s.A_s' \\ T_{s1} &= f_y.A_s \end{aligned} \tag{7.34}$$

$$M_u = 0.55 C_c x + C_s\left(x - d'\right) + T_s\left(d - x\right) \tag{7.35}$$

In the SDOF analysis, blast loads are converted into an equivalent point load R acting at the tip of the cantilever RC column. When the column fails, R is assumed to reach R_u with the plastic hinge at the base of the cantilever RC column. R_u is obtained from the ultimate moment resistance M_u divided by the length of the column L as given in Equation 7.36.

$$M_u = R_u L$$

$$R_u = \frac{M_u}{L} \tag{7.36}$$

The R_u values of twenty such cantilever columns of various sizes with f_y, f_{cu} and d' equal to 460 MPa, 37.5 MPa and 50 mm, respectively, are given in Table 7.3.

Table 7.3 Yield force of cantilever RC column

Model	Loading Direction	B (mm)	H (mm)	L (m)	T (msec)	R_u (kN)
1	x	400	400	2	19.242	33.12
2	x	250	650	2	30.887	21.03
	y	250	650	2	12.259	54.56
3	x	250	500	2	30.889	20.22
	y	250	500	2	15.493	40.69
4	x	250	400	2	30.868	19.25
	y	250	400	2	19.119	31.44
5	x	250	350	2	30.847	18.72
	y	250	350	2	19.119	26.82
6	x	250	300	2	30.812	18.17
	y	250	300	2	25.438	22.19
7	x	250	250	2	30.767	17.57
8	x	300	800	2	25.632	26.04
	y	300	800	2	10.326	69.03
9	x	300	600	2	25.611	25.48
	y	300	600	2	13.179	50.54
10	x	300	500	2	25.567	24.85
	y	300	500	2	13.179	41.29
11	x	300	400	2	25.489	23.87
	y	300	400	2	19.176	32.04
12	x	300	300	2	25.495	22.79
13	x	400	1000	2	19.317	35.63
	y	400	1000	2	8.699	88.62
14	x	400	800	2	19.312	35.29
	y	400	800	2	10.348	70.12
15	x	400	600	2	19.266	34.73
	y	400	600	2	13.220	51.62
16	x	400	500	2	19.216	34.10
	y	400	500	2	15.591	42.37
17	x	500	500	2	15.621	43.35
18	x	600	600	2	13.254	53.22
19	x	600	500	2	13.240	52.60
	y	600	500	2	15.638	43.97
20	x	250	600	2	30.890	20.85
	y	250	600	2	13.145	49.94

Figure 7.22 shows the relationship between the yield forces R_u and natural period T of the twenty cantilever RC columns. It is indeed shown that the force needed to yield the structure with smaller T is higher than those of higher T.

For inelastic analysis, NONLIN software developed by the Federal Emergency Management Agent (FEMA) is utilized. Three input data are needed; ultimate resistance force R_u, initial stiffness K_1 and secondary stiffness K_2. The initial stiffness K_1 or the so called elastic stiffness is obtained from the section analysis depending on the type and the dimensions of the column. For the secondary stiffness K_2, there are three possible values; positive, negative or zero K_2. A positive K_2 represents the strain hardening process; meanwhile a negative K_2 represents the strain softening behavior or P-Delta effect of structure. In this study, elastic-fully plastic resistance curve as shown in Figure 7.26 is invoked as an approximate resistance curve and thus, the secondary stiffness K_2 is assumed to be zero representing a constant resistance force reached after yielding.

NONLIN software provides inelastic SDOF dynamic analytical solution derived from the Duhamel integral using Step by Step Integration method (Clough and Penzien, 1975). The step by step integration procedure is carried out using NONLIN software to solve incrementally the inelastic equations of motion. A series of small time increments Δt of the structural response is evaluated. Inelastic behavior of the column is taken into account by calculating the structural stiffness at the current deformed state K_i at the beginning of each time increment. The conditions at the end of each time increment are used as the initial conditions of the subsequent time increment interval assuming a “linear” change within each time increment to obtain the complete inelastic structural response.

Herein, the equivalent dynamic system is introduced to the SDOF inelastic analysis to obtain equivalent SDOF inelastic analysis. Transformation factors of load, stiffness and mass are once again introduced to the SDOF system. Combining the step by step integration procedure derived by Clough and Penzien (1975) with the equivalent system, the derivation of an equivalent SDOF inelastic system is thus obtained.

Recalling Equations 7.2 and 7.3, a structural dynamic concept for equivalent SDOF system is built. The governing equation of SDOF system is given as

$$m_e\ddot{u} + c\dot{u} + k_e u = F_e(t) \tag{7.2}$$

$$\begin{aligned} m_e &= K_M.m \\ k_e &= K_S.k \\ F_e(t) &= K_L.F(t) \end{aligned} \tag{7.3}$$

In the inelastic SDOF analysis, the cantilever RC column is assumed to have one plastic hinge at its fixed end and that the deflection function $\phi(x)$ follows Equation 7.37. This deflection function is derived from the boundary conditions of the column.

$$\phi(x) = \frac{x}{l} \tag{7.37}$$

The equivalent mass, stiffness and force are given as in Equation 7.6. This equation equals Equation 7.3.

$$\begin{aligned} m_e &= \int_l m(x)\phi(x)^2\,dx \\ k_e &= \int_l EI(x)\phi''(x)^2\,dx \\ F_e &= \int_l q(x)\phi(x)\,dx \end{aligned} \tag{7.6}$$

Mass, stiffness, and load transformation factors for inelastic SDOF analysis may be obtained as

$$K_M = \frac{\int_l \phi(x)^2 \, dx}{l} = \frac{\int_l \left(\frac{x}{l}\right)^2 dx}{l} = \frac{1}{3} = 0.33 \tag{7.38}$$

$$K_S = \frac{\int_l \phi''(x)^2 \, dx}{l^3} = \frac{\int_l (0)^2 \, dx}{l^3} = 0 \tag{7.39}$$

$$K_L = \frac{\int_l \phi(x) \, dx}{l} = \frac{\int_l \left(\frac{x}{l}\right) dx}{l} = \frac{1}{2} = 0.50 \tag{7.40}$$

In terms of forces at certain time *t*, the above governing equation can also be written as

$$F_{Ie}(t) + F_D(t) + F_{Se}(t) = F_e(t) \tag{7.41}$$

where F_{Ie} and F_{Se} are the equivalent inertia and spring forces respectively, F_D is the damping force and F_e is the equivalent applied load. Or in terms of time step *i* and step *i+1* as

$$\begin{gathered} F_{Iei} + F_{Di} + F_{Sei} = F_{ei} \\ F_{Ie(i+1)} + F_{D(i+1)} + F_{Se(i+1)} = F_{e(i+1)} \\ \Delta F_{Iei} + \Delta F_{Di} + \Delta F_{Sei} = \Delta F_{ei} \\ m_e \Delta \ddot{u}_i + c_i \Delta \dot{u}_i + k_{ei} \Delta u_i = \Delta F_{ei} \end{gathered} \tag{7.42}$$

As shown in Figure 7.23, assuming that the excitation during the time interval under consideration is approximated as a linear function having time step Δt for time duration of $t_i \le t \le t_{i+1}$, the velocity and the displacement functions at time *t* are obtained as follows.

$$\ddot{u}(t) = \ddot{u}_i + \frac{\Delta \ddot{u}_i}{\Delta t}(t - t_i) \tag{7.43}$$

$$\dot{u}(t) = \dot{u}_i + \ddot{u}_i (t - t_i) + \frac{1}{2} \frac{\Delta \ddot{u}_i}{\Delta t}(t - t_i)^2 \tag{7.44}$$

$$u(t) = u_i + \dot{u}_i (t - t_i) + \frac{1}{2}\ddot{u}_i (t - t_i)^2 + \frac{1}{6}\frac{\Delta\ddot{u}_i}{\Delta t}(t - t_i)^3 \tag{7.45}$$

Therefore, the displacement and the velocity at time t_{i+1} are given as

$$\Delta\dot{u}_i = \ddot{u}_i \Delta t + \frac{1}{2}\Delta\ddot{u}_i \Delta t \tag{7.46}$$

$$\Delta u_i = \dot{u}_i \Delta t + \frac{1}{2}\ddot{u}_i \Delta t^2 + \frac{1}{6}\Delta\ddot{u}_i \Delta t^2 \tag{7.47}$$

Equation 7.47 can also be written in terms of $\Delta\ddot{u}_i$ as

$$\Delta\ddot{u}_i = \frac{6}{\Delta t^2}\Delta u_i - \frac{6}{\Delta t}\dot{u}_i - 3\ddot{u}_i \tag{7.48}$$

Hence, substitution of Equation 7.48 into Equation 7.46 provides a velocity increment as

$$\Delta\dot{u}_i = \frac{3}{\Delta t}\Delta u_i - 3\dot{u}_i - \frac{1}{2}\ddot{u}_i \Delta t \tag{7.49}$$

By substituting Equations 7.48 and 7.49 into Equation 7.42, the equivalent SDOF system is therefore governed as

$$\Delta F_{ei} = m_e\left(\frac{6}{\Delta t^2}\Delta u_i - \frac{6}{\Delta t}\dot{u}_i - 3\ddot{u}_i\right) + c_i\left(\frac{3}{\Delta t}\Delta u_i - 3\dot{u}_i - \frac{1}{2}\ddot{u}_i \Delta t\right) + k_{ei}\Delta u_i \tag{7.50a}$$

or

$$\Delta F_{ei} + m_e\left[\frac{6}{\Delta t}\dot{u}_i + 3\ddot{u}_i\right] + c_i\left[3\dot{u}_i + \frac{1}{2}\ddot{u}\Delta t\right] = \left(k_{ei} + m_e\frac{6}{\Delta t^2} + c_i\frac{3}{\Delta t}\right)\Delta u_i \tag{7.50b}$$

Alternatively, Equation 7.50b may be written in terms of the effective stiffness and effective incremental force as follows:

$$\Delta\bar{F}_{ei} = \bar{k}_{ei}\,\Delta u_i \tag{7.51}$$

In which the effective stiffness and effective incremental force are given by

$$\bar{k}_{ei} = k_{ei} + m_e \frac{6}{\Delta t^2} + c_i \frac{3}{\Delta t}$$
$$\Delta \bar{F}_{ei} = \Delta F_{ei} + m_e \left[\frac{6}{\Delta t} \dot{u}_i + 3\ddot{u}_i \right] + c_i \left[3\dot{u}_i + \frac{1}{2} \ddot{u}_i \Delta t \right] \tag{7.52}$$

Therefore, the incremental displacement is obtained using Equations 7.52 as

$$\Delta u_i = \frac{\Delta \bar{F}_{ei}}{\bar{k}_{ei}} \tag{7.53}$$

The incremental displacement as obtained in Equation 7.53 is then utilized to generate the incremental acceleration and velocity using Equations 7.48 and 7.49, respectively.

The blast pressure is applied as a triangular blast pressure p having a peak of 0.5 MPa and a loading duration t_D of 10 msec. The displacement time histories for each column are obtained using the aforementioned procedures and the peak lateral displacements at the tip of the cantilever RC columns are shown in Figures 7.24 and 7.25. It may be noted that the higher the stiffness of the column the higher the stiffness of the column (smaller *B/H*, smaller T, and larger R_u as in Figure 7.22), the smaller the peak lateral displacement is obtained. As shown in Figure 7.25, there are 5 to 6 data of various lateral displacements scattering at around the same t_D/T value. Such data are from columns of various breadth B dimension having the same depth H. They possess nearly the same natural period T in the minor axis direction. Thus, the peak inelastic response is given as a function of the breadth to depth ratio *B/H*, the loading duration t_D, the applied blast pressure p and the natural period T of the cantilever RC column.

Peak response time is measured from time zero to the time when the column reaches its peak lateral displacement. The zero time is the time when the blast pressures reach the surface of the column. As shown in Figure 7.24 there is a tendency for the peak response

time to be longer in columns with larger peak displacement. Columns with lower stiffness (larger natural period *T*) tend to exhibit larger peak displacement.

Figures 7.26 to 7.29 show the displacement time history of column 4 (250 mm x 400 mm) and column 10 (300 mm x 500 mm) when subjected to blast directed along the major and minor axis. It is shown that in the inelastic SDOF case, once a significant amount of energy has been dissipated by the column to form a plastic hinge, the column deflection oscillates with time and is expected to "flat lined" to its plastic displacement.

7.3.2 MDOF Analysis using LS DYNA

Numerical modeling of the inelastic cantilever RC column under blast loading is carried out. Using the material specifications and the material models discussed in Chapter 6, twenty cantilever RC columns as described in Table 7.1 are analyzed and discussed in this section.

By applying triangular blast pressure to the surface of the cantilever column, the displacement time histories for each case are obtained. The peak displacement results of all twenty columns are then plotted in Figures 7.30 and 7.31. Figure 7.30 shows that there is a tendency for a longer peak response time as a larger peak displacement is achieved. Columns with larger natural period *T* tend to exhibit higher peak displacement. Moreover, larger displacements may be observed for smaller t_D/T ratios as shown in Figure 7.31. These two trends are similar to those of the results of the inelastic SDOF analysis.

Figures 7.32 to 7.35 show a comparison of the displacement time history obtained from SDOF and MDOF analyses of column 4 (250x400) and column 10 (300x500) subjected

to 0.5 MPa triangular pressure load p applied for a T_d of 10 msec along the major axis direction and along the minor axis of the column. The results show that peak responses (peak displacement and peak response time) obtained from SDOF and MDOF analyses are relatively similar, with slightly larger peak lateral displacement and longer peak response time obtained from SDOF analysis. However, the residual displacements measured at the tip of the cantilever at time 0.2 second are significantly different. The residual displacements obtained from MDOF analysis using LS DYNA are much smaller than those obtained from SDOF analysis.

7.3.3 Inelastic Analysis and Its Load Transformation Factor

Inelastic analysis of cantilever RC columns subjected to uniformly-distributed triangular pressure load has been studied using equivalent SDOF inelastic analysis and MDOF inelastic analysis. Both the SDOF and MDOF results are then compared as shown in Figure 7.36 and Figure 7.37. Good agreement between numerical modeling MDOF results and equivalent SDOF results is observed with relatively small differences.

Load transformation factor (K_L) in cantilever RC columns in an inelastic condition is evaluated herein. Based on TM5-1300 code and structural dynamic theory, the transformation factors of a structure in an inelastic condition depend on the loading condition and the boundary conditions of the structure. However, as shown in Figures 7.38 and 7.39 it is found that the load transformation factor may also be affected by the following parameters: the loading duration t_D, the natural period T and the loaded breadth to depth ratio B/H of the column. The B/H ratio also determines the column's R_u to resist the blast load, an important factor in inelastic analysis.

The TM5-1300 code and the structural dynamics theory provided a unique value of the load transformation factor (K_L) of cantilever RC columns in an inelastic condition of 0.50, while the K_Ls obtained from the proposed theoretical study cluster around the line K_L=0.5 (Figures 7.38 and 7.39). The effect of t_D/T to the load transformation factor is not clear although K_L seemed to decrease for t_D/T>0.8. Meanwhile, when plotted against the *B/H* ratio, the effect of *B/H* on K_L seemed to increase linearly. This shows that the K_L value, in addition to boundary and loading conditions, is also a function of t_D/T and *B/H* ratios.

Moreover, two groups of outliers are found and circled by the dotted lines as shown in Figures 7.38 and 7.39. The first group of outliers (Outliers_1) are found in the area where $t_D/T > 0.9$ or $B/H \leq 0.5$. Values of K_Ls in the group Outliers_1 that represent cases for blast directed along the major axis of column ranged from 0.37 to 0.42. Columns in group Outliers_1 exhibited severe plastic behavior at the base of the incident (tension) and distal (compression) faces of column as shown in Figure 7.40a, while most regions of the column remained in an elastic condition. This seemed to contradict that predicted using the inelastic SDOF analysis and is much closer to the elastic analysis ($\sim K_{L\ \text{structural dynamics theory}} = 0.363$). Meanwhile for the group Outliers_2 where $t_D/T < 0.4$ or $B/H > 2.5$ representing blasts along the minor axis direction, the columns are in a highly inelastic condition with all cases in the group failing due to the applied blast loads (Figure 7.40b).

7.4 Summary

Cantilever RC columns under both elastic and inelastic conditions have been investigated using SDOF and MDOF analyses. The results show good agreement between the MDOF numerical results and the equivalent SDOF results in terms of peak displacement at the tip of the cantilever. Therefore, the material models of concrete (MAT 72 Rel. III) and steel

(MAT 3) utilized in this study were shown to be able to model the behavior of RC and produce generally accurate results under both elastic and inelastic conditions.

Investigation of the transformation factors provided by TM5–1300 US code and structural dynamics theory are also carried out. From the investigation of the cantilever RC column in an elastic or inelastic condition, it may be concluded that at least three major parameters affect the elastic behavior and the transformation factors when the column was subjected to blast loads: the loading duration t_D, the natural period T and the loaded breadth to depth ratio B/H of the column. Moreover, under elastic loading condition, TM5-1300 specifies a higher K_M value of 0.26 while the K_M value calculated using the structural dynamic theory is relatively similar to those obtained in this study. In the evaluation of the elastic load transformation factor, the TM5-1300 proposed somewhat higher K_L value whereas the structural dynamic theory provides a lower estimate of the K_L value.

Under inelastic loading conditions, it is found that the effect of t_D/T to the load transformation factor is not clear although K_L seemed to tend to decrease for $t_D/T>0.8$. Meanwhile, when plotted against the B/H ratio, the effect of B/H on K_L seemed to increase linearly. Also, it was found that the inelastic SDOF analysis could not be applied to the columns with most of the regions behaving elastically (Outliners_1) and the columns behaving in a highly inelastic condition (Outliners_2). The columns in Outliers_2 seemed to have collapsed due to the applied blast loads. For a highly nonlinear column behavior, numerical analysis provides a better approach than the equivalent SDOF analysis. The numerical analysis of RC frame structures subjected to blast loads

carried out using LS DYNA FE code is studied and discussed further in the following chapters.

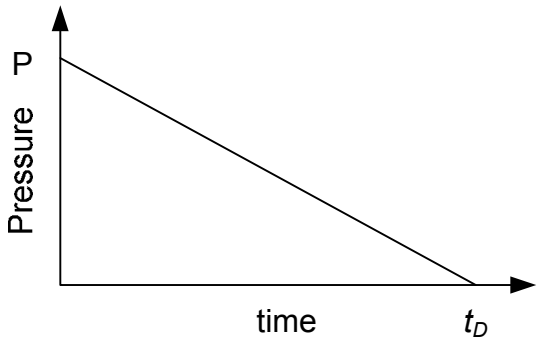

Figure 7.1 Triangular blast pressure applied to cantilever column

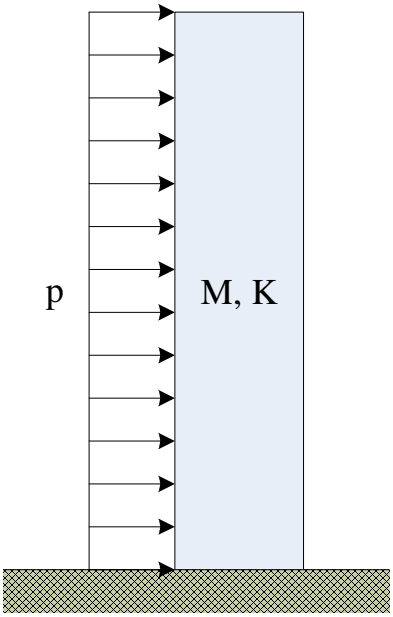

Figure 7.2 MDOF system of cantilever column

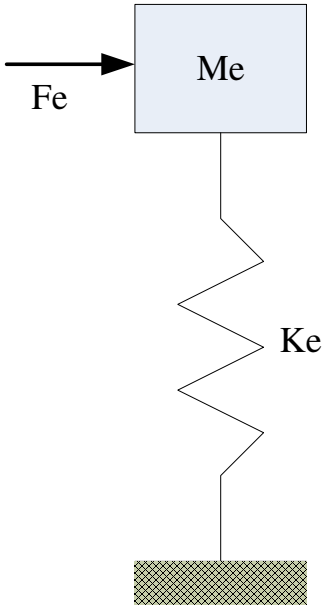

Figure 7.3 Equivalent SDOF system

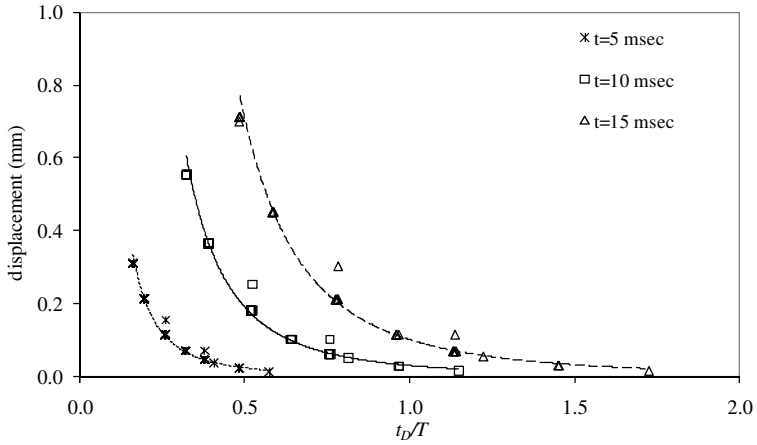

Figure 7.4 SDOF analysis _ peak displacement of cantilever RC column subjected to uniformly distributed dynamic pressure 0.01 MPa

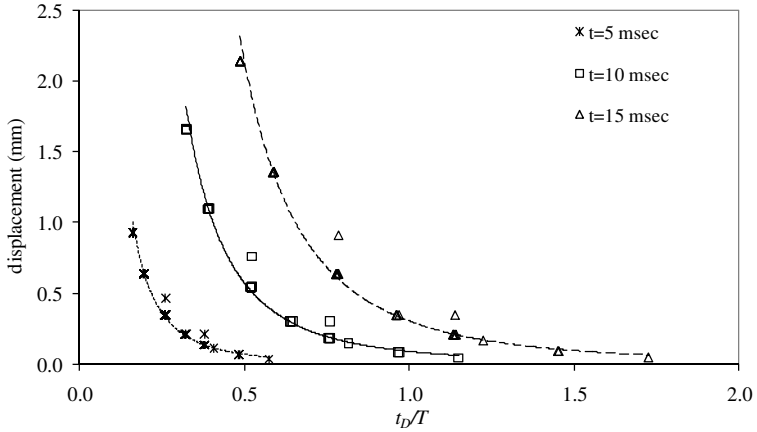

Figure 7.5 SDOF analysis _ peak displacement of cantilever RC column subjected to uniformly distributed dynamic pressure 0.03 MPa

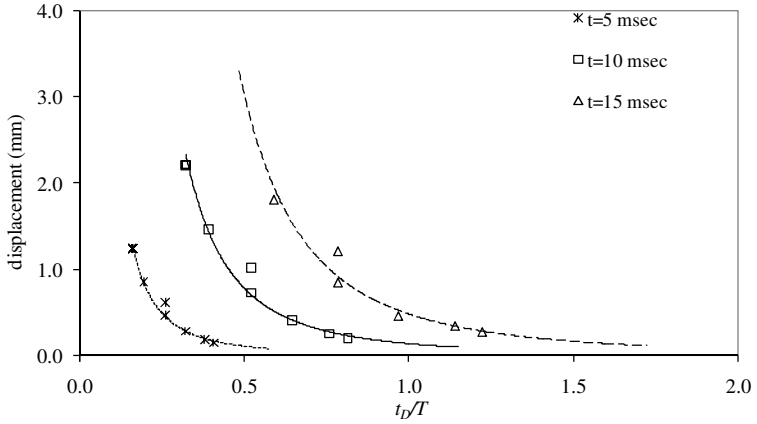

Figure 7.6 SDOF analysis _ peak displacement of cantilever RC column subjected to uniformly distributed dynamic pressure 0.04 MPa

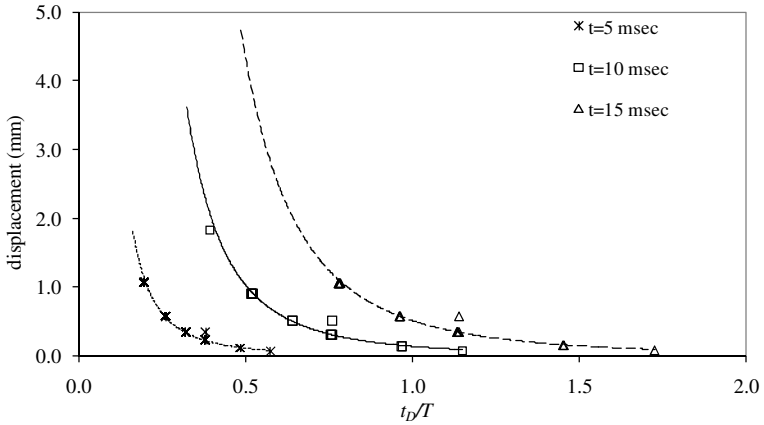

Figure 7.7 SDOF analysis _ peak displacement of cantilever RC column subjected to uniformly distributed dynamic pressure 0.05 MPa

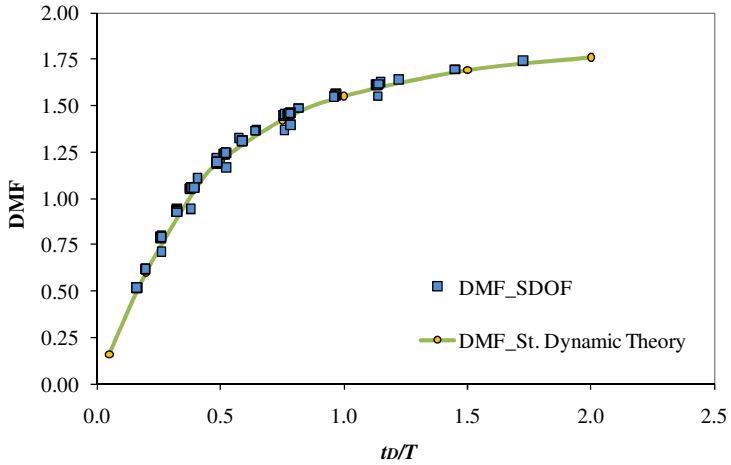

Figure 7.8 SDOF analysis _ maximum DMF of cantilever RC column subjected to uniformly distributed dynamic pressure

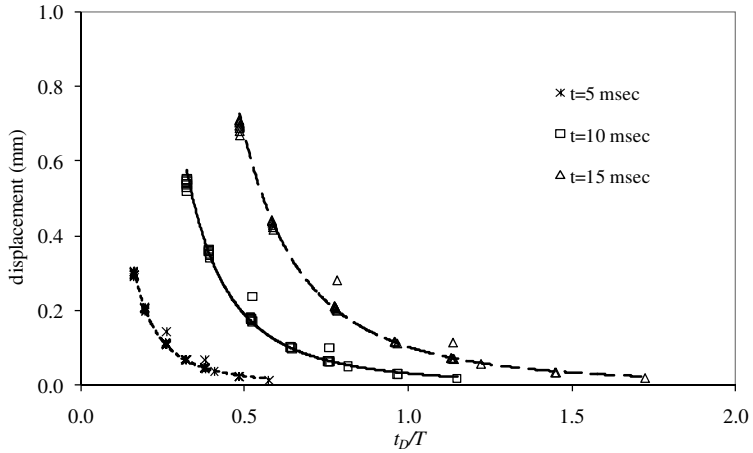

Figure 7.9 MDOF analysis _ peak displacement of cantilever RC column subjected to uniformly distributed dynamic pressure 0.01 MPa

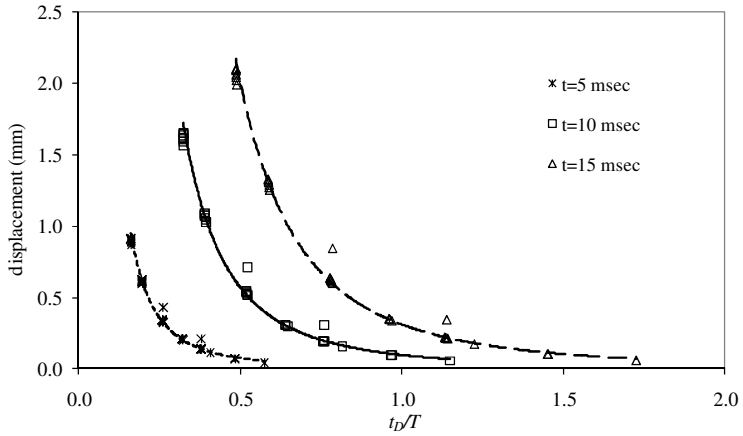

Figure 7.10 MDOF analysis _ peak displacement of cantilever RC column subjected to uniformly distributed dynamic pressure 0.03 MPa

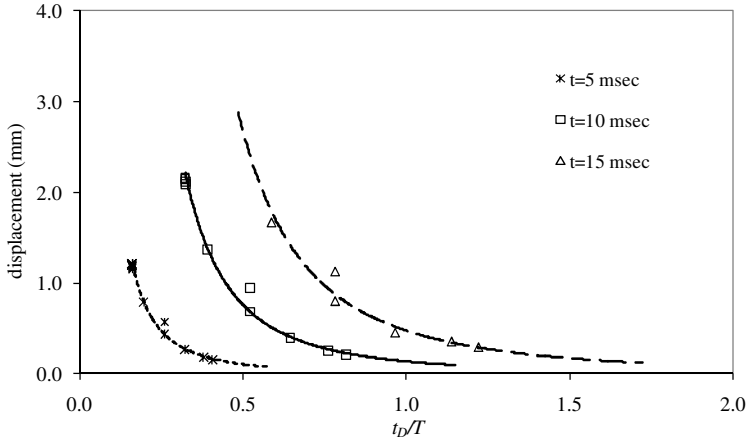

Figure 7.11 MDOF analysis _ peak displacement of cantilever RC column subjected to uniformly distributed dynamic pressure 0.04 MPa

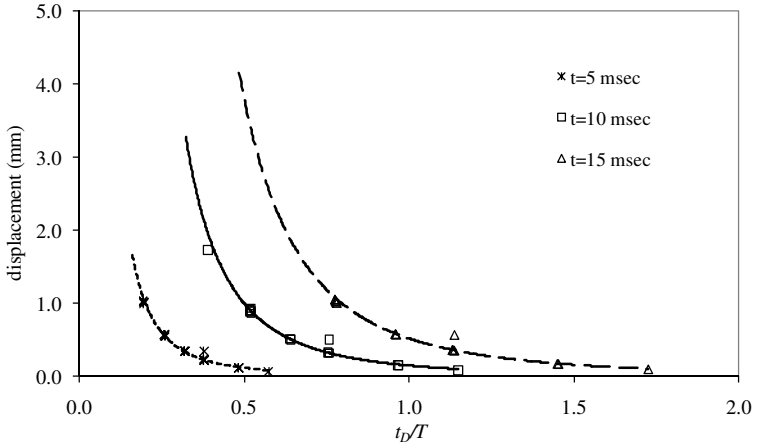

Figure 7.12 MDOF analysis _ peak displacement of cantilever RC column subjected to uniformly distributed dynamic pressure 0.05 MPa

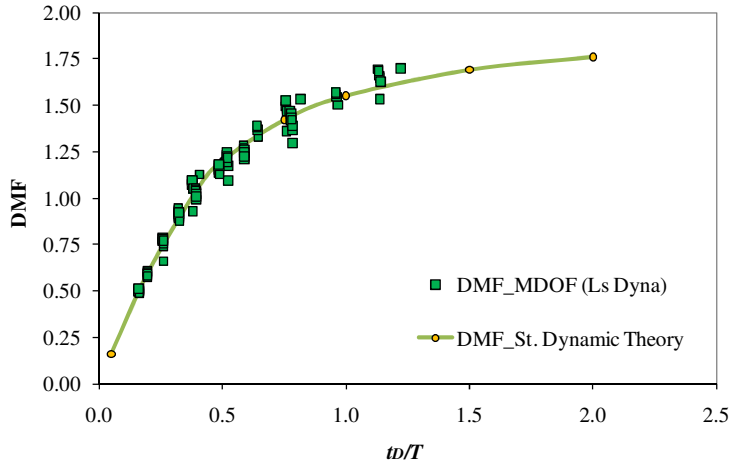

Figure 7.13 MDOF analysis _ maximum DMF of cantilever RC column subjected to uniformly distributed dynamic pressure

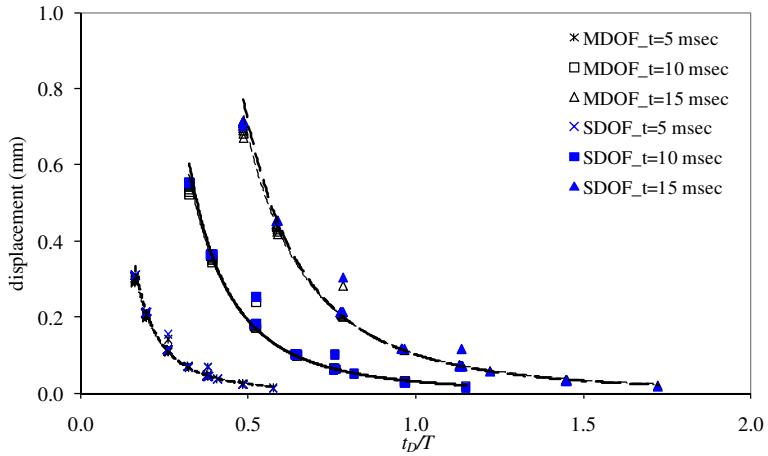

Figure 7.14 SDOF vs. MDOF analysis _ peak displacement of cantilever RC column subjected to uniformly distributed dynamic pressure 0.01 *MPa*

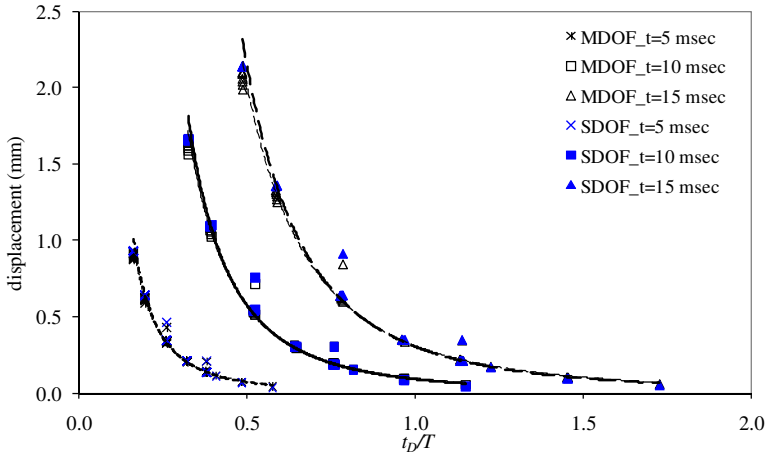

Figure 7.15 SDOF vs. MDOF analysis _ peak displacement of cantilever RC column subjected to uniformly distributed dynamic pressure 0.03 *MPa*

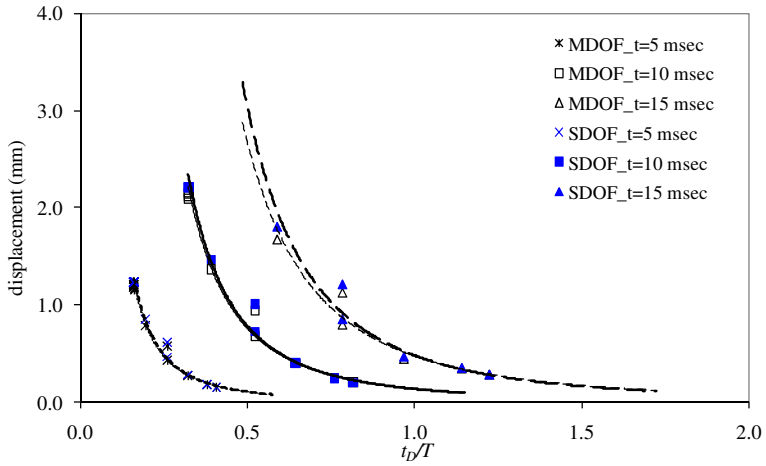

Figure 7.16 SDOF vs. MDOF analysis _ peak displacement of cantilever RC column subjected to uniformly distributed dynamic pressure 0.04 *MPa*

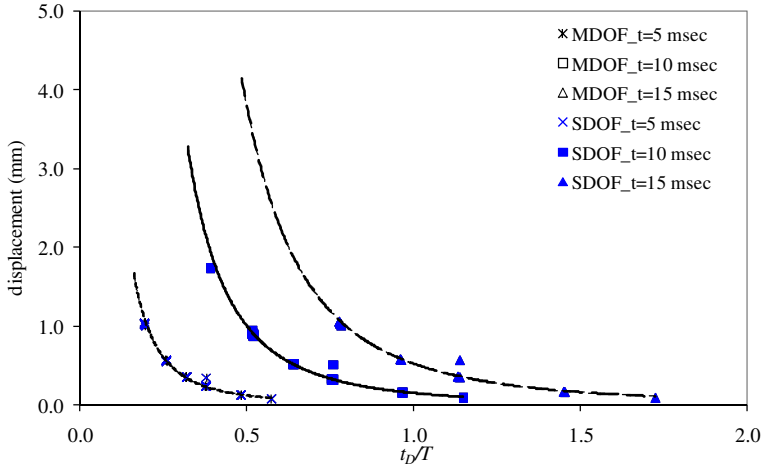

Figure 7.17 SDOF vs. MDOF analysis _ peak displacement of cantilever RC column subjected to uniformly distributed dynamic pressure 0.05 *MPa*

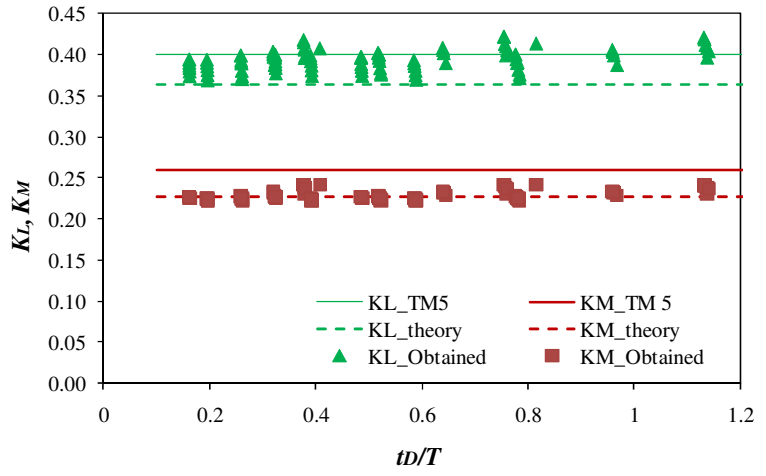

Figure 7.18 TM 5 – 1300, theory and the obtained transformation factors for cantilever column subjected to uniformly distributed load under elastic condition wrt. t_D/T

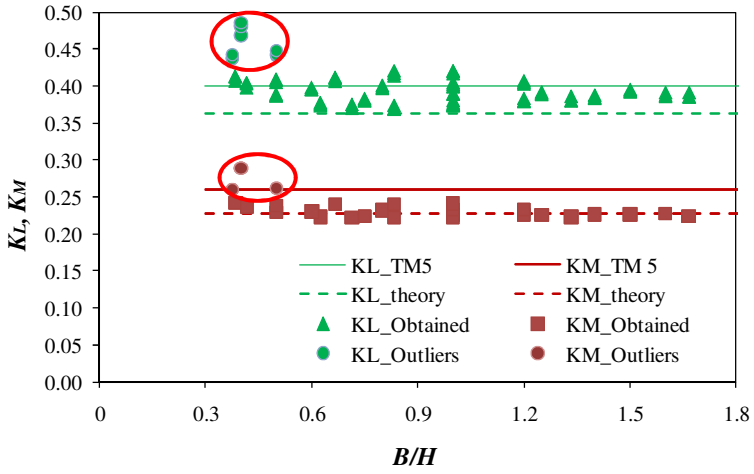

Figure 7.19 TM 5 – 1300, theory and the obtained transformation factors for cantilever column subjected to uniformly distributed load under elastic condition wrt. *B/H*

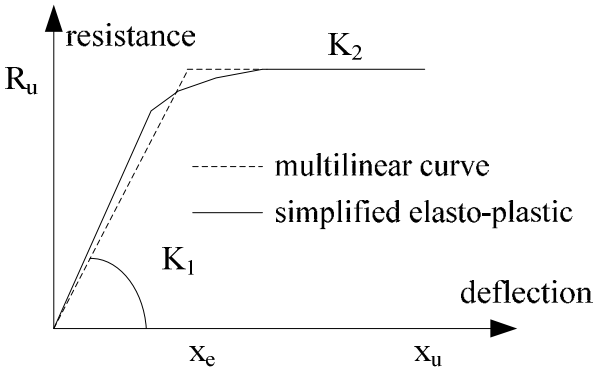

Figure 7.20 Simplified elasto-plastic resistance curve

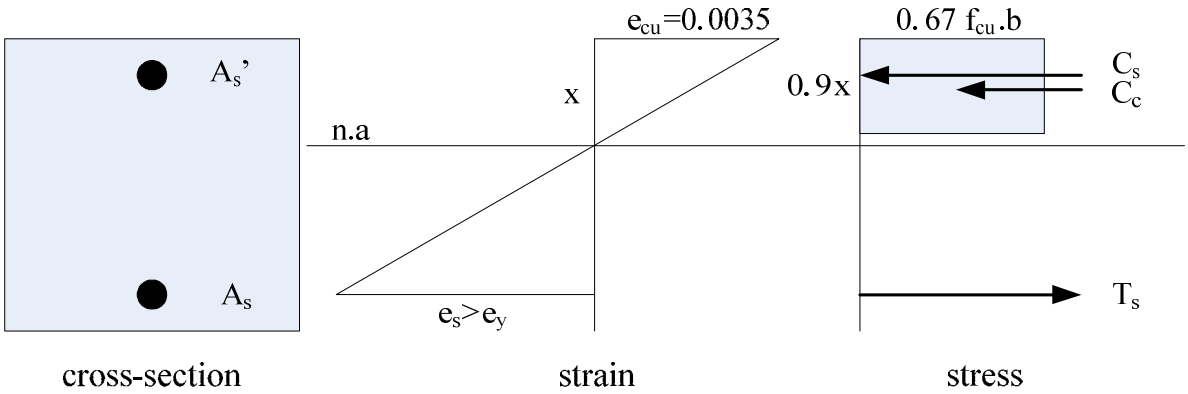

Figure 7.21 Ultimate condition of RC structural element

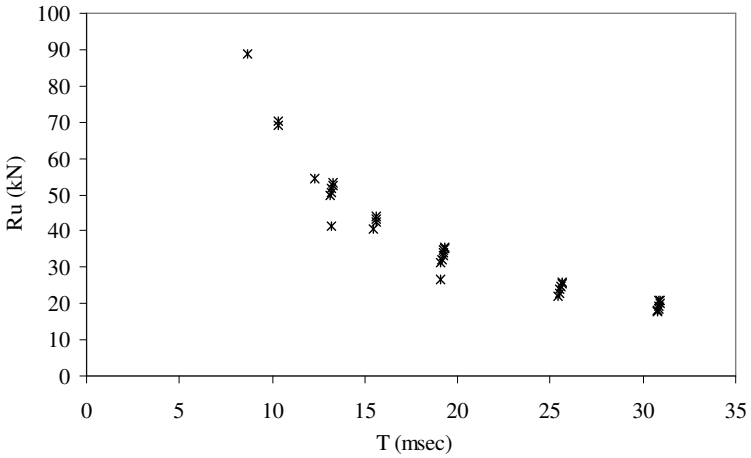

Figure 7.22 R_u values of the observed cantilever RC columns

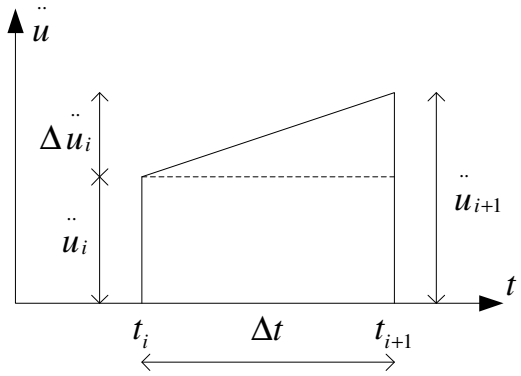

Figure 7.23 Assumed linear acceleration over time duration of $t_i \le t \le t_{i+1}$

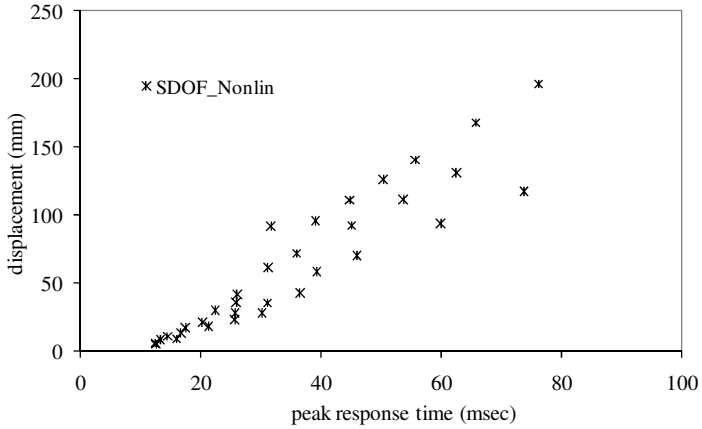

Figure 7.24 Inelastic peak responses of SDOF analysis of the cantilever RC column subjected to triangular blast pressure

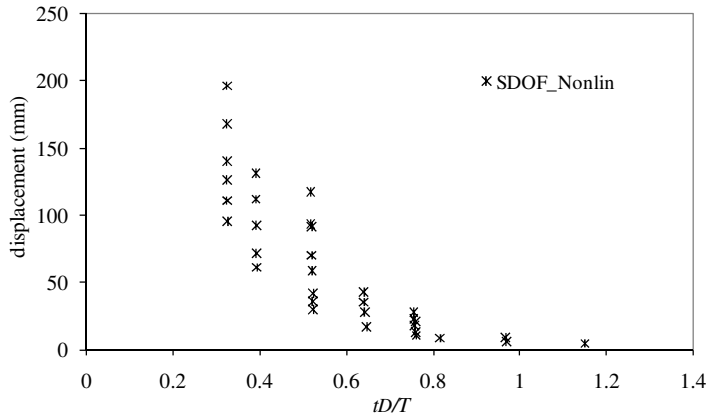

Figure 7.25 Inelastic peak SDOF lateral displacements plotted against t_D/T ratio of the cantilever RC column subjected to triangular blast pressure

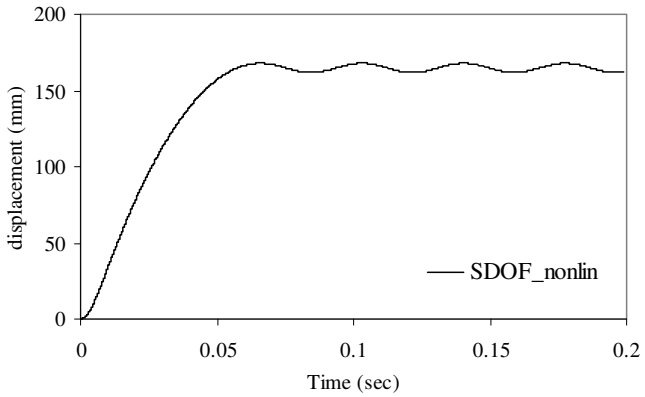

Figure 7.26 SDOF displacement time history of column 4 subjected to triangular pressure loaded in its minor axis direction

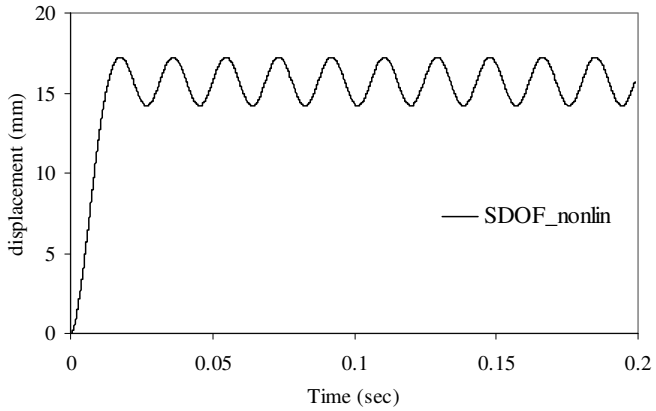

Figure 7.27 SDOF displacement time history of column 4 subjected to triangular pressure loaded in its major axis direction

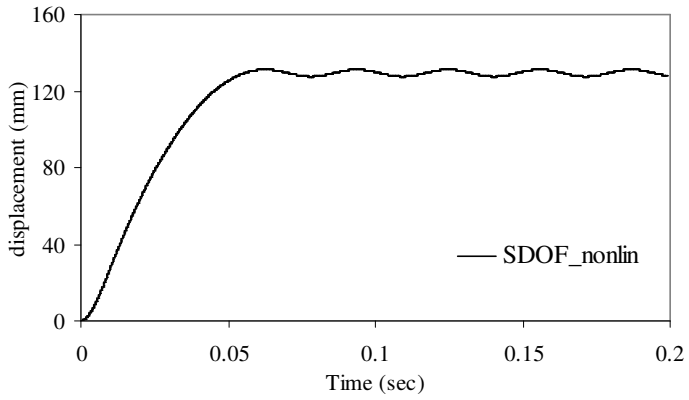

Figure 7.28 SDOF displacement time history of column 10 subjected to triangular pressure loaded in its minor axis direction

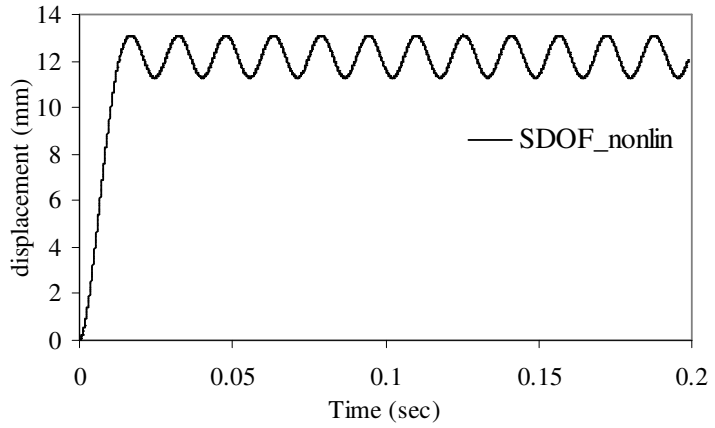

Figure 7.29 SDOF displacement time history of column 10 subjected to triangular pressure loaded in its major axis direction

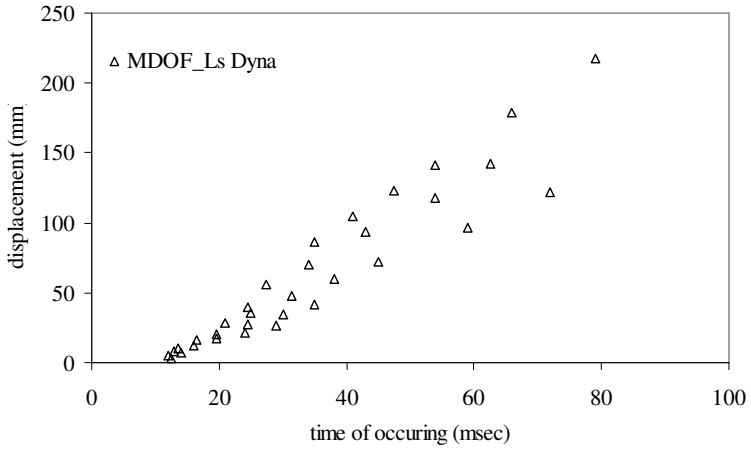

Figure 7.30 Inelastic peak responses of MDOF analysis of cantilever RC column subjected to triangular blast pressure

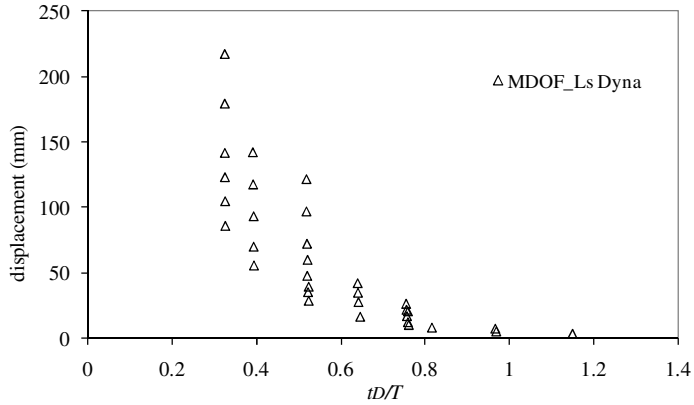

Figure 7.31 Inelastic peak MDOF lateral displacements plotted against ratio of t_D/T of cantilever RC column subjected to triangular blast pressure

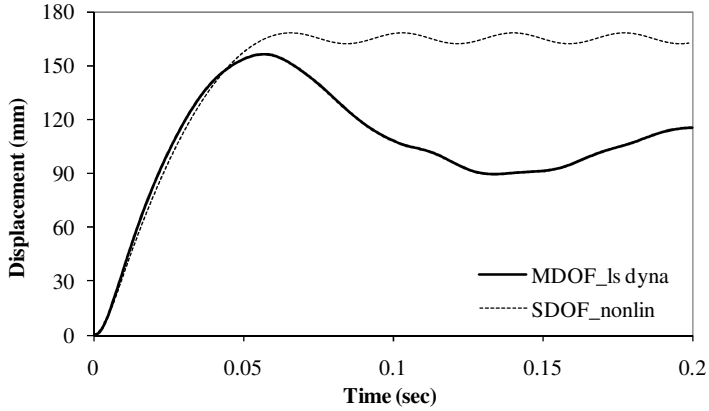

Figure 7.32 MDOF displacement time history of column 4 subjected to triangular pressure loaded in its minor axis direction

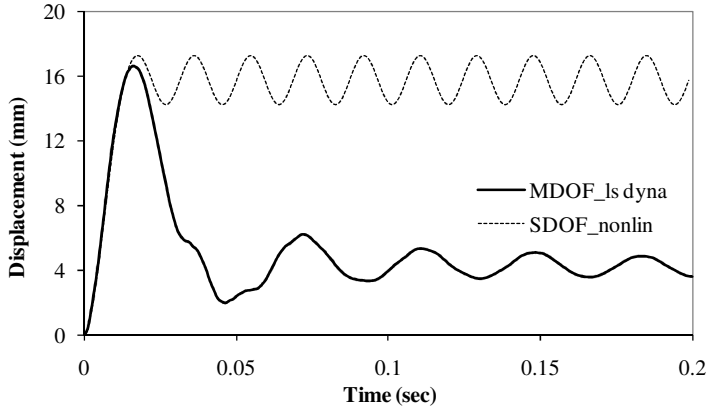

Figure 7.33 MDOF displacement time history of column 4 subjected to triangular pressure loaded in its major axis direction

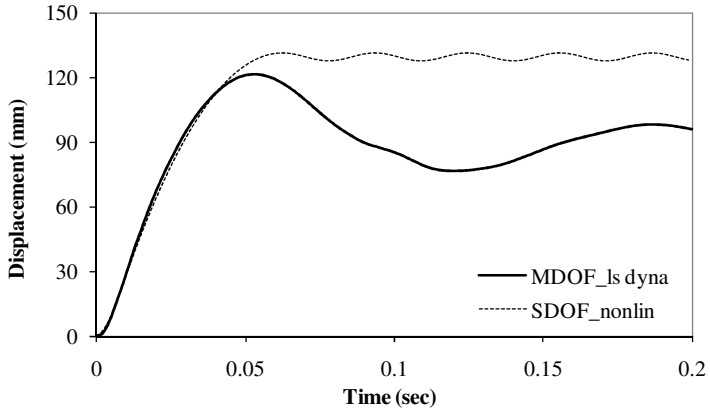

Figure 7.34 MDOF displacement time history of column 10 subjected to triangular pressure loaded in its minor axis direction

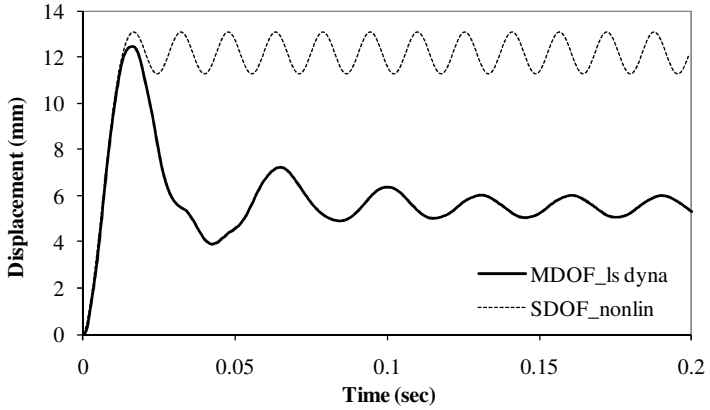

Figure 7.35 MDOF displacement time history of column 10 subjected to triangular pressure loaded in its major axis direction

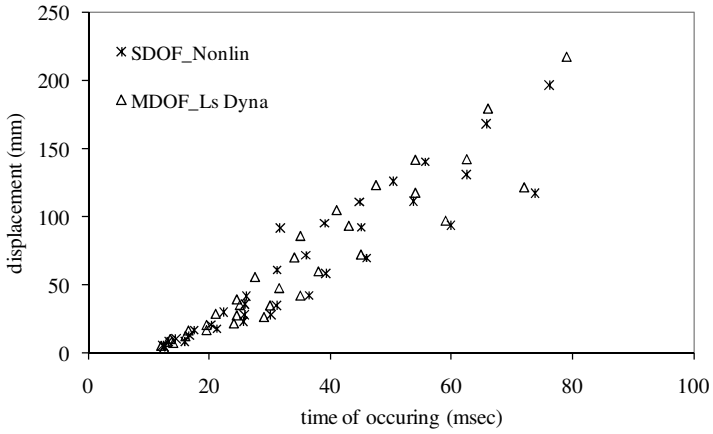

Figure 7.36 Inelastic peak responses of SDOF and MDOF analysis of cantilever RC column subjected to triangular blast pressure

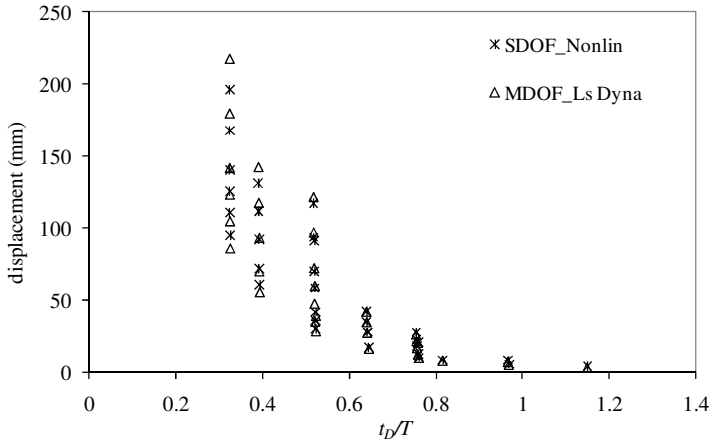

Figure 7.37 Peak displacements of SDOF and MDOF analysis plotted against t_D/T of cantilever RC column subjected to triangular blast pressure

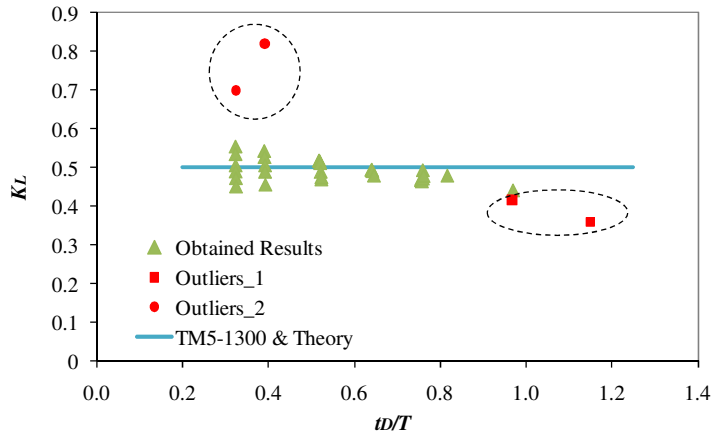

Figure 7.38 Load transformation factors of cantilever columns in inelastic condition plotted against the ratio of loading duration to natural period of structure t_D/T

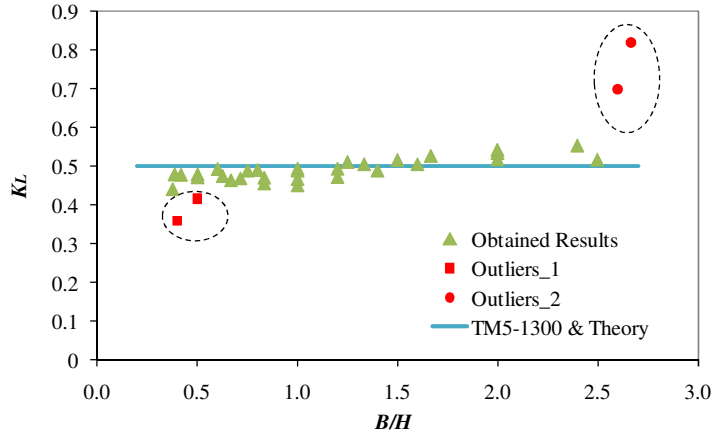

Figure 7.39 Load transformation factors of cantilever columns in inelastic condition plotted against B/H ratio

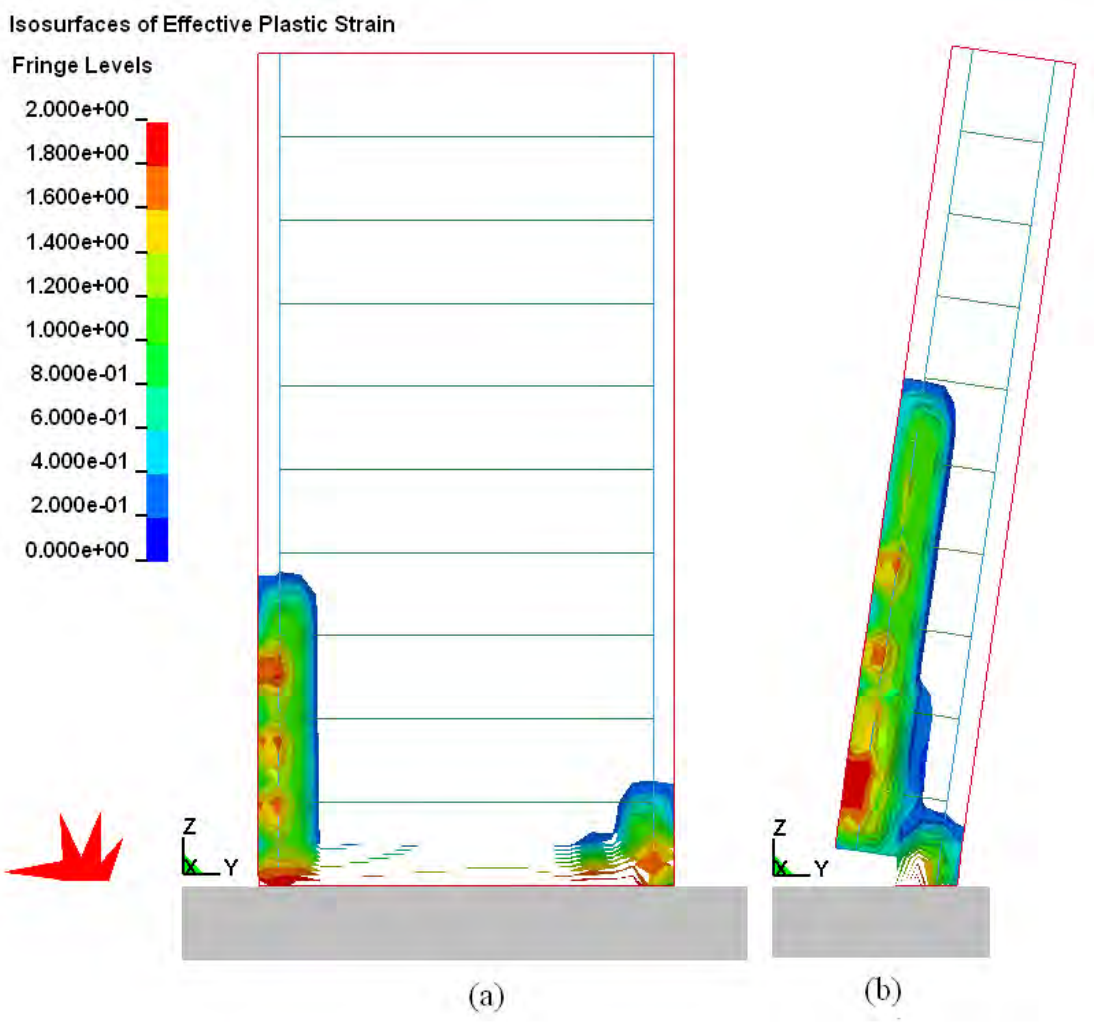

Figure 7.40 (a) Column 13 (b) Column 8 at final stage (t=0.2 second)

Numerical Modeling of a Conventional RC Structure Subjected to Blast Loads

8

8.1 Introduction

Nowadays, terrorist threats to infrastructure are of increasing concern. The use of vehicular bombs against buildings is a common type of terrorist threats. The resultant blast acting on the building may cause damage to its structural components and such damage may also seriously compromise the structural integrity of the whole structure which may lead to structural collapse with serious losses to property and lives. Typically such blast loads, with its high pressurized waves occurring within very short time durations, results in very large impulsive-dynamic loads that may exceed the ultimate load carrying capacity of the structure. Some buildings, e.g. embassies, government offices and power plants may be designed against such extreme loading conditions. However, the design of blast resistant structures may not be economically viable for conventional commercial and residential buildings. One way to minimize damage to such conventional structures, especially existing ones, is to first study their response to various possible scenarios of such blast loads occurring and assess possible ways of mitigating and minimizing the impact of such loads on their structural integrity.

The RC structure analyzed in this study represents a typical residential apartment building in Singapore. For conventional RC residential apartments found typically in Singapore, the impact of blast loads on structural response could pose potential hazards due to the possibility of close-in blast threats and the presence of a void deck on the ground floor as briefly described in Sections 3.3 and 5.6. Therefore, in this chapter, the dynamic response of structural elements typical of such residential apartment blocks subjected to blast loads is discussed. The structure is modeled numerically using LS DYNA FE code. Characteristics of the blast loads and structural geometry are provided and the results obtained discussed and benchmarked against analytical solutions obtained using the Equivalent-Inelastic SDOF method.

8.2 Description of Structure

Due to the presence of a void deck on the ground floor of a typical apartment block (Figure 3.3), the ground floor column nearest the car park, the source of the close-in explosion, is expected to experience highest reflected blast pressure and impulse (P_R and I_R) and is considered most critical.

Although conventional design of RC column is well established, designing columns against high-intensity blast loads from close-in explosion requires consideration of other parameters not normally important in conventional design codes. Another parameter to consider besides the presence of the void deck is the dimension of columns. In Singapore such columns generally have breadth, B, to depth, H, ratio greater than two. When subjected to blast loads, there are thus two blast directions to consider, viz., the major axis (SA) and minor axis (WA) threats. The SA and WA threats occur when the explosive is placed at the stand-off distance applicable for the building under consideration with the

direction of blast aligned in a direction perpendicular or parallel to the column depth *H* (its longer dimension) respectively. It is apparent that in the case where the blast load is directed parallel to its minor axis (WA) as shown in Figure 8.1, the columns respond very much like RC walls in resisting the blast loads. In case of the major axis (SA) threat, the blast pulse is more dispersed onto the surroundings and the adjacent neighboring elements. The wider the loading area, the larger the blast loads acting on the individual element.

Based on the aforementioned considerations, this study is focused on the dynamic response of exterior columns at ground floor level with *B/H* ratio > 2 subjected to close-in explosions. Since the critical column is more susceptible to collapse with the blast directed along the minor axis (WA), the column's response against a typical WA threat is dealt with in this chapter.

8.3 Range of Blast Studied

As discussed in Sections 3.3 and 3.4, the magnitude and the range of blast studied are based on a range of VBIED threats specified in the BATF Explosive Standard by taking into account the available stand-off distance in a typical apartment block in Singapore. It is realized that the provision of structural protection against such threats is likely to be very expensive and some protective installations may impede the function for which the structure is designed. Instead less intrusive methods are preferred to mitigate against such threats include instituting stringent security procedures at entrances and restricting access of vehicles thus increasing the stand-off distance *R*.

In this chapter, the blast load, typically exponential when plotted versus time is idealized as a triangular blast loads with the reflective pressure P_R, and the impulse I_R equal to those of the positive phase as shown in Figure 8.2. The impulse may therefore be given as $I=0.5P_{r.}t_{de}$. Three triangular blast loads having different reflected pressure P_R, reflected impulse I_R, and equivalent loading duration t_{De} as summarized in Table 8.1 are studied. To study the effects of the simplified triangular blast loads on the dynamic response of the critical column, two blast loading conditions i.e. exponential and triangular blast pulses are modeled and the responses are compared in the following section.

Table 8.1 Triangular Blast Loads Studied

Load	Triangular Blast Load			Equivalent ConWep	
	P_R	I_R	t_{De}	W	R
	MPa	*MPa.msec*	*msec*	*kg*	*m*
P1	1.933	2.57	2.66	250	10
P2	5	5.00	2	437	8.6
P3	10	5.00	1	208	4.85

Blast threat is generally defined by two parameters, the charge weight W and the stand-off distance R between the blast source and the structure. Thus, the equivalent blast of similar reflected pressure and impulse based on ConWep is specified in terms of the respective charge weight W and stand-off distance R. As an example, Figure 8.3 shows the blast pressure time history of an equivalent charge weight W=250 kg TNT at R=10 m (Load P1).

The blast loads may vary along the height of the structure, especially when the charge is located very near the targeted structure. The further the blast loads from the structure the

more uniform the loads applied on to the structure. In this chapter, the blast loads are applied uniformly along the full height of the targeted column.

8.4 Numerical Analysis of RC Structures Subjected to Blast Loads

The structural response may be obtained using three methods: theoretical analysis, numerical analysis and experimental test. As field test results are generally unavailable, only the first two methods are carried out in this chapter.

The LS DYNA FE code is occupied to model the structure numerically and to analyze the structural response. As described in Chapter 6, herein normal strength concrete (NSC) of f_c' equal to 30 MPa is carried out. The NSC is modeled using MAT 72_CONCRETE DAMAGE Rel. III in the form of 3D hexahedron solid elements with single integration and 6 DOFs. On the other hand, the steel reinforcements, both longitudinal and transverse, are modeled using MAT 3_PLASTIC KINEMATIC in the form of 2D beam elements capable of sustaining only axial compressive or tensile force. The material properties, material parameters, DIFs and EOS of NSC and the steel reinforcement are as described in Sections 6.3 to 6.6.

8.5 Parametric Studies on Responses of RC Structure against Blast Loads

8.5.1 Boundary Conditions

In a typical full frame analysis, the slabs provide lateral stiffness to the frame. It restrains the beam column joints from deforming laterally. When the frame is subjected to blast loads, the adjacent exterior columns will be severely loaded by the blast. Hence, it may undergo large deformations and may be damaged. The critical ground floor exterior column with the shortest stand-off distance is analyzed to study how this column

responds to blast loads. Five nodes are investigated: Nodes 1 and 5 which are at the reaction pad, Nodes 2 and 4 which are located at a quarter and three quarter height of the column, and Node 3 which is at mid height of the column. The response of Nodes 1 and 5 and Nodes 2 and 4 should be equal due to symmetry.

The intention is to model the columns in such a way that their response mirrors that of an analysis carried out on the full frame. For this reason, three types of boundary condition are modeled and discussed: fixed end (1A), pinned end (1B) and HF pinned end (1C). The targeted column is an RC column of size 350mm by 800 mm reinforced with 1% longitudinal reinforcement.

The columns are subjected to triangular load P1 (Figure 8.3). The peak lateral responses of all three types of columns subjected to blast loads are given in Table 8.2. It is shown that the peak lateral displacement is indeed affected by boundary conditions assumed. Symmetry is noted at Nodes 1-5 and 2-4. Case 1A corresponds to that of a frame with a stiffer beam column joint. For the fully fixed end condition at the beam column joint (both δ_1 and δ_5 are zero).

Table 8.2 Peak lateral response of column subjected to load P1 (P_R = 1.933 MPa, t_{De} = 2.66 msec) for different boundary conditions

Case	Reaction Pad	Node 1		Node 2		Node 3		Node 4		Node 5	
		δ	time	δ	time	δ	Time	δ	time	δ	time
		(mm)	(msec)	(mm)	(msec)	(mm)	(msec)	(mm)	(msec)	(mm)	(msec)
1A	Fixed End	0.00	0	6.91	6	11.27	6	6.91	6	0.00	0
1B	Pinned End	0.44	6	7.31	6	12.14	6	7.31	6	0.44	6
1C	HF PE	0.10	6	7.48	6	13.07	7	7.48	7	0.10	6

It is evident in real life that the structural joint may not be fully fixed. Hence, Case 1B is modeled with pinned end joints. The perimeter nodes of the reaction pad are constrained to translate in the x, y, and z directions whereas the top and bottom faces nodes are constrained to z translations only. However, in this case the lateral deformation of Node 1 and Node 5 nearly reached 0.5 mm even though the columns are still behaving elastically. For the case of a larger blast resulted in severe damage to the column modeled, the lateral displacement of Nodes 1 and 5 are likely to be much larger.

Another BC model is Case 1C, "head" and "footing" (HF) pinned end (PE). For the HF pinned end case, a "head" and a "footing" are attached to the tip and the base of the column, respectively. The "head" (H) of width equal to the column width is of depth 400mm. It is used to represent the constraint afforded by the 1st floor beams and slabs. The "footing" (F) of the same column width is of depth 500mm. They are used to represent typical ground beams commonly used in Singapore of dimension 300mm wide and 500mm deep. The outer vertical face of the "head" and "footing" are constrained against horizontal motion. Meanwhile, the top face of the "head" and the bottom face of the "footing" are constrained against vertical motion.

From Table 8.2, it was found that the lateral displacement at the reaction pads (Nodes 1 and 5) of the HF pinned end column (Case 1C) are smaller and closer to zero while displacements at mid height of the is closer to that of pinned end column (Case 1B). Figure 8.4 shows the plastic damage evolution of the HF pinned end column. For the results presented hereafter, the HF pinned end boundary condition is utilized.

8.5.2 Loading variables

As described in Section 3.5, three regimes of structural dynamic loading, viz. impulsive, dynamic and quasi-static loading are possible. As reported by Cormey et al. (2009), these three regimes are characterized in terms of the natural period of the structure T, and the loading duration, t_D. The duration of blast loads varies as a function of stand-off distance R and charge weight W, while the natural period of the structure is a function of structural geometry, boundary conditions and material properties. In obtaining the natural periods, Eigen value analysis is carried out. The natural periods of the columns considered with the three typical geometric dimensions with a 1% longitudinal reinforcement ratio and with transverse reinforcement of 2T6-250 are given in Table 8.3.

Table 8.3 ω and T of Columns Considered

Dimension (mm)	Boundary Condition	ω (rad)	T (msec)
200 x 500	Fixed End	267.52	23.49
	HF Pinned End	247.93	25.34
300 x 750	Fixed End	400.31	15.70
	HF Pinned End	58.84	16.99
350 x 800	Fixed End	464.53	13.53
	Pinned End	460.77	13.64
	HF Pinned End	429.42	14.63

Cormey et al. (2009) reported that when the structure is subjected to impulsive loading, the structure is more sensitive to the associated impulse I rather than to the peak pressure P. When it is subjected to quasi-static loading, the response of the structure becomes more sensitive to the peak pressure P rather than to impulse I. However, for dynamic loading, response sensitivity is not well understood. In this study, the blast loads acting on the columns are selected such that they will fall at the boundary between impulsive and dynamic loading.

8.5.2.1 Variable *P* and t_D for constant *I*

To study the sensitivity of peak pressure *P*, the impulse *I* is kept constant at *I* =5MPa.msec. The column investigated is of dimension 350 x 800 mm. As shown in Table 8.4, based on the magnitude of the natural period, blast loads with a loading duration t_{De} of 1 and 1.25 are considered as impulsive loading while those with t_{De} = 2 and 3 msec are considered as dynamic loadings. The peak displacement of the columns considered when subjected to the various loading conditions is summarized in Table 8.5. Under various peak pressures, *P,* with constant impulse, *I*, the peak displacements are shown to vary within a broad range (up to 28% difference). Thus, the displacement response seems to be sensitive to changes in *P*. The larger the *P* with a smaller loading duration t_d, the larger is the peak lateral displacement of the column.

Table 8.4 Loading type of HF pinned end column of size 350 x 800 mm

T	ω	t_{De}	t_{De}/T	Loading Type
(msec)	(rad)	(msec)	(-)	
14.632	429.421	1.00	0.068	impulsive
		1.25	0.085	impulsive
		2.00	0.137	dynamic
		3.00	0.205	dynamic

From Tables 8.2 and 8.5 the results also show that between the symmetrical nodes, the peak displacements are equal, confirming symmetry of the column analyzed. This is observed not only for the case of small blast loading but also for larger loads when the structure responds in a highly nonlinear manner. Thus, the results presented hereafter will be the peak response of Nodes 1 to 3.

Table 8.5 Peak lateral response of HF pinned end column of size 350 x 800 mm subjected to various blast loads (P, t_{De}) with constant I = 5 MPa.msec

Case	P; t_{De} (MPa, msec)	Node 1		Node 2		Node 3		Node 4		Node 5	
		δ (mm)	time (msec)	δ (mm)	Time (msec)	δ (mm)	time (msec)	Δ (mm)	time (msec)	δ (mm)	time (msec)
2A1	5 ; 2	0.169	0	54.171	40	98.530	30	54.171	40	0.169	0
2A2	8; 1.25	0.176	1	69.157	40	114.020	29	69.157	40	0.176	1
2A3	10 ; 1	0.170	0	84.564	40	126.570	34	84.564	40	0.170	0

8.5.2.2 Variable I and t_{De} for constant P

The sensitivity of impulse I is also examined. The peak pressure P is kept at a constant value, in this case P = 5MPa. The column considered is of dimension 350 x 800 mm. The loading durations are varied from 1 to 3 msec. Based on the magnitude of the natural period, such loading are considered as dynamic loading. The peak displacement of the columns considered subjected to various loading conditions is given in Table 8.6. It may be observed that under various impulses I, the peak displacement of the columns vary.

Table 8.6 Peak lateral response of HF pinned end column of size 350 x 800 mm subjected to various blast loads (I, t_{De}) with constant P = 5 MPa

Case	Impulse (MPa.msec)	T	t_{De}/T	Node 1		Node 2		Node 3	
				δ	time	δ	time	δ	time
		(msec)	(-)	(mm)	(msec)	(mm)	(msec)	(mm)	(msec)
2B1	2.5	14.6	0.068	0.090	0	7.799	6	12.524	6
2B2	5.0		0.137	0.169	2	54.171	40	98.530	30
2B3	7.5		0.205	0.487	40	117.440	40	177.430	31

The structural response was observed to transition from an elastic to a plastic state with yielding when the loading impulse increases from 2.5 to 5.0 *MPa.msec* as shown in Figure 8.5 and Table 8.6. The peak displacement of Case 2B2 (I=5.0 *MPa.msec)* is around eight times the peak displacement of Case 2B1 (I=2.5 *MPa.msec*). From Tables 8.5 and 8.6 it may be concluded that structural response is sensitive to both changes in P

as well as *I*. It was found that the larger the impulse *I* applied to the column considered, the larger is the peak lateral displacement. As *I* increases further, this may lead to failure of the column.

8.5.3 Loading Types (exponential and triangular blast pulses)

For design purposes, generally the blast load is idealized as a triangular load pulse uniformly applied to the impact face of the column. The triangular load is of the same impulse as the exponential blast load. Here, *I* and *P* are constant, but the loading pattern and t_d are different. The decay coefficient α of the exponential load equals to one and pressure applied is $P(t) = P_r e^{(-\alpha t)}$.

The blast pressure time history is shown to affect the nonlinear behavior of the column (Figure 8.6 and Table 8.7). Both the peak response time and peak displacement are affected. Columns subjected to exponential load experiences peak response earlier than that of the triangular load case, but the magnitude of the peak displacement is smaller. This is because the blast energy is applied within a longer loading duration, resulting in a smaller peak displacement. Nevertheless, the difference in peak displacement is not significant, less than 4%. Thus in this study, triangular loading is applied on to the columns analyzed.

Table 8.7 Peak lateral response of HF pinned end column of size 350 x 800 mm subjected to Load P3 (*I*=5 *MPa.msec* with *P*=10 MPa)

Case	Loading Type	*T*	t_{De}/T	Node 1		Node 2		Node 3	
				δ	time	δ	time	δ	time
		(msec)	(-)	(mm)	(msec)	(mm)	(msec)	(mm)	(msec)
2C1	Exponential P=10 I=5 α=1	14.6	0.137	0.20	0	70.56	40	121.96	29
2C2	Triangular P=10 I=5 t_{De}=1		0.068	0.17	0	84.56	40	126.57	34

8.5.4 Dimension of column

Column of three typical dimensions, viz. 200x500, 300x750 and 350x800 mm, are subjected to loads P1 (I=2.5 MPa.msec) and P2 (I=5 MPa.msec). Triangular blast loads are applied onto the column. The reinforcement ratio is kept the same as in the previous analytical model (1% longitudinal reinforcement ratio with shear reinforcement of 2T6-250). The dimensions are chosen such that the *B/H* ratio is greater than 2, typical of residential apartment blocks in Singapore.

Table 8.8 Peak lateral response of HF pinned end columns of various dimensions subjected to Load P1 (P=1.933 *MPa*, t_{De}=2.66 msec)

Case	Dimension	T	t_{De}/T	Node 1		Node 2		Node 3	
				δ	time	δ	time	δ	time
	(mm)	(msec)	(-)	(mm)	(msec)	(mm)	(msec)	(mm)	(msec)
3A1	200 x 500	25.3	0.105	0.056	0	29.501	13	51.278	15
3A2	300 x 750	17.0	0.156	0.105	7	10.813	7	17.701	7
3A3	350 x 800	14.6	0.182	0.101	6	7.483	6	13.074	7

Table 8.9 Peak lateral response of HF pinned end columns of various dimensions subjected to Load P2 (P=5 MPa t_d=2 msec)

Case	Dimension	T	t_{De}/T	Node 1		Node 2		Node 3	
				δ	time	δ	time	δ	time
	(mm)	(msec)	(-)	(mm)	(msec)	(mm)	(msec)	(mm)	(msec)
3B1	200 x 500	25.3	0.105	Collapse					
3B2	300 x 750	17.0	0.156	0.217	2	97.530	46	149.920	29
3B3	350 x 800	14.6	0.182	0.169	2	54.171	40	98.530	30

Results from the numerical analysis yield peak responses as summarized in Tables 8.8 and 8.9. Table 8.8 shows that the columns are still behaving elastically (Cases 3A1 and 3A2) or in the early stages of nonlinear response (Case 3A3) when subjected to load P1 (P=1.933 *MPa*, I=2.57 *MPa.msec*). When the intensity of the blast was increased in the case of load P2 (P=5 *MPa*, I=5 *MPa.msec*), the columns behaved in a highly nonlinear

manner and some collapsed (Table 8.9). Columns of smaller dimensions have smaller bending and shear strengths, and were observed to experience larger lateral deformation.

8.5.5 Longitudinal reinforcement percentage

Generally, the longitudinal reinforcement percentage of the columns lies within a range of 1 to 8% of the gross cross-sectional area (A_c). The reinforcement needed is calculated based on the prevailing design codes. In this study, the longitudinal reinforcement ratio assumed for the columns ranged from 1 to 3%.

It is observed from Tables 8.10, 8.11 and 8.12 that the increase in longitudinal reinforcement significantly enhances the bending strength of the column considered. Hence, one way of strengthening columns against blast loads is by increasing the longitudinal reinforcement ratio beyond what is required under static loads.

Table 8.10 Peak lateral response of HF pinned end columns with various longitudinal reinforcement percentage subjected to Load P1 (P=1.933 MPa, t_{De}=2.66 msec)

Case	% Longitudinal Reinf	T	t_{De}/T	Node 1		Node 2		Node 3	
				δ	time	δ	time	δ	Time
		(msec)	(-)	(mm)	(msec)	(mm)	(msec)	(mm)	(msec)
4A1	1%	14.6	0.182	0.101	0	7.483	7	13.074	7
4A2	2%	14.2	0.187	0.104	6	6.436	6	10.314	5
4A3	3%	13.8	0.193	0.092	6	5.732	6	9.161	5

Table 8.11 Peak lateral response of HF pinned end columns with various longitudinal reinforcement percentage subjected to Load P2 (P=5 MPa t_{De}=2 msec)

Case	% Longitudinal Reinf	T	t_{De}/T	Node 1		Node 2		Node 3	
				δ	time	δ	time	δ	Time
		(msec)	(-)	(mm)	(msec)	(mm)	(msec)	(mm)	(msec)
4B1	1%	14.6	0.137	0.169	0	54.171	40	98.530	30
4B2	2%	14.2	0.141	0.164	1	20.179	32	57.826	24
4B3	3%	13.8	0.145	0.166	1	13.795	6	39.947	22

Table 8.12 Peak lateral response of HF pinned end columns with various longitudinal reinforcement percentage subjected to Load P3 (P=10 MPa t_{De}=1 msec)

Case	% Longitudinal Reinf	T	t_{De}/T	Node 1		Node 2		Node 3	
				δ	time	δ	time	δ	Time
		(msec)	(-)	(mm)	(msec)	(mm)	(msec)	(mm)	(msec)
4C1	1%	14.6	0.068	0.170	0	84.564	40	126.570	34
4C2	2%	14.2	0.070	0.176	0	70.745	36	101.550	30
4C3	3%	13.8	0.072	0.166	0	76.849	33	92.530	31

8.5.6 Transverse reinforcement

The amount of transverse reinforcement or stirrups needed is determined based on the prevailing design codes. In seismic design the amount of transverse reinforcement required is rather stringent, especially with regards to detailing. The requirement of minimum spacing of reinforcement is also specified. Insufficient provision of transverse reinforcement may lead to poor confinement, leading to premature failure of the column.

As shown in Tables 8.13 and 8.14, the transverse reinforcement spacing of the columns considered is reduced from 250 mm to 150 or 100 mm. The resulting peak displacement is reduced by less than 1 mm under linear elastic loading conditions (Table 8.13) and 10 mm under nonlinear loading condition (Table 8.14).

Table 8.13 Peak lateral response of HF pinned end column 3C with various transverse reinforcement spacing subjected to Load P1 (P=1.933 MPa, t_{De}=2.66 msec)

Case	Transverse Reinforcement	Node 1		Node 2		Node 3	
		Δ	time	δ	time	δ	Time
		(mm)	(msec)	(mm)	(msec)	(mm)	(msec)
5A1	2D6-250	0.101	0	7.483	7	13.074	7
5A2	2D6-150	0.113	6	7.491	6	12.260	6
5A3	2D6-100	0.098	6	7.460	6	11.968	6

Table 8.14 Peak lateral response of HF pinned end column 3C with various transverse reinforcement spacing subjected to Load P2 (P=5 MPa t_{De}=2 msec)

Case	Transverse Reinforcement	Node 1		Node 2		Node 3	
		δ	time	δ	time	δ	Time
		(mm)	(msec)	(mm)	(msec)	(mm)	(msec)
5B1	2D6-250	0.169	0	54.171	40	98.530	30
5B2	2D6-150	0.166	2	22.166	40	88.853	31

Table 8.15 Peak lateral response of HF pinned end column 3C with various transverse reinforcement configuration subjected to Load P2 (P=5 MPa t_d=2 msec)

Case	Transverse Reinforcement	Node 1		Node 2		Node 3	
		Δ	time	δ	time	δ	time
		(mm)	(msec)	(mm)	(msec)	(mm)	(msec)
5C1	2D6-250	0.169	0	54.171	40	98.530	30
5C2	2D10-250	0.170	2	36.119	40	86.195	27
5C3	4D10-250	0.171	2	16.205	7	37.855	11

The increase in strength as a result of reducing the transverse reinforcement spacing (Table 8.14) is, however, not as significant when compared with increasing the amount of transverse reinforcement at the same stirrup spacing (Table 8.15). Doubling the amount of stirrups results in smaller peak displacement (less than half in Case 5C3).

8.6 Verification using Theoretical Equivalent SDOF Analysis

To verify the results from the numerical analysis, Equivalent SDOF analysis using step by step integration method for inelastic analysis as derived and implemented in Chapter 7 has been carried out for Case 1C (Column dimension of 350x800 mm with 1% longitudinal reinforcement and transverse reinforcement of 2T6-200).

The results as shown in Figure 8.7 show that there is a good agreement between peak responses obtained using the two methods of analysis. In Case 1C, the results from SDOF analysis seems to show slightly larger displacement (Δ=4%).

8.7 Summary

In this chapter, a comprehensive parametric study of RC columns subjected to blast loads has been carried out. Several blast loading parameters (*W, R, P,* and *I*) as well as structural parameters (boundary condition, column dimensions, % longitudinal reinforcement, and amount of transverse reinforcement) on the effects to structural responses have been investigated. The study on the loading variables (Section 8.5.2) to investigate the sensitivity of the dynamic response of RC columns under dynamic and impulsive blast loading shows that column displacement is sensitive to changes in both pressure *P* and impulse *I*. The study on columns with dimension *B/H*>2 showed that columns of smaller dimensions with smaller bending and shear strength experiences larger lateral deformation. Some RC columns collapsed when subjected to blast loads especially when directed parallel to the minor axis (WA). This demonstrates the needs for strengthening and retrofitting existing RC columns against such unforeseen blasts. Potential retrofitting methods for existing RC columns against nearby explosion is discussed in Chapter 9.

The results of the numerical method are also validated analytically using Equivalent SDOF method. It is shown that the numerical and analytical solutions of the peak responses within time are in good agreement.

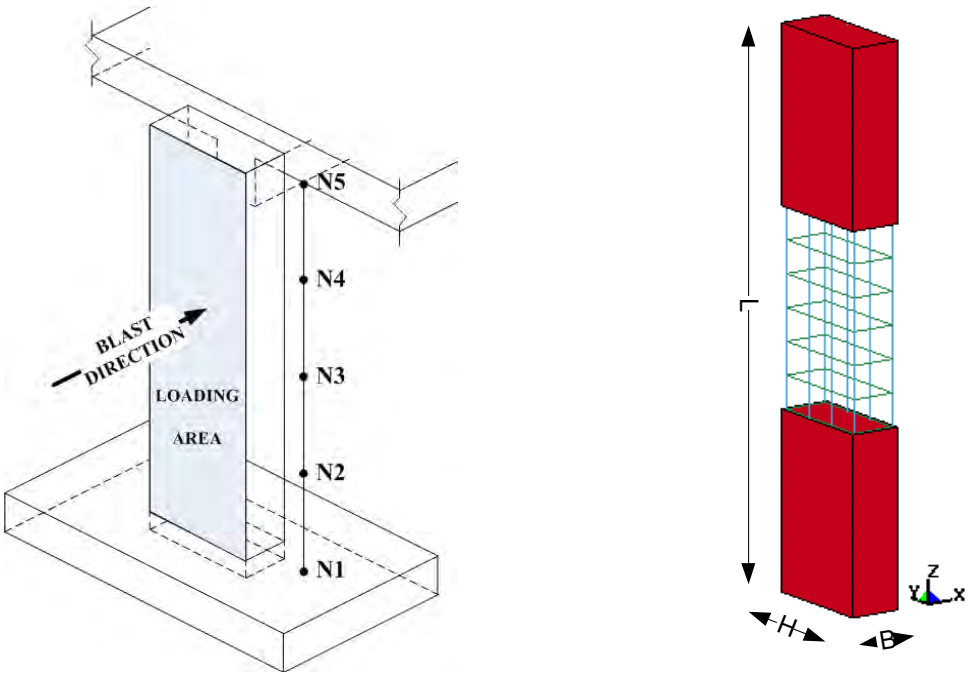

(a) (b)

Figure 8.1 Column cut-out (a) First floor exterior column (b) Typical reinforcement details

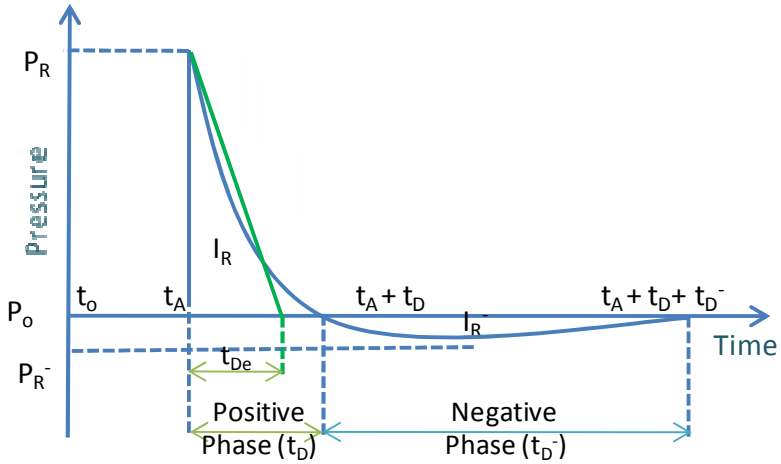

Figure 8.2 Triangular blast pressure time history

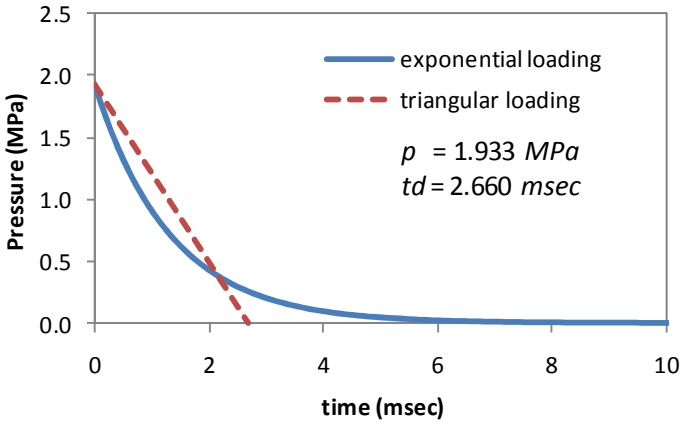

Figure 8.3 Blast pressure time history of load P1

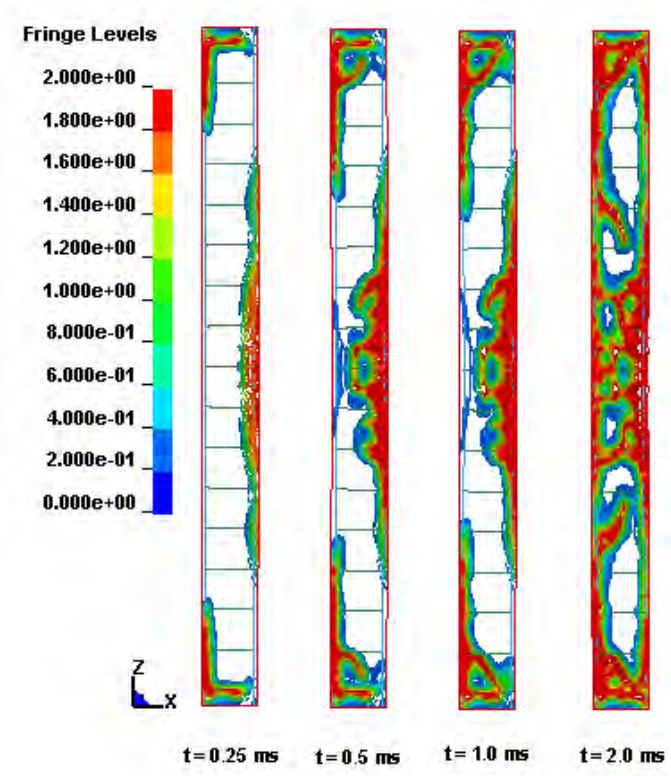

Figure 8.4 Plastic damage evolution of column Case 1C

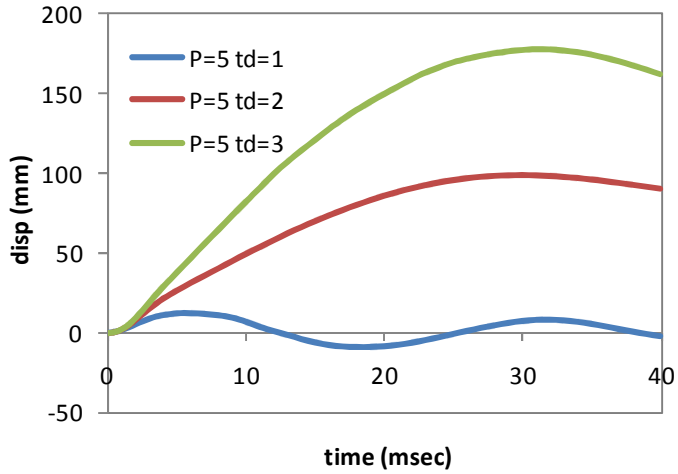

Figure 8.5 Displacement time history of Node 3 on Case 2B

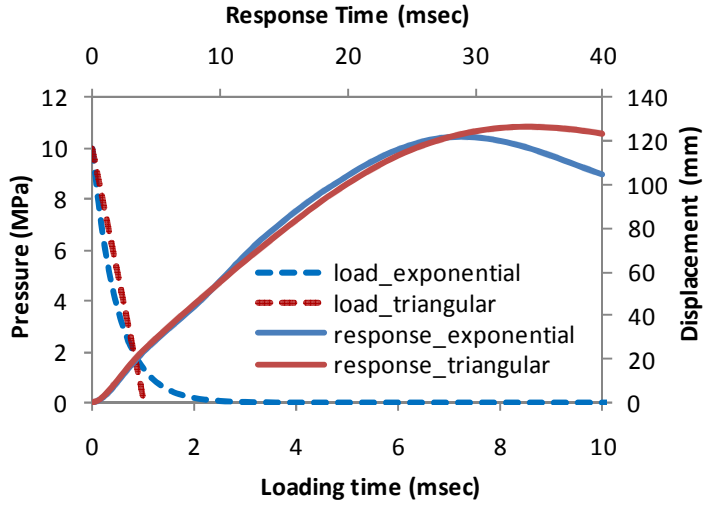

Figure 8.6 Displacement time history of Node 3 on Case 2C Subjected to Load P3

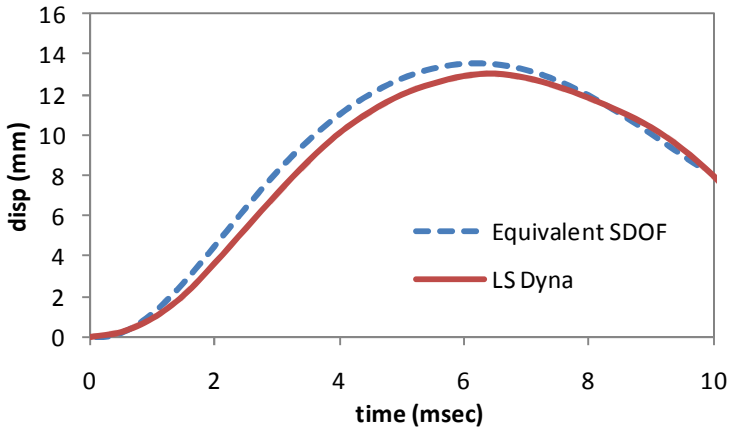

Figure 8.7 Displacement time history of Node 3 on Case 1C

Enhancing the Strength of RC Column Subjected to Close-In Blast Loads Using ECC Encasement Materials

9

9.1 Introduction

This chapter presents the results of a numerical study to evaluate the potential of using ECC encasement to retrofit existing RC columns to resist blast loads arising from Vehicle Born Improvised Explosive Device (VBIED). The aim is to quantify the extent to which ECC improves the resistance of RC columns against blast loading. Normal strength concrete (NSC) and high strength concrete (HSC) encasement are also modeled. The blast resistance of RC columns (800mm × 300mm) encased by different materials (25 – 50mm thick) is evaluated in terms of the extent of damage, energy absorption capacity and residual resistance against blast loads. Experimental testing was also carried out on quarter scale unencased and ECC encased RC columns to validate the numerical results.

In enhancing the resistance of existing RC columns against blast loading, delaying tensile cracks in concrete under tension is a key concern. ECC with its remarkable characteristics under tension is proposed for use as encasement for retrofitting existing RC columns against blast loading. Both numerical approach and experimental study are carried out to analyze the dynamic response of default and encased RC columns against blast. Through

this study, the dynamic behavior of RC columns with and without ECC encasement when subjected to close-in blast loads is described.

9.2 Description of Case Study

As described in Chapter 6, the structure investigated in this study is a conventional RC apartment block found typically in Singapore. A common feature of such structures is the ground floor void deck used for social functions, while the 1st storey up is an RC infilled frame. The blast may propagate freely through the ground floor void deck channeled by the columns, the ground and the ceiling (soffit of the slab above). Another characteristic of such a structure is that the RC columns as used in a typical apartment block generally have a breadth to depth ratio (*B/H*) that is greater than two.

In this chapter, to obtain the blast loads on columns, blast wave propagation through the ground floor void deck is studied numerically focusing on the blast loads acting on critical ground floor RC columns, taking into account the effects of the geometry of the ground floor void deck. To strengthen the columns, Engineered Cementitious Composite (ECC) encasement is proposed (Figure 9.1) and compared with two other types of encasement material, viz. normal (NSC) and high strength concrete (HSC, as per ACI 363) encasements having compressive strength of 30 and 55 *MPa*, respectively. Other structural elements such as beams and slabs are beyond of the scope of study. The critical ground floor RC column studied herein is of dimension 800mm x 300mm containing 2 legs of R6 transverse reinforcements spaced center to center at 250mm, with 1.67% longitudinal reinforcements, loaded by an external hemispherical close-in explosion in the direction of its minor axis (MI) as illustrated in Figure 9.2a. The explosion of a 100 kg TNT charge weight, *W* is placed just above the ground at a stand-off distance, *R*. The

range of stand-off distances, *R* studied herein is between 3 to 10 meters; representing the range of stand-off distance available in a typical apartment block due to the presence of adjacent carparks (Figure 9.2b). The types of columns studied are summarized in Table 9.1. The notation used for the unencased RC column subjected to 100kg TNT at a stand-off distance, *R*, in meters is UC-*R*, while for NSC, HSC, and ECC encased columns, *t* refers to the thickness of the encasement layer in mm.

Table 9.1 Types of RC800x300 Column

Specimen	Type of Encasement	Thickness of Encasement, *t*	Stand-off Distance, *R*	Charge Weight, *W*
		t	*R*	
UC-3	-	-	3 m	
UC-5	-	-	5 m	
UC-10	-	-	10 m	
NSC25-3	NSC	25 mm	3 m	
NSC25-5	NSC	25 mm	5 m	
NSC25-10	NSC	25 mm	10 m	
NSC50-3	NSC	50 mm	3 m	
NSC50-5	NSC	50 mm	5 m	
NSC50-10	NSC	50 mm	10 m	
HSC25-3	HSC	25 mm	3 m	100 kg TNT
HSC25-5	HSC	25 mm	5 m	
HSC25-10	HSC	25 mm	10 m	
HSC50-3	HSC	50 mm	3 m	
HSC50-5	HSC	50 mm	5 m	
HSC50-10	HSC	50 mm	10 m	
ECC25-3	ECC	25 mm	3 m	
ECCC25-5	ECC	25 mm	5 m	
ECC25-10	ECC	25 mm	10 m	
ECC50-3	ECC	50 mm	3 m	
ECC50-5	ECC	50 mm	5 m	
ECC50-10	ECC	50 mm	10 m	

9.3 Blast Loads on RC Column

To provide a better understanding of the effects of blast waves propagating through the ground floor void deck and the blast loads on the critical ground floor RC column, numerical simulation of the fluid flow problem is carried out using AUTODYN software. The details of the algorithms of the computational fluid dynamics by AUTODYN, the material models and the equation of states (EOS) of air and TNT used in this chapter follow those given in Section 5.3.

9.3.1 Basic Assumptions

The propagation of blast waves through air and its interaction with the surrounding structure comprise a huge number of possible scenarios. Assumptions are usually made to facilitate analysis. In this present study, several assumptions are made. These include:

4. The air is simulated as an ideal gas.
5. Only hemispherical explosion is considered. Thus, in the 2D axial symmetry explosion model, the charge weight W of 100 kg TNT is modeled as 200kg TNT to account for the perfect reflection of the surface burst explosion from the ground floor slabs.
6. The explosive is located along at the center line of the target column at the ground level. Thus, in the 3D explosion model, only half of the structure is simulated due to symmetry.
7. The structure comprises critical ground floor column and slabs, with the 1st storey walls and slabs assumed rigid. Thus, all the surfaces of the ground floor columns, the ground floor slabs, and the 1st storey walls as well as the soffit of the slab above the void deck are assumed to be fully reflective surfaces.

9.3.2 Numerical Analysis of Blast Loading on Critical RC Column

In this study, half of a symmetrical 3D numerical model is simulated using AUTODYN as shown in Figure 9.3. Before the blast wave encounters the ground floor column and 1st storey structure, it propagates through the air as a hemispherical blast wave. During this period, to reduce computational time, a 2D axially symmetrical model of the hemispherical blast explosion is analyzed.

The results from the 2D hemispherical explosion simulation are then remapped into the 3D model at the beginning of the second stage analysis. The blast waves may interact with the ground floor columns and slabs, and the floor slab above the void deck during the blast event. This two stage analysis helped reduce the computational time needed with no loss in the accuracy as a finer 2D mesh is occupied.

9.3.3 Blast Propagation through the Ground Floor Void Deck

Blast loads of 100 kg TNT acting on an RC 800x300 column at a stand-off distance *R* of 3 m, 5 m, or 10 m are analyzed numerically using AUTODYN. Several gauges are located on the surfaces and the corners along the height of column at both incident and distal faces of the RC column. The pressure and impulse obtained are compared to those calculated using ConWep software, an implementation of empirical blast model obtained in studies conducted by Kingery and Bulmash (1984). As shown in Figure 9.4, pressure and impulse obtained from the numerical analysis and ConWep are plotted for an explosion of 100kg TNT at a stand-off distance of 3 meters. On the surface and corner nodes, ConWep estimates roughly similar values of pressure and impulse while the numerical results show significant difference in terms of impulse obtained. Based on the numerical results, the pressures on the surface and corner nodes are similar for nodes at a

height less than 2 meters. The differences are more obvious at nodes located between heights of 2.25 to 3 meters.

In Figure 9.4, differences in terms of pressure and impulse between the numerical results and ConWep are very obvious. ConWep provides much higher estimates for both pressure and impulse, more than 40% of those obtained from the numerical analysis. This is most likely due to the different assumptions made. ConWep assumed an infinite incident surface such as walls which reflect fully the blast waves with no diffraction phenomenon. Using empirical equations suitable for walls may not predict accurately the response of the columns considered in this study.

For better understanding of the interaction of the blast waves with columns, in this study the numerical analysis is carried out using AUTODYN to model the actual condition of the ground floor void deck with the target column having a finite reflection area. For the target column, when the blast waves impinge on the incident face, reflected waves immediately form with greater magnitude than those of the overpressure in case of free field explosions. These waves will then propagate towards the free edges of the incident face of the column and create an air flow that commences from the higher to the lower pressure region once a free edge is reached. The air flow proceeds to diffract around the target column as relief waves and progress inward towards the center of column. In this study, the effects of such relief waves on the distal face of the target column are neglected. For a close-in explosion typical of that shown in Figure 9.5, such relief waves result in a negligible decrease in the reflected impulse on the incident face of the column. The pressure and impulse results from numerical analysis conducted using AUTODYN for 3, 5 and 10 meters stand-off distance are shown in Figure 9.6.

9.4 Modeling of RC Columns

Numerical analysis on the dynamic response of RC columns of dimension 800mm x 300mm subjected to blast loads is carried out using LS-DYNA finite element software version 971. The details of the algorithms of the structural dynamics of LS-DYNA, the material properties, the material models, the equation of states (EOS) and the strain rate enhancement (DIF) of the steel reinforcement, the normal strength (NSC) and high strength concrete (HSC) and the engineered cementitious composite (ECC) used in this chapter follow those given in Chapter 6.

9.4.1 Basic Assumptions

The ground floor RC column of dimension 800x300mm is modeled as shown in Figures 9.1 and 9.2a. Similar to the HF pinned end BC described in Section 8.5.1, the tip and the base of the column are attached to the "head" and "footing" which provide the lateral constraint from the 1st floor beams and slabs, and the ground beams, respectively. The details of the dimensions of the "head" and "footing" and the constraints assigned were similar to those in Section 8.5.1 except for the vertical constraint of the "head". In this chapter, the "head" is allowed to move vertically downward as the imposed loads from upper storeys are taken into account and represented by an axial load applied on top of the "head" of the column. Similar conditions are also applied for the encased RC columns.

9.4.2 Loading Steps

In order to evaluate the ground floor RC column for its resistance against explosions, a series of numerical simulations are carried out to obtain the damage level of the default RC column. The damage levels of the default column are then compared to those of the

encased RC columns. To observe the damage level of the target column, three steps of loading are introduced into the model as given in the following:

Step 1: Initial Stress Analysis

Herein, an axial force is applied initially to the column prior to the blast loads to simulate the stress state arising from the existing imposed and dead loads. In this study, the axial load applied onto the column represents the imposed loads from the 2nd and the 3rd floor structure. Two methods are used to apply initial stress on to the target column:

i. Displacement control method (DC)

A prescribed motion control is applied at the tip of the target column. By assuming that at this stage the column is still in elastic condition, the axial displacement, Δ, experienced at the column's tip is given as:

$$\Delta = PL/(EA) = P/k \tag{9.1}$$

where P = total axial loads, L = height of column, E = elastic modulus of column, A = cross-sectional area, and k = axial stiffness. This prescribed motion control must be applied gradually due to explicit dynamic analysis used. In this study, an initial duration of 200ms is invoked.

ii. Load control method (LC)

An axial load is applied on the top of the target column. Similar to that of displacement control, this axial force is applied gradually within a duration of 200ms.

Step 2: Blast Loading Analysis

At the beginning of this loading stage, the velocity of the model is reset to zero. During this step, the target column is evaluated for its response when subjected to blast loads

applied. The blast loads are applied as non-uniform pressure segments over the incident face of the column. The dynamic analysis is executed for a specified duration of time, depending on the type of column encasement applied, to enable capture of the peak and steady state response. Three methods are presented to control the vertical movement of the target column during this stage and in applying the axial loads from upper storeys:

i. Displacement control method with an unconstrained column tip (DCU)

   The prescribed motion control is stopped and the column tip is now released to allow vertical deformation.

ii. Displacement control method with a constrained column tip (DCC)

   The prescribed motion control is stopped and the column tip is restrained against any vertical motion.

iii. Load control method with an unconstrained column tip (LCU)

   The axial load which was applied on the top of the column during step 1 is maintained. In this case, the top of column is also free to move vertically downward.

Step 3: Residual Capacity Check

Similar to step 2, the procedure is also initiated by resetting the velocity of the column to zero. In step 3, a prescribed motion control is applied at the tip of the target column using a specified displacement rate to obtain the load deflection curve and the residual axial load carrying capacity of the target column after being subjected to blast loads.

9.5 Dynamic Response of UC Column Subjected to Blast Loads and Its Plastic Damage Evolutions

The UC column, which has dimension of 800x300mm, when subjected to close-in explosion in the direction of its minor axis seems susceptible to failure. Three explosions with a constant charge weight of 100 kg TNT at three stand-off distance *R* of 3, 5 and 10 meters were analyzed.

When the UC column is subjected to 100 kg TNT at R = 3 meters (UC-3), the plastic damage evolution as shown in Figure 9.7 indicated shear failure of the column. Such a shear failure mode occurs as the flexural deflection has no time to develop, while the shear strains and stresses at locations near to the ends of column greatly increase within a short duration of time (within less than 10 msec). Severe plastic hinges formed at the locations shown in red colour in Figure 9.7. Based on blast loading regimes proposed by Cormey et al. (2008), impulsive loading occurs when $t_d/T < 0.1$ or $t_m/t_d > 3$. The blast load applied on UC-3 is within this range with t_d/T equal to 0.065. Similar condition is also found when the stand-off distance increases to 5 meters. An impulsive blast load having t_d/T equals to 0.094 leads to the failure of column UC-5.

For UC-10, the target column still stands after the blast with no significant damage. The post damage condition of the target column is shown in Figure 9.8 with no significant shear strain found at the two ends. Besides, the evolution of the plastic damage indicates that the response of UC-10 $(t_d/T = 0.26)$ is a combination of flexure and shear, typical of dynamic loading with $0.1 < \frac{t_D}{T} < 10$. The early stage plastic hinges shown in red colour occur at mid height of the column and at the two ends.

To evaluate the effect of stand-off distances on the dynamic response of the target column, the lateral and axial displacement time histories of the relevant target columns are plotted in Figure 9.9. The lateral displacement plotted is the maximum value observed along the column height, while the axial displacement is that at the tip of the column (h = 3m). Positive lateral displacement is towards the distal face of the column, while for axial displacement a positive value is towards the ground. Very large lateral and axial displacements are observed for both cases of UC-3 and UC-5 showing that the columns have collapsed. For UC-10, the target column experiences significantly smaller displacements (both lateral and axial) with less plastic damage.

The axial reaction forces of the three target columns are also compared in Figure 9.10a. The largest reaction force obtained is for UC-3, followed by that for UC-5 and UC-10. It is obvious that when R=3m, the target column experiences the most severe damage as shown in Figure 9.10b. For UC-3 and UC-5, after the second oscillation, the reaction force curve converges quickly to an asymptotic value indicating that the column has failed, no longer able to sustain any axial load. Compared to UC-3, UC-5 experienced a smaller peak axial reaction force, nearly half that of UC-3.

Among the three cases, UC-10 experiences the least damage with very small deformation observed. Nevertheless, the residual axial capacity C_{RA} of UC-10 still needs to be determined. From step 3 analysis, the C_{RA} of UC-10 is 5500kN. Since the axial capacity C_{UA} of an undamaged UC is 9240kN, the damage index, DI, of UC-10 calculated based on Equation 9.2 is 40.4%.

$$DI = (1 - C_{RA}/C_{UA}) \times 100\% \tag{9.2}$$

Such a significant decrease in the axial capacity of UC-10, however, may not lead to the complete collapse of the column and UC-10 is still expected to be able to sustain some imposed axial loads.

A recent study on the damage index *DI* of blast loaded structure had been carried out by Shi et al. (2008) on conventional RC columns of dimension 600mmx400mm with a height of 3.6 meters containing 1.05% longitudinal reinforcement. The columns with *DIs* equal to 20%, 50%, and 80% were reported when uniform impulsive blast loads having reflected impulses I_R of 1.0, 1.7, and 2.8 *MPa.msec* were applied, respectively. It may be noted that the blast load is non-uniformly distributed along the column height arising from a hemispherical close-in explosion, thus the results herein may not be directly comparable to those obtained by Shi et al. (2008). However, the general trend shows an increase in the blast impulse leading to higher *DI* of the column. The aforementioned study on the UC column indicates the need to strengthen the RC columns considered herein to increase resistance against close-in explosions.

9.6 Enhancing Blast Resistance of RC Column by Encasement Method

To enhance the RC column's blast resistance, encasement is proposed as shown in Figure 9.1. In this study, three encasement materials are evaluated against the blast loads from close-in explosions, viz. normal concrete (NSC) of f_c'=30*MPa*, high strength concrete (HSC) of f_c'=55*MPa* and engineered cementitious composites (ECC) of f_c'=55*MPa*. The properties of all three materials were given in Table 6.3.

Similar to that of the UC columns, the study on encased columns is focused on the plastic damage level sustained, the dynamic response, and the residual axial capacity of columns

after being subjected to blast loads from a constant charge weight of 100 kg TNT at three stand-off distances *R* of 3, 5 or 10 meters.. The damage index *DI* is calculated for all the columns.

9.6.1 Effects of Types of Encasement Layer

Among the three materials (NSC, HSC and ECC), ECC has the lowest young modulus *E*, with E_{HSC} nearly twice and E_{NSC} 1.45 times that of E_{ECC}. In this section, an encasement layer 25 mm thick is analyzed.

Subjected to blast loads of 100kg TNT at a stand-off distance of 5 meters, the dynamic response of columns NSC25-5, HSC25-5 and ECC25-5 are studied. As shown in Figure 9.11, ECC25-5 experiences the least damage with smaller plastic regions observed compared to HSC25-5 and NSC25-5. The level of damage of columns NSC25-5 and HSC25-5 are rather severe with most parts of the columns already in a plastic state.

The lateral displacement time histories which are the maximum observed on NSC25-5, HSC25-5 and ECC25-5 respectively are shown in Figure 9.12a. The figure indicates that ECC25 exhibited the smallest displacement, around 72% and 62% of those observed on HSC25 and NSC25, respectively. ECC25-5 also exhibited the lowest residual lateral displacement, although its Young's modulus E_{ECC} is significantly lower. This is probably due to higher energy dissipation as a result of microcracking of the ECC layer.

The axial reaction force time histories of the three encased RC columns when subjected to 100 kg TNT at *R*=5 meters are plotted in Figure 9.12b. As the blast loads applied are similar, the peak reaction force of each of the three columns is roughly similar with slight

differences observed arising from the difference in stiffness. After the blast loads are applied within a short duration of time (t_d< 5 msec), the axial reaction force of a smaller magnitude in the opposite direction is observed. And after several oscillations (~60 milliseconds), the loads on the columns are expected to stabilize, reaching a reaction force equal to the imposed load applied at Step 1.

From the discussion above it is clear that severe plastic damage is observed on columns NSC25-5 and HSC25-5. To examine the damage level of such columns after being subjected to blast loads of 100 kg TNT at R = 5 meters, the residual analysis (Step 3) is carried out and the results obtained are shown in Figure 9.13. As expected, columns NSC25-5 and HSC25-5 almost failed, registering very small residual axial capacity (less than 500kN or approximately 97% reduction in axial capacity). Column ECC25-5 registered higher residual axial capacity, more than five times that of columns HSC25-5 and NSC25-5. Column ECC25-5 is more effective vis-à-vis columns HSC25-5 and NSC25-5 in resisting blast loads as the damage index (*DI*) of ECC25-5 is 79%.

The lateral displacements, residual axial capacity and damage index (*DI*) observed from being subjected to 100kg TNT at R = 3, 5 and 10 meters are summarized in Table 9.2. When subjected to blast loads from a stand-off distance R = 3 meters, column ECC25-3 exhibited very large lateral deformation (120.5 mm), while columns HSC25-3 and NSC25-3 effectively collapsed. This implies that ECC25 is more ductile. In the case of HSC25-5 and NSC25-5 it may be noted that their DI's are rather similar to the DI of ECC25-3 (97.3%). The deformation of HSC25-5 and NSC-5 are 16.2 and 18.8, respectively.

Table 9.2 Lateral Displacement and Damage Indexes of ECC25, HSC25, NSC25 and UC after Being Subjected to 100kg TNT at Various Stand-off Distances

Specimen	Lateral Displacement (mm)			Damage Index (%)		
	R=3m	R=5m	R=10m	R=3m	R=5m	R=10m
ECC25	120.5	11.6	3.0	97.3	79.4	21.4
HSC25	failed	16.2	3.1	100.0	96.7	27.4
NSC25	failed	18.8	3.4	100.0	96.6	24.3
UC	failed	failed	4.3	100.0	100.0	40.5

When the stand-off distance increases to R=10 meters, the performance of column ECC25-10 is similar to columns HSC25 and NSC25. The *DI* of ECC25-10 is 21.4%, rather similar to that of columns HSC25-10 and NSC25-10, hovering between 24% and 27%. The similarity in the *DI* may be due to a trade-off in terms of the performance of ECC material, i.e. microcracking of ECC layer which increase energy dissipation vs. a lower Young's modulus contributing to a lower overall stiffness of the encased column.

The residual axial capacities of the columns subjected to 100kg TNT at various stand-off distances are also plotted in Figure 9.14. Columns HSC25 achieved higher residual capacity C_{RA} than columns NSC25. However, due to the higher axial capacity of the undamaged columns C_{UA}, the *DIs* of columns HSC25-5 and HSC25-10 are larger than that of columns NSC25-5 and NSC25-10.

9.6.2 Effects of Thickness of Encasement Layer

The study is also carried out on columns with 50mm thick encasement layers. The residual axial capacities of columns UC, NSC50, HSC50 and ECC50 are plotted in Figure 9.15a. The lateral displacements and damage indices (*DIs*) of the columns are also summarized in Table 9.3.

Table 9.3 Lateral Displacement and Damage Index Level of ECC50, HS50, NSC50 and UC after Being Subjected to 100kg TNT at Various Stand-off Distances

Specimen	Lateral Displacement (mm)			Damage Index (%)		
	R=3m	R=5m	R=10m	R=3m	R=5m	R=10m
ECC50	49.4	8.2	2.1	83.7	53.8	5.0
HSC50	failed	10.9	2.2	100.0	87.7	23.8
NSC50	failed	12.4	2.6	100.0	88.2	21.0
UC	failed	failed	4.3	100.0	100.0	40.5

Results of columns with the two thicknesses of encasement, viz. 25mm and 50mm as summarized in Tables 9.2 and 9.3, and Figures 9.14 and 9.15. An increase in the thickness of NSC and HSC encasement from 25mm to 50mm upon being subjected to 100kg TNT at a stand-off distance *R*=3m did not help prevent the failure of both column NSC50-3 and HSC50-3. On the other hand, column ECC50-3 survived with a reduced *DI*, equal to 83.7%. Increasing the thickness of the ECC layer from 25mm to 50mm, ECC25-3 vs ECC50-3 resulted in a reduction in lateral displacement and *DI* by 60% and 14%, respectively.

From Tables 9.2 and 9.3, the lateral displacements exhibited by columns NSC50 and HSC50 are reduced, by 23% to 34% vis-à-vis columns NSC25 and HSC25, while the *DIs* are also reduced, up to 13.4% lower (Figure 9.16). On the other hand, column ECC50 showed a significant decrease in lateral displacements, by 28% to 60% vis-à-vis column ECC25, and in *DIs*, up to 77% lower. The improved performance of columns with thicker encasement layers could be due to the combined effect of higher stiffness and more effective confinement.

9.6.3 Effects of Displacement Control and Load Control Methods on the Dynamic Analysis

Three methods, viz. LCU, DCU and DCC methods in the step 2 analysis to control the vertical movement of the target column and to apply the axial imposed loads from the upper parts of the RC frame structure are evaluated. Three similar columns, ECC25-5, are analyzed using the three different methods and the plastic damage contours of the columns shown in Figure 9.17. Column ECC25-5 analyzed using LCU and DCU methods show similar plastic damage patterns having a larger plastic region with less severe plastic damage than that analyzed using the DCC method.

The axial and lateral displacement time histories as plotted in Figure 9.18 also show that the LCU and DCU methods obtained roughly similar results. It is probably due to the lack of constraint at the column tip, allowing vertical movement to the place as shown in Figure 9.18b.

The constant axial load applied at any time during Step 2 analysis in the LCU method resulted in slightly smaller lateral and axial displacements obtained as compared to those obtained using DCU method. The axial reaction force time history is shown in Figure 9.19a. It may be noted that the axial reaction force obtained using the LCU method “flat lined” to 210kN while that obtained using the DCU method “flat lined” to zero. The DCC method, on the other hand, resulted in the smallest lateral displacement with the largest axial reaction force due to the effects of vertical constraints at the column tip during the Step 2 analysis.

The residual capacities C_{RA} of ECC25-5 are shown in Figure 9.19b. The DCC method applied during step 2 analysis resulted in the highest residual value, followed by the LCU method showing slightly smaller values. This indicates that the columns with vertical restraint imposed (DCC) or axial loads applied (LCU) at the column tip during step 2 analysis experienced higher residual strength in the post blast analysis (Step 3). The DCU analysis, on the other hand, with no restraint or axial load applied during the step 2 analysis registered the lowest residual axial capacity.

9.7 Experimental Validation on Quarter Scale RC Columns

The experimental study was carried out to benchmark the numerical results obtained from numerical modeling on quarter scale RC cantilever columns of dimension 200 mm x 75 mm and of height 0.75 m as described in detail in Chapter 4. Four specimens of Q-UC-5-MI, Q-ECC10-5-MI, Q-UC-5-MA and Q-ECC10-5-MA were tested in sets of two (Table 4.4). Based on the preliminary numerical study, a combination of specific charge weight W and stand-off distance R having scaled distance Z of 1.08 $m/kg^{1/3}$ was chosen for the quarter scale specimens tested.

For blast loads directed along the minor axis of column, Figure 9.20a shows that column Q-UC-5-MI collapsed after the test. The large bending deformation and the stress wave propagation on the specimen's surface resulted in profuse cracking, leading to severe delamination of the concrete cover. On the other hand, column Q-ECC10-5-MI remained intact (Figure 9.20b) after the blast test even though it experienced rather large lateral deformation.

When the blast load is directed along the major axis (Figure 9.20c), no significant damage was observed in column Q-UC-5-MA, except for some localized spalling and local crushing at the corners and on the incident face due to impact from high velocity flying debris. Similarly for the strengthened column Q-ECC10-5-MA (Figure 9.20d), only minor non-structural damage was observed on the incident face where some localized gouging had been observed. However, particularly at one corner of the incident face, the encasement layer delaminated locally, probably due to impact from flying debris.

Numerical analysis was also carried out using LS DYNA and the results were compared to the experimental data for validation as shown in Figure 9.21. Numerical results showed good agreement with the experimental data with minor errors. The differences in peak lateral displacement and residual lateral displacement between numerical and experimental values observed for column Q-ECC10-5-MI are 1.5% and around 15% respectively. In the case of column Q-ECC10-5-MA, less than 1.5% difference in residual displacement was noted.

9.8 Summary

Numerical simulations have been carried out to study the effects of blast loads on a number of critical columns of a typical RC frame by taking into account the axial imposed loads from the upper floors. The study shows that UC-5 experienced very severe damage when subjected to close-in explosions being directed along its minor axis.

To enhance blast resistance, encasement using three types of cementitious materials were studied, NSC, HSC and ECC. Among the three materials, ECC performed best. Use of a 25mm thick encasement layer of ECC resulted in smaller displacement, higher residual

axial capacity and smaller plastic damage level. It also seemed to be able to shift the failure mode from one of shear to bending when subjected to close-in explosions. Increasing the thickness of the ECC layer also enhanced the residual capacity of column, resulting in smaller lateral and axial displacements of column. Use of NSC and HSC as encasement seemed to be not as effective with the retrofitted column still failing even when a thickness of 50 mm is used.

The parametric study has been validated using some experimental data conducted on quarter scale unencased and ECC encased RC columns models. Good agreement between numerical and the experimental peak and residual lateral displacement was observed. The experimental results showed a reduction in lateral displacement especially in the case of Q-ECC10-5-MI as compared to Q-UC-5-MI. The ECC encasement also seemed to be able to reduce concrete spalling and crushing as observed in the case of Q-ECC10-5-MA.

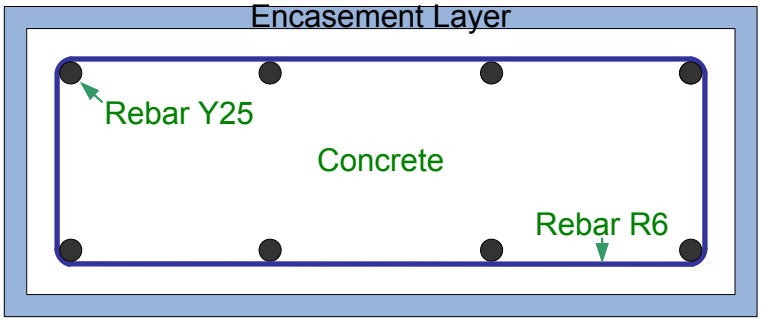

Figure 9.1 Cross Section of encased RC 800x300

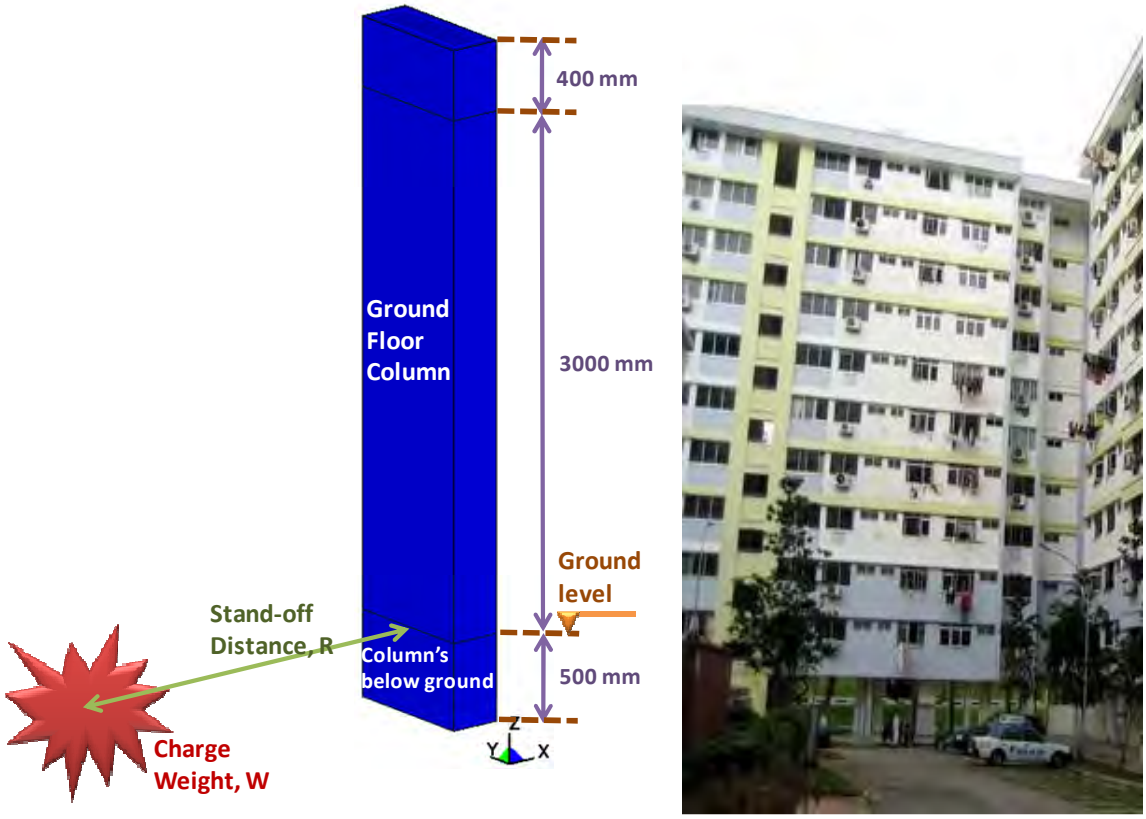

(a) (b)

Figure 9.2 (a) Illustration of hemispherical close-in explosion (b) Typical apartment block in Singapore

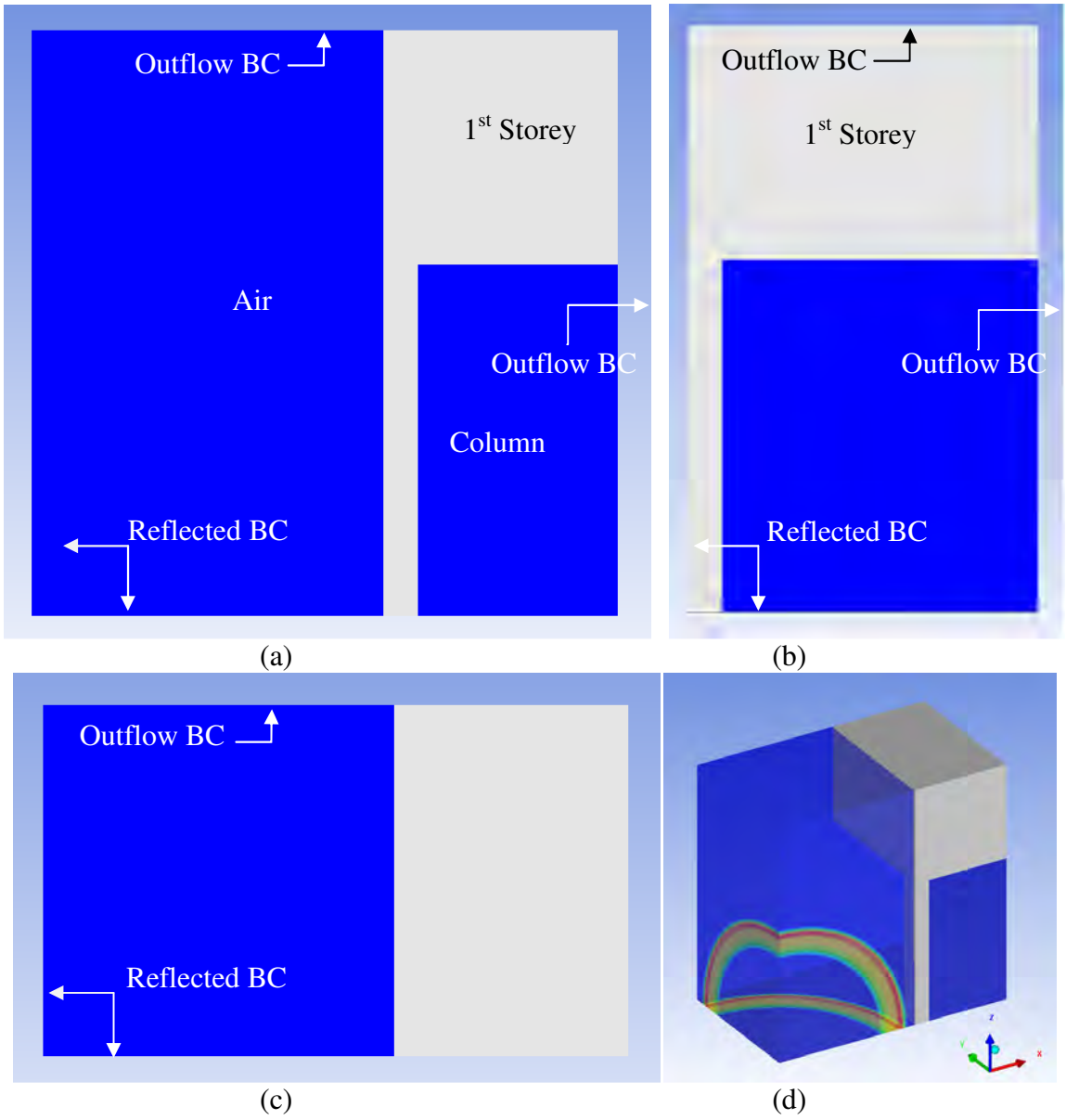

Figure 9.3 Configuration of the 3D blast loads analysis model (a) X-Z plan, (b) Y-Z plan, (c) X-Y plan, and (d) 3D views

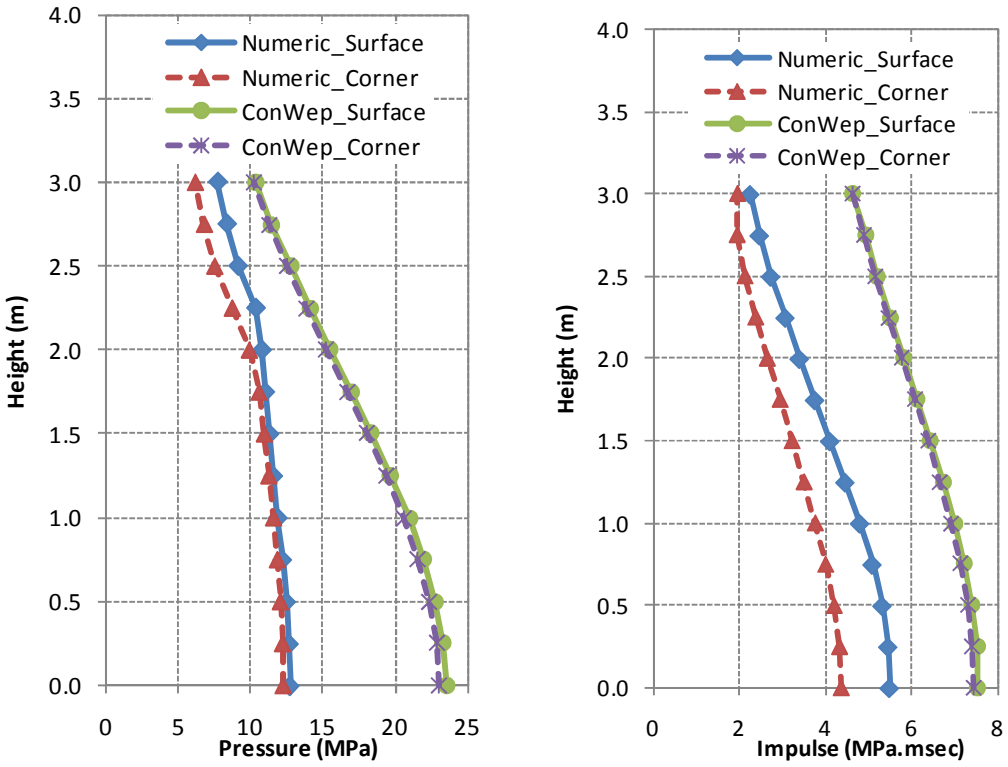

(a) (b)

Figure 9.4 Reflected (a) Pressure and (b) Impulse at different location on UC-3, numerical analysis vs. ConWep

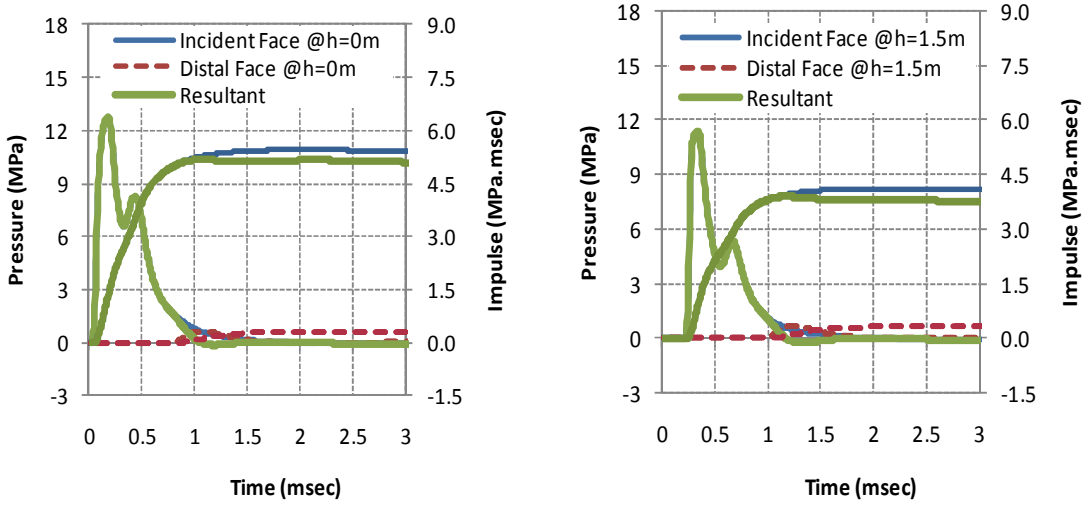

(a) (b)

Figure 9.5 Pressure and Impulse time histories on surface nodes of UC-3 at incident and distal faces at height (a) h = 0 m, and (b) h = 1.5 m

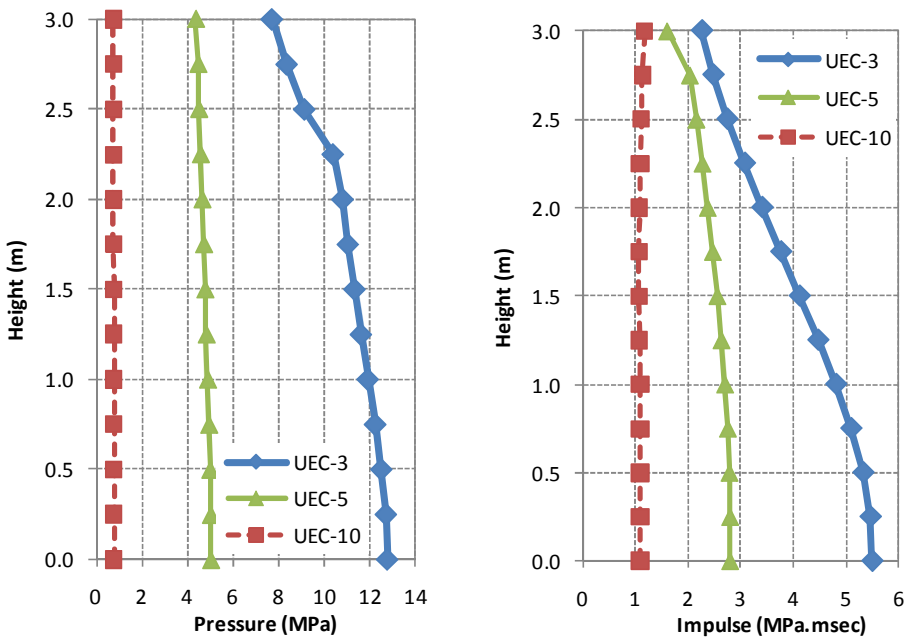

(a) (b)

Figure 9.6 Reflected (a) Pressure and (b) Impulse curves at different locations on UC-3, UC-5 and UC-10

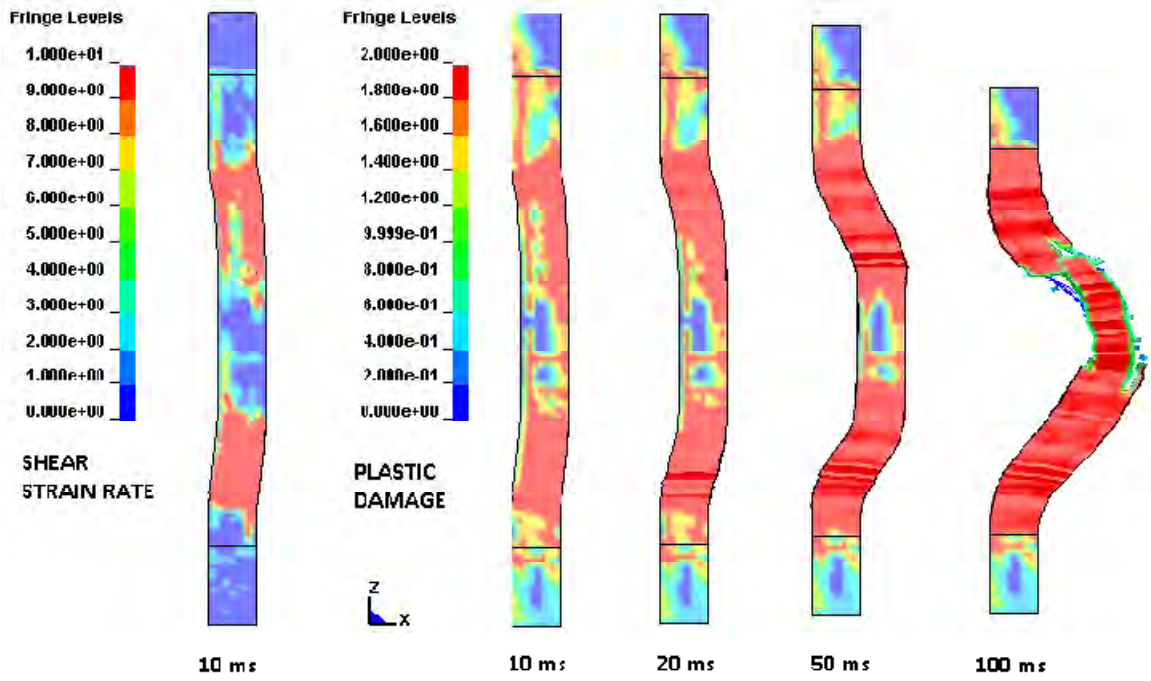

Figure 9.7 Shear strain and plastic damage evolution of UC-3 using LC method

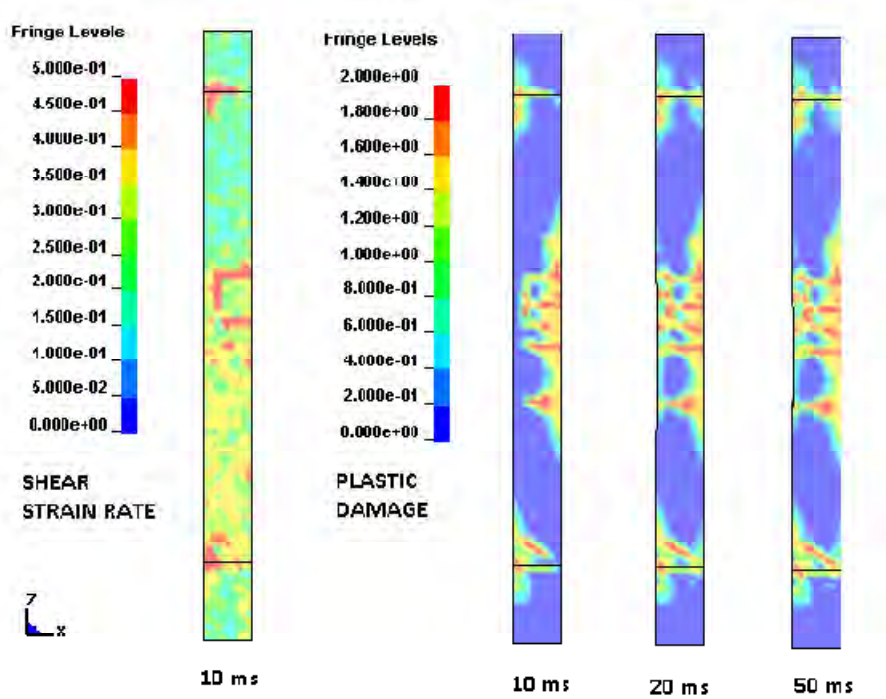

Figure 9.8 Shear strain and plastic damage evolution of UC-10 analyzed using LC method

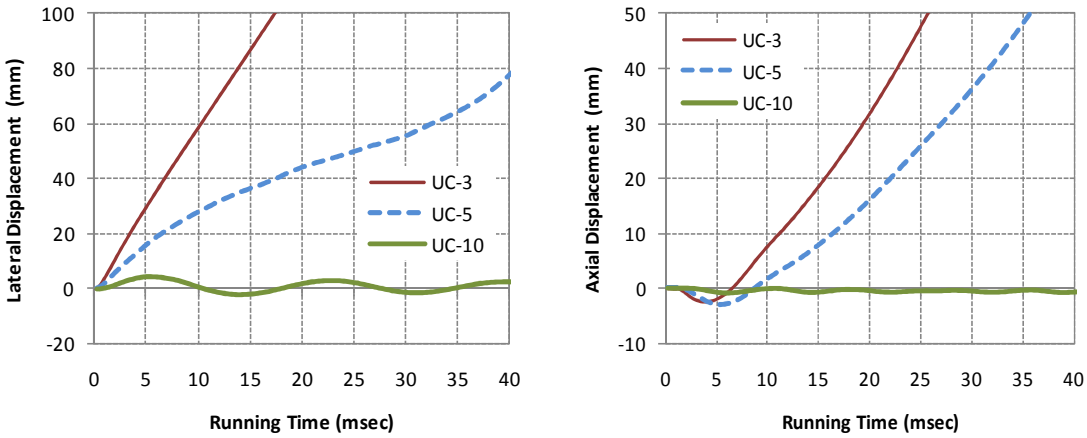

(a) (b)

Figure 9.9 (a) Lateral and (b) Axial displacements of UC-3, UC-5 and UC-10 at step 2

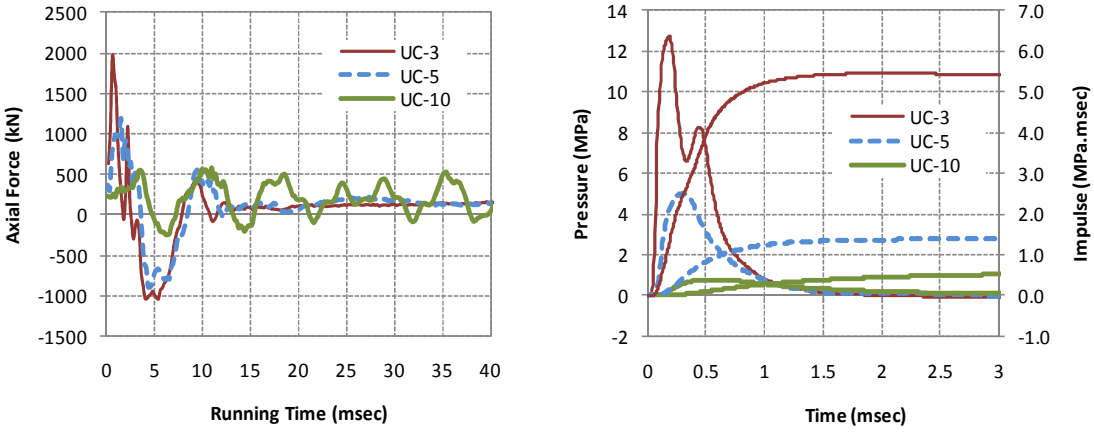

(a) (b)

Figure 9.10 (a) Reaction forces of and (b) Maximum reflected pressures and impulses at *h*=0m on UC-3, UC-5 and UC-10 at step 2

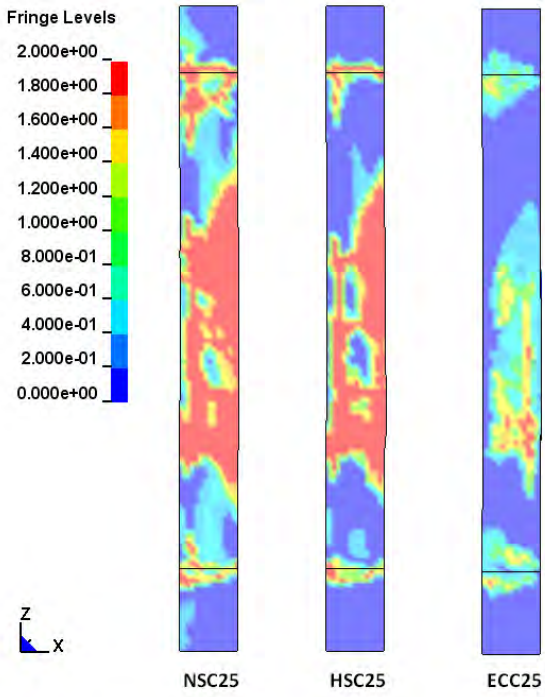

Figure 9.11 Plastic damage contour of NSC25-5, HSC25-5 and ECC25-5 analyzed using LC method

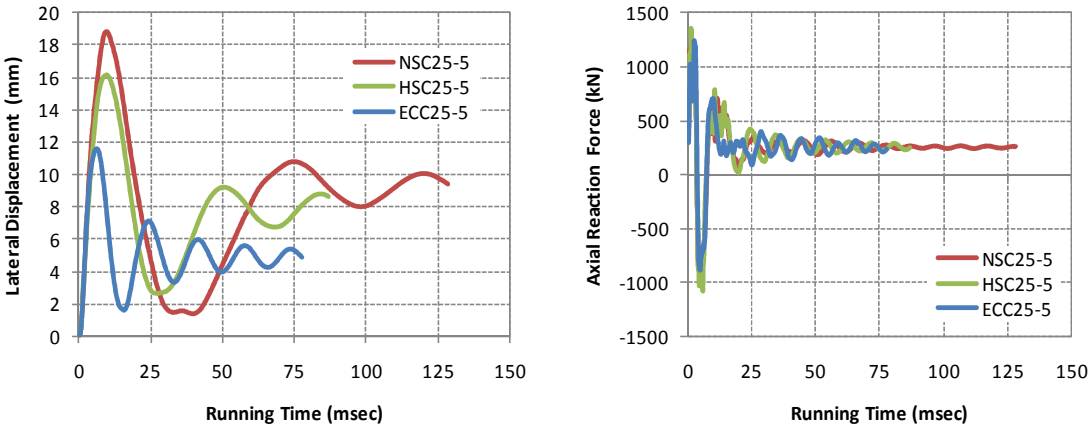

(a) (b)

Figure 9.12 (a) Lateral displacements and (b) Axial reaction forces of NSC25-5, HSC25-5 and ECC25-5 at step 2

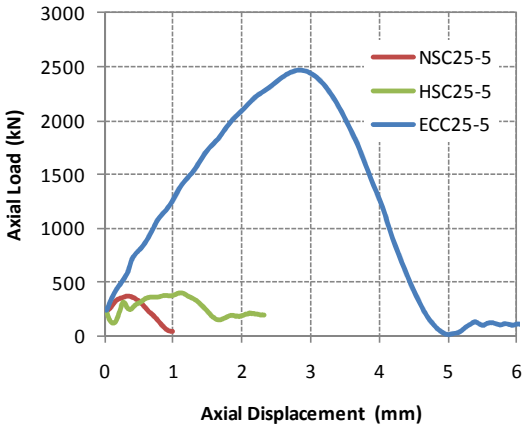

Figure 9.13 Residual capacities of NSC25-5, HSC25-5 and ECC25-5

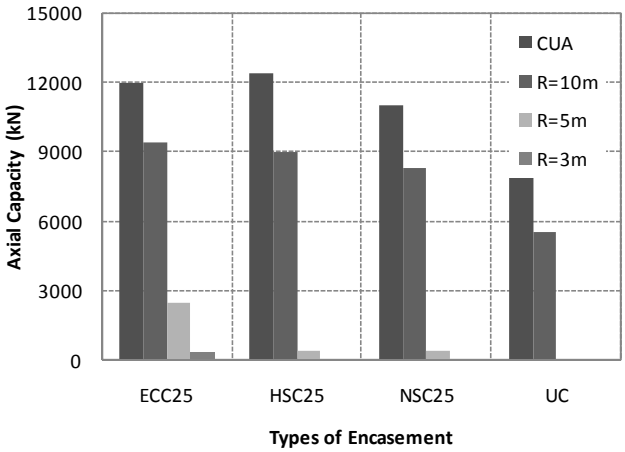

Figure 9.14 C_{RA} vs. C_{UA} of ECC25, HSC25, NSC25 and UC

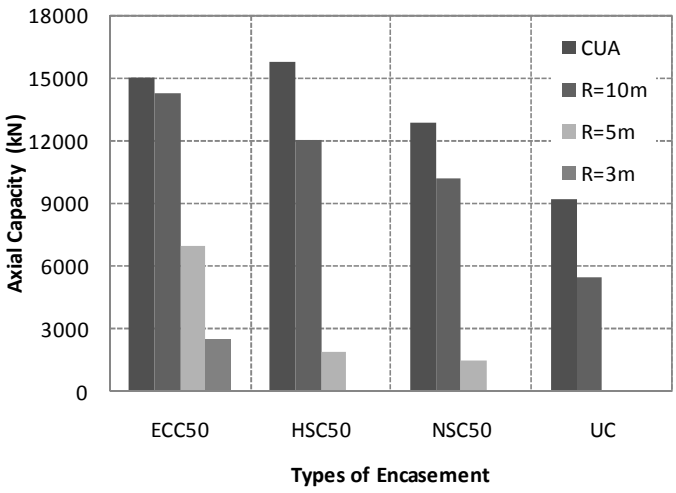

(a)

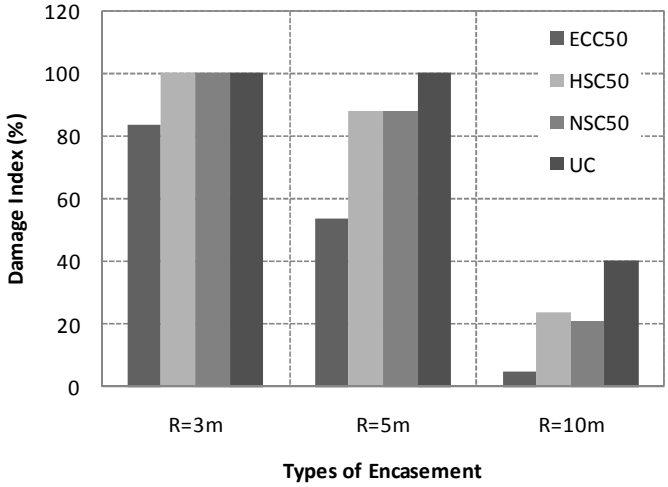

(b)

Figure 9.15 (a) C_{RA} vs. C_{UA} and (b) Damage indices of ECC50, HSC50, NSC50 and UC after being subjected to 100kg TNT at various stand-off distances

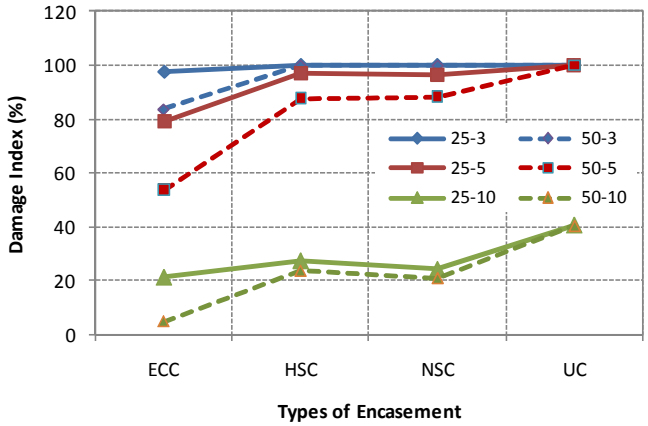

Figure 9.16 Damage indices of 25 and 50 mm thick encased and default RC800x300 subjected to 100kg TNT at various stand-off distances

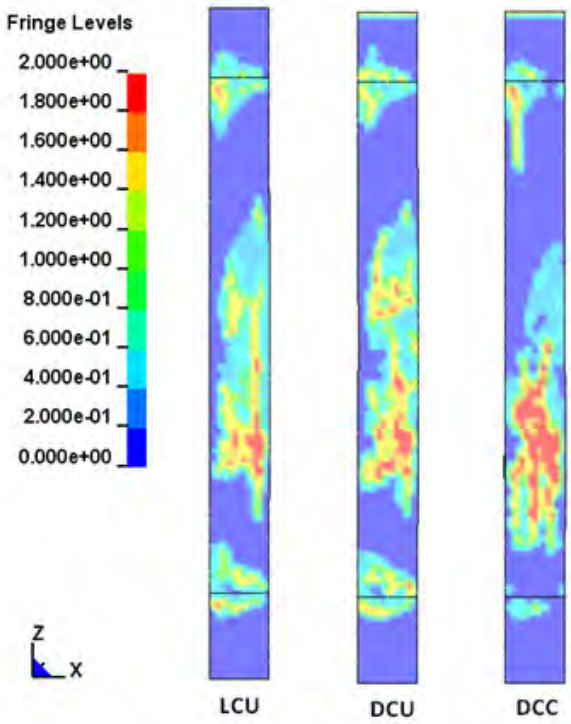

Figure 9.17 Plastic damage contour of ECC25-5 at step 2 analyzed using LCU, DCU and DCC methods

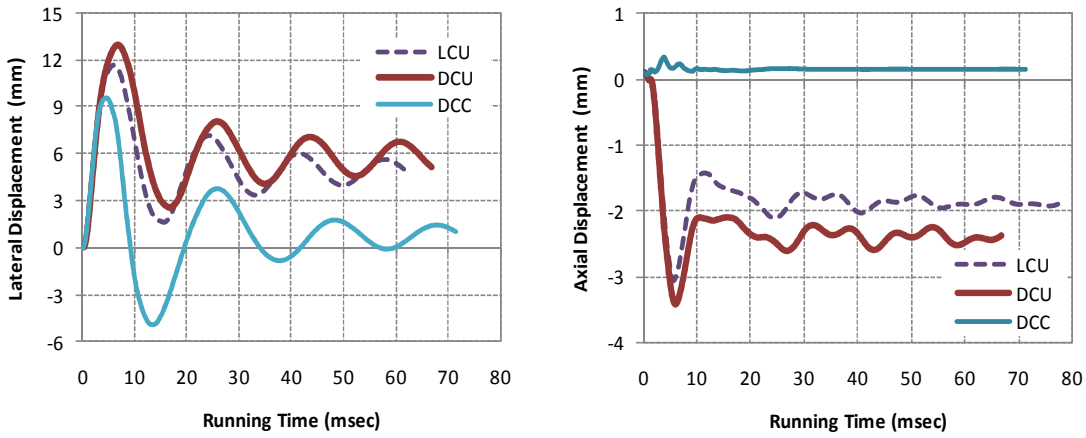

(a) (b)

Figure 9.18 (a) Lateral and (b) Axial displacements of ECC25-5 at step 2 analyzed using LCU, DCU and DCC methods

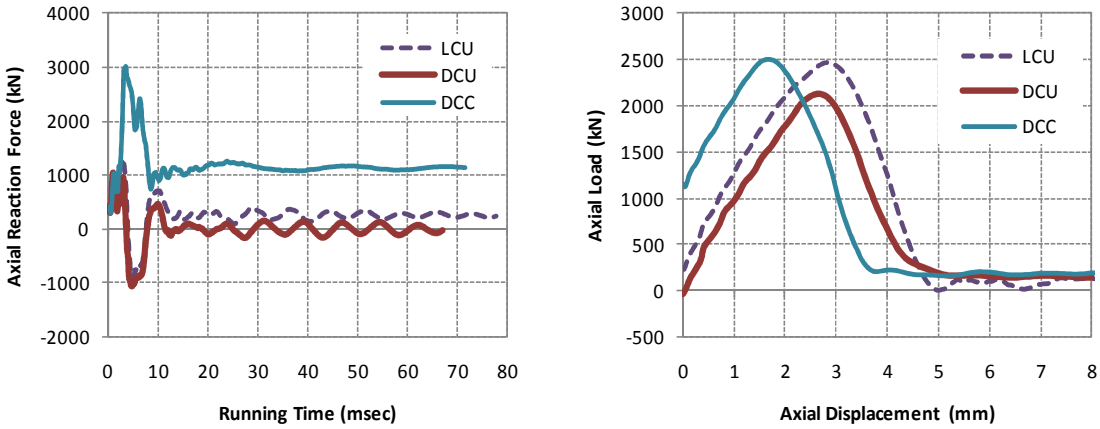

(a) (b)

Figure 9.19 (a) Axial reaction force at step 2 and (b) C_{RA} of ECC25-5 analyzed using LCU, DCU and DCC methods

(a) (b) (c) (d)

Figure 9.20 Post blast damage on Columns (a) Q-UC-5-MI, (b) Q-ECC10-5-MI, (c) Q-UC-5-MA, and (d) Q-ECC10-5-MA

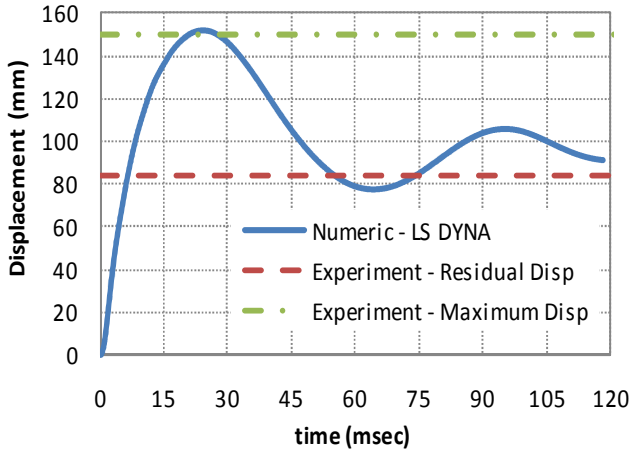

(a)

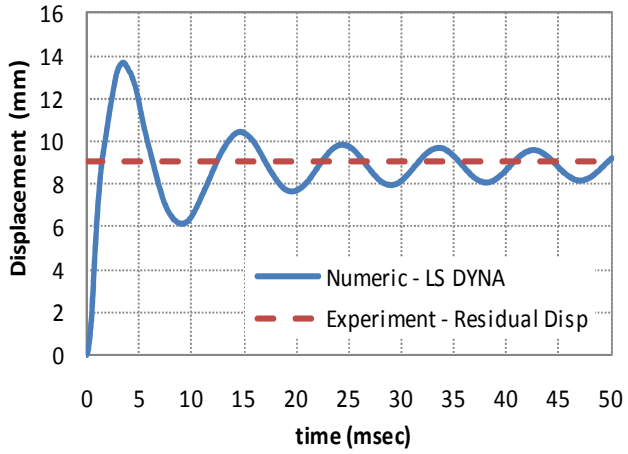

(b)

Figure 9.21 Lateral displacement time history of (a) Q-ECC10-5-MI and (b) Q-ECC10-5-MA

10 Conclusion

10.1 Review of Completed Research Work

The main objective of this research is to study the structural response of a typical existing RC apartment block in Singapore having a void deck on the ground floor with infilled RC frame from the 1st storey onwards subjected to close-in blast loads. The void deck on the ground floor may lead to channeling of the blast wave as it propagates from the source of explosion. The RC columns as used in a typical apartment block generally have *B/H* greater than two. What is apparent with such columns is that the column may fail when subjected to close-in blast loads directed parallel along its minor axis due to the large incident surface area coupled with a lower blast resistance. To enhance the blast resistance of such columns, encasement using hybrid-fiber Engineered Cementitious Composite (ECC) material was proposed.

Finite element analysis was carried in this study by utilizing LS DYNA, a commercial finite element software built by LSTC. MAT 72 Concrete Damage Release III which incorporates plasticity, hardening and softening characteristics of concrete/cementitious materials was selected as the material model for the concrete and hybrid-fiber ECC. It has three failure surfaces (initial, maximum and residual failure surfaces) and is capable of

migrating the failure surface from one curve to another by incorporating damage scale factor.

In the first phase of the present study, twenty RC cantilever columns of various dimensions were examined for both elastic and inelastic conditions when subjected to blast loads along the major and minor axes of the columns. The objective of this phase of study is to validate the numerical FE results obtained using LS DYNA against the proposed theoretical solution using an equivalent SDOF analysis. Besides, the transformation factors (*TFs*) provided by TM5–1300 US code and structural dynamics theory were also examined.

In the second part of this research, three dimensional numerical models were applied to simulate the blast wave propagation through the void deck of the ground floor. AUTODYN numerical software, which incorporates a finite difference solver for CFD analysis, was occupied. The numerical approach applied was first verified using experimental data from available literature and relevant empirical equations. By taking into account the effect of the geometric configuration of the ground floor void deck, the lateral loads on critical ground floor columns when subjected to specific blast were established.

The third phase of this research was a parametric study of standalone RC columns. Three types of boundary conditions were simulated with specified constrains provided at the top and bottom ends of the columns against the horizontal and vertical motions. Since blast loading is within the dynamic region, the blast pressure from 250kg TNT at 10m stand-off distance was applied uniformly onto the columns. The effects of several loading and

geometric parameters on the dynamic response of the columns were analyzed. The numerical FE results of the third phase were verified through calculations using the equivalent SDOF method.

In the fourth phase of this research, a numerical finite element (FE) study to evaluate the potential of ECC encasement to retrofit existing RC columns to resist close-in blast loads arising from Vehicle Borne Improvised Explosive Device (VBIED) was carried out. The aim is to quantify the extent to which ECC improves the resistance of RC columns against blast loading. The study was focused on analyzing the damage sustained by the ground floor columns of typical RC frames after being subjected to 100kg TNT within a stand-off distance ranging from 3 to 10 meters. Both ends of the columns were constrained against the horizontal motion, based on the assumption that the 1st storey slab abutting the top of the ground floor column is rigid enough to provide sufficient lateral stiffness. Moreover, non uniform blast pressure loads were applied onto the columns since most of the loadings studied occurred within an impulsive region, one of the parameters for close-in blasts. Parametric studies were carried out for three encasement materials (NSC, HSC and ECC) and two thicknesses of encasement layer (25mm and 50mm). Three methods taking into consideration the axial imposed loads applied arising from the upper structure were used to control the vertical movement of the column when subjected to blast loads. The results obtained were compared in terms of the lateral displacement and the residual axial capacity of the columns.

Lastly, experimental study on quarter scale RC columns was carried out with the assistance from DSTA, Singapore to further enhance the understanding of the blast performance of standalone RC columns typical of Singapore's apartment blocks and to

study the effectiveness of ECC encasement as a potential strengthening method for blast resistance. The main objective of this experiment is to calibrate the results of and provide results for benchmarking against the numerical finite element (FE) study conducted with special focus on the performance of columns with *B/H* ratios exceeding 2. Four specimens, comprising two RC and two ECC encased RC columns were tested in sets of two. Each set was subjected to blast loads of a scaled distance Z of 1.08 $m/kg^{1/3}$ parallel to the major or minor axis of the columns. The lateral displacements of the columns were measured and the results were compared to those obtained from numerical FE analysis.

10.2 General Conclusions

From the numerical FE analysis of the RC columns and ECC encased RC columns subjected to blast loads, good agreement between the numerical FE results and the experimental data was achieved. Thus, the numerical FE material models for steel, concrete (NSC and HSC), and ECC as a column component were verified. In the parametric studies, in the absence of experimental data, the numerical FE results were verified using a proposed equivalent SDOF analysis for both elastic and inelastic conditions and good agreement was observed.

From the parametric study on the type of encasement layer, it was concluded that the hybrid-fiber ECC material demonstrates a significantly better potential for the retrofitting of existing columns as compared to NSC and HSC. It was shown that the ECC encased RC column is much more efficient in resisting close-in blast as compared to the NSC and HSC encased RC columns of the same dimension and with the same reinforcement ratio. It was also found that a relatively thinner ECC encasement layer may be used in place of the thicker NSC and HSC encasement layers.

10.3 Summary of Findings

The findings of this study, which have been given earlier, are summarized in the following sections.

10.3.1 Standalone Cantilever RC Columns

Numerical and theoretical studies on twenty standalone cantilever RC columns of various dimensions subjected to blast load directed along the major and minor axes were carried out under both elastic and inelastic conditions, the following conclusions were drawn

10.3.1.1 Elastic Analysis of Standalone Cantilever RC Columns

1. From a comparison of the elastic lateral displacements obtained from the numerical analysis to those obtained from the Equivalent SDOF – Direct Integration method, it was found that the numerical models gave very similar predictions.
2. The dynamic magnification factors (DMF) obtained from the lateral displacements analyzed using Equivalent SDOF – Direct Integration method and the proposed numerical method were in good agreement with values calculated using methods based on structural dynamics theory.
3. Based on the results obtained, the load transformation factors obtained ranged between 0.368 and 0.421 with most of the values falling below 0.40. This compares well with the K_L=0.40 value specified in the TM5-1300. Meanwhile, the structural dynamics theory gave a unique K_L value of 0.363, providing a lower bound of K_L.

4. Based on the results obtained, the mass transformation factors obtained ranged between 0.222 and 0.242. This compares well with the K_M=0.227 value calculated using the structural dynamics theory. Meanwhile, the TM5-1300 specifies a higher K_M value of 0.26.

10.3.1.2 Inelastic Analysis of Standalone Cantilever RC Columns

1. The correlation between the yield forces R_u and the natural periods T of the observed cantilever RC columns were found to follow an exponential decay pattern.
2. The inelastic peak responses (peak lateral displacement and peak response time) obtained from the proposed numerical analysis were in a good agreement to those obtained from the Equivalent SDOF – Step by Step Integration method.
3. On the basis of load transformation factors (K_Ls) plotted against t_D/T and B/H, the values obtained from the proposed analysis showed some minor scaterring around the line K_L=0.5, a value recommended by the TM5-1300 code and the structural dynamics theory for cantilever column subjected to uniformly distributed load.
4. The inelastic equivalent SDOF analysis could not be applied to the columns with most regions behaving elastically (Outliers_1). It is also not applicable for columns behaving in a highly inelastic condition (Outliers_2). The latter columns seemed to have collapsed under the effects of the applied blast loads.

10.3.2 Blast Loads on Ground Floor Columns at the Void Deck

The study on blast propagation on buildings and RC frames show that the proposed numerical analysis using AUTODYN agrees well with available experimental data and code. Thus, the proposed numerical method was then extended to study the effects of the

upper reflecting surface and typical configuration of the ground floor columns most commonly observed in Singapore's HDB apartments. The findings are summarized as follows:

10.3.2.1 The Effects of Arrangement of Upper Reflecting Surface and Closely Spaced Columns

From the numerical simulation of the effects of arrangement of upper reflecting surface and closely spaced columns, the following conclusions were made:

1. The arrangement of the upper reflecting surface affects the pressure and impulse obtained at the incident face of the target column only when $R_{soffit} < R_{column}$. If such condition is met:
    a. The impulses observed are significantly greater, reaching up to 3 times that of standalone columns and columns with upper reflecting surface having $R_{soffit} = R_{column}$ especially at nodes located within a 1m wide band adjacent to the tip of the column.
    b. The difference in terms of pressure observed is significant only the region near to the upper reflecting surface within a 0.5m wide band adjacent to the tip of the column. The pressures observed at nodes located within height z=0-2.5m are however similar to those of standalone columns and columns with an upper reflecting surface having $R_{soffit} = R_{column}$.
2. The arrangement of the upper reflecting surface also affects the pressure and impulse obtained at the distal face of the target column when Rsoffit ≤ Rcolumn. If such condition is met:
    a. The impulse observed are significantly greater, reaching twice of those on standalone column, especially at the area near the column ends. In the case

with the upper reflecting surface having $R_{soffit} = R_{column}$, the largest impulse is observed at the column's tip on the distal face. For a case with the upper reflecting surface having $R_{soffit} < R_{column}$, the largest impulse observed is at the column's base on the distal face.

b. The difference in terms of pressure observed is significant only in the region adjacent to the upper reflecting surface within a 1m wide band adjacent to the tip of the column. It is also discovered that the shorter the R_{soffit} relative to R_{column}, the higher the pressure is observed. The pressures observed at nodes located within a 2m wide band adjacent to the column's base are however similar to those of the standalone column.

3. The particular arrangement of closely spaced columns studied enhances the impulses obtained at nodes located on the incident face of the target column and reduces those on the distal face. The columns nearby act as an additional reflection surface, channel and diffract the blast waves to the surrounding depending on how thay are arranged and may result in lower distal impulse.

10.3.2.2 The Effects of Configuration of Ground Floor Columns in Singapore's Apartment Block (HDB)

The following conclusions were drawn from the numerical study on the effects of the configuration of columns in the void deck on the ground floor

1. The pressure and impulse observed on the incident face of the exterior columns located at the edge of the building (critical columns) are not affected by any blast wave reflection from the 1st storey slab's soffit for the arrangement studied. The magnitudes of both the pressure and impulse on the nodes reduce with height of the nodes above the base of the column.

2. The blast waves reflection from the 1st storey slab's soffit affects the pressure and impulse observed at the incident faces on the interior and exterior columns adjacent to the critical columns. The results showed an increase in the pressure and impulse with the height above the base of the column.

10.3.3 Parametric Study on RC Columns Subjected to Blast Loads

The following conclusions are drawn based on the numerical parametric study conducted on RC columns subjected to blast loads. The RC column studied is of size 800x350mm with HF pinned end boundary conditions, unless stated otherwise. The extent of damage was based on the deformed shapes, the plastic damage contours and displacement time histories of the column.

10.3.3.1 Loading Variables

1. The lateral displacement of the column is found to be sensitive to the change in peak pressure P of blast load having a constant impulse I. The larger the P with a smaller loading duration t_d, the larger is the peak lateral displacement of the column. The difference in terms of lateral displacement obtained may reach up to 30%.
2. The lateral displacement of the column is found to be sensitive to the change in the impulse I of the blast load having a constant peak pressure P. The larger the I, the larger is the peak lateral displacement of the column. When the I is doubled, the lateral displacement may increase by up to 8 times. As the I increases further, it leads to the occurrence of column failure.

10.3.3.2 Loading Types

1. The blast pressure time history, either an exponential or a triangular load pulse, having similar peak pressure *P* and impulse *I* was found to have insignificant effects on the nonlinear behavior of the column i.e. the peak response time and peak lateral displacement.
2. The columns subjected to exponential load experienced peak response earlier than that of the triangular load case, with a smaller magnitude of the peak lateral displacement.
3. It was found that for the same amount of blast energy applied within a longer time duration, the column exhibited smaller peak lateral displacement.

10.3.3.3 Dimension of Column

1. The analysis was carried out for three dimensions of RC columns having *B/H* ratio > 2, viz. 500x200, 750x300 and 800x350 mm. It was found that columns having *B/H* ratio > 2 are prone to failure when subjected to blast loads directed along the minor axis.
2. Under low (*I*=2.5 *MPa.msec*) and high (*I*=5 *MPa.msec*) intensity blast loads, columns with smaller dimensions having smaller bending and shear strengths were found to experience larger lateral deformation.

10.3.3.4 Longitudinal Reinforcement Percentage and Transverse Reinforcement

1. It was observed that increasing the longitudinal reinforcement by two or three times significantly enhance the bending strength of the column. Columns with a higher percentage of longitudinal reinforcement exhibited smaller peak lateral displacement and showed less visible damage compared.

2. Columns with a smaller centre to centre spacing of the transverse reinforcement was found to exhibit slightly smaller peak lateral displacement. Under low (*I*=2.5 *MPa.msec*) and high (*I*=5 *MPa.msec*) intensity blast loads, 50 and 100 mm reductions in the spacing resulted in a less than 10% reduction in the peak lateral displacement.
3. The increase in strength as a result of increasing the number of transverse reinforcement with the same stirrup spacing was found to be more significant as compared to reducing the transverse reinforcement spacing. Doubling the number of stirrups may reduce peak displacement by half.

10.3.4 Enhancing the Strength of RC Column Subjected to Close-In Blast Loads Using ECC Encasement Materials

The following conclusions are drawn based on the numerical parametric study conducted on 800x300mm RC columns subjected to blast loads, unless stated otherwise. The extent of damage in this study was based on the displacement time histories, the plastic damage contours and damage index (*DI*) of the column.

10.3.4.1 Dynamic Response of Conventional RC Column Subjected to Close In-Blast Loads and Its Plastic Damage Evolution

1. It was observed that when subjected to impulsive blast loads from close-in explosion (*W*=100kg TNT, *R*=3 or 5m), the plastic damage evolution indicated shear failure of the column. It occurred as the flexural deflection has no time to develop, while the shear strains and stresses at locations near the ends of column increase greatly within a short duration of time.
2. When subjected to dynamic loads (*W*=100kg TNT, *R*=10m), no significant shear strain was found at both ends. Besides, the evolution of the plastic damage

indicated that the column's response is a combination of flexure and shear with plastic hinges at the mid height and at both ends of the column.

3. An increase in the blast impulse loaded on the RC column was found to increase the *DI* of the damaged column.

4. Based on the results obtained, existing RC columns subjected to close-in explosion are unable to resist the close-in blast loads especially when directed along the minor axis.

10.3.4.2 Enhancing Blast Resistance of RC Column by Encasement Method

Three encasement materials were evaluated against the blast loads from close-in explosions, viz. normal concrete (NSC), high strength concrete (HSC) and engineered cementitious composites (ECC).

1. Effects of Types of Encasement Layer

   - From the parametric study, it was demonstrated that ECC25-5 exhibit the lowest peak lateral displacement, the lowest residual lateral displacement, as well as the highest residual axial capacity although ECC has the lowest Young's modulus *E* compared to HSC and NSC.
   - ECC25-3 with a stand-off distance *R* of 3m was found to experience similar *DI* as columns HSC25-5 and NSC25-5 with a 5m stand-off distance.
   - It was also shown that the ECC25-3 is able to exhibit larger peak lateral displacement before failure, when compared to columns HSC25-5 and NSC25-5.

2. Effects of Thickness of Encasement Layer

- It was observed that an increase in the thickness of NSC and HSC encasement from 25mm to 50mm did not help prevent the failure of columns NSC50-3 and HSC50-3 upon being subjected to 100kg TNT at a stand-off distance R=3m.
- On the other hand, increasing the thickness of the ECC layer from 25mm to 50mm (ECC25-3 to ECC50-3) resulted in a reduction in the lateral displacement and *DI* (by 60% and 14% respectively).
- Overall, the improved performance of columns with thicker encasement layers is probably due to the combined effect of higher stiffness and more effective confinement.

3. Effects of Displacement and Load Control Methods on Residual Axial Capacity

   The DCC method applied during step 2 analysis resulted in the highest residual value, followed by the LCU method showing slightly smaller values. This indicated that the columns with vertical restraint imposed (DCC) or axial loads applied (LCU) at the column tip during step 2 analysis experienced higher residual strength in the post blast analysis (Step 3). The DCU analysis, on the other hand, with no restraint or axial load applied during the step 2 analysis registered the lowest residual axial capacity.

10.3.5 Experimental Validation on Quarter Scale RC and ECC Encased RC Columns

1. It was observed that for blast loads directed along the minor axis of column, the RC column specimen collapsed due to large bending deformation and the stress wave propagation on the specimen's surface resulted in profuse cracking, leading

to severe delamination of the concrete cover. On the other hand, the ECC encased RC column specimen remained intact after the blast test even though it experienced rather large lateral deformation.

2. When the blast load is directed along the major axis, no significant damage was observed in the RC column specimen, except for some localized spalling and local crushing at the corners and on the incident face due to impact from high velocity flying debris. Similarly for the ECC encased RC column, only minor non-structural damage was observed on the incident face where some localized gouging had been observed. However, particularly at one corner of the incident face, the encasement layer delaminated locally, probably due to impact from flying debris.
3. It was observed that the numerical results in terms of peak lateral and residual displacement showed good agreement with the experimental data with minor errors.

10.4 Recommendations for Further Studies

In order to fully understand the behavior of RC frames and columns subjected to blast loads and the full potential of ECC as a retrofit material the existing columns subjected to close-in blast, further studies are recommended in the following areas

1. For a given design based on the required blast resistance criteria, a parametric study of ECC encasement should be carried out to arrive at an optimal thickness of ECC encasement layer appropriate to the critical RC column and to establish the relationship between the required ECC encasement thickness and the blast loading in terms of the applied impulse given as a function of charge weight W, and stand-off distance R.

2. Field tests on full-scale unencased and encased RC columns subjected to close-in blast with an applied axial load from the design imposed load of upper storey structure can be carried out to further verify the blast resistance analysis.
3. Static test on undamaged and damaged, unencased and encased RC columns can be performed in order to verify the results obtained from the numerical analysis conducted on the total and residual axial capacity of such columns.
4. The numerical analysis can be further expanded to evaluate the dynamic response and the blast resistance of full scale 2D and 3D RC frames.

REFERENCES

Baker, W. E., (1967) Prediction and scaling of reflected impulse from strong blast waves. *International Journal of Mechanical Science V.9(1), pp.45-51*

Baker, W., Cox, P., Westine, P., Kulesz, J., Strehlow, R., (1983) Explosion hazard and evaluation. *Elsevier, Amsterdam*

Baker, W.E., Westine, P.S., Dodge, F.T., (1991) Similarity methods in engineering dynamics: Theory and practice of scale modelling. *Elsevier, Amsterdam*

Bogosian, D., Piepenburg, D., (2002) Effectiveness of frangible barriers for blast shielding. *Proceeding of 17th International Symposium on the Military Aspects of Blast and Shock, Las Vegas*

Brode, H.L., (1955) Numerical solutions of spherical blast waves. *Journal of Applied Physics V.*26 *pp.766–774*

Brode, H. L., (1958) TSL-107-10 64: A calculation of blast wave from spherical charge of TNT. *Defense Technical Information Center, Santa Monica*

CEB Comité Euro-International du Bèton, (1993) CEB-FIP model code 1990: Design code. *ASCE Wiltshire, UK: Redwood Books*

Century Dynamics, (2007) AUTODYN User Documentation

Chen W.F., (1994) Constitutive equations for engineering materials Volume 2: Plasticity and modeling. *Elsevier, Netherland*

Chapman, T. C., Rose, T. A., Smith, P. D., (1995) Reflected blast wave resultants behind cantilever walls: A new prediction technique. *International Journal of Impact Engineering, V.16(3), pp.397-403*

Chapman, T. C., Rose, T. A., Smith, P. D., (1995). Blast wave simulation using AUTODYN2D: A parametric study. *International Journal of Impact Engineering, V.16(5-6), pp.777-787*

Cormie, D., Mays, C., Smith, P. (2009) Blast effects on buildings 2nd Edition. *Thomas Telford Ltd., London*

Crawford J.E., Malvar J.L., Wesevich J.W., Valancius J., Aaron D.R., (1997) Retrofit of RC structures to resist blast effects. *ACI Structural Journal V.94 pp. 371-377*

Crawford J.E., Malvar J.L., Morril K.B., Ferritto J.M., (2001) Composite retrofits to increase the blast resistance of RC buildings. *Proceeding of 10th International Symposium on Interaction of the Effects of Munitions with Structures*

Clough R.W., Penzien J., (1975) Dynamics of structures. *McGraw Hill, New York*

Hallquist, J.O., (2006) LS-DYNA keyword user manual - Nonlinear dynamic analysis of structures. *Livermore, California: Livermore Software Technology Corporation, California*

Hallquist, J.O., (1998) LS-DYNA theoretical manual - Nonlinear dynamic analysis of structures. *Livermore, California: Livermore Software Technology Corporation. Livermore, California*

Hayes J.R., Woodson S.C., Pekelnicky R.G., Poland C.D., Corley W.G., Sozen M., (2005) Can strengthening for earthquake improve blast and progressive collapse resistance?. *Journal of Structural Engineering V.131 pp. 1157-1177*

Harris, H.G., Sabnis, G.M., (1999) Structural modeling and experimental techniques 2nd ed. *CRC Press Inc., Boca Raton*

Henrych, J., (1979) The dynamics of explosion and its use. *Elsevier, Amsterdam*

Hinman, E. E., Hammond, D. J., (1997) Lessons from the Oklahoma city bombing, Defensive design techniques. *ASCE Press, New York*

Jayasooriya, R., Thambiratnam, D., Perera, N., Kosse, V., (2009) Response and damage evaluation of reinforced concrete frames subjected to blast loading. *Proceedings, 34th Conference on Our World in Concrete and Structures, Singapore*

Kingery, C.N., (1966) Airblast parameters versus distance for hemispherical TNT surface burst ARBL-TR-1344. *US Army Ballistic Research Laboratories, Aberdeen Proving Ground*

Kingery, C.N., Bulmash, G., (1984) Airblast parameters from TNT spherical air burst and hemispherical surface burst ARBL-TR-02555. *US Army Ballistic Research Laboratories, Aberdeen Proving Ground*

Kinney, G.F., Graham, K.J., (1985) Explosive shocks in air. *Springer, New York*

Krauthammer T., Frye M, Schoedel T.R., Seltzer M., (2003) Advanced SDOF approach for structural concrete systems under blast and impact loads. *Proceeding of 11th International Symposium on Interaction of the Effects of Munitions with Structures*

Kupfer H., Hilsdorf H.K., Rusch H., (1969) Behavior of concrete under biaxial stresses. *ACI Journal V.66 pp. 656-666*

Lan S., Crawford J.E., Morril K.B., (2005) Design of reinforced concrete columns to resist the effects of suitcase bombs. *The 6th Asia-Pacific Conference on Shock and Impact Loads on Structures pp. 325-332*

Lan S., Crawford J.E., Morril K.B., (2005) Design of reinforced concrete columns to resist the effects of suitcase bombs. *The 6th Asia-Pacific Conference on Shock and Impact Loads on Structures pp. 325-332*

Le, J., (1999) Numerical simulation of shock (blast) wave interaction with bodies. *Communications in Nonlinear Science and Numerical Simulation, V.4(1), pp.1-7*

Lee S.C., (2006) Finite element modeling of hybrid-fiber ECC targets subjected to impact and blast. *PhD Thesis, Department of Civil Engineering National University of Singapore*

Lu X., Jiang J., (2002) Dynamic FEA and simulation of a series of blast-resist-door. *Proceeding of International Symposium on Safety Science and Technology pp. 839-843*

Luccioni B.M., Ambrosini R.D., Danesi R.F., (2005) Analysing explosive damage in an urban environment. *Proceedings of the Institution of Civil Engineers V.158(1) pp. 1-12*

Luccioni B.M., Ambrosini R.D., Danesi R.F., (2004) Analysis of building collapse under blast loads. *Engineering Structures V.26 pp. 63-71*

Luccioni B.M., Luege M., (2006) Concrete pavement slab under blast loads. *International Journal of Impact Engineering V.32 pp. 1248-1266*

Maalej M., Hashida T., Li V.C., (1995) Effect of fiber volume fraction on the off-crack plane energy in strain-hardening ECC. *Journal of American Ceramics Society V.72 pp. 3369-3375*

Maalej M., Quek S.T., Zhang J., (2005) Behavior of hybric-fiber engineered cementitious composites subjected to dynamic tensile loading and projectile impact. *Journal of Materials in Civil Engineering V.17 pp. 143-152*

Malvar L.J., Crawford J.E., Wesevich J.W., Simons D., (1997) A plasticity concrete material model for Dyna 3D. *International Journal of Impact Engineering V.19 pp. 847-873*

Malvar, L.J., Crawford, J.E., (1998) Dynamic increase factor for concrete. *Twenty-Eight DDESB Seminar, Orlando, USA*

Malvar, L.J., (1998) Review of static and dynamic properties of steel reinforcing bars. *ACI Material Journal V.95 pp.609-616*

Malvar L.J., Ross A., (1998) Review of strain rate effects for concrete in tension. *ACI Materials Journal V.95 pp. 735-739*

Malvar L.J., Crawford J.E., Morril K.B., (2000) K&C concrete material model release III –Automated generation of material model input. *Technical Report TR-99-24.3 Karagozian & Case Structural Engineers, CA, USA*

Mays C.G., Smith P.D., (1995) Blast effects on buildings. *Thomas Telford Publication, London*

Morison C.M., (2006) Dynamic response of walls and slabs by single-degree-of-freedom analysis-a critical review and revision. *International Journal of Impact Engineering V.32 pp. 1214-1247*

Morrill, K. B., Malvar, L. J., Crawford, J. E., (2001) Full scale testing of RC column retrofits to resist blast loads. *10th International Symposium on the Interaction of the Effects of Munitions with Structures, San Diego*

Mosalam K.M., Mosallam A.S., (2001) Nonlinear transient analysis of reinforced concrete slabs subjected to blast loading and retrofitted with CFRP composites. *Composites: Part B pp. 623-636*

Muszynski L.C., Purcell M.R., (2003) Use of composite reinforcement to strengthen concrete and air-entrained concrete masonry wall against air blast. *Journal of Composites for Construction V.7 pp.98-108*

Naumenko, I.A., Petrovski, I.G., (1956) The shock wave of a nuclear explosion. *Moskau*

Newmark, N. M., Hansen, R. J., (1961) Design of Blast-Resistant Structures. *on Shock and Vibration Handbook C. M. Harris and C. E. Crede, eds., McGraw Hill, New York, pp.49-1 to 49-24*

Ngo T., Mendis P.A., Teo D., Kusuma G., (2003) Behavior of high-strength concrete columns subjected to blast loading. *The Proceeding of the 7th International Conference on Steel Concrete Composite Structures (ASCCS), Sydney, Australia*

Ngo, T., Mendis, P., Gupta, A., Ramsay, J., (2007) Blast loading and blast effects on structures - an overview. *Electronic Journal of Structural Engineering, Special Issue 2007*

Ottosen N.S., Ristinmaa M., (2005) The mechanics of constitutive modeling. *Elsevier*

Pheeraphan T., Joyklad P., Nimityongskul P.., (2006) Experimental study on blast load resistance of ferrocement panels. *Journal of Ferrocement V.36 pp. 808-817*

Remennikov, A. M., and Rose, T. A., (2005) Modelling blast loads on buildings in complex city geometries. *Computers & Structures, V.83(27), pp.2197-2205*

Rickman, D. D., Murrell, D. W., and Armstrong, B. J. (2006) Improved predictive methods for airblast shielding by barrier walls. *on Structures Congress 2006 Structural Engineering and Public Safety by Cross, B. and Finke (eds.), J., St. Louis, pp. 1-14*

Rose, T. A., Smith, P. D., (2002) Influence of the principal geometrical parameters of straight city streets on positive and negative phase blast wave impulses. *International Journal of Impact Engineering, V.27(4), pp.359-376*

Sadovskyi, M.A., (1952) Mechanical effects of air shock waves from explosions according to experiments. *Moskau*

Schwer L.E., (2004) Preliminary assessment of non-lagrangian methods for penetration simulation. *The 8th International LS-Dyna User Conference, Michigan, USA*

Schwer L.E., Malvar L.J., (2005) Simplified concrete modeling with Mat_Concrete_Damage_Rel3. *JRI LS-Dyna User Week*

Shi, Y., Hao, H., Li, Z.X., (2007) Numerical simulation of blast wave interaction with structure columns. *Shock Waves, V.17, pp.113-133*

Shi, Y., Hao, H., Li, Z.X., (2008) Numerical derivation of Pressure-Impulse diagrams for prediction of RC column damage to blast loads. *International Journal of Impact Enginering V.35, pp.1213-1227*

Siddiqui, J. I., Ahmad, S., (2007) Impulsive loading on a concrete structure. *Proceeding of the Institution of Civil Engineers, V.160(4), pp.231-241*

Singhal A.C., Larson D., Govil S., Karmakar V., (1994) Simulation of blast pressure on flexible panel. *Journal of Structural Engineering V.120 pp. 2011-2019*

Smith, P. D., Mays, G. C., Rose, T. A., Teo, K. G., Roberts, B. J., (1992). Small scale models of complex geometry for blast overpressure assessment. *International Journal of Impact Engineering, V.12(3), pp.345-360*

Smith, P. D., Whalen, G. P., Feng, L. J., Rose, T. A., (2001). Blast loading on buildings from explosions in city streets. *Proceeding of the Institution of Civil Engineers, V.146(1), pp.47-55*

Smith, P. D., Rose, T. A., Krahe, S. L., Franks, M. A., (2003) Facade failure effects on blast propagation along city streets. *Proceeding of the Institution of Civil Engineers, V.156(4), pp.359-365*

Sun, J., Li, G., Liu, C., Chen, S., (2009) Research on analysis method for concrete column to resist vehicle bomb. *on Computational Structural Engineering by Yuan Y., Cui, J.Z., and Mang, H. (eds.), Springer Science, pp.669-680*

TM5-855-1, (1986) Fundamentals of protective design for conventional weapons. *US Department of Army, Washington DC: Headquarters*

TM5-1300, (1990) Technical Manual - Structures to resist the effects of the accidental explosions. *US Department of Army, Picatinny Arsenal, New Jersey*

Watson, S., MacPherson, W. N., Barton, J. S., Jones, J. D. C., Tyas, A., Pichugin, A. V., Hindle, A., Parkes, W., Dunare, C., Stevenson, T., (2006). Investigation of shock waves

in explosive blasts using fibre optic pressure sensor. *Measurement Science and Technology, V.17(6), pp.1337-1342.*

William K.J., Warnke E.P., (1974) Constitutive model for the triaxial behaviour of concrete. *Seminar on: Concrete Structures Subjected to Triaxial Stresses, Bergamo, Italy*

Wong A.K., Yeh S.H.K., (1985) Housing a nation, 25 years of public housing in Singapore. *Marusen Asia for Housing and Development Board, Singapore*

Woodson S.C., Baylot J.T., (1999) Structural collapse: Quarter-scale model experiment TR SL-99-B. *US Army Corps of Engineers, Vicksburg*

Wu C., Hao H., (2005) Dynamic response and collapse analysis of structures to blast load. *The 6th Asia-Pacific Conference on Shock and Impact Loads on Structures pp. 619-626*

Wu C., Hao H., Zhou X.Q., (2005) Dynamic response of structures to airblast load with surrounding protective walls. *The 6th Asia-Pacific Conference on Shock and Impact Loads on Structures pp. 627-634*

Wu C., Hao H., (2007) Numerical simulation of structural response and damage to simultaneous ground shock and airblast loads. *International Journal of Impact Engineering V.34 pp. 556-572*

Zhang J., Maalej M., Quek S.T., (2005) Drop-weight impact on hybric fiber ECC blast doors. *Proceeding The Third International Conference on Construction Materials: Performance, Innovations and Structural Implication, Canada pp.79*

Zhang, J., Maalej, M., Quek, S.T., (2007) Performance of hybrid-fiber ECC blast/shelter panels subjected to drop weight impact. *Journal of Materials in Civil Engineering V.19, pp.855-863*

Zhou X.Q., Hao H., Deeks A.J.,(2005) Modelling dynamic damage of concrete slab under blast loading. *The 6th Asia-Pacific Conference on Shock and Impact Loads on Structures pp.703-717*

APPENDIX A

Dimensional Analysis of RC Column Subjected to Blast Loads

The displacement at a section of a RC column subjected to a known blast loading of pressure *P* varies dynamically with time for the duration of the blast event.

A.1 Dimensional Parameters

Typical dimensional parameters to be considered include:

a. displacement, u

b. young's modulus, E

c. column's inertia, I

d. column's height, L

e. column's depth, B

f. pressure, P

g. time, t

h. mass density, ρ

The aforementioned dimensional parameters only consider flexural stiffness. With respect to the shear design calculation, although its effect on the column's stiffness in the analysis of flexural behavior is negligible, transverse reinforcement $TR = f(A_v, s)$ is another

parameter that also needs to be considered in the dynamic response analysis of RC column. Such parameters, in turn, also needs to be scaled down.

The moment of inertia *I* of RC column depends on the column's response, i.e. whether it behaves elastically (uncracked) or inelastically (when cracking has occured). It is a function of the column's dimension, amount and distribution of reinforcements. A more detail analysis of the moment of inertia *I* of a typical RC column and its derivation with respect to uncracked (I_G) and cracked (I_{CR}) conditions is given in Section A.3.

The load pressure *P* in the case of hemispherical explosion refers to the blast reflected pressure P_R applied onto RC column. It occurs within a very short loading duration t_D. Both reflected pressure P_R and loading duration t_D are a function of charge weight *W* and stand-off distance *R* between the explosive charge and the structure.

$$(P, t_D) = f(W, R) \tag{A.1}$$

A.2 Dimensional Analysis and π Term

To model the effects of the blast on the column, the pressure, *P*, is multiplied by the columns's depth, *B*, to give a load of *q N/m* of the column. The functional relationship therefore consists of seven dimensional parameters as follows,

$$F(X_1, X_2, X_3, X_4, X_5, X_6, X_7) = 0$$

$$F(u, E, I, L, q, t, \rho) = 0 \tag{A.2}$$

Such equation can be written as a function *u*,

$$u = F'(E, I, L, q, t, \rho) \tag{A.3}$$

or can be expressed in the continued product form

$$u = K(E^a t^b\ L^c q^d I^e \rho^f) \tag{A.4}$$

Table A.1 Dimensional Analysis of RC Column Subjected to Blast Loads

Exponent		a	b	c	d	e	f	Total
Parameter	u	E	t	l	q	I	ρ	
F (Force)	0	1	0	0	1	0	1	$a+d+f$
L (Length)	1	-2	0	1	-1	4	-4	$-2a+c-d+4e-4f$
T (Time)	0	0	1	0	0	0	2	$b+2f$

Forcing the expression to be dimensionally homogeneous, three equations are then obtained as,

$$\text{F: } 0 = a + d + f \tag{A.5a}$$

$$\text{L: } 1 = -2a + c - d + 4e - 4f \tag{A.5b}$$

$$\text{T: } 0 = b - 2f \tag{A.5c}$$

There are three equations with six unknowns. By selecting a, b and c as dependent parameters, the equations can therefore be solved for a, b, and c in terms of d, e, and f.

$$b = -2f \tag{A.6a}$$

$$a = -d - f \tag{A.6b}$$

$$c = 1 - d - 4e + 2f \tag{A.6c}$$

Substituting Eq. A.6 into Eq. A.4, the displacement function is now given as

$$u = K(E^{-d-f} t^{-2f}\, L^{1-d-4e+2f} q^d I^e \rho^f) \tag{A.7}$$

By grouping the same exponent value, Eq. A7 becomes

$$\left(\frac{u}{l}\right) = K\left[\left(\frac{q}{EL}\right)^d \left(\frac{I}{L^4}\right)^e \left(\frac{\rho L^2}{Et^2}\right)^f\right] \tag{A.8}$$

It can also be expressed as a function of a set of dimensionless products of π terms as

$$G(\pi_1, \pi_2, \pi_3, \pi_4) = 0$$

$$G\left(\frac{u}{L}, \frac{q}{EL}, \frac{I}{L^4}, \frac{\rho L^2}{Et^2}\right) = 0 \tag{A.9}$$

$$\frac{u}{L} = \phi\left(\frac{q}{EL}, \frac{I}{L^4}, \frac{\rho L^2}{Et^2}\right) \tag{A.10}$$

A.3 Moment of Inertia, *I*, of RC Column

To obtain the moment of inertia, *I*, of a RC column, the steel-concrete column (RC column) is hypothetically transformed either to an equivalent steel column or concrete column. In the present analysis, RC concrete is transformed to an equivalent concrete column. This is done by replacing the area of steel with an equivalent area of concrete having the same axial stiffness *AE*. Taking the modular ratio of $= \frac{E_S}{E_C}$, the resulting area of steel is equal to nA_S. This transformed area of steel is assumed to be concentrated at the same location where the steel reinforcement is placed. The calculation of elastic inertia I_G (uncracked concrete) and inelastic inertia I_{CR} (cracked concrete) of RC column is as follows.

A.3.1 Elastic Moment of Inertia

The first step is to find the centroid of the uncracked concrete section. The modular ratio is given as,

$$n = \frac{E_S}{E_C} \tag{A.11}$$

The modular ratio is then used to transform the steel reinforcements as in Fig. A.1 to an equivalent area of concrete given as,

$$A_{CS}{}' = (n-1)A_S{}' \tag{A.12a}$$

$$A_{CS} = (n-1)A_S \tag{A.12b}$$

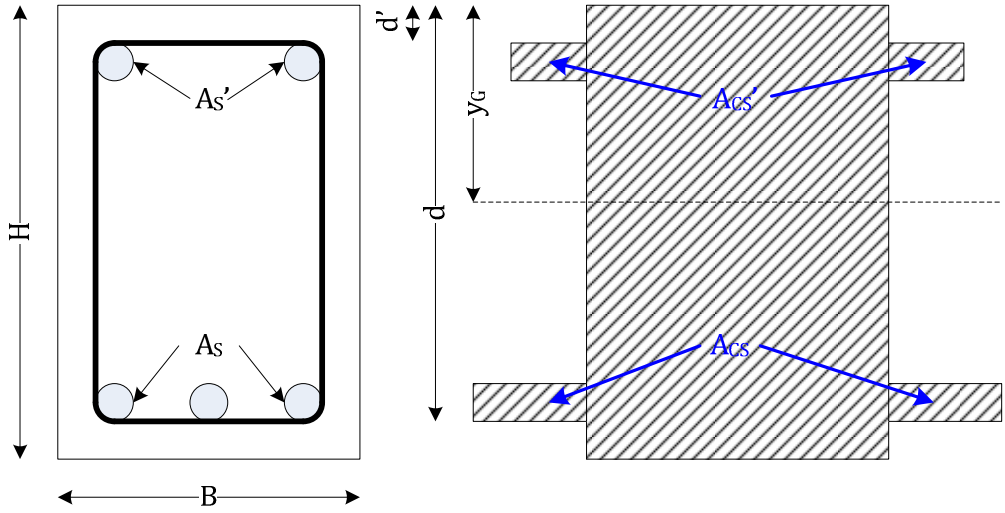

Figure A.1 Uncracked Concrete Section

The centroid of uncracked section is given as,

$$y_G = \frac{\sum A.y}{\sum A} = \frac{0.5BH^2 + A'_{CS}d' + A_{CS}d}{BH + A'_{CS} + A_{CS}} \tag{A.13}$$

Once the centroid is obtained, the moment of inertia of RC column can be easily calculated. The inertia of the uncracked concrete section is therefore obtained as,

$$I_G = \frac{\sum I + A.y^2}{\sum A}$$

$$I_G = \frac{\frac{1}{12}BH^3 + BH(0.5H - y_G)^2 + A_{CS}'(y_G - d')^2 + A_{CS}(d - y_G)^2}{BH + A'_{CS} + A_{CS}} \tag{A.14}$$

A.3.2 Inelastic Inertia

In obtaining the inelastic inertia of the RC column, the steel reinforcement is replaced by an equivalent area of concrete. Neglecting the concrete below the neutral axis, the equivalent area of tensile steel reinforcement is given as,

$$A_{CS}{}' = (n-1)A_S{}' \tag{A.15a}$$

$$A_{CS} = nA_S \tag{A.15b}$$

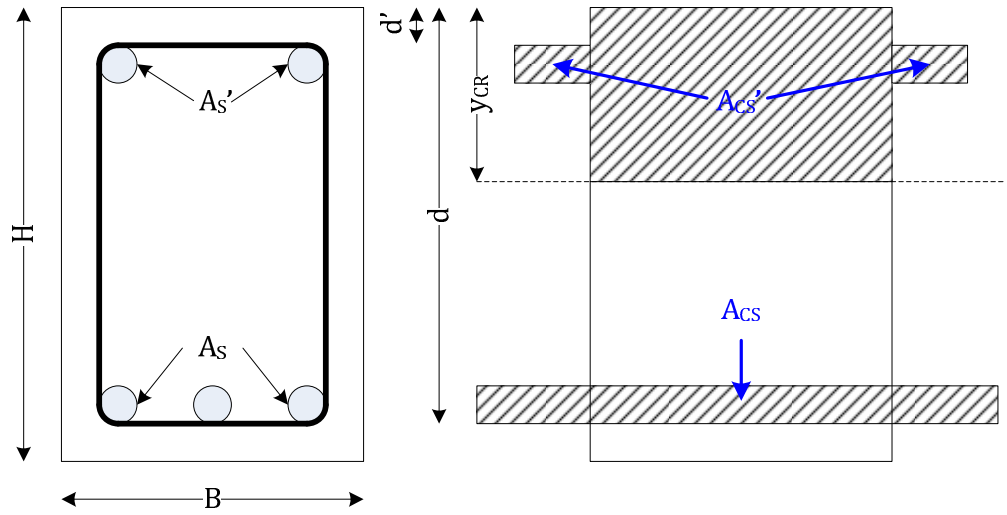

Figure A.2 Cracked Concrete Section

The centroid of cracked section can be obtained by equating the compressive and tensile areas as,

$$\sum Ay = 0$$

$$\sum Ay_{Compression} = \sum Ay_{Tension}$$

$$0.5By_{CR}{}^2 + A'_{CS}(y_{CR} - d') = A_{CS}(d - y_{CR})$$

$$0.5By_{CR}{}^2 + (A'_{CS} + A_{CS})y_{CR} - (A'_{CS}d' + A_{CS}d) = 0 \tag{A.16}$$

Eq. A.17 is of a polynomial equation having two square roots,

$$y_{CR1,2} = \frac{-(A'_{CS} + A_{CS}) \pm \sqrt{(A'_{CS} + A_{CS})^2 + 2B(A'_{CS}d' + A_{CS}d)}}{B} \quad \text{(A.17)}$$

Since the centroid of the cracked section lies within the concrete section itself, y_{CR} should be a positive value. Thus,

$$y_{CR} = \frac{-(A'_{CS} + A_{CS}) + \sqrt{(A'_{CS} + A_{CS})^2 + 2B(A'_{CS}d' + A_{CS}d)}}{B} \quad \text{(A.18)}$$

Once the centroid of cracked section is known, the inertia can be calculated. Herein, the inertia of the cracked concrete section is obtained as,

$$I_G = \frac{\sum I + A.y^2}{\sum A}$$

$$I_G = \frac{\frac{1}{12}By_{CR}{}^3 + 0.25By_{CR}{}^3 + A_{CS}{}'(y_{CR} - d')^2 + A_{CS}(d - y_{CR})^2}{By_{CR} + A'_{CS} + A_{CS}} \quad \text{(A.19)}$$

Similar to the uncracked section, the inertia of cracked section is summarized as a function of,

$$I_{CR} = f(B, H, d', d, A_S, A'_S, E_C, E_S) \quad \text{(A.20)}$$

A.4 Summary of Scaled Parameters

Summing up the aforementioned derivations, the parameters considered as a function of displacement are as follows:

- young's modulus, E_C
- column's inertia, $I = f(B, H, d', d, A_S, A'_S, E_C, E_S)$
- column's length, *L*
- column's depth, *B*

- pressure and loading duration, $P, t_d = f(W, R)$
- time, t
- mass density, ρ

The material parameters are kept to be the same as those of the prototype. Only geometrical and loading parameters are scaled down. In total, there are seven dimensional parameters that need to be scaled down based on similitude requirements to obtain a reduced scaled model. They are:

- column's height, L
- column's depth, B
- column's depth, H
- longitudinal reinforcements, A_S and $A_S^{'}$
- transverse reinforcements , A_v and s
- charge weight, W
- stand-off distance, R

APPENDIX B

Experimental Data on Quarter Scale RC and ECC Encased RC Columns

As mentioned in Chapter 4, the data obtained from the field tests proved not to be useful due to the malfunction of the trigger of the data acquisition (DAQ) system. Only data pertaining to the peak lateral displacements and residual displacements were useful for correlation with analytical and numerical studies. Figures B1 to B12 shows the recorded data obtained from concrete (C1, C2) and steel (S1, S2) strain gauges, displacement gauges (DG1, DG2), and accelerometers (A1).

The concrete strain gauges C1 and C2 were installed on the distal face of the specimen. C1 was at half height of the column at h=375mm while C2 was 20 mm below the tip of the column at h=730mm. As for the displacement gauges, DG1 was installed on the distal face of the specimen at h=375mm above the ground while DG2 was 10 mm below the column's tip at h=740mm. The steel strain gauges S1 and S2 were installed on the longitudinal rebars at ground level, h=0mm; S1 was on the tensile rebar at the incident face of column while the S2 was on the compressive rebar at the column's distal face. The accelerometer A1, as it required larger mounting space, was installed 50 mm below the column's tip at h=700mm.

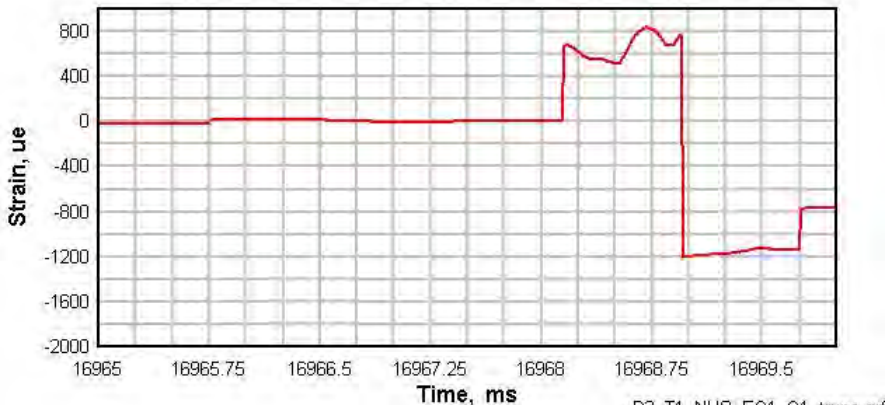

(a)

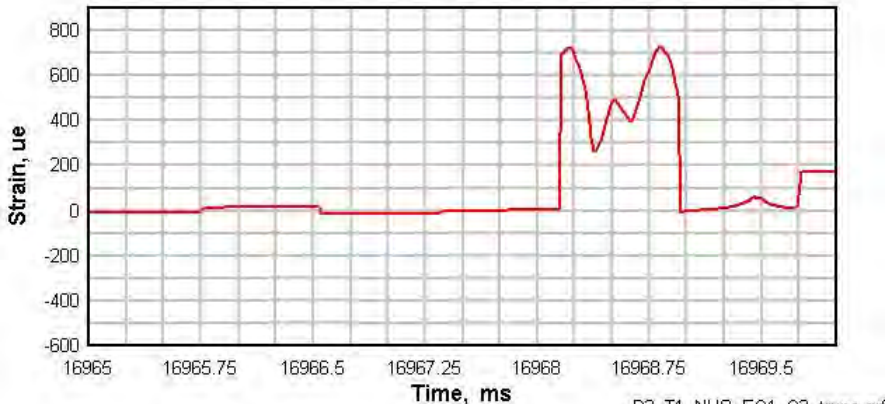

(b)

Figure B.1 Concrete strain reading of Q-ECC10-5-MI specimen from (a) Q-ECC10-5-MI_C1 located at *h*=375mm (b) Q-ECC10-5-MI_C2 located at *h*=730mm

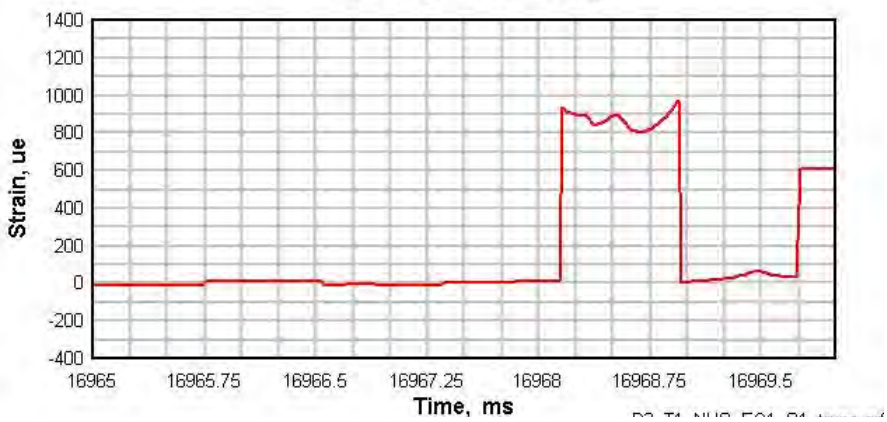

(a)

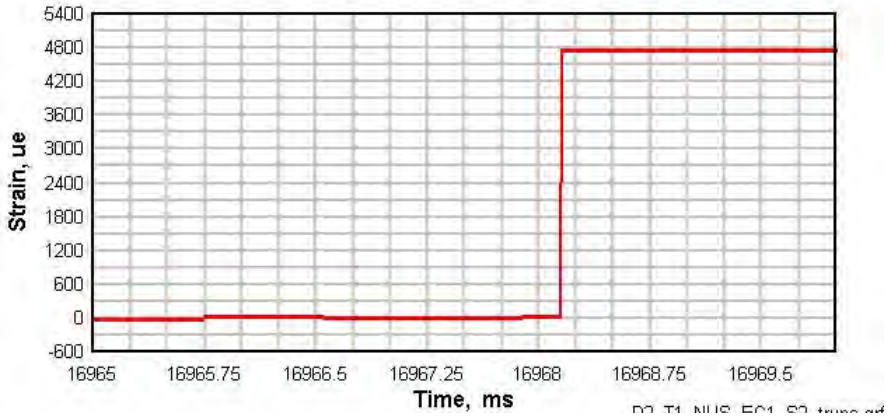

(b)

Figure B.2 Steel strain reading of Q-ECC10-5-MI specimen from (a) Q-ECC10-5-MI_S1 on tensile longitudinal reinforcement located at *h*=0mm (b) Q-ECC10-5-MI_S2 on compressive longitudinal reinforcement located at *h*=0mm

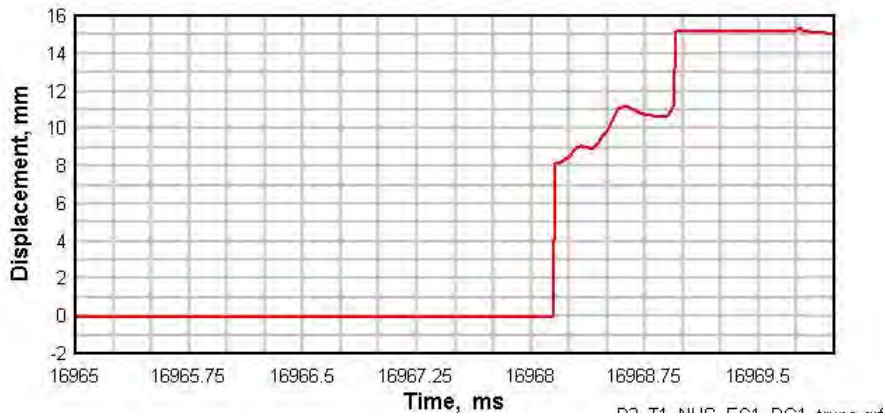

(a)

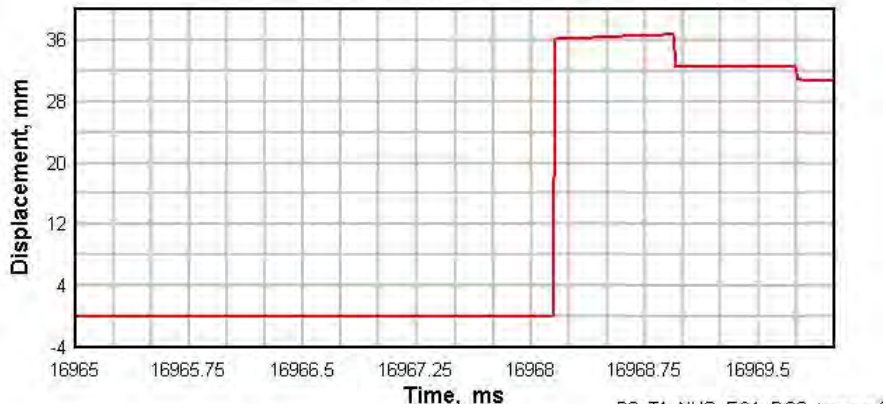

(b)

Figure B.3 Displacement reading of Q-ECC10-5-MI specimen from (a) Q-ECC10-5-MI_DG1 located at *h*=375mm (b) Q-ECC10-5-MI_DG2 located at *h*=740mm

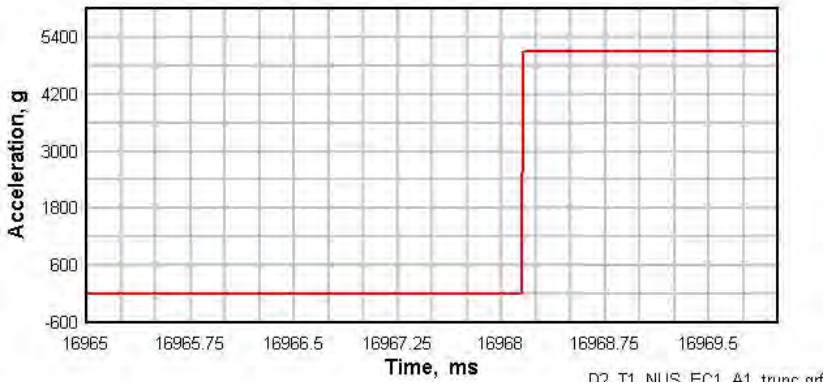

Figure B.4 Acceleration reading of Q-ECC10-5-MI specimen from Q-ECC10-5-MI_A1 located at *h*=700mm

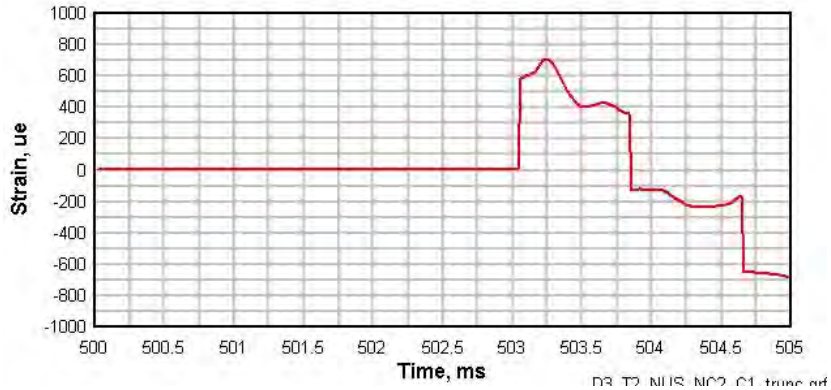

(a)

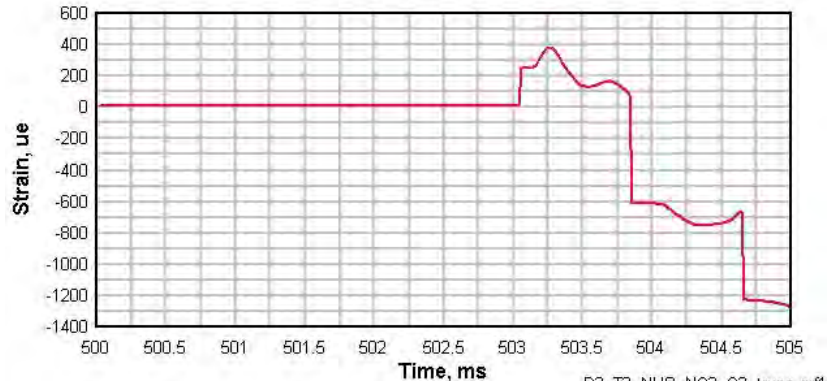

(b)

Figure B.5 Concrete strain reading of Q-UC-5-MA specimen from (a) Q-UC-5-MA_C1 located at *h*=375mm (b) Q-UC-5-MA_C2 located at *h*=730mm

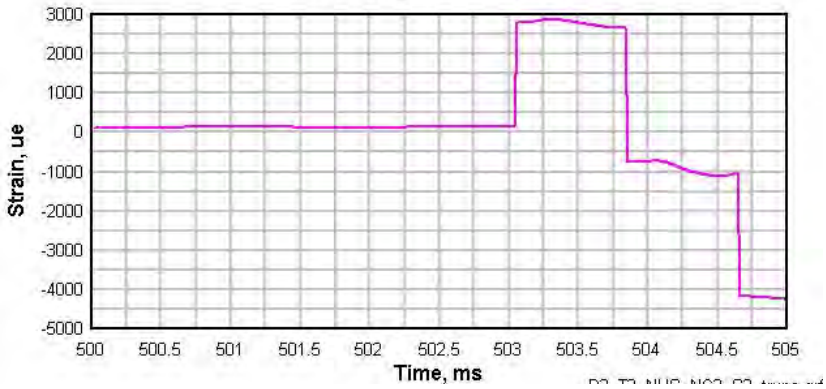

Figure B.6 Steel strain reading of Q-UC-5-MA specimen from Q-UC-5-MA_S2 on compressive longitudinal reinforcement located at *h*=0mm

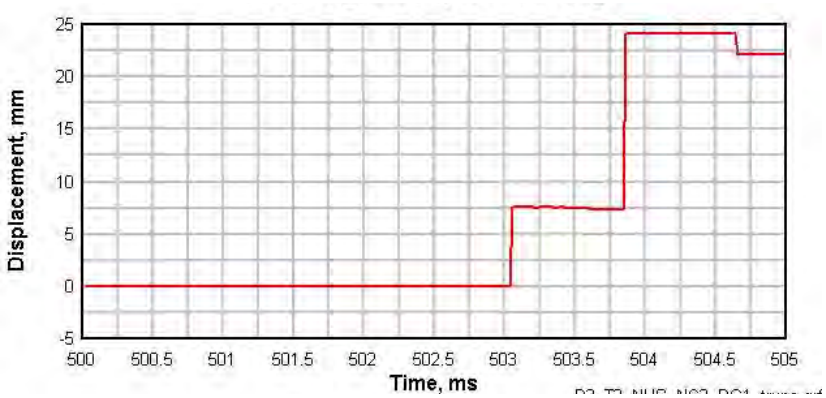

(a)

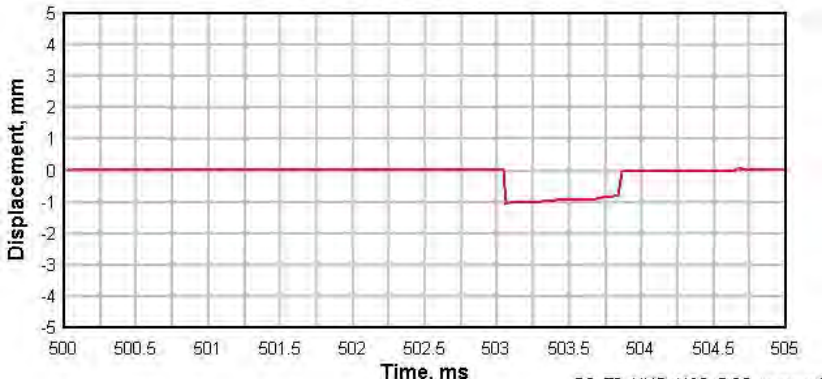

(b)

Figure B.7 Displacement reading of Q-UC-5-MA specimen from (a) Q-UC-5-MA_DG1 located at *h*=375mm (b) Q-UC-5-MA_DG2 located at *h*=740mm

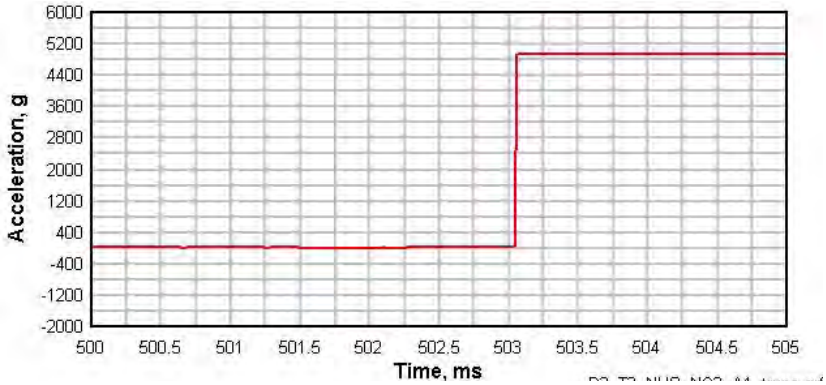

Figure B.8 Acceleration reading of Q-UC-5-MA specimen from Q-UC-5-MA_A1 located at h=700mm

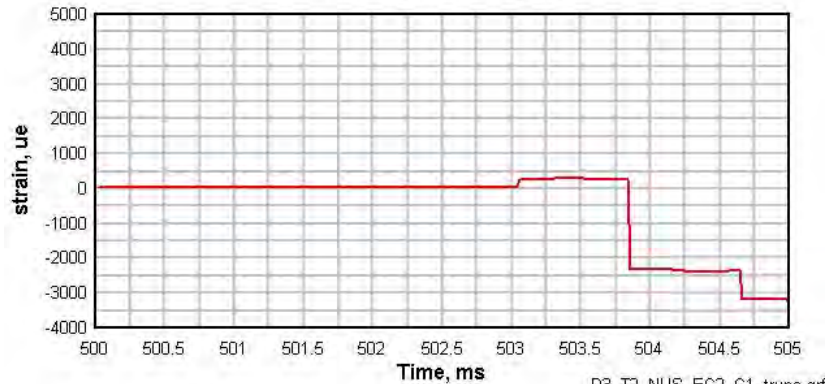

(a)

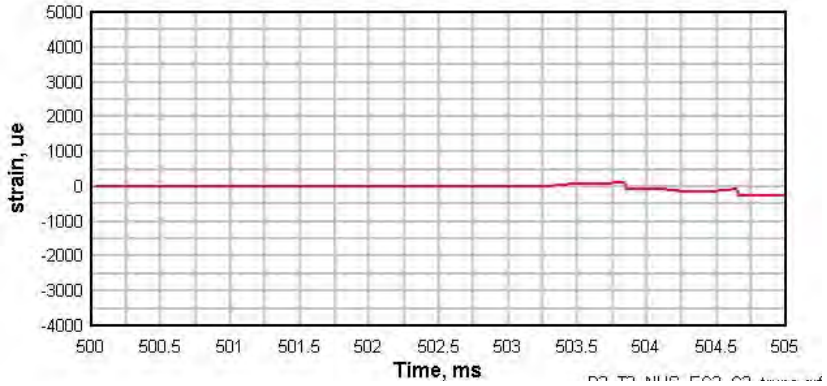

(b)

Figure B.9 Concrete strain reading of Q-ECC10-5-MA specimen from (a) Q-ECC10-5-MA_C1 located at *h*=375mm (b) Q-ECC10-5-MA_C2 located at *h*=730mm

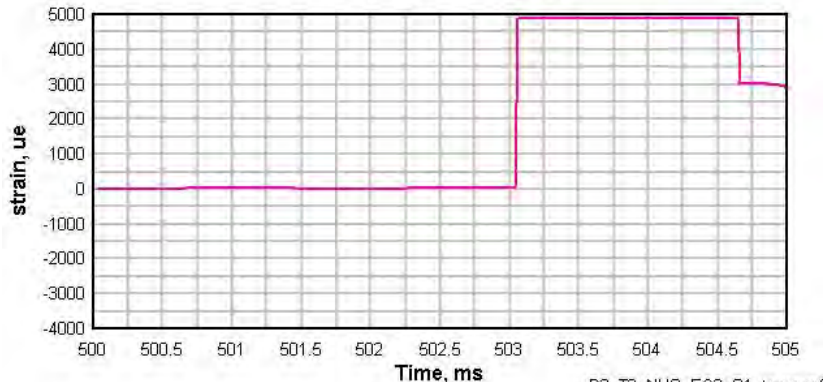

(a)

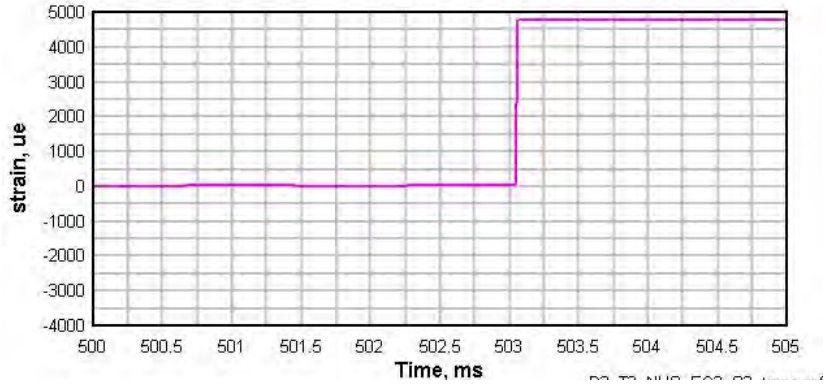

(b)

Figure B.10 Steel strain reading of Q-ECC10-5-MA specimen from (a) Q-ECC10-5-MA_S1 on tensile longitudinal reinforcement located at *h*=0mm (b) Q-ECC10-5-MA_S2 on compressive longitudinal reinforcement located at *h*=0mm

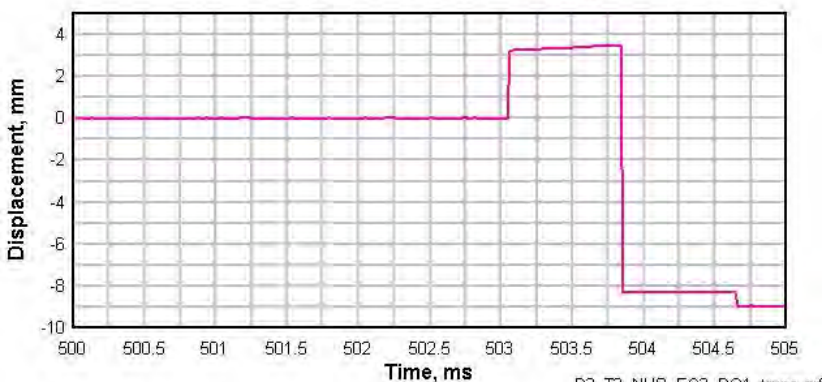

(a)

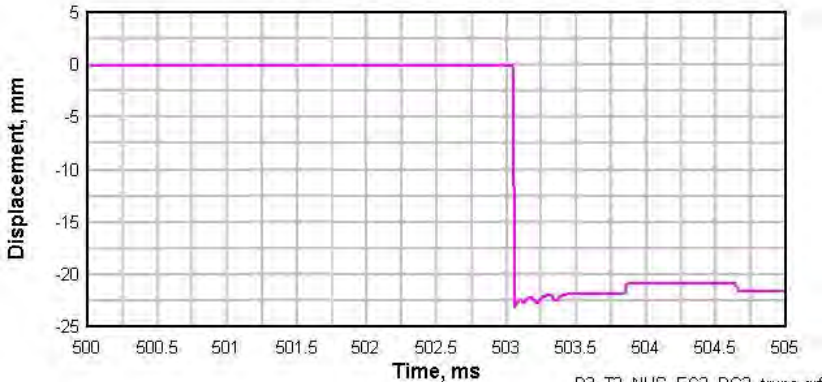

(b)

Figure B.11 Displacement reading of Q-ECC10-5-MA specimen from (a) Q-ECC10-5-MA_DG1 located at *h*=375mm (b) Q-ECC10-5-MA_DG2 located at *h*=740mm

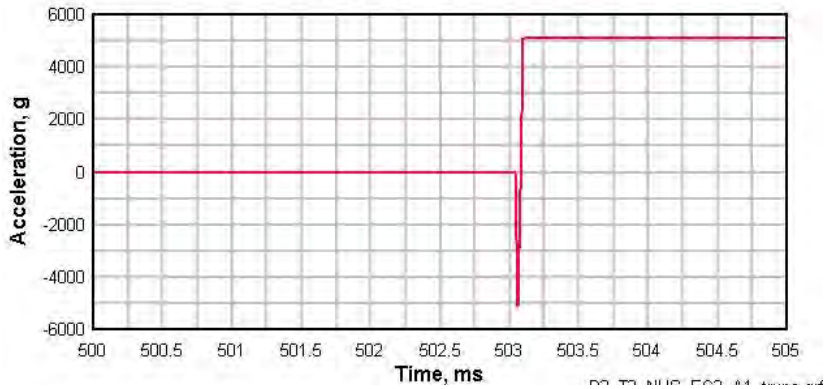

Figure B.12 Acceleration reading of Q-ECC10-5-MA specimen from Q-ECC10-5-MA_A1 located at *h*=700mm

APPENDIX C

Derivation of the Dynamic Magnification Factor (DMF) for Triangular Blast Load

Homogeneous Solution

Based on the Newton's 2nd Law for zero load condition of an undamped structure:

$$m\ddot{u} + ku = 0 \tag{C.1}$$

The homogeneous solution for this equation is:

$$u = A\cos\omega t + B\sin\omega t \tag{C.3}$$

$$\dot{u} = -\omega A\sin\omega t + \omega B\cos\omega t \tag{C.4}$$

$$\ddot{u} = -\omega^2 A\cos\omega t - \omega^2 B\cos\omega t \tag{C.5}$$

Substituting Equation C.1 into C.4 results in

$$m\left(-\omega^2 A\cos\omega t - \omega^2 B\cos\omega t\right) + k\left(A\cos\omega t + B\sin\omega t\right) = 0$$
$$-m\omega^2\left(A\cos\omega t - \omega^2 B\cos\omega t\right) + k\left(A\cos\omega t + B\sin\omega t\right) = 0$$

To obtain the nontrivial solution of this equation, $u = A\cos\omega t + B\sin\omega t \neq 0$

$$-m\omega^2 + k = 0$$
$$m\omega^2 = k$$

$$\omega = \sqrt{\frac{k}{m}} \tag{C.6}$$

Interval 1 ($0 \le t \le t_d$)

Initial Condition For Homogeneous Equation

Initial condition is needed to obtain the constants A and B. Assuming that loading is started at t=0 and the initial condition is at t=0, therefore

At time t=0, the initial conditions are:

$$\begin{aligned} u &= u_0 \\ \dot{u} &= v_0 \end{aligned} \tag{C.7}$$

Constants for the homogeneous solution are obtained as follow

$$A = u_0 \tag{C.7}$$

$$B = \frac{v_0}{\omega} \tag{C.8}$$

Therefore, the solution of homogeneous equation is given as follows

$$u = u_0 \cos \omega t + \frac{v_0}{\omega} \sin \omega t \tag{C.9}$$

Non-homogeneous Solution

This solution is a particular solution depending on the load applied on the structure. Duhamel integral is used as a particular solution of non-homogeneous equation.

$$u = \frac{1}{m\omega} \int_0^t F(\tau) \sin \omega (t - \tau)\, d\tau \tag{C.10}$$

Total Solution

Compiling both the homogeneous and non-homogeneous solution, a complete solution can be obtained as follows.

$$u = u_{\text{homogen}} + u_{\text{nonhomogen}}$$

$$u = u_0 \cos \omega t + \frac{v_0}{\omega} \sin \omega t + \frac{1}{m\omega} \int_0^t F(\tau) \sin \omega (t - \tau) \, d\tau \tag{C.11}$$

Triangular blast load is applied within a certain period of time t_d.

$$F(\tau) = F_0 \left(1 - \frac{\tau}{t_d}\right) \tag{C.12}$$

In this study, the boundary conditions for time interval, $0 \le t \le t_d$, given in Equation C.7 are all set to zero. Thus, only the non-homogeneus solution from Equation C.11 for time interval, $0 \le t \le t_d$, exists. Integration of the non-homogeneous equation is carried out using the partial integral method.

$$u = \frac{1}{m\omega} \int_0^t F(\tau) \sin \omega (t - \tau) \, d\tau$$

$$= \frac{1}{m\omega} \left\{ \int_0^t F_0 \sin \omega (t - \tau) d\tau + \int_0^t \frac{F_0 \tau}{t_d} \sin \omega (t - \tau) \, d\tau \right\}$$

$$u = \frac{1}{m\omega} \left\{ \frac{F_0}{\omega} (1 - \cos \omega t) + \frac{F_0}{t_d} \left(\frac{t}{\omega} - \frac{1}{\omega^2} \sin \omega t \right) \right\}$$

$$u = \frac{F_0}{k} (1 - \cos \omega t) + \frac{F_0}{k t_d} \left[\frac{1}{\omega} \sin \omega t - t \right] \tag{C.13}$$

$$v = u' = \frac{F_0}{k} \left\{ \omega \sin \omega t + \frac{\cos \omega t}{t_d} - \frac{1}{t_d} \right\} \tag{C.14}$$

For a structure loaded by static loading, the elastic displacement is calculated as follows:

$$u_{static} = \frac{F_0}{k} \tag{C.15}$$

Therefore, dynamic magnification factor for a SDOF structure loaded by a triangular blast load is obtained as follows.

$$DMF = \frac{u}{u_{static}} = 1 - \cos \omega_e t + \frac{1}{\omega_e t_d} \sin \omega_e t - \frac{t}{t_d} \tag{C.16}$$

In order to obtain the displacement for the next time interval, displacement and velocity at time $t = t_d$ are used as boundary conditions for the next time interval.

$$u(t_d) = -\frac{F_0}{k}\cos \omega t_d + \frac{F_0}{\omega k t_d}\sin \omega t_d \tag{C.17}$$

$$v(t_d) = \frac{F_0}{k}\left\{\omega \sin \omega t_d + \frac{\cos \omega t_d}{t_d} - \frac{1}{t_d}\right\} \tag{C.18}$$

INTERVAL 2 ($t \geq t_d$)

Displacement equation is obtained using the same step as time interval 1, by using boundary condition at time $t = t_d$. No load is applied within time interval 2, therefore the displacement equation of structure at time $t \geq t_d$ over this time interval is as follows:

$$\begin{aligned} u &= u_t \cos \omega(t - t_d) + \frac{v_t}{\omega}\sin \omega(t - t_d) \\ &= \frac{F_0}{k}\left\{-\cos\left(\omega(t - t_d) + \omega t_d\right) + \frac{1}{\omega t_d}\sin\left(\omega t_d + \omega(t - t_d)\right) - \frac{1}{\omega t_d}\sin \omega(t - t_d)\right\} \\ &= \frac{F_0}{k}\left\{-\cos \omega t + \frac{1}{\omega t_d}\sin \omega t - \frac{1}{\omega t_d}\sin \omega(t - t_d)\right\} \end{aligned} \tag{C.19}$$

$$u = \frac{F_0}{\omega t_d k}\left\{\sin \omega t - \sin \omega(t - t_d)\right\} - \frac{F_0}{k}\cos \omega t \tag{C.20}$$

Thus, for time interval 2 the dynamic magnification value is given as follows:

$$DMF = \frac{u}{u_{static}} = \frac{1}{\omega_e t_d}\left\{\sin \omega_e t - \sin \omega_e (t - t_d)\right\} - \cos \omega_e t \tag{C.21}$$